A macroscopic chemistry method for the direct simulation of non-equilibrium gas flows

Thesis by

Charles R. Lilley
Bachelor of Engineering (Hons I)
University Medal
The University of Queensland, 1994

Submitted for the Degree of
Doctor of Philosophy

Centre for Hypersonics
Division of Mechanical Engineering
School of Engineering
The University of Queensland
Brisbane, AUSTRALIA

28th June 2005

Statement of originality

To the best of my knowledge, this thesis consists wholly of my own research, except where acknowledged herein. No material presented in this thesis has been submitted for another degree at any other university.

Charles R. Lilley

28th June 2005

Acknowledgements

I would like to thank my PhD advisor Dr. Michael Macrossan, who provided valuable academic guidance throughout the course of my candidature. Dr. Macrossan spent many hours discussing all aspects of this project with me. His physical insight and ability to explain complex topics in simple terms have been invaluable. I also thank my associate advisor Associate Professor David Mee for many helpful discussions, and Professor Iain Boyd for hosting my visit to the Department of Aerospace Engineering at the University of Michigan in Ann Arbor, Michigan, USA.

This project was supported by a departmental scholarship from May 2001 to December 2001, and by an Australian Postgraduate Award from January 2002 to October 2004. The support of a Graduate School Research Travel Award to fund travel to the University of Michigan is also acknowledged.

Publications

1. Lilley, C. R. and Macrossan, M. N., "A macroscopic chemistry method for the direct simulation of gas flows," *Phys. Fluids*, Vol. 16, No. 6, June 2004, pp. 2054–2066.

2. Macrossan, M. N. and Lilley, C. R., "Viscosity of argon at temperatures >2000 K from measured shock thickness," *Phys. Fluids*, Vol. 15. No. 11, November 2003, pp. 3452–3457.

3. Lilley, C. R. and Macrossan, M. N., "Methods for implementing the stream boundary condition in DSMC computations," *Int. J. Numer. Meth. Fluids*, Vol. 42, No. 12, 30th August 2003, pp. 1363–1371.

4. Macrossan, M. N. and Lilley, C. R., "Modified generalized hard sphere collision model for direct simulation Monte Carlo calculations," *J. Thermophys. Heat Transfer*, Vol. 17, No. 2, April–June 2003, pp. 289–291.

5. Lilley, C. R. and Macrossan, M. N., "Modeling dissociation-vibration coupling with the macroscopic chemistry method," *Rarefied Gas Dynamics: Proceedings of the 24th International Symposium*, American Institute of Physics, New York, In press.

6. Lilley, C. R. and Macrossan, M. N., "DSMC calculations of shock structure with various viscosity laws," *Rarefied Gas Dynamics: Proceedings of the 23rd International Symposium*, edited by A. D. Ketsdever and E. P. Muntz, American Institute of Physics, New York, 2003, Included on CD-ROM.

7. Lilley, C. R. and Macrossan, M. N., "An investigation of a Sutherland molecular model for DSMC simulations," Tech. Rep. 09/2002, Department of Mechanical Engineering, The University of Queensland, Brisbane, July 2002.

8. Lilley, C. R. and Macrossan, M. N., "New implementation of the upstream boundary condition for DSMC simulations of rarefied flow," Tech. Rep. 04/2001, Department of Mechanical Engineering, The University of Queensland, Brisbane, October 2001.

9. Lilley, C. R., "Estimation of freestream Mach numbers in the X1 expansion tube facility from continuum considerations of pitot pressure measurements," Tech. Rep. 03/2001, Department of Mechanical Engineering, The University of Queensland, Brisbane, October 2001.

Abstract

The macroscopic chemistry method for modelling non-equilibrium reacting gas flows with the direct simulation Monte Carlo (DSMC) method is developed and tested. In the macroscopic method, the calculation of chemical reactions is decoupled from the DSMC collision routine. The number of reaction events that must be performed in a cell is calculated with macroscopic rate expressions. These expressions use local macroscopic information such as kinetic temperatures and density. The macroscopic method is applied to a symmetrical diatomic gas. For each dissociation event, a single diatom is selected with a probability based on internal energy and is dissociated into two atoms. For each recombination event, two atoms are selected at random and replaced by a single diatom. To account for the dissociation energy, the thermal energies of all particles in the cell are adjusted. The macroscopic method differs from conventional collision-based DSMC chemistry procedures, where reactions are performed as an integral part of the collision routine.

The most important advantage offered by the macroscopic method is that it can utilise reaction rates that are any function of the macroscopic flow conditions. It therefore allows DSMC chemistry calculations to be performed using rate expressions for which no conventional chemistry model may exist. Given the accuracy and flexibility of the macroscopic method, it has significant potential for modelling reacting non-equilibrium gas flows.

The macroscopic method is tested by performing DSMC calculations and comparing the results to those obtained using conventional DSMC chemistry models and experimental data. The macroscopic method gives density profiles in good agreement with experimental data in the chemical relaxation region downstream of a strong shock. Within the shock where strongly non-equilibrium conditions prevail, the macroscopic method provides good agreement with a conventional chemistry model. For the flow over a blunt axisymmetric cylinder, which also exhibits strongly non-equilibrium conditions, the macroscopic method also gives reasonable agreement with conventional chemistry models.

The ability of the macroscopic method to utilise any rate expression is demonstrated by using a two-temperature rate model that accounts for dissociation-vibration coupling effects that are important in non-equilibrium reacting flows. Relative to the case without dissociation-vibration coupling, the macroscopic method with the two-temperature model gives reduced dissociation rates in vibrationally cold flows, as expected. Also, for the blunt cylinder flow, the two-temperature model gives reduced surface heat fluxes, as expected. The macroscopic method is also tested with a number density dependent form of the equilibrium constant. For zero-dimensional chemical relaxation, the resulting relaxation histories are in good agreement with those provided by an exact Runge-Kutta solution of the relaxation behaviour.

Reviews of basic DSMC procedures and conventional DSMC chemistry models are also given. A method for obtaining the variable hard sphere parameters for collisions between particles of different species is given. Borgnakke-Larsen schemes for modelling internal energy exchange are examined in detail. Both continuous rotational and quantised vibrational energy modes are considered. Detailed derivations of viscosity and collision rate expressions for the generalised hard sphere model of Hassan and Hash [*Phys. Fluids* **5**, 738 (1993)] and the modified version of Macrossan and Lilley [*J. Thermophys. Heat Transfer* **17**, 289 (2003)] are also given.

Contents

List of Figures

List of Tables

Nomenclature

Throughout this study, conventional aerothermodynamic and mathematical notation has been used where possible. Locally, some nomenclature different to the standard has been used for clarity. To maintain consistency with the SI system of units, the kmol has been adopted as the standard unit for amount.

a	=	Isentropic sound speed $= (\gamma RT)^{1/2}$	(m/s)
A_{TLD}	=	TLD model parameter	
b	=	Miss distance	(m)
B	=	Continuum breakdown parameter	
$\mathbf{c}$	=	Thermal velocity	(m/s)
c_{mp}	=	Most probable thermal speed in an equilibrium gas	(m/s)
C^+	=	Arrhenius reaction rate parameter for bimolecular forward reaction	(m^3/kmol/s)
C^-	=	Arrhenius reaction rate parameter for termolecular recombination reaction	($\mathrm{m}^6/\mathrm{kmol}^2$/s)
C^*	=	Parameter for common form of the equilibrium constant K_c^*	($\mathrm{kmol}/\mathrm{m}^3$)
C_D	=	Drag coefficient	
Ch	=	Cheng's parameter	
C_H	=	Heat transfer coefficient	
$d\sigma$	=	Differential scattering cross-section	(m^2)
$d\omega$	=	Element of solid angle	
$d\Omega$	=	Element of solid angle	
D	=	Characteristic dimension	(m)
Da	=	Damköhler number	
e	=	Specific internal energy	(J/kg)
$f(x)$	=	Continuous probability distribution of x	Units of x^{-1}
f_s	=	Symmetry factor, equals two for like particles and unity otherwise	
F_{rot}	=	$\epsilon'_{\mathrm{rot}}/\epsilon_{\mathrm{ex}}$	
$\mathbf{g}$	=	Relative velocity of an intermolecular collision	(m/s)
g_r	=	Reference relative speed	(m/s)
$\tilde{g}$	=	Reduced relative speed $\equiv g\left[\tilde{m}/(2kT)\right]^{1/2}$	
h	=	Specific enthalpy	(J/kg)
J	=	Jacobian	
k	=	Boltzmann's constant $= 1.38066 \times 10^{-23}$ J/K	
k^+	=	Reaction rate coefficient for bimolecular forward reaction	(m^3/kmol/s)
k^+_{Arr}	=	Reaction rate coefficient for bimolecular forward reaction using Arrhenius rate model	(m^3/kmol/s)

k_{2T}^{+}	=	Reaction rate coefficient for bimolecular forward reaction using two-temperature rate model of Park [137]	(m^3/kmol/s)
k^{-}	=	Reaction rate coefficient for termolecular recombination reaction	(m^6/kmol^2/s)
K^*	=	Equilibrium constant	(kmol/m^3)
K_c^*	=	Common form of K^* that depends on T only, given by Eq. 5.2	(kmol/m^3)
K_{G}^*	=	Form of K^* from Gupta *et al.* [70] that depends on T and n, given by Eq. 5.3	(kmol/m^3)
Kn	=	Knudsen number = λ/D	
$l_{\mathrm{grad}}(Q)$	=	Gradient length scale of macroscopic flowfield quantity Q	(m)
m	=	Molecular mass = $\mathcal{M}/\mathcal{N}$	(kg)
$\tilde{m}$	=	Reduced mass	(kg)
M	=	Mach number = u/a	
$\mathcal{M}$	=	Molar mass	(kg/kmol)
n	=	Molecular number density	(m^{-3})
$\dot{n}_{\mathrm{colls}}$	=	Number of collisions occurring per unit volume per unit time	($m^{-3}s^{-1}$)
n_r	=	TCER model parameter	(m^{-3})
$\dot{n}_R$	=	Number of reactions occurring per unit volume per unit time	($m^{-3}s^{-1}$)
N_{colls}	=	Number of collisions	
N_i	=	Number of particles of species i	
N_{pairs}	=	Number of possible collision pairs to test in the NTC procedure	
N_R	=	Number of reactions	
N_{sp}	=	Number of species in a gas mixture	
$\mathcal{N}$	=	Avogadro's number = 6.02214×10^{26}/kmol	
p	=	Pressure	(Pa)
P_R	=	Reaction probability	
P_s	=	Selection probability for dissociating diatomic particle in macroscopic method	
q	=	Vibrational energy level	
q_d	=	Vibrational energy level immediately below the dissociation limit	
q_{ex}	=	Maximum possible vibrational energy level corresponding to $\epsilon_{\mathrm{ex}} = \epsilon_g + \epsilon_{\mathrm{vib}}$	
q_{max}	=	Maximum possible vibrational energy level. For unbounded harmonic oscillators $q_{\mathrm{max}} \to \infty$. For bounded harmonic oscillators, $q_{\mathrm{max}} = q_d$.	
q_t	=	Maximum possible vibrational energy level corresponding to $\epsilon_t = \epsilon + \epsilon_{\mathrm{vib}}$	
q'	=	Post-exchange vibrational energy level	
Q	=	Partition function	
r_c	=	Blunt cylinder radius	(m)
R	=	Specific gas constant = $\mathcal{R}/\mathcal{M} = k/m$	(J/kg/K)
Re	=	Reynolds number = $\rho u D/\mu$	
R_f	=	Uniformly distributed random fraction in the range (0,1)	

$R_i(a,b)$	=	Uniformly distributed random integer in the range $[a,b]$	
R_n	=	Random number sampled from a normal distribution with zero mean and unit variance	
$\mathcal{R}$	=	Universal gas constant = 8314.4 J/kmol/K	
s	=	Parameter for controlling DV coupling in two-temperature rate model of Park [137]	
S	=	Speed ratio $\equiv u/c_{\rm mp} = u\beta$	
$S(g,\chi)$	=	Angular distribution function for scattered molecules	(m^2)
t	=	Time	(s)
T	=	Thermodynamic temperature	(K)
T_e	=	Effective temperature used in two-temperature rate model of Park [137]	(K)
$T_{\rm kin}$	=	Overall kinetic temperature	(K)
T_r	=	Reference temperature	(K)
$T_{\rm rot}$	=	Rotational kinetic temperature	(K)
$T_{\rm tr}$	=	Translational kinetic temperature	(K)
$T_{\rm tr+rot}$	=	Kinetic temperature of translation and rotation	(K)
$T_{\rm vib}$	=	Vibrational kinetic temperature	(K)
$T_{\rm wall}$	=	Wall temperature	(K)
T^*	=	Equilibrium temperature	(K)
T^*	=	Reduced temperature characteristic of intermolecular potential	
$\mathbf{u}$	=	Macroscopic flow velocity	(m/s)
$\mathbf{v}$	=	Molecular velocity	(m/s)
V	=	σg	(m^3/s)
V_c	=	Cell volume	(m^3)
w	=	VSS scattering parameter	
W	=	Particle weighting factor	
x_s	=	Mole fraction of species s	
Z	=	Collision number	
α	=	Characteristic of IPL intermolecular potential	
α	=	Dissociation fraction	
α	=	TLD model parameter	
α'	=	Dissociation fraction at end of time step	
β	=	$1/c_{\rm mp}$	(s/m)
$\beta_{\rm TCE}$	=	TCE model parameter	
$\beta_{\rm VFD}$	=	VFD model parameter	
γ	=	Ratio of specific heats = c_p/c_v	
$\Gamma(x)$	=	Gamma function of x	
Δt	=	Simulation time step	(s)
ϵ	=	Orientation of collision plane relative to reference plane	
ϵ_a	=	Activation energy = $k\Theta_a$	(J)
ϵ_c	=	Total energy in a collision	(J)
ϵ_d	=	Dissociation energy = $k\Theta_d$	(J)
ϵ_d^*	=	Reduced dissociation energy for TLD model	(J)

ϵ_{ex}	=	Energy participating in a BL energy exchange event	(J)
ϵ_F	=	Threshold energy for TLD model	(J)
ϵ_g	=	Relative translational energy of two molecules in a collision	(J)
ϵ_{int}	=	Internal energy of a molecule $= \epsilon_{\text{rot}} + \epsilon_{\text{vib}}$	(J)
ϵ_{rot}	=	Rotational energy of a molecule	(J)
ϵ_{tr}	=	Translational energy of a molecule	(J)
ϵ_{vib}	=	Vibrational energy of a molecule	(J)
$\tilde{\epsilon}$	=	Reduced energy $\equiv \epsilon/(kT)$	
ϵ_3	=	Total energy in a termolecular collision, as used in the TCER model	(J)
ζ_c	=	Total number of DOF in a collision	
ζ_{ex}	=	Total number of DOF of molecules participating in a BL exchange event	
ζ_g	=	Effective number of translational DOF in a collision	
ζ_{int}	=	Effective number internal DOF in a collision	
$\bar{\zeta}_{\text{int}}$	=	Mean number of internal DOF in a collision	
ζ_{rot}	=	Number of rotational DOF	
ζ_{vib}	=	Effective number of vibrational DOF	
ζ_3	=	DOF in third body, used in TCER model	
η^+	=	Arrhenius reaction rate parameter for bimolecular forward reaction	
η^-	=	Arrhenius reaction rate parameter for termolecular recombination reaction	
η^*	=	Parameter for common form of the equilibrium constant K_c^*	
θ	=	Collision rate ratio	
Θ_a	=	Characteristic temperature of activation energy	(K)
Θ_d	=	Characteristic temperature of dissociation	(K)
Θ_{vib}	=	Characteristic temperature of vibration	(K)
κ	=	TCER model parameter	
λ_{nom}	=	Nominal mean free path $= 2\mu/(\rho\bar{c})$	(m)
λ_{VHS}	=	Mean free path for VHS molecules	(m)
μ	=	Coefficient of dynamic viscosity	(Pa·s)
$\mu_{\text{A+B}}$	=	Viscosity characteristic of the interaction between molecules of species A and B	(Pa·s)
μ_r	=	Reference viscosity	(Pa·s)
ν	=	Mean molecular collision frequency	(s^{-1})
Ξ	=	VHS model parameter $\equiv 15kT_r/[2\mu_r(2-\upsilon)(3-\upsilon)]$	(m^3/s)
ρ	=	Mass density	(kg/m^3)
σ	=	Total collision cross-section	(m^2)
σ_D	=	Momentum transfer cross-section	(m^2)
σ_r	=	Reference cross-section	(m^2)
σ_μ	=	Viscosity cross-section	(m^2)
τ	=	Mean time between collisions	(s)
υ	=	VHS model parameter $= 2/\alpha$	

ϕ	=	Energy exchange probability used in the BL method
ϕ	=	VFD model parameter for controlling extent of DV coupling
$\Phi(x)$	=	Discrete probability distribution of x
χ	=	Deflection angle in the centre-of-mass reference frame
χ_1	=	TCE and VFD model parameter $= 1 - \upsilon + \bar{\zeta}_{\text{int}}$
χ_2	=	TCE and VFD model parameter $= \eta^+ + \upsilon - \frac{1}{2}$
ψ	=	VFD model parameter $= \chi_1 + \chi_2$
Ψ_c	=	Parameter for adjusting thermal velocity components in the macroscopic chemistry method
Ψ_ϵ	=	Parameter for adjusting post-reaction energies in conventional chemistry models
$\Omega^{(l,s)\star}$	=	Non-dimensional collision integral
BL	=	Borgnakke-Larsen
CFD	=	Computational fluid dynamics
DOF	=	Degrees of freedom
DSMC	=	Direct simulation Monte Carlo
DV	=	Dissociation-vibration
EAE	=	Exact available energy
GHS	=	Generalised hard sphere
IPL	=	Inverse power law
MCM	=	Macroscopic chemistry method
MGHS	=	Modified generalised hard sphere
NTC	=	No time-counter
TCE	=	Total collision energy
TCER	=	Recombination model of Boyd [32]
TLD	=	Threshold line dissociation
VFD	=	Vibrationally favoured dissociation
VHS	=	Variable hard sphere
VSS	=	Variable soft sphere

CHAPTER 1

Introduction

Non-equilibrium flow conditions exist where the local intermolecular collision rate is insufficient to achieve equilibrium conditions before the molecules are swept downstream. In aerospace applications, non-equilibrium flow conditions are encountered under the extreme conditions imposed by hypersonic flight at high altitude. This occurs during ascent to orbit, atmospheric entry, and during transits of planetary atmospheres conducted during aerobraking and aerogravity assist manoeuvres. Non-equilibrium conditions are a defining characteristic of rarefied flows. Several schemes have been proposed for characterising the extent of rarefaction. These are considered in Chapter 3. Accurate simulation of non-equilibrium gas flows is critically important in designing and predicting the performance of hypersonic vehicles [131].

The direct simulation Monte Carlo (DSMC) method is the most common computational technique for modelling non-equilibrium gas flows in an engineering context. The DSMC method recognises the discrete molecular character of gases, and models the macroscopic gas behaviour by simulating the motions and collisions of a set of simulator particles, representative of the real gas molecules, as they move through physical space and interact with the imposed boundary conditions. In principle, any level of physical detail can be included in the simulation. The DSMC method is well documented by Bird [21]. Chapter 4 considers basic DSMC procedures, with particular emphasis on DSMC collision models and the phenomenological Borgnakke-Larsen [26] scheme for modelling internal energy exchange processes. Some aspects of kinetic theory relevant to the DSMC procedures used in this study are presented in Chapter 2. The appendices include some additional material that extends the discussions presented in the chapters.

This study is concerned with methods for modelling non-equilibrium reacting flows using the DSMC method. In most DSMC codes, the probability of a chemical reaction occurring, denoted P_R, is calculated when collision partners are selected. This reaction probability usually depends on the energies of the molecules participating in the collision. A reaction is performed if $R_f < P_R$. Chemical reactions are therefore an integral part of the DSMC collision routine. Here, these collision-based chemistry models are called conventional DSMC chemistry models. A review of common conventional DSMC chemistry models is provided in Chapter 6. Some aspects of molecular reaction dynamics relevant

to DSMC chemistry calculations are considered in Chapter 5.

Conventional chemistry models rely on an expression for P_R that plausibly approximates the expected real gas behaviour, within the limitations of mathematical tractability, numerical stability and computational efficiency. The expression for P_R is often selected to recover a suitable rate equation in the equilibrium limit, with the hope that realistic behaviour will be captured under non-equilibrium conditions. Often, conventional models result in $P_R > 1$, which is physically unrealistic. Also, achieving detailed balancing can be a problem for some models.

Several DSMC chemistry models have been proposed in which the calculation of chemical reactions is decoupled from the DSMC collision routine. In these decoupled chemistry methods, reaction events are performed after the collision routine in an independent procedure. The primary objective of this study is the development and testing of a decoupled chemistry method, called the macroscopic chemistry method. The macroscopic method is introduced in Chapter 7. The fundamental premise of the macroscopic method is that chemical reactions are infrequent events, and provided that the macroscopic reaction rate is maintained, the microscopic details of the reaction processes have a minimal influence on the flowfield properties of engineering interest. Simple, approximate schemes can therefore be used to select reacting particles and perform post-reaction energy disposal. Using the macroscopic method with such approximate schemes will provide good agreement with flowfields calculated using conventional collision-based DSMC chemistry models that attempt to accurately model reaction processes at the molecular level.

The macroscopic method is developed for a symmetrical diatomic dissociating gas, and applied to nitrogen. The number of reaction events that must be performed in a cell is based on the number required to maintain a macroscopic reaction rate. This rate is calculated with local macroscopic information such as kinetic temperature and density. For each dissociation event, a single diatomic particle is selected according to a simple selection rule, and is dissociated into two atomic particles. For each recombination event, two atomic particles are selected at random, and are combined into a single diatomic particle. To account for the dissociation energy, the translational thermal velocities of all particles in the cell are adjusted. The macroscopic method offers several significant advantages over conventional DSMC chemistry models, as discussed in Chapters 7 and 8.

The macroscopic method is tested by simulating zero-dimensional chemical relaxation, a strong one-dimensional shock, and the flow over an axisymmetric blunt cylinder. The simulation results are presented in Chapter 8, and show that the macroscopic method gives good agreement with the results of existing conventional collision-based DSMC chemistry models. By calculating dissociation rates with a two-temperature model, it is shown that macroscopic method can capture the effects of dissociation-vibration coupling, which is an important phenomenon in non-equilibrium hypersonic flows.

CHAPTER 2

Kinetic theory

2.1 Introduction and summary

This chapter gives some results from elementary kinetic theory that are relevant to the particle simulation methods considered in this study. Firstly, consideration is given to the basic dynamics of intermolecular collisions and the definition of the collision cross-section. The discussion then proceeds to the Boltzmann equation and associated Chapman-Enskog solution, equilibrium velocity and energy distributions, and then molecular transport properties. Particular emphasis is given to expressions for calculating the coefficient of viscosity. Thermal relaxation processes in which energy is exchanged between various energy modes are then discussed. Finally, methods for calculating the kinetic temperatures of different energy modes in a gas mixture are given.

Before starting the discussion, molecular and thermal velocities must be defined. The thermal velocity $\mathbf{c}$ of a gas molecule is the velocity in the stationary gas reference frame, and is given by

$$\mathbf{c} \equiv \mathbf{v} - \mathbf{u}.$$

Here $\mathbf{v}$ is the velocity of the molecule in the laboratory reference frame and $\mathbf{u}$ is the macroscopic flow velocity. In a pure gas, the flow velocity $\mathbf{u}$ is simply the mean molecular velocity $\bar{\mathbf{v}}$. In a gas mixture containing $N_{\rm sp}$ species, $\mathbf{u}$ is given by

$$\mathbf{u} = \sum_{s=1}^{N_{\rm sp}} y_s \mathbf{u}_s,$$

where y_s and $\mathbf{u}_s$ are the mass fraction and mean velocity of species s respectively.

2.2 Intermolecular collision dynamics

Consider two molecules A and B with initial velocities $\mathbf{v}_{\rm A}$ and $\mathbf{v}_{\rm B}$ participating in a binary elastic collision. These molecules have a pre-collision relative velocity $\mathbf{g} = \mathbf{v}_{\rm A} - \mathbf{v}_{\rm B}$. In the centre-of-mass reference frame, the initial velocities are

$$\mathbf{v}_{{\rm A}/m} = \frac{m_{\rm B}}{m_{\rm A} + m_{\rm B}}\mathbf{g} \quad \text{and} \quad \mathbf{v}_{{\rm B}/m} = -\frac{m_{\rm A}}{m_{\rm A} + m_{\rm B}}\mathbf{g},$$

where

$$\mathbf{v}_m = \frac{m_\mathrm{A}\mathbf{v}_\mathrm{A} + m_\mathrm{B}\mathbf{v}_\mathrm{B}}{m_\mathrm{A} + m_\mathrm{B}}$$

is the centre-of-mass velocity. It is convenient to define a reduced mass $\tilde{m}$, given by

$$\tilde{m} \equiv \frac{m_\mathrm{A} m_\mathrm{B}}{m_\mathrm{A} + m_\mathrm{B}}. \tag{2.1}$$

When $m_\mathrm{A} = m_\mathrm{B} = m$, $\mathbf{v}_m = (\mathbf{v}_\mathrm{A} + \mathbf{v}_\mathrm{B})/2$ and $\tilde{m} = m/2$. In terms of $\tilde{m}$, the initial velocities in the centre-of-mass reference frame are

$$\mathbf{v}_{\mathrm{A}/m} = \frac{\tilde{m}}{m_\mathrm{A}}\mathbf{g} \quad \text{and} \quad \mathbf{v}_{\mathrm{B}/m} = -\frac{\tilde{m}}{m_\mathrm{B}}\mathbf{g}.$$

From energy and momentum conservation, the post-collision velocities of the molecules are

$$\mathbf{v}'_\mathrm{A} = \mathbf{v}_m + \frac{\tilde{m}}{m_\mathrm{A}}\mathbf{g}' \quad \text{and} \quad \mathbf{v}'_\mathrm{B} = \mathbf{v}_m - \frac{\tilde{m}}{m_\mathrm{B}}\mathbf{g}'.$$

where $\mathbf{g}' = \mathbf{v}'_\mathrm{A} - \mathbf{v}'_\mathrm{B}$ is the relative velocity after the collision. From energy conservation, the pre-collision relative speed g and post-collision relative speed g' are equal. In the centre-of-mass reference frame, the post-collision velocities are

$$\mathbf{v}'_{\mathrm{A}/m} = \frac{\tilde{m}}{m_\mathrm{A}}\mathbf{g}' \quad \text{and} \quad \mathbf{v}'_{\mathrm{B}/m} = -\frac{\tilde{m}}{m_\mathrm{B}}\mathbf{g}'.$$

The geometry of a binary collision may be defined in terms of two impact parameters. The miss distance b and the collision plane orientation, denoted ϵ, are used here, as illustrated in Fig. 2.1. The miss distance b is the separation of the initial trajectories, and is also called the distance of closest approach [148]. The angle ϵ is the angle between the plane containing the initial trajectories of the molecules and some reference plane. The deflection angle $\chi = \chi(g, b)$ for a collision is defined in the centre-of-mass reference frame as the angle between the vectors $\mathbf{g}$ and $\mathbf{g}'$. This deflection angle is the same for both molecules in the centre-of-mass reference frame [148]. Calculating χ and hence $\mathbf{g}'$ requires detailed consideration of the collision dynamics with the intermolecular force. Generally, χ decreases with increasing b and g. Bird [21] gives

$$\mathbf{g}' = \begin{pmatrix} g'_x \\ g'_y \\ g'_z \end{pmatrix} = \cos\chi\,\mathbf{g} + \sin\chi \begin{pmatrix} \sin\epsilon\, g_{yz} \\ \left(g g_z - g_x g_y \sin\epsilon\right)/g_{yz} \\ -\left(g g_y + g_z g_x \sin\epsilon\right)/g_{yz} \end{pmatrix} \tag{2.2}$$

where $g_{yz} = \left(g_y^2 + g_z^2\right)^{1/2}$.

Intermolecular forces are established through the specification of a molecular model. Usually, molecular models are defined by an intermolecular potential ψ. For spherically

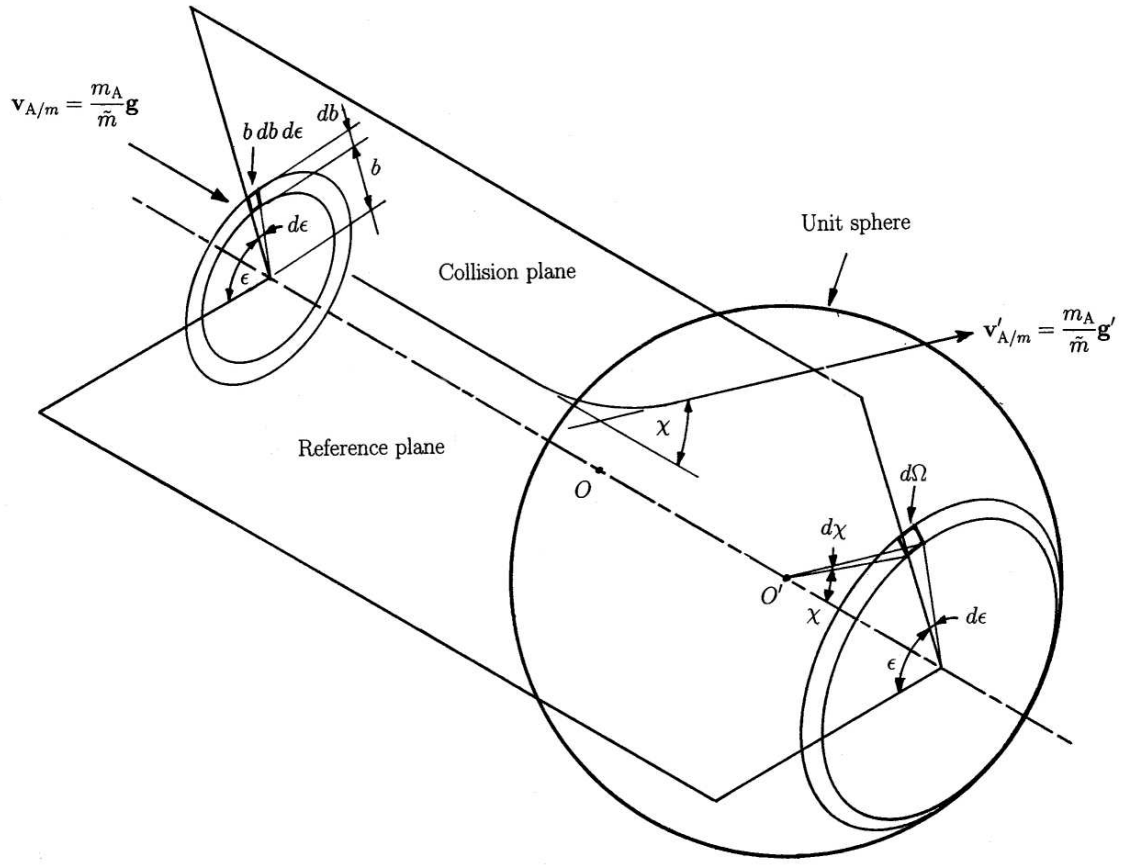

Figure 2.1: Interaction of molecule A with molecule B in the centre-of-mass reference frame. The scattering centre is O. The collision plane is at angle ϵ to the reference plane and b is the miss distance. The solid angles $d\Omega$ and $d\omega$ are represented on the unit sphere centred at O'.

symmetric potentials, ψ is related to the force F between molecules by

$$F = -d\psi(r)/dr,$$

where r is the distance between the molecular centres. A simple yet common intermolecular potential considers molecules as points surrounded by a repulsive potential specified by

$$\psi(r) = a/r^{\alpha}. \tag{2.3}$$

The parameter α describes the strength of repulsion. Here, this potential is called the inverse power law (IPL) potential. Real intermolecular potentials are comprised of both short range repulsion and weak long range attraction. The IPL potential ignores the relatively weak long range attractive forces between molecules. Another common model is the Sutherland potential, which consists of a hard sphere surrounded by a weak attractive field. Many model potentials have been proposed to capture both the repulsive and attractive portions of real potentials. Examples include the Lennard-Jones, Morse and Maitland-Smith potentials.

To calculate binary collisions, the range of intermolecular forces must be specified.

This is described in terms of the collision cross-section, which is related to the strength of interaction between molecules, and can be regarded as a measure of the collision probability. Traditionally, the collision cross-section is defined by considering a homogeneous molecular beam of intensity I interacting with a single fixed molecule that acts as a centre of force to deflect incident molecules. The beam intensity is the rate at which molecules pass through a unit area perpendicular to the beam axis, and has units of $(\mathrm{m}^2\mathrm{s})^{-1}$. For hard sphere interactions, the collision cross-section is constant and is given by $\sigma = \dot{N}/I$ where $\dot{N}$ is the rate at which incident molecules are deflected by collisions with the fixed molecule [140]. The units of σ are m^2.

For molecules that are represented by spherically symmetric point centres of force, the collision cross-section is defined in terms of the differential scattering cross-section $d\sigma$, which is related to the rate at which incident molecules are deflected by an angle between χ and $\chi + d\chi$. From Fig. 2.1, collisions with these class χ deflections that lie within the collision plane oriented at angle ϵ are scattered into the element of solid angle $d\Omega$. This solid angle is given by

$$d\Omega = \sin\chi d\chi d\epsilon.$$

All molecules in collision class χ are deflected into the element of solid angle $d\omega$, which is evaluated by

$$d\omega = \int_{\epsilon=0}^{\epsilon=2\pi} d\Omega = \int_0^{2\pi} (\sin\chi d\chi) d\epsilon = 2\pi \sin\chi d\chi.$$

Present [140] defined the differential scattering cross-section $d\sigma$ by

$$d\sigma \equiv S(g,\chi)\, d\omega = S(g,\chi)\, 2\pi \sin\chi d\chi, \tag{2.4}$$

where $S(g,\chi)$ may be regarded as an angular distribution function for scattered molecules. The rate at which molecules are scattered into $d\Omega$ equals the rate at which the molecules pass through the elemental are $b\, db\, d\epsilon$. Similarly, the rate of class χ deflections equals the rate at which molecules pass through the annular area $2\pi b\, db$. Therefore

$$d\sigma = 2\pi b\, db. \tag{2.5}$$

Eqs. 2.4 and 2.5 give

$$S(g,\chi) = \frac{b}{\sin\chi}\left|\frac{db}{d\chi}\right|.$$

The total cross-section σ is given by integrating $d\sigma$ over the range $0 \le \chi \le \pi$. Therefore

$$\sigma = 2\pi \int_0^{\pi} S(g,\chi) \sin\chi d\chi.$$

For hard sphere molecules, this total cross-section is simply the hard sphere cross-section $\sigma = \pi d^2$. For many potentials, including the IPL potential, this integral diverges because deflections still occur as $b \to \infty$. Essentially, this means that all molecules in the gas

interact with all others simultaneously. For practical purposes, the collision cross-section for such potentials must be limited. Usually, this is achieved by specifying a minimum deflection angle $\chi_{\min}$. Collisions for which the deflection angle is less than $\chi_{\min}$ are ignored, because such collisions result in small deflections and so should have a small effect on the bulk gas behaviour. In reality, quantum effects dictate that such a cut-off is physically realistic [148].

For the IPL potential, χ depends on the dimensionless impact parameter

$$z = b\left(\frac{\tilde{m}g^2}{a\alpha}\right)^{1/\alpha}$$

alone. Specifying a maximum z value $z_{\max}$ effectively defines a minimum deflection angle $\chi_{\min} = \chi_{\min}(z_{\max})$. It can be shown [21] that this results in a total collision cross-section $\sigma \propto g^{4/\alpha}$. Hard spheres are represented by $\alpha \to \infty$, giving constant σ. Using $\alpha = 4$ provides analytical simplicity because $\sigma \propto g$. IPL molecules with $\alpha = 4$ are called Maxwell molecules.

2.3 The Boltzmann equation

In kinetic theory, the state of a pure monatomic gas is described by the molecular velocity distribution function $f(\mathbf{x}, \mathbf{v}, t)$. The position of a point in phase space is given by both the position vector $\mathbf{x} = (x, y, z)$ and the velocity vector $\mathbf{v} = (v_x, v_y, v_z)$. At time t, the number of molecules dN in the six-dimensional element of phase space $dx\,dy\,dz\,dv_x\,dv_y\,dv_z$, denoted $d\mathbf{x}\,d\mathbf{v}$, is given by

$$dN = n(\mathbf{x}, t)\, f(\mathbf{x}, \mathbf{v}, t)\, d\mathbf{x}\, d\mathbf{v}.$$

The spatial and temporal evolution of f in a dilute gas is described by the Boltzmann equation. The dilute gas assumption means that the effective range of intermolecular forces is much smaller than the mean molecular spacing, and that molecules interact through binary collisions only. The Boltzmann equation is

$$\frac{\partial(nf)}{\partial t} + \mathbf{v}\cdot\frac{\partial(nf)}{\partial \mathbf{x}} + \mathbf{F}\cdot\frac{\partial(nf)}{\partial \mathbf{v}} = \left[\frac{\partial(nf)}{\partial t}\right]_{\text{coll}}. \tag{2.6}$$

The term $\mathbf{v}\cdot\partial(nf)/\partial\mathbf{x}$ represents the movement of molecules out of spatial element $d\mathbf{x}$ due to the molecular velocity $\mathbf{v}$. The term $\mathbf{F}\cdot\partial(nf)/\partial\mathbf{v}$ accounts for the acceleration of molecules out of velocity class $d\mathbf{v}$ due to the external force per unit mass $\mathbf{F}$. The collision term $[\partial(nf)/\partial t]_{\text{coll}}$ describes velocity changes due to intermolecular collisions.

The collision term represents the net effect of two competing processes on the distribution function f. The first process is the depletion of class $\mathbf{v}_1$ molecules due to class $(\mathbf{v}_1, \mathbf{v}_2) \to (\mathbf{v}_1', \mathbf{v}_2')$ collisions. Per unit volume, it can be shown [148] that the rate of these

depleting collisions that have the impact parameters b and ϵ is

$$n^2 f(\mathbf{v}_1) f(\mathbf{v}_2) gb\, db\, d\epsilon\, d\mathbf{v}_1 d\mathbf{v}_2.$$

Integrating over $0 \leq \epsilon < 2\pi$ gives

$$2\pi n^2 f(\mathbf{v}_1) f(\mathbf{v}_2) gb\, db\, d\mathbf{v}_1 d\mathbf{v}_2,$$

which is the number of depleting collisions in class $(\mathbf{v}_1, \mathbf{v}_2) \rightarrow (\mathbf{v}_1', \mathbf{v}_2')$ that have miss distance b.

The second process is the replenishment of class $\mathbf{v}_1$ molecules due to inverse collisions of class $(\mathbf{v}_1, \mathbf{v}_2) \leftarrow (\mathbf{v}_1', \mathbf{v}_2')$. Per unit volume, it can be shown that the rate of these inverse replenishing collisions is

$$2\pi n^2 f\left(\mathbf{v}_1'\right) f\left(\mathbf{v}_2'\right) gb\, db\, d\mathbf{v}_1' d\mathbf{v}_2'.$$

Inverse collisions are a special case of the principle of detailed balancing, which is the hypothesis that each molecular process and its inverse proceed, on average, at the same rate in an equilibrium system. Detailed balancing is a consequence of microscopic reversibility. Although the principle of detailed balancing does not apply with absolute generality, the exceptions are unimportant in the study of molecular gas dynamics [148].

The net change in the number of class $\mathbf{v}_1$ molecules, due to class $(\mathbf{v}_1, \mathbf{v}_2)$ collisions with miss distance b is then

$$\left[\frac{\partial\left(nf\, d\mathbf{v}_1\right)}{\partial t}\right]_{\text{coll}}^{(\mathbf{v}_1,\mathbf{v}_2),b} = 2\pi n^2 \Big[f\left(\mathbf{v}_1'\right) f\left(\mathbf{v}_2'\right) - f(\mathbf{v}_1) f(\mathbf{v}_2)\Big] gb\, db\, d\mathbf{v}_1 d\mathbf{v}_2.$$

The $d\mathbf{v}_1$ factor cancels, and using $b\, db = S(g,\chi) \sin\chi d\chi$ from Eqs. 2.4 and 2.5,

$$\left[\frac{\partial(nf)}{\partial t}\right]_{\text{coll}}^{(\mathbf{v}_1,\mathbf{v}_2),b} = 2\pi n^2 \Big[f\left(\mathbf{v}_1'\right) f\left(\mathbf{v}_2'\right) - f(\mathbf{v}_1) f(\mathbf{v}_2)\Big] gS(g,\chi) \sin\chi d\chi d\mathbf{v}_2.$$

For all collision classes, the collision term is obtained by integrating this expression over all possible velocities $-\infty < \mathbf{v}_2 < \infty$ and all possible deflection angles $0 \leq \chi \leq \pi$ to give

$$\left[\frac{\partial(nf)}{\partial t}\right]_{\text{coll}} = 2\pi \int_{-\infty}^{\infty} \int_0^{\pi} n^2 \Big[f(\mathbf{v}_1') f(\mathbf{v}_2') - f(\mathbf{v}_1) f(\mathbf{v}_2)\Big] gS(g,\chi) \sin\chi d\chi d\mathbf{v}_2. \qquad (2.7)$$

In formulating the collision term of the Boltzmann equation, a key assumption is that successive collisions of a given molecule are widely separated in space relative to the mean molecular spacing, such that there is no correlation between the initial velocities $\mathbf{v}_1$ and $\mathbf{v}_2$ of molecules in a collision [148]. This means that the velocities of collision partners are distributed independently. This important assumption is known as the molecular chaos assumption.

It is useful to consider a non-dimensional form of the Boltzmann equation. This is

achieved by defining the normalised conditions $\hat{n} \equiv n/n_r$, $\hat{f} \equiv u_r^3 f$, $\hat{t} \equiv t/t_{\text{flow}} = tu_r/x_r$, $\hat{\mathbf{v}} \equiv \mathbf{v}/u_r$, $\hat{\mathbf{x}} \equiv \mathbf{x}/x_r$ and $\hat{\mathbf{F}} \equiv x_r\mathbf{F}/u_r^2$. Here the subscript r denotes a reference value. Also the differential collision frequency $2\pi ngS(g,\chi)\sin\chi d\chi$ is normalised by dividing by a reference collision frequency ν_r [148]. By substituting these values into Eqs. 2.6 and 2.7, the non-dimensional Boltzmann equation

$$\frac{\partial(\hat{n}\hat{f})}{\partial\hat{t}} + \hat{\mathbf{v}}\cdot\frac{\partial(\hat{n}\hat{f})}{\partial\hat{\mathbf{x}}} + \hat{\mathbf{F}}\cdot\frac{\partial(\hat{n}\hat{f})}{\partial\hat{\mathbf{v}}} = \frac{1}{\xi}\left[\frac{\partial(\hat{n}\hat{f})}{\partial\hat{t}}\right]_{\text{coll}} \tag{2.8}$$

is obtained. The non-dimensional parameter ξ is

$$\xi = \frac{u_r}{x_r\nu_r},$$

and may be regarded as a non-dimensional collision time. ξ is a measure of the departure from local translational equilibrium [148]. This parameter is further examined in §3.3.

The Boltzmann equation can be extended to gas mixtures and can include molecules with internal energy, chemical reactions and radiation by adding additional dimensions and appropriate source terms [59].

The Chapman-Enskog method is used to obtain solutions of the Boltzmann equation. The Chapman-Enskog method proceeds by assuming that the normalised distribution function $\hat{f}$ may be approximated by the power series expansion

$$\hat{f} \approx \hat{f}^*\left(1 + \xi\phi_1 + \xi^2\phi_2 + \ldots\right)$$

for small ξ [148]. Here $\hat{f}^*$ denotes the local equilibrium distribution. The Chapman-Enskog method involves substituting this expression for $\hat{f}$ into the Boltzmann equation and obtaining solutions to the resulting expression. The solution method is mathematically complicated, and full details are given by Chapman and Cowling [47]. Increasingly accurate approximations of $\hat{f}$ are obtained by considering successive ξ^i terms. By retaining only first order ξ terms, the Navier-Stokes equations can be obtained. This demonstrates that the Navier-Stokes equations are only accurate for small departures from equilibrium conditions. Solutions including ξ^2 terms give the Burnett equations. The Chapman-Enskog solution also provides expressions that relate the transport coefficients to the intermolecular potential, as discussed in §2.6.

Bhatnagar, Gross and Krook [10] proposed a simplified collision term that retains many features of the detailed collision term of Eq. 2.7. This BGK collision term provides an approximation to the Boltzmann equation that is more mathematically tractable than the original form that includes the detailed collision term. The BGK collision term is

$$\left[\frac{\partial(nf)}{\partial t}\right]_{\text{coll}}^{\text{BGK}} = n\nu\left(f^* - f\right).$$

Here, f^* is the local equilibrium distribution. ν may be interpreted as a local collision frequency that is proportional to density and may depend on temperature but is assumed to be independent of molecular velocity [148]. By using the normalised parameters $\hat{n}$, $\hat{f}$, $\hat{t}$, $\hat{\mathbf{v}}$, $\hat{\mathbf{x}}$ and $\hat{\mathbf{F}}$ defined above and $\hat{\nu} \equiv \nu/\nu_r$, the BGK collision term can be written in the non-dimensional form

$$\left[\frac{\partial(\hat{n}\hat{f})}{\partial\hat{t}}\right]_{\text{coll}}^{\text{BGK}} = \frac{\hat{n}\hat{\nu}}{\xi}\left(\hat{f}^* - \hat{f}\right)$$

The BGK equation results in a Prandtl number of unity, which is physically unrealistic compared to typical values of 2/3 and 3/4 in monatomic and diatomic gases respectively [148].

2.4 Equilibrium distributions of velocity and speed

In an isolated spatially homogeneous volume of a dilute monatomic gas free of external forces, the Boltzmann equation can be written

$$\frac{df}{dt} = 2\pi \int_{-\infty}^{\infty}\int_{0}^{\pi} n\Big[f(\mathbf{v}_1')f(\mathbf{v}_2') - f(\mathbf{v}_1)f(\mathbf{v}_2)\Big] gS(g,\chi)\sin\chi d\chi d\mathbf{v}_2. \tag{2.9}$$

By defining the quantity

$$H(t) = \int_{-\infty}^{\infty} f\ln(nf)d\mathbf{v} = \langle\ln(nf)\rangle,$$

and substituting Eq. 2.9 into

$$\frac{dH}{dt} = \int_{-\infty}^{\infty}\left[1+\ln(nf)\right]\frac{df}{dt}d\mathbf{v},$$

it can be shown [47, 86, 21] that dH/dt is never positive, and that H decreases until it reaches a minimum value at the equilibrium state where $dH/dt = 0$. This is known as the Boltzmann H-theorem. The H-theorem shows the basic irreversible nature of non-equilibrium systems, and may be regarded as the kinetic theory analogue of the second law of thermodynamics. Using the H-theorem, the equilibrium Maxwell-Boltzmann distribution of molecular velocities can be determined. This is given by

$$f(\mathbf{c}) = \left(\frac{m}{2\pi kT}\right)^{\frac{1}{2}}\exp\left(-\frac{m}{2kT}\mathbf{c}^2\right) = \left(\frac{1}{2\pi RT}\right)^{\frac{1}{2}}\exp\left(-\frac{\mathbf{c}^2}{2RT}\right).$$

This normal distribution has a mean of zero and a standard deviation of $(kT/m)^{\frac{1}{2}} = (RT)^{\frac{1}{2}}$. The distribution of thermal speeds $c = |\mathbf{c}|$ is

$$f(c) = 4\pi c^2\left(\frac{m}{2\pi kT}\right)^{\frac{3}{2}}\exp\left(-\frac{m}{2kT}c^2\right) = 4\pi c^2\left(\frac{1}{2\pi RT}\right)^{\frac{3}{2}}\exp\left(-\frac{c^2}{2RT}\right).$$

The most probable thermal speed $c_{\rm mp}$ is

$$c_{\rm mp} = (2kT/m)^{\frac{1}{2}} = (2RT)^{\frac{1}{2}}$$

and the mean thermal speed $\bar{c}$ is

$$\bar{c} = \left[8kT/(\pi m)\right]^{\frac{1}{2}} = (8RT/\pi)^{\frac{1}{2}}.$$

For convenience, the reciprocal of $c_{\rm mp}$ is often used, denoted

$$\beta \equiv 1/c_{\rm mp} = \left[m/(2kT)\right]^{\frac{1}{2}} = 1/(2RT)^{\frac{1}{2}}.$$

This definition allows $f(\mathbf{c})$ and $f(c)$ to be written in the more convenient forms

$$f(\mathbf{c}) = \left(\beta/\pi^{\frac{1}{2}}\right)\exp\left(-\beta^2\mathbf{c}^2\right) \quad \text{and} \quad f(c) = \left(4\beta^3/\pi^{\frac{1}{2}}\right)c^2\exp\left(-\beta^2c^2\right).$$

By defining a reduced velocity $\tilde{\mathbf{c}} \equiv \mathbf{c}/c_{\rm mp} = \mathbf{c}\beta$ and a reduced speed $\tilde{c} \equiv c/c_{\rm mp} = c\beta$, these distributions become

$$f(\tilde{\mathbf{c}}) = \exp\left(-\tilde{\mathbf{c}}^{\,2}\right)/\pi^{\frac{1}{2}} \quad \text{and} \quad f(\tilde{c}) = \left(4/\pi^{\frac{1}{2}}\right)\tilde{c}^{\,2}\exp\left(-\tilde{c}^{\,2}\right).$$

These distributions are shown in Fig. 2.2. The distribution of molecular velocities is given by

$$f(\mathbf{v}) = \left(\beta/\pi^{\frac{1}{2}}\right)\exp\left[-\beta^2\left(\mathbf{v}-\mathbf{u}\right)^2\right].$$

The speed ratio S, which is analogous to the Mach number $M = u/a = u/(\gamma RT)^{1/2}$, is defined by

$$S \equiv u/c_{\rm mp} = u\beta = u/(2RT)^{\frac{1}{2}}.$$

In a pure gas $M/S = (2/\gamma)^{1/2}$. For a monatomic gas with $\gamma = 5/3$ then $M/S \approx 1.10$. For a diatomic gas with $\gamma = 7/5$ then $M/S \approx 1.20$.

For species s in a gas mixture containing $N_{\rm sp}$ species, the fraction of molecules in thermal speed class c is $x_s f_s(c)dc$, where $f_s(c)$ and x_s are the thermal speed distribution and mole fraction of species s respectively. The fraction of molecules of all species in class c is

$$f(c)dc = \sum_{s=1}^{N_{\rm sp}} x_s f_s(c)dc = \left[\sum_{s=1}^{N_{\rm sp}} x_s f_s(c)\right]dc.$$

For a gas mixture, the thermal speed distribution is therefore

$$f(c) = \sum_{s=1}^{N_{\rm sp}} x_s f_s(c),$$

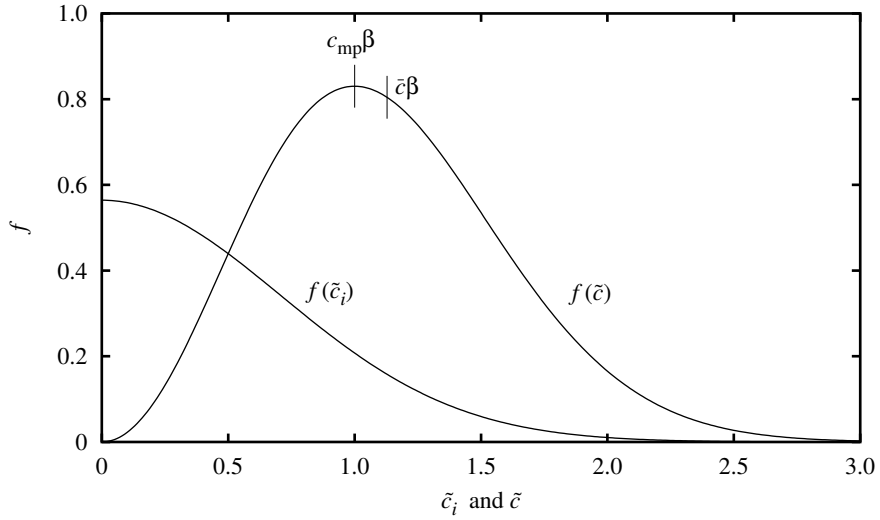

Figure 2.2: Equilibrium distributions of reduced thermal velocity component $\tilde{c}_i$ and reduced thermal speed $\tilde{c} = |\tilde{\mathbf{c}}|$.

and the mean thermal speed is simply

$$\bar{c} = \sum_{s=1}^{N_{\rm sp}} x_s \bar{c}_s.$$

The most probable thermal speed in a gas mixture is found by evaluating

$$\frac{d}{dc} f(c) = \frac{d}{dc} \sum_{s=1}^{N_{\rm sp}} x_s f_s(c) = 0.$$

In an equilibrium gas, the distribution of relative speeds g between molecules is

$$f(g) = \frac{4}{\pi^{\frac{1}{2}}} \left(\frac{\tilde{m}}{2kT} \right)^{\frac{3}{2}} g^2 \exp\left(-\frac{\tilde{m} g^2}{2kT} \right). \tag{2.10}$$

By defining a reduced relative speed

$$\tilde{g}^2 \equiv \tilde{m} g^2 / (2kT), \tag{2.11}$$

Eq. 2.10 becomes

$$f(\tilde{g}) = \left(4/\pi^{\frac{1}{2}} \right) \tilde{g}^2 \exp\left(-\tilde{g}^2 \right). \tag{2.12}$$

2.5 Equilibrium distributions of energy

The translational kinetic energy of a molecule, denoted $\epsilon_{\rm tr}$, is given by $\epsilon_{\rm tr} = mc^2/2$. The distribution of $\epsilon_{\rm tr}$ is obtained by evaluating $f(\epsilon_{\rm tr}) = f(c) dc/d\epsilon_{\rm tr}$, and is

$$f(\epsilon_{\rm tr}) = \frac{2}{\pi^{\frac{1}{2}} kT} \left(\frac{\epsilon_{\rm tr}}{kT} \right)^{\frac{1}{2}} \exp\left(-\frac{\epsilon_{\rm tr}}{kT} \right).$$

When considering equilibrium molecular energy distributions, it is often convenient to employ the reduced energy

$$\tilde{\epsilon} \equiv \epsilon/(kT).$$

$f(\epsilon_{\rm tr})$ then becomes

$$f(\tilde{\epsilon}_{\rm tr}) = \left(2/\pi^{\frac{1}{2}}\right) \tilde{\epsilon}_{\rm tr}^{\frac{1}{2}} \exp\left(-\tilde{\epsilon}_{\rm tr}\right). \tag{2.13}$$

From statistical mechanics, the distribution of discrete energy levels in an equilibrium gas can be obtained [148]. This discrete Boltzmann distribution is given by

$$\Phi(l) = \frac{N^*(l)}{N} = \frac{1}{Q}\, g_l \exp\left[-\frac{\epsilon(l)}{kT}\right]. \tag{2.14}$$

Here $N^*(l)$ is the number of molecules in level l at equilibrium and N is the total number of molecules, so $\Phi(l)$ is the fraction of molecules in level l at equilibrium. $\epsilon(l)$ and g_l are the energy and degeneracy of level l respectively. The partition function Q is the normalisation constant for the discrete distribution, given by

$$Q = \sum_l g_l \exp\left[-\frac{\epsilon(l)}{kT}\right].$$

In the classical limit where the separation of energy levels tends to zero, it can be shown [85] that Eq. 2.14 reduces to the continuous distribution

$$f(\epsilon) = \frac{1}{\Gamma(\zeta/2)kT}\left(\frac{\epsilon}{kT}\right)^{\zeta/2-1} \exp\left(-\frac{\epsilon}{kT}\right), \tag{2.15}$$

where ζ is the effective number of DOF. Here this will be called the continuous Boltzmann distribution. In terms of the reduced energy $\tilde{\epsilon} \equiv \epsilon/(kT)$, Eqs. 2.14 and 2.15 become

$$\Phi(l) = \frac{N^*(l)}{N} = \frac{g_l \exp\left[-\tilde{\epsilon}(l)\right]}{Q}.$$

and

$$f\left(\tilde{\epsilon}\right) = \tilde{\epsilon}^{\,\zeta/2-1} \exp\left(-\tilde{\epsilon}\right)/\Gamma(\zeta/2). \tag{2.16}$$

respectively. The mean energy $\langle\tilde{\epsilon}\rangle$ of the continuous Boltzmann distribution $f\left(\tilde{\epsilon}\right)$ is evaluated by

$$\langle\tilde{\epsilon}\rangle = \int_0^\infty \tilde{\epsilon} f\left(\tilde{\epsilon}\right) d\tilde{\epsilon} = \zeta/2, \quad \text{so} \quad \langle\epsilon\rangle = \zeta kT/2. \tag{2.17}$$

This provides a definition of the effective DOF ζ. The translational energy distribution of Eq. 2.13 is an example of this distribution with $\zeta = 3$ for the three DOF in translation.

2.5.1 Rotational energy

For the species typically of interest in hypersonics, the characteristic rotational temperature $\Theta_{\rm rot} \sim 2$ K. In hypersonic flows, $T \gg \Theta_{\rm rot}$ so the rotational energy mode may

be assumed to be fully excited. The distribution of rotational energies is then accurately approximated by a continuous Boltzmann distribution with ζ_{rot} DOF. For diatomic molecules, $\zeta_{\text{rot}} = 2$ and Eq. 2.16 reduces to the exponential distribution

$$f\left(\tilde{\epsilon}_{\text{rot}}\right) = \exp(-\tilde{\epsilon}_{\text{rot}}). \tag{2.18}$$

2.5.2 Vibrational energy

In contrast to rotation, vibration is usually only partially excited at the temperatures of interest in hypersonics, so the quantised nature of vibrational energy should be considered. For diatomic molecules, the degeneracy is unity and Eq. 2.14 gives

$$\begin{aligned} \Phi(q) \;=\; \frac{N^*(q)}{N} \;&=\; \frac{1}{Q_{\text{vib}}} \exp\left[-\frac{\epsilon_{\text{vib}}(q)}{kT}\right] \\ &=\; \frac{\exp\left[-\tilde{\epsilon}_{\text{vib}}(q)\right]}{Q_{\text{vib}}} \quad \text{where} \quad q = 0, 1, \ldots, q_{\max}. \end{aligned} \tag{2.19}$$

Here, the energy levels $\epsilon_{\text{vib}}(q)$ and the maximum level $q_{\max}$ depend on the vibration model. The partition function Q_{vib} is

$$Q_{\text{vib}} = \sum_q \exp\left[-\frac{\epsilon_{\text{vib}}(q)}{kT}\right] = \sum_q \exp\left[-\tilde{\epsilon}_{\text{vib}}(q)\right].$$

The discrete vibrational energy distribution of Eq. 2.19 can be expressed in a continuous form by using the Dirac δ function. Here the vibrational energy in a continuous representation is denoted $\tilde{\epsilon}^\star_{\text{vib}}$. In terms of the δ function, the continuous distribution of $\tilde{\epsilon}^\star_{\text{vib}}$ is

$$f\left(\tilde{\epsilon}^\star_{\text{vib}}\right) = \frac{\exp\left(-\tilde{\epsilon}^\star_{\text{vib}}\right)}{Q_{\text{vib}}}\, \delta\left[\tilde{\epsilon}^\star_{\text{vib}} - \tilde{\epsilon}_{\text{vib}}(q)\right] \quad \text{where} \quad q = 0, 1, \ldots, q_{\max}. \tag{2.20}$$

For anharmonic oscillators, the energy levels $\epsilon_{\text{vib}}(q)$ are obtained from spectroscopic data. For the harmonic oscillator model, energy levels are equally spaced. The ground state with $q = 0$ is used as the reference state. The ground state has vibrational energy $k\Theta_{\text{vib}}/2$, where Θ_{vib} is the characteristic vibrational temperature. Relative to the ground state, the vibrational energy of level q is

$$\epsilon_{\text{vib}}(q) = qk\Theta_{\text{vib}} \quad \text{giving} \quad \tilde{\epsilon}_{\text{vib}}(q) = q\Theta_{\text{vib}}/T. \tag{2.21}$$

For unbounded harmonic oscillators, the maximum level $q_{\max} \to \infty$ and the partition function is given by

$$1/Q_{\text{vib}} = 1 - \exp\left(-\Theta_{\text{vib}}/T\right).$$

For bounded harmonic oscillators with maximum energy level q_d, the partition function is

$$Q_{\text{vib}} = \sum_{q=0}^{q_d} \exp\left(-\frac{q\Theta_{\text{vib}}}{T}\right). \tag{2.22}$$

The mean reduced vibrational energy is given by

$$\langle\tilde{\epsilon}_{\text{vib}}\rangle = \sum_{q=0}^{q_{\max}} \tilde{\epsilon}_{\text{vib}}(q)\Phi(q).$$

For unbounded harmonic oscillators

$$\langle\tilde{\epsilon}_{\text{vib}}\rangle = \sum_{q=0}^{\infty} \frac{q\Theta_{\text{vib}}}{T}\Phi(q) = \frac{\Theta_{\text{vib}}/T}{Q_{\text{vib}}} \sum_{q=0}^{\infty} q \exp\left(-\frac{q\Theta_{\text{vib}}}{T}\right).$$

Using $x = \exp\left(-\Theta_{\text{vib}}/T\right)$ and $\sum_{q=0}^{\infty} qx^q = x/(1-x)^2$, it can be shown that

$$\langle\tilde{\epsilon}_{\text{vib}}\rangle = \frac{\Theta_{\text{vib}}/T}{\exp\left(\Theta_{\text{vib}}/T\right) - 1}. \tag{2.23}$$

Eq. 2.17 gives $\langle\tilde{\epsilon}\rangle = \zeta/2$, so the effective number of vibrational DOF for unbounded harmonic oscillators is

$$\zeta_{\text{vib}} = \frac{2\Theta_{\text{vib}}/T}{\exp\left(\Theta_{\text{vib}}/T\right) - 1}. \tag{2.24}$$

This ζ_{vib} is often used in Eq. 2.16 to provide a continuous approximation of the discrete vibrational energy distribution. Discrete and continuous distributions of $\tilde{\epsilon}_{\text{vib}}$ have been compared in Fig. 2.3. As $T \to \infty$, vibration becomes fully excited and Eq. 2.24 shows that $\zeta_{\text{vib}} \to 2$. In reality however, at $T \sim \Theta_{\text{vib}}$, significant dissociation usually occurs. Therefore vibration can rarely be regarded as fully excited.

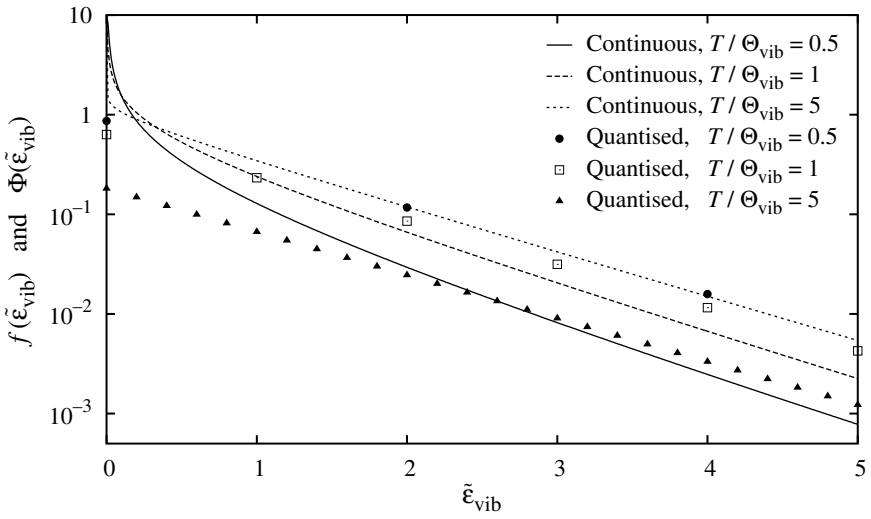

Figure 2.3: Distribution of vibrational energy levels for unbounded harmonic oscillators compared to the continuous Boltzmann approximation of Eq. 2.15. For $T/\Theta_{\text{vib}} = (0.5, 1, 5)$, $\zeta_{\text{vib}} = (0.626, 1.164, 1.807)$. Because $\zeta_{\text{vib}}/2 - 1 < 0$, $f\left(\tilde{\epsilon}_{\text{vib}}\right) \to \infty$ as $\tilde{\epsilon}_{\text{vib}} \to 0$.

2.5.3 Electronic energy

The spacing of electronic energy levels is generally an order of magnitude larger than vibrational energy levels. This study does not consider the excitation of electronic energy levels or the attendant ionisation and radiation phenomena.

2.6 Collision integrals and transport properties

In the Chapman-Enskog theory [47], integrals appear that are used to evaluate transport properties. Of particular interest are the convergent integrals

$$\begin{aligned}\sigma_D &= 2\pi \int_0^\infty (1-\cos\chi)\, b\, db \\ &= 2\pi \int_0^\pi S(g,\chi)\,(1-\cos\chi)\sin\chi d\chi\end{aligned}$$

which is called the momentum transfer cross-section, and

$$\begin{aligned}\sigma_\mu &= 2\pi \int_0^\infty \sin^2\chi b\, db \\ &= 2\pi \int_0^\infty \left(1-\cos^2\chi\right) b\, db \\ &= 2\pi \int_0^\pi S(g,\chi)\sin^3\chi d\chi\end{aligned}$$

which is called the viscosity cross-section. From the Chapman-Enskog theory [47], the first approximation to the coefficient of dynamic viscosity μ of a pure gas is

$$\mu = \frac{(5/8)(\pi m k T)^{\frac{1}{2}}}{[m/(4kT)]^4 \int_0^\infty g^7 \sigma_\mu(g) \exp\left[-mg^2/(4kT)\right] dg}.$$

Using the reduced relative speed $\tilde{g}^2 \equiv \tilde{m}g^2/(2kT) = mg^2/(4kT)$ from Eq. 2.11, this becomes

$$\mu = \frac{(5/8)(\pi m k T)^{\frac{1}{2}}}{\int_0^\infty \tilde{g}^7 \sigma_\mu \exp\left(-\tilde{g}^2\right) d\tilde{g}}. \tag{2.25}$$

Hirschfelder *et al.* [86] introduced the general collision integral, denoted $\Omega^{(l,s)}$, and defined by

$$\Omega^{(l,s)}(T) \equiv \left(\frac{2\pi kT}{\tilde{m}}\right)^{\frac{1}{2}} \int_0^\infty \int_0^\infty \tilde{g}^{2s+3} \exp\left(-\tilde{g}^2\right) \left(1-\cos^l\chi\right) b\, db\, d\tilde{g}.$$

The non-dimensional collision integral $\Omega^{(l,s)\star}(T^*)$ is obtained by dividing $\Omega^{(l,s)}$ by the corresponding hard sphere value [86]

$$\left(\frac{kT}{2\pi\tilde{m}}\right)^{\frac{1}{2}} \frac{(s+1)!}{2}\left[1-\frac{1+(-1)^l}{2+2l}\right]\pi d^2.$$

Here πd^2 is the effective hard sphere cross-section which is a measure of the molecular size. $\Omega^{(l,s)\star}$ is expressed in terms of the reduced temperature $T^* = kT/\epsilon$, where the energy ϵ characterises the potential. For hard spheres $\Omega^{(l,s)\star} = 1$. From Hirschfelder *et al.* [86], it can be shown that

$$\pi d^2 \Omega^{(1,1)\star}(T^*) = \int_0^\infty \tilde{g}^5 \sigma_D \exp\left(-\tilde{g}^2\right) d\tilde{g} \quad \text{and} \tag{2.26}$$

$$\pi d^2 \Omega^{(2,2)\star}(T^*) = \frac{1}{2}\int_0^\infty \tilde{g}^7 \sigma_\mu \exp\left(-\tilde{g}^2\right) d\tilde{g}. \tag{2.27}$$

Eq. 2.27 allows the viscosity expression of Eq. 2.25 to be written

$$\mu = \frac{5}{16}\frac{(\pi m k T)^{\frac{1}{2}}}{\pi d^2 \Omega^{(2,2)\star}}. \tag{2.28}$$

The effective hard sphere cross-section πd^2 and ϵ are obtained from experimental viscosity data with an assumed potential function [86]. For collisions between molecules of species A and species B, Hirschfelder *et al.* [86] defined the characteristic viscosity

$$\mu_{\mathrm{A+B}} = \frac{5}{16}\frac{\left[\pi\left(2\tilde{m}\right)kT\right]^{\frac{1}{2}}}{\pi d_{\mathrm{A+B}}^2 \Omega_{\mathrm{A+B}}^{(2,2)\star}}, \tag{2.29}$$

which may be regarded as the viscosity of a hypothetical gas in which all molecules have mass $2\tilde{m}$ and interact according to an intermolecular potential curve characteristic of A + B collisions. The first approximations for the diffusion and thermal conductivity coefficients are

$$D = \frac{3}{8}\frac{(\pi m k T)^{\frac{1}{2}}}{\pi d^2 \Omega^{(1,1)\star}}\frac{1}{\rho} \quad \text{and} \quad K = \frac{25}{32}\frac{(\pi m k T)^{\frac{1}{2}}}{\pi d^2 \Omega^{(2,2)\star}}\frac{c_v}{m}$$

respectively.

2.6.1 Viscosity formulae for various molecular models

Hard sphere molecules have a constant collision cross-section σ and hence the constant viscosity cross-section [86]

$$\sigma_\mu = 2\sigma/3.$$

Substituting this σ_μ into Eq. 2.25 gives

$$\mu = \frac{5}{16}\frac{(\pi m k T)^{\frac{1}{2}}}{\sigma}. \tag{2.30}$$

Hard sphere molecules therefore have $\mu \propto T^{1/2}$.

It can be shown [47] that the IPL potential of Eq. 2.3 gives $\sigma_\mu \propto g^{-4/\alpha}$ which leads to the power law viscosity behaviour where $\mu \propto T^{1/2+2/\alpha}$. This can be written

$$\mu = \mu_r \left(T/T_r\right)^{\frac{1}{2}+\frac{2}{\alpha}}, \tag{2.31}$$

where the reference viscosity μ_r and reference temperature T_r are obtained from experimental data. Hard spheres have $\alpha \to \infty$ giving $\mu \propto T^{1/2}$, and Maxwell molecules have $\alpha = 4$ giving $\mu \propto T$.

Real intermolecular potentials are comprised of both attractive and repulsive parts. At high temperatures, where typical collision speeds are high, the attractive portion of a potential, which is usually weak, becomes insignificant, and the repulsive portion of the potential dominates the collision dynamics [86]. This repulsive part of the potential can often be accurately described by an inverse power repulsion. Consequently, at high temperatures, real molecules approach the behaviour of molecules that have an IPL potential, which gives the power law viscosity behaviour apparent at high temperatures. For argon, the accuracy of the power law viscosity model at high temperatures has been demonstrated by Macrossan and Lilley [126].

The Sutherland potential results in the Sutherland viscosity formula

$$\frac{\mu}{\mu_r} = \left(\frac{T}{T_r}\right)^{\frac{3}{2}} \frac{T_r + T_s}{T + T_s} = \left(\frac{T}{T_r}\right)^{\frac{1}{2}} \frac{1 + T_s/T_r}{1 + T_s/T}. \tag{2.32}$$

As $T \to \infty$, the Sutherland viscosity approaches hard sphere viscosity $\mu \propto T^{1/2}$. Despite the simplicity of the Sutherland model, the resulting viscosity behaviour is accurate over limited temperature ranges and is therefore often used in gas dynamics. In hypersonic flows where T is high, the Sutherland viscosity formula may be inaccurate.

For realistic intermolecular potentials, the viscosity behaviour is often described in terms of tabulated values of $\Omega^{(2,2)\star}$ at various T^*. These are used in Eq. 2.28 to calculate viscosity.

It appears that experimental viscosity data is limited to $T \lesssim 2500$ K [108, 126]. Various curve fits have been proposed for viscosity at higher temperatures and some examples for nitrogen are given in §B.1.

2.6.2 Viscosity of a binary mixture

For a binary gas mixture of species A and B, the first approximation to the mixture viscosity μ_{mix} is given by Hirschfelder *et al.* [86] and is

$$\frac{1}{\mu_{\text{mix}}} = \frac{X + Y}{1 + Z}, \tag{2.33}$$

$$\text{where } X = \frac{x_{\rm A}^2}{\mu_{\rm A}} + \frac{2x_{\rm A}x_{\rm B}}{\mu_{\rm A+B}} + \frac{x_{\rm B}^2}{\mu_{\rm B}},$$

$$Y = \frac{3A^\star_{\rm A+B}}{5}\left[\frac{x_{\rm A}^2}{\mu_{\rm A}}\left(\frac{\mathcal{M}_{\rm A}}{\mathcal{M}_{\rm B}}\right) + \frac{2Wx_{\rm A}x_{\rm B}}{\mu_{\rm A+B}}\left(\frac{\mu_{\rm A+B}^2}{\mu_{\rm A}\mu_{\rm B}}\right) + \frac{x_{\rm B}^2}{\mu_{\rm B}}\left(\frac{\mathcal{M}_{\rm B}}{\mathcal{M}_{\rm A}}\right)\right],$$

$$Z = \frac{3A^\star_{\rm A+B}}{5}\left\{x_{\rm A}^2\left(\frac{\mathcal{M}_{\rm A}}{\mathcal{M}_{\rm B}}\right) + 2x_{\rm A}x_{\rm B}\left[W\left(\frac{\mu_{\rm A+B}}{\mu_{\rm A}} + \frac{\mu_{\rm A+B}}{\mu_{\rm B}}\right) - 1\right] + x_{\rm B}^2\left(\frac{\mathcal{M}_{\rm B}}{\mathcal{M}_{\rm A}}\right)\right\},$$

$$W = \frac{\left(\mathcal{M}_{\rm A} + \mathcal{M}_{\rm B}\right)^2}{4\mathcal{M}_{\rm A}\mathcal{M}_{\rm B}} \quad \text{and} \quad A^\star_{\rm A+B} = \Omega^{(2,2)\star}_{\rm A+B}/\Omega^{(1,1)\star}_{\rm A+B}.$$

Here, $\mathcal{M}_s$ and x_s are the molar mass and mole fraction of species s respectively. For heavy isotopes, an approximate binary mixture viscosity $\mu^*_{\rm mix}$ is given by [86]

$$\frac{1}{\sqrt{\mu^*_{\rm mix}}} = \frac{x_{\rm A}}{\sqrt{\mu_{\rm A}}} + \frac{x_{\rm B}}{\sqrt{\mu_{\rm B}}}. \tag{2.34}$$

For mixtures of diatomic and atomic nitrogen, the accuracy of this approximate formula is assessed in §B.1.

2.7 Molecular collision rate and mean free path

The mean collision rate for a species A molecule with molecules of species B is

$$\nu_{\rm A+B} = \langle\sigma g\rangle_{\rm A+B}\, n_{\rm B}.$$

For a species A molecule in a gas mixture containing $N_{\rm sp}$ species, the mean collision rate is

$$\nu_{\rm A} = \sum_{s=1}^{N_{\rm sp}} \nu_{{\rm A}+s} = \sum_{s=1}^{N_{\rm sp}} \langle\sigma g\rangle_{{\rm A}+s} n_s.$$

The mean collision rate per molecule in a gas mixture is obtained from [21]

$$\nu = \sum_{s=1}^{N_{\rm sp}} \left(\frac{n_s}{n}\right)\nu_s = \sum_{s=1}^{N_{\rm sp}}\left[\left(\frac{n_s}{n}\right)\sum_{p=1}^{N_{\rm sp}}\langle\sigma g\rangle_{s+p} n_p\right]. \tag{2.35}$$

The mean collision time τ is simply

$$\tau = 1/\nu. \tag{2.36}$$

The number of collisions occurring between species A and B molecules, per unit volume per unit time is

$$(\dot{n}_{\rm colls})_{\rm A+B} = n_{\rm A}\nu_{\rm A+B}/f_s = n_{\rm A}n_{\rm B}\langle\sigma g\rangle_{\rm A+B}/f_s \tag{2.37}$$

where f_s is a symmetry factor that is two for like molecules and unity otherwise. The

total number of collisions occurring per unit volume per unit time is

$$\dot{n}_{\text{colls}} = \frac{1}{2}\sum_{s=1}^{N_{\text{sp}}} n_s \nu_s = \frac{n\nu}{2}.$$

For a total of N molecules, the total number of collisions occurring during time Δt is

$$N_{\text{colls}} = \frac{N\nu\Delta t}{2} = \frac{N\Delta t}{2\tau}. \tag{2.38}$$

The mean free path λ is the average distance travelled by a gas molecule between successive collisions. It is defined in the reference frame in which $\mathbf{u} = 0$ and is a state property of the gas. From elementary kinetic theory, the approximate viscosity formula $\mu \sim \rho\bar{c}\lambda/2$ can be obtained for hard sphere molecules [148]. A measured viscosity $\mu = \mu(T)$ then allows the definition of a nominal mean free path λ_{nom} using

$$\lambda_{\text{nom}} \equiv 2\mu/\left(\rho\bar{c}\right). \tag{2.39}$$

The nominal collision rate ν_{nom} is obtained from λ_{nom} using

$$\nu_{\text{nom}} \equiv \frac{\bar{c}}{\lambda_{\text{nom}}} = \frac{4}{\pi}\frac{\rho RT}{\mu} = \frac{4}{\pi}\frac{nkT}{\mu} = \frac{4}{\pi}\frac{p}{\mu}. \tag{2.40}$$

A nominal collision time τ_{nom} may also be specified using

$$\tau_{\text{nom}} \equiv \frac{1}{\nu_{\text{nom}}} = \frac{\pi}{4}\frac{\mu}{nkT} = \frac{\pi}{4}\frac{\mu}{p}. \tag{2.41}$$

2.8 Thermal relaxation processes

Collision-induced energy exchange processes between molecular energy modes are complex phenomena. In macroscopic studies, these complex processes are often embodied in a single, temperature dependent relaxation time, which characterises of the time required for a disturbance to an initial equilibrium state to relax to a new equilibrium state. For energy mode i, the relaxation time τ_i is conventionally defined by the formula of Jeans [89] for adiabatic conditions where

$$\frac{d\bar{\epsilon}_i}{dt} = \frac{\bar{\epsilon}_i^*(t) - \bar{\epsilon}_i(t)}{\tau_i}. \tag{2.42}$$

Here, $\bar{\epsilon}_i(t)$ is the mean energy per molecule in mode i and $\bar{\epsilon}_i^*(t)$ is the instantaneous mean energy per molecule at the translational temperature of the heat bath T_{tr}. For ζ_i DOF in mode i, $\bar{\epsilon}_i^*$ is defined in terms of the translational temperature by

$$\bar{\epsilon}_i^*(t) = \zeta_i k T_{\text{tr}}(t)/2. \tag{2.43}$$

It can be shown that [75]

$$\bar{\epsilon}_i^*(t) - \bar{\epsilon}_i(t) = \left(\frac{3+\zeta_i}{3}\right)\left[\bar{\epsilon}_i^*(\infty) - \bar{\epsilon}_i(t)\right],$$

where $\bar{\epsilon}^*(\infty)$ is the equilibrium mean energy per molecules in mode i. For constant τ_i, Eq. 2.42 has the general solution

$$\frac{\bar{\epsilon}_i^*(\infty) - \bar{\epsilon}_i(t)}{\bar{\epsilon}_i^*(\infty) - \bar{\epsilon}_i(0)} = \exp\left[-\frac{t}{\tau_i}\left(\frac{\zeta_i+3}{3}\right)\right].$$

In general, τ_i may be temperature dependent, so $\tau_i = \tau_i(t)$ because there is a one-to-one correspondence between temperature and time in a simple relaxation process. By separating variables in Eq. 2.42, the expression

$$\frac{d\bar{\epsilon}_i}{\bar{\epsilon}_i^*(\infty) - \bar{\epsilon}_i(t)} = \left(\frac{3+\zeta_i}{3}\right)\frac{dt}{\tau_i(t)}$$

is obtained. If a non-dimensional time

$$\hat{t} \equiv \int_0^t \frac{dt}{\tau_i(t)} \tag{2.44}$$

is defined, then

$$\int_{\bar{\epsilon}_i(0)}^{\bar{\epsilon}_i(t)} \frac{d\bar{\epsilon}_i}{\bar{\epsilon}_i^*(\infty) - \bar{\epsilon}_i(t)} = \ln\left[\frac{\bar{\epsilon}_i(t) - \bar{\epsilon}_i^*(\infty)}{\bar{\epsilon}_i(0) - \bar{\epsilon}_i^*(\infty)}\right] = \left(\frac{3+\zeta_i}{3}\right)\int_0^t \frac{dt}{\tau_i(t)} = \left(\frac{3+\zeta_i}{3}\right)\hat{t}.$$

By defining a normalised energy

$$\Delta\hat{\epsilon}_i \equiv \frac{\bar{\epsilon}_i(t) - \bar{\epsilon}_i^*(\infty)}{\bar{\epsilon}_i(0) - \bar{\epsilon}_i^*(\infty)},$$

the relaxation behaviour can be expressed as

$$\Delta\hat{\epsilon}_i = \exp\left[-\left(\frac{3+\zeta_i}{3}\right)\hat{t}\right]. \tag{2.45}$$

Therefore, when relaxation behaviour is plotted as $\Delta\hat{\epsilon}_i$ versus $\hat{t}$, the resulting curve will be purely exponential, regardless of the temperature dependence of τ_i. When $\hat{t} = 3/(3+\zeta_i)$, $\Delta\hat{\epsilon}_i = 1/e \approx 0.3679$.

For energy mode i, the relaxation time is often defined in terms of the collision number

$$Z_i = \tau_i/\tau, \tag{2.46}$$

which is mean number of collisions that occur per molecule during relaxation the time τ_i. Values of τ_i measured by experiment are usually reduced to Z_i using the nominal collision

time of Eq. 2.41, so that

$$\tau_i = Z_i \tau_{\text{nom}} = Z_i \frac{4}{\pi} \frac{\mu(T)}{p}.$$

With the definition of Z_i from Eq. 2.46, the non-dimensional time $\hat{t}$ from Eq. 2.44 is given by

$$\hat{t} = \int_0^t \frac{dt}{Z_i \tau} = \int_0^t \frac{\nu}{Z_i} dt, \tag{2.47}$$

and may be regarded as the cumulative number of relaxing collisions per molecule between time 0 and t.

Generally, the rotational collision number Z_{rot} is in the range $1 \lesssim Z_{\text{rot}} \lesssim 10$. When most molecules are in the ground vibrational state, vibrational excitation occurs predominantly through vibrational-translational (VT) energy exchange. Under such conditions, the approximate Landau-Teller theory [102] applies and vibrational transitions occur only between adjacent energy states. It can be shown [148] that this results in vibrational relaxation as described by Eq. 2.42. At low temperatures, the vibrational relaxation number $Z_{\text{vib}} \gg Z_{\text{rot}}$. When higher levels are populated, vibration-vibration (VV) transitions become significant, which are generally considered to be more rapid than VT transitions [49]. The different rates of VT and VV transitions at different temperatures result in a vibrational relaxation equation that differs from Eq. 2.42. At high temperatures, $Z_{\text{vib}} \sim Z_{\text{rot}}$. According to Meador *et al.* [131] comprehensive models of vibrational relaxation processes, validated by experiment, do not exist.

Many theoretical and experimental investigations have demonstrated that rotational and vibrational relaxation rates depend on temperature. Over limited temperature ranges, Z_i may be assumed to be constant. However, in flowfields with large temperature variations, the temperature dependence of Z_i should be considered. In general, the rotational collision number Z_{rot} increases with temperature. Usually $Z_{\text{rot}}(T)$ is described by the model of Parker [139]. In contrast, the vibrational collision number Z_{vib} usually decreases with temperature. The vibrational relaxation time τ_{vib} given by the Landau-Teller theory [102] is not accurate due to the approximations inherent in the simple one-dimensional treatment. From experimental data, Millikan and White [133] proposed an empirical expression for τ_{vib} that is generally considered to be accurate to $T \sim 8000$ K [28]. At $T \gg 8000$ K, a condition common in hypersonic flowfields, τ_{vib} calculated with the Millikan-White formula can be smaller than the mean collision time τ. This prompted Park [136] to introduce an empirical modification to the Millikan-White formula to provide more realistic τ_{vib} at high T.

2.9 Kinetic temperatures

This section gives expressions for calculating the kinetic temperatures of individual energy modes in a gas mixture, and the overall kinetic temperature T_{kin}. The definition of the effective DOF ζ from Eq. 2.17 can be used to define the kinetic temperature. Here, the

kinetic temperature of energy mode i for species s, denoted $(T_i)_s$ is defined by

$$(T_i)_s \equiv \frac{2\langle\epsilon_i\rangle_s}{k(\zeta_i)_s} = \frac{2(e_i)_s}{R_s(\zeta_i)_s} = \frac{2(E_i)_s}{k(\zeta_i)_s N_s}. \tag{2.48}$$

Here, $\langle\epsilon_i\rangle_s$ is the mean energy in mode i per species s molecule, $(\zeta_i)_s$ is the effective number of DOF in mode i for species s molecules, $(e_i)_s$ is the specific internal energy in mode i for species s molecules, R_s is the specific gas constant for species s and $(E_i)_s$ is the total energy contained in mode i for a total of N_s molecules of species s.

In a gas mixture, the kinetic temperature of a particular energy mode may differ for different species. The kinetic temperature of mode i in a gas mixture containing N_{sp} species, denoted T_i, each of which has $(\zeta_i)_s$ effective DOF in mode i is given by

$$T_i = \frac{2\langle\epsilon_i\rangle}{k\langle\zeta_i\rangle}, \tag{2.49}$$

where

$$\langle\epsilon_i\rangle = \frac{1}{N}\sum_{s=1}^{N_{\text{sp}}}\sum_{p=1}^{N_s}(\epsilon_i)_s^p, \quad \langle\zeta_i\rangle = \frac{1}{N}\sum_{s=1}^{N_{\text{sp}}}(\zeta_i)_s N_s \quad \text{and} \quad N = \sum_{s=1}^{N_{\text{sp}}} N_s. \tag{2.50}$$

Here N_s is the number of molecules of species s and N is the total number of molecules in the mixture. Similarly, for energy modes i_i to i_n, the kinetic temperature $T_{i_1,\ldots,i_n}$ is

$$T_{i_1,\ldots,i_n} = \frac{2\langle\epsilon_{i_1,\ldots,i_n}\rangle}{k\langle\zeta_{i_1,\ldots,i_n}\rangle}.$$

2.9.1 Translational kinetic temperatures

The translational kinetic temperature T_{tr} is calculated from sampled thermal velocities. Each velocity component has one translational DOF, so $\zeta_{\text{tr}} = 3$ for all gas molecules. For a particular species with molecular mass m, the mean translational energy of velocity component x, denoted $\langle\epsilon_x\rangle$, is given by

$$\langle\epsilon_x\rangle = \int_0^\infty \epsilon_x f(\epsilon_x)d\epsilon_x = \int_{-\infty}^\infty \frac{mc_x^2}{2} f(c_x)dc_x = \frac{m}{2}\int_{-\infty}^\infty (v_x - u_x)^2 f(v_x)dv_x.$$

This integral is the variance of the distribution $f(v_x)$. For a sample of N random variates X, the best estimate of the variance of the parent population is [152]

$$\big[S(X)\big]^2 = \frac{1}{N(N-1)}\left[N\sum_{j=1}^N X_j^2 - \left(\sum_{j=1}^N X_j\right)^2\right], \tag{2.51}$$

so the best estimate of $\langle\epsilon_x\rangle$ using a sample of N velocities is

$$\langle\epsilon_x\rangle = m\big[S(v_x)\big]^2/2. \tag{2.52}$$

Using N^2 in the denominator in Eq. 2.51 rather than $N(N-1)$ gives a low estimate of $\langle \epsilon_x \rangle$. For large sample sizes, the difference will be insignificant. However, if translational temperatures are required from a small sample size, then Eqs. 2.51 and 2.52 must be used to calculate $\langle \epsilon_x \rangle$.. For a gas mixture,

$$\langle \epsilon_x \rangle = \frac{1}{N} \sum_{s=1}^{N_{\rm sp}} N_s \langle \epsilon_x \rangle_s. \tag{2.53}$$

Similar expressions are used for the kinetic temperatures of the y and z velocity components.

For a particular species s, the mean translational energy $\langle \epsilon_{\rm tr} \rangle_s$ is

$$\langle \epsilon_{\rm tr} \rangle_s = \langle \epsilon_x \rangle_s + \langle \epsilon_y \rangle_s + \langle \epsilon_z \rangle_s.$$

From Eq. 2.48,

$$(T_{x,y,z})_s = 2\langle \epsilon_{x,y,z} \rangle_s / k \quad \text{and} \quad (T_{\rm tr})_s = 2\langle \epsilon_{\rm tr} \rangle_s / (3k),$$

so the mean translational temperature of species s, denoted $(T_{\rm tr})_s$, is given by

$$(T_{\rm tr})_s = \big[(T_x)_s + (T_y)_s + (T_z)_s\big]/3.$$

For a gas mixture, the mean translational energy $\langle \epsilon_{\rm tr} \rangle$ is given by

$$\begin{aligned} \langle \epsilon_{\rm tr} \rangle &= \frac{1}{N} \sum_{s=1}^{N_{\rm sp}} N_s \langle \epsilon_{\rm tr} \rangle_s = \frac{1}{N} \sum_{s=1}^{N_{\rm sp}} N_s \big(\langle \epsilon_x \rangle_s + \langle \epsilon_y \rangle_s + \langle \epsilon_z \rangle_s \big) \\ &= \frac{1}{N} \left(\sum_{s=1}^{N_{\rm sp}} \langle \epsilon_x \rangle_s + \sum_{s=1}^{N_{\rm sp}} \langle \epsilon_y \rangle_s + \sum_{s=1}^{N_{\rm sp}} \langle \epsilon_z \rangle_s \right), \end{aligned}$$

where N is from Eq. 2.50. Using Eq. 2.53, this gives

$$\langle \epsilon_{\rm tr} \rangle = \langle \epsilon_x \rangle + \langle \epsilon_y \rangle + \langle \epsilon_z \rangle$$

for a gas mixture. From Eq. 2.49,

$$T_{x,y,z} = 2\langle \epsilon_{x,y,z} \rangle / k \quad \text{and} \quad T_{\rm tr} = 2\langle \epsilon_{\rm tr} \rangle / (3k),$$

so

$$T_{\rm tr} = (T_x + T_y + T_z)/3$$

for a gas mixture.

2.9.2 Rotational kinetic temperatures

In a gas mixture, the overall rotational kinetic temperature is given by

$$T_{\text{rot}} = \frac{2}{k}\frac{\langle \epsilon_{\text{rot}} \rangle}{\langle \zeta_{\text{rot}} \rangle} = \frac{2}{k}\left(\sum_{s=1}^{N_{\text{sp}}}\sum_{p=1}^{N_s}(\epsilon_{\text{rot}})_s^p\right)\left(\sum_{s=1}^{N_{\text{sp}}}(\zeta_{\text{rot}})_s N_s\right)^{-1}.$$

In a partially dissociated mixture of a diatomic gas A_2 and A atoms, the atomic species do not contribute to T_{rot} and can therefore be excluded from the calculation of $\langle \epsilon_{\text{rot}} \rangle$ and $\langle \zeta_{\text{rot}} \rangle$. Therefore,

$$T_{\text{rot}} = \langle \epsilon_{\text{rot}} \rangle_{A_2}/k = (e_{\text{rot}})_{A_2}/R_{A_2}.$$

2.9.3 Vibrational kinetic temperatures

For quantised vibration models, a vibrational kinetic temperature T_{vib} can be obtained from the discrete Boltzmann distribution of vibrational energy levels [21]. From Eq. 2.19, the ratio of the number molecules in the ground state $N^*(0)$ to the number in the first energy level $N^*(1)$ for species s is

$$\frac{N^*(0)}{N^*(1)} = \frac{\exp\left\{-\epsilon_{\text{vib}}(0)/\left[k(T_{\text{vib}})_s\right]\right\}}{\exp\left\{-\epsilon_{\text{vib}}(1)/\left[k(T_{\text{vib}})_s\right]\right\}} \quad \text{which gives} \quad (T_{\text{vib}})_s = \frac{\epsilon_{\text{vib}}(1) - \epsilon_{\text{vib}}(0)}{k \ln\left[N^*(0)/N^*(1)\right]}. \tag{2.54}$$

For harmonic oscillators of species s, $\epsilon_{\text{vib}}(q) = qk(\Theta_{\text{vib}})_s$, so

$$(T_{\text{vib}})_s = (\Theta_{\text{vib}})_s / \ln\left[N^*(0)/N^*(1)\right]. \tag{2.55}$$

Based on Eq. 2.49, the overall vibrational temperature in a gas mixture is calculated using

$$T_{\text{vib}} = \frac{2\langle \epsilon_{\text{vib}} \rangle}{k\langle \zeta_{\text{vib}} \rangle}. \tag{2.56}$$

This requires the effective number of vibrational DOF $(\zeta_{\text{vib}})_s$ for each species. From Eq. 2.48, these are calculated using

$$(\zeta_{\text{vib}})_s = \frac{2\langle \epsilon_{\text{vib}} \rangle_s}{k(T_{\text{vib}})_s}.$$

Eqs. 2.50 are then used to calculate the overall vibrational temperature T_{vib} for the mixture.

Eq. 2.54 gives negative temperatures if there is a population inversion such that more molecules occupy the first level than the ground state [21]. From Eq. 2.54, it can be shown that the gradient of the line of ϵ_{vib}/k versus $\ln N^*$ is $-1/(T_{\text{vib}})_s$. Ideally, $(T_{\text{vib}})_s$ should be determined by using linear regression to estimate the gradient from the populations of all energy levels.

For unbounded harmonic oscillators, an alternative method exists because ζ_{vib} has a

closed form solution. Eq. 2.24 gives

$$(\zeta_{\text{vib}})_s = \frac{2(\Theta_{\text{vib}})_s}{\exp\left[(\Theta_{\text{vib}})_s/(T_{\text{vib}})_s\right] - 1}.$$

Here $(T_{\text{vib}})_s$ is obtained from Eq. 2.23 and is given by

$$\begin{aligned}(T_{\text{vib}})_s &= \frac{(\Theta_{\text{vib}})_s}{\ln\left[k\,(\Theta_{\text{vib}})_s\,/\langle\epsilon_{\text{vib}}\rangle_s + 1\right]} \\ &= \frac{(\Theta_{\text{vib}})_s}{\ln\left[R_s\,(\Theta_{\text{vib}})_s\,/(e_{\text{vib}})_s + 1\right]} \\ &= \frac{(\Theta_{\text{vib}})_s}{\ln\left[kN_s\,(\Theta_{\text{vib}})_s\,/(E_{\text{vib}})_s + 1\right]}.\end{aligned}$$

In a partially dissociated mixture of A_2 harmonic oscillators and A atoms,

$$T_{\text{vib}} = \frac{2\langle\epsilon_{\text{vib}}\rangle_{A_2}}{k\langle\zeta_{\text{vib}}\rangle_{A_2}}.$$

2.9.4 Overall kinetic temperature

Using Eq. 2.49, the overall kinetic temperature in a gas mixture, denoted T_{kin}, may be defined by

$$T_{\text{kin}} \equiv \frac{2\langle\epsilon\rangle}{k\langle\zeta\rangle}.$$

This overall kinetic temperature may be regarded as an average temperature for all energy modes in a gas. Here, $\langle\epsilon\rangle$ is the mean energy in all modes and is calculated using

$$\langle\epsilon\rangle = \frac{1}{N}\left(\sum_{s=1}^{N_{\text{sp}}} N_s\langle\epsilon_{\text{tr}}\rangle_s + \sum_{p=1}^{N}\left[\,(\epsilon_{\text{rot}})_p + (\epsilon_{\text{vib}})_p\,\right]\right) = \langle\epsilon_{\text{tr}}\rangle + \langle\epsilon_{\text{rot}}\rangle + \langle\epsilon_{\text{vib}}\rangle.$$

$\langle\zeta\rangle$ is the mean number of DOF and is calculated using

$$\langle\zeta\rangle = 3 + \frac{1}{N}\sum_{s=1}^{N_{\text{sp}}}\left[(\zeta_{\text{rot}})_s + (\zeta_{\text{vib}})_s\right]N_s.$$

Therefore

$$T_{\text{kin}} = \frac{2}{k} \times \frac{\langle\epsilon_{\text{tr}}\rangle + \langle\epsilon_{\text{rot}}\rangle + \langle\epsilon_{\text{vib}}\rangle}{\langle\zeta\rangle},$$

where $\langle\epsilon_{\text{rot}}\rangle = \left[\sum_{p=1}^{N}(\epsilon_{\text{rot}})_p\right]/N$ is the mean rotational energy of all molecules, including monatomic molecules without any rotational energy. Similarly, $\langle\epsilon_{\text{vib}}\rangle$ is the mean vibrational energy of all molecules. In a partially dissociated mixture of A_2 harmonic oscillators and A atoms, $\langle\zeta\rangle$ is given by

$$\langle\zeta\rangle = 3 + (2 + \zeta_{\text{vib}})\,(1 - \alpha)\,/\,(1 + \alpha)\,,$$

where the dissociation fraction α is the mass fraction of the atomic species. The overall kinetic temperature is then given by

$$T_{\mathrm{kin}} = \frac{2}{k} \times \frac{\langle \epsilon_{\mathrm{tr}} \rangle + \langle \epsilon_{\mathrm{rot}} \rangle + \langle \epsilon_{\mathrm{vib}} \rangle}{3 + (2 + \zeta_{\mathrm{vib}})\,(1 - \alpha)\,/\,(1 + \alpha)}.$$

CHAPTER 3

Characteristics of hypersonic rarefied flowfields

3.1 Introduction and summary

In the hypersonic flow of rarefied gas over a blunt body, gas molecules generally have insufficient collisions to achieve local equilibrium conditions near the body before being swept downstream. Consequently, non-equilibrium conditions prevail in the shock layer, where molecular velocity distributions are perturbed significantly from equilibrium. Under such conditions, the Chapman-Enskog distribution, and the corresponding Navier-Stokes equations, are not accurate descriptions of the gas. Furthermore, internal energy distributions may be perturbed from their equilibrium forms. Non-equilibrium conditions in the shock layer may be characterised by different kinetic temperatures of translation $T_{\rm tr}$, rotation $T_{\rm rot}$ and vibration $T_{\rm vib}$. Under rarefied conditions, the shock layer merges with the viscous boundary layer to form a merged shock layer. The influence of surface scattering is significant, because reflected molecules travel a relatively large distance into the flow before colliding with other molecules [38]. Such thermal non-equilibrium conditions and thick shock layers are characteristic of hypersonic rarefied flowfields.

The translational kinetic temperature $T_{\rm tr}$ rises rapidly through the shock layer, and is followed quite closely by $T_{\rm rot}$ because translation-rotation energy exchange requires relatively few collisions. However, many collisions are generally needed to transfer energy to the vibrational mode. Therefore $T_{\rm vib}$ is typically much lower than both $T_{\rm tr}$ and $T_{\rm rot}$ in rarefied hypersonic blunt body flowfields. Such conditions are called vibrationally cold because $T_{\rm vib} < T_{\rm rot} \lesssim T_{\rm tr}$.

It might be expected that intermolecular collision rates in rarefied flows are so low that flowfield chemistry is essentially frozen. However, under the extreme conditions imposed by hypersonic flight, intermolecular collisions can be sufficiently energetic to result in a significant amount of flowfield chemistry, despite the rarefaction.

In all flow regimes, the presence of flowfield chemistry generally has a small effect on surface pressures and skin friction relative to those for a non-reacting flow. Therefore the coefficients of lift and drag are essentially unchanged. Dissociation reactions essentially convert flow kinetic energy into chemical potential energy, and thereby reduce the flowfield kinetic temperature. Ignoring surface catalysis, this usually results in reduced surface heat

fluxes relative to those for non-reacting flows. As discussed in §5.3, dissociation-vibration (DV) coupling results in reduced dissociation rates under vibrationally cold conditions. When DV coupling effects are present, less flow kinetic energy is converted into chemical potential energy, and there is a significant increase in the heat fluxes relative to flowfields in which DV coupling is absent. The increased heat fluxes are an important effect which must be captured for engineering studies. Modelling non-equilibrium reacting flowfields is the primary focus of this study and is considered in detail in Chapters 5 to 8.

The aerothermodynamic effects of flowfield chemistry are strongly influenced by vehicle geometry. Flowfield chemistry can increase the extent of flow separation regions and thus significantly change the operating characteristics of aerodynamic control surfaces [88]. Chemistry generally results in an upstream displacement of the aerodynamic centre relative to that for a non-reacting flow. This results in a change in the pitching moment. Such effects are generally more marked at higher angles of attack.

This chapter discusses several non-dimensional parameters often used to characterise the extent of rarefaction in a gas flow. The Knudsen number, a continuum breakdown parameter and Cheng's parameter are considered in detail.

3.2 Knudsen number

The non-dimensional Knudsen number Kn is the parameter usually used to characterise the extent of rarefaction. Kn is defined by

$$\mathrm{Kn} \equiv \lambda / D, \tag{3.1}$$

where D is some characteristic flow dimension. This dimension may be the length scale of a local macroscopic flowfield gradient Q, defined by

$$l_{\mathrm{grad}}(Q) \equiv Q \left| \frac{\partial Q}{\partial x} \right|^{-1}. \tag{3.2}$$

Here Q may be the density, temperature, pressure or flow speed [135]. This gradient length scale provides a local Knudsen number $\mathrm{Kn} = \lambda / l_{\mathrm{grad}}$.

It is useful to write Kn in terms of other non-dimensional flow parameters. Using the Reynolds number $\mathrm{Re} \equiv \rho u D / \mu$ and $\lambda_{\mathrm{nom}} \equiv 2\mu / (\rho \bar{c})$ from Eq. 2.39, the expression

$$\mathrm{Kn} = \frac{2\mu}{\rho \bar{c} D} = \frac{2u}{\bar{c}\,\mathrm{Re}} = \frac{\pi^{\frac{1}{2}} S}{\mathrm{Re}} = \left(\frac{\pi\gamma}{2}\right)^{\frac{1}{2}} \frac{M}{\mathrm{Re}} \approx \frac{M}{\mathrm{Re}}$$

is obtained, which can be applied to estimate Kn.

Tsien [146] considered rarefaction effects in boundary layer development and introduced a Knudsen number based on the boundary layer thickness δ, denoted Kn_δ and

defined by

$$\mathrm{Kn}_\delta = \frac{\lambda}{\delta} = \frac{\lambda}{D}\frac{D}{\delta} = \mathrm{Kn}\frac{D}{\delta} \propto \frac{M}{\mathrm{Re}}\frac{D}{\delta}.$$

For flows with $\mathrm{Re} \ll 1$, $D/\delta \sim 1$, and where $\mathrm{Re} \gg 1$, $D/\delta \sim \sqrt{\mathrm{Re}}$. Therefore

$$\mathrm{Kn}_\delta \sim \begin{cases} M/\mathrm{Re} \sim \mathrm{Kn} & \text{for } \mathrm{Re} \ll 1, \\ M/\sqrt{\mathrm{Re}} & \text{for } \mathrm{Re} \gg 1. \end{cases} \tag{3.3}$$

Tsien's parameter Kn_δ therefore includes consideration of viscous effects in characterising rarefied flow. Kn_δ should be considered when $\mathrm{Re} \gg 1$, where viscous effects are significant.

3.3 Continuum breakdown parameter

The Knudsen number was originally defined to characterise rarefaction where the flow speed was small compared to the mean thermal speed. In hypersonic flows, it may be expected that rarefaction effects will depend in some way on the flow speed as well as the mean free path. The flow speed should be important because it affects the number of collisions that molecules can have before being swept downstream. At high flow speeds, molecules have less collisions as they traverse the flowfield. This promotes local non-equilibrium conditions.

The continuum breakdown parameter is a rarefaction parameter that considers the flow speed. Two simple derivations of the breakdown parameter are presented here, followed by the more detailed results of Bird [12] and a result obtained directly from the Boltzmann equation.

Firstly, it is possible to characterise the extent of rarefaction by the ratio of the mean collision time $\tau = \lambda/\bar{c}$ to the time for the flow to traverse a characteristic dimension, denoted t_{flow}. Over a body of size D, $t_{\mathrm{flow}} = D/u$. The ratio of τ to t_{flow} is

$$\frac{\tau}{t_{\mathrm{flow}}} = \frac{\lambda u}{D\bar{c}} = \mathrm{Kn}\frac{u}{\bar{c}} = \frac{\pi^{\frac{1}{2}}}{2}\mathrm{Kn}\ S = \left(\frac{\pi\gamma}{8}\right)^{\frac{1}{2}} \mathrm{Kn}\, M \propto \mathrm{Kn}\, M. \tag{3.4}$$

Ignoring the leading constants, this suggests that rarefaction in hypersonic flows can be characterised by the product $\mathrm{Kn}M \sim M^2/\mathrm{Re}$.

Secondly, consider the shear stress τ_x given by

$$\tau_x = \mu\frac{du_x}{dy}.$$

A body with characteristic dimension D in a flow with a velocity u can induce a maximum velocity gradient of approximately u/D. Therefore,

$$\tau_x \approx \mu\frac{u}{D} = \frac{\rho\bar{c}\lambda}{2}\frac{u}{D} = \frac{\rho\bar{c}u}{2}\mathrm{Kn}.$$

In rarefied flows, this shear stress is comparatively high relative to the static pressure p,

when compared to continuum flows. The ratio of τ_x to p is given by

$$\frac{\tau_x}{p} \approx \frac{\rho \bar{c} u}{2} \frac{\mathrm{Kn}}{\rho R T} = \frac{\bar{c}}{c_{\mathrm{mp}}} \mathrm{Kn}\, S = \frac{2}{\pi^{\frac{1}{2}}} \mathrm{Kn}\, S = \left(\frac{2\gamma}{\pi}\right)^{\frac{1}{2}} \mathrm{Kn}\, M \propto \mathrm{Kn}\, M.$$

Bird [12] proposed a non-dimensional parameter P, defined by

$$P \equiv \frac{u}{\rho \nu} \left| \frac{d\rho}{dx} \right|, \tag{3.5}$$

to characterise the breakdown of the continuum model in steady one-dimensional gaseous expansions. Using Eqs. 2.41, 3.1 and 3.2, this parameter reduces to

$$P = \frac{\pi^{\frac{1}{2}}}{2} \mathrm{Kn}\, S = \left(\frac{\pi\gamma}{8}\right)^{\frac{1}{2}} \mathrm{Kn}\, M \propto \mathrm{Kn}\, M.$$

Consider the non-dimensional form of the Boltzmann equation from Eq. 2.8. This form includes the non-dimensional parameter $\xi = u_r/(x_r \nu_r) = u_r \tau_r / x_r$ which can be regarded as a non-dimensional collision time. As $\xi \to 0$, the collision rate becomes infinite and equilibrium conditions prevail. As $\xi \to \infty$, the collision rate approaches zero and the flow is free molecular. The parameter ξ can therefore be used to characterise the extent of rarefaction. ξ can be defined using $u_r = u_\infty$, $x_r = D$ and $\tau_r = \tau_\infty$, giving $\xi = \tau_\infty / t_{\mathrm{flow}}$. Eq. 3.4 then provides

$$\xi \propto \mathrm{Kn}\, M.$$

The above results all suggest that the parameter $\mathrm{Kn}\, M \sim M^2/\mathrm{Re}$ is useful for characterising rarefaction in hypersonic flows. Thus a continuum breakdown parameter B may be defined by

$$B \equiv \mathrm{Kn}\, M \sim M^2/\mathrm{Re}. \tag{3.6}$$

For typical γ values, the parameter P of Bird [12] and the breakdown parameter B are related by $B \sim 1.3P$. Note that B is related to Tsien's parameter Kn_δ by

$$B \sim (\mathrm{Kn}_\delta)^2 \quad \text{when} \quad \mathrm{Re} \gg 1.$$

3.4 Cheng's parameter

For blunt bodies in rarefied hypersonic flow, the merged shock layer is expected to dominate the flow behaviour. Consequently, the Knudsen number based on the freestream mean free path λ_∞ may not be the appropriate non-dimensional parameter for characterising the flow. A rarefaction parameter based on the conditions within the merged shock layer rather than the freestream conditions, should be more useful for flow characterisation [124]. Based on the theory of merged shock layers in hypersonic flows with low Re, Cheng

[48] introduced a rarefaction parameter, denoted here by Ch and defined by

$$\mathrm{Ch} \equiv \frac{\mu_\infty u_\infty C^*}{p_\infty r}. \tag{3.7}$$

Here, r is the body radius and the non-dimensional parameter C^* is defined by

$$C^* \equiv \frac{\mu^*}{\mu_\infty}\frac{T_\infty}{T^*}$$

where μ^* is the viscosity evaluated at temperature T^* which is characteristic of the merged layer [124]. This characteristic temperature is simply the mean of the post-shock temperature T_2 and the wall temperature T_{wall} [48, 124]. For a flow with significant chemistry, μ^* may be evaluated where the post-shock composition may differ significantly from that in the freestream. Note that Ch has been defined here such that it increases with increasing rarefaction, as do Kn and B. Also, Ch is related to the χ notation of Macrossan *et al.* [124] by $\chi = 2/\mathrm{Ch}$.

Using $r = D/2$, $p = \rho RT$ and $\mu/\rho = \lambda\bar{c}/2$, it can be shown that

$$\mathrm{Ch} = \frac{\lambda_\infty \bar{c}_\infty u_\infty}{RT_\infty}\frac{C^*}{D}.$$

Using $\bar{c}_\infty \sim a_\infty$ and $RT_\infty \sim a_\infty^2$, this reduces to

$$\mathrm{Ch} \sim \frac{\lambda_\infty}{D}\frac{u_\infty}{a_\infty}C^* = \mathrm{Kn}_\infty M_\infty C^* \sim C^* B$$

This shows that Ch is essentially the breakdown parameter B modified by the factor C^*. This factor accounts for different collision cross-sections and hence different collision rates in the shock layer of a hypersonic flow [123]. Anderson [6] gives a viscous interaction parameter

$$\bar{V}^2 \equiv C^* M^2/\mathrm{Re} \sim C^* B,$$

which is similar to Ch.

3.5 Classification schemes for rarefied flow

Several schemes have been proposed by various authors to classify flow regimes using the Knudsen number [146, 143, 21]. Although such schemes are somewhat arbitrary, they can be used to identify the dominant flow behaviour. Generally, a gas may be regarded as a continuum when $\mathrm{Kn} \lesssim 10^{-3}$. In continuum flows, the mean free path near a surface is very small and many collisions occur near the surface. This results in the formation of boundary layer near the surface, in which the stream velocity increases continuously from zero at the surface to the stream velocity in a thin layer.

When $10^{-3} \lesssim \mathrm{Kn} \lesssim 10^{-1}$, there are insufficient collisions near the surface to give a boundary layer with a continuous velocity profile, and a finite flow velocity can exist at the

surface. This flow regime is often called slip flow. The slip flow regime can be modelled using the Navier-Stokes equations with appropriate modifications for the boundary conditions. The Navier-Stokes equations can therefore be applied to flows with $\mathrm{Kn} \lesssim 10^{-1}$. The range where $10^{-1} \lesssim \mathrm{Kn} \lesssim 10^{1}$ is often called the transition regime, and refers to the transition between continuum and free molecular flow regimes. For $\mathrm{Kn} \gtrsim 10^{1}$, the flow approaches the free molecular limit and is considered to be collisionless. The term rarefied typically refers to those flows that cannot be accurately described by the continuum model, and includes the slip, transition and free molecular flow regimes where $\mathrm{Kn} \gtrsim 10^{-3}$. The approximate Knudsen number ranges for each flow regime are included in Table 3.1.

Table 3.1: Approximate Knudsen number ranges for rarefied flow regimes.

Flow regime	Kn range
Continuum	$\mathrm{Kn} \lesssim 10^{-3}$
Slip	$10^{-3} \lesssim \mathrm{Kn} \lesssim 10^{-1}$
Transition	$10^{-1} \lesssim \mathrm{Kn} \lesssim 10^{1}$
Free molecular	$10^{1} \lesssim \mathrm{Kn}$

According to Bird [12, 21], the continuum gas model fails for $P \gtrsim 0.02$. In terms of the breakdown parameter B, this continuum breakdown criterion becomes $B \gtrsim 0.03$. According to Macrossan *et al.* [124] rarefaction effects become important when $\mathrm{Ch} \gtrsim 0.2$. For high speed flows over blunt bodies, Macrossan [123] showed that Ch was the most useful parameter for characterising rarefied flow conditions.

CHAPTER 4

The direct simulation Monte Carlo method

4.1 Introduction and summary

The fundamental description of a dilute gas is provided by the Boltzmann equation. In principle, a method that solves the Boltzmann equation can be applied under any conditions, as long as the dilute gas assumption holds. The Chapman-Enskog method shows that a solution of the Navier-Stokes equations accurately approximates a solution of the Boltzmann equation where departures from equilibrium conditions are small. Consequently, many computational fluid dynamics (CFD) codes give numerical solutions of the Navier-Stokes equations. However, in rarefied flows where non-equilibrium conditions exist, the Navier-Stokes equations fail to provide an accurate description of the gas. Furthermore, CFD solutions using the Burnett equations and more detailed approximations of the Boltzmann equation are difficult, and few solutions have been attempted [49]. In non-equilibrium flows, the molecular nature of the gas must be considered, and a method that solves the more fundamental Boltzmann equation is required.

The Boltzmann equation has remained analytically intractable for all but the simplest problems. Furthermore, numerical solution of the Boltzmann equation using conventional CFD methods, known as direct Boltzmann CFD [21], is generally difficult and for engineering applications, accurate solutions of realistic problems have extreme computational expense. Consequently, particle-based simulation methods that recognise the discrete molecular character of gases are generally used to obtain accurate flow solutions in the rarefied regime. For flows of engineering interest, the most common of these is the direct simulation Monte Carlo (DSMC) method.

The DSMC method models macroscopic gas behaviour by simulating the motions and collisions of a set simulator particles, representative of the real gas molecules, as they move through physical space, undergo intermolecular collisions and interact with imposed boundary conditions. Each DSMC simulator particle represents a very large number of real gas molecules. Probabilistic rather deterministic techniques are employed to simulate molecular collision processes. Physical space is divided into grid of computational cells in which intermolecular collisions are performed.

The most important feature of the DSMC method is that it allows modelling of thermal

non-equilibrium processes, because all flow phenomena can be simulated at the molecular level. In this respect, the method is the only available CFD technique that can accurately capture general non-equilibrium gas behaviour. In principal, models incorporating any level of physical detail can be used with the DSMC method [134]. In practice, the level of physical detail is limited by computational expense and the availability of physical data.

The DSMC method was first used by Bird [11], when it was applied to the translational relaxation of a homogeneous hard sphere gas. The method has been described in detail by Bird [14, 21]. Other reviews have been conducted by Bird [16], Ivanov and Gimelshein [88] and Oran *et al.* [135]. Cheng and Emanuel [49] have reviewed the DSMC method in the context of non-equilibrium hypersonic flows. More recently, Bird [23, 24] has summarised the current state and future prospects of the DSMC method. A diverse range of flows have been studied with the DSMC method, as summarised below.

- Rarefied aerothermodynamics, including thermal non-equilibrium and high temperature gas effects such as flowfield chemistry, ionisation and thermal radiation. Such flow conditions occur during ascent to orbit, atmospheric entry and during aerobraking and aerogravity-assist manoeuvres executed by interplanetary exploration vehicles. Also, atmospheric drag on spacecraft in low Earth orbit occurs in the rarefied regime.
- Shock wave structure.
- Structure of jets and spacecraft plumes.
- Spacecraft contamination and outgassing.
- Electric spacecraft propulsion systems.
- Interaction of gas flows with micro-electromechanical systems.
- Thin film growth and plasma etching in plasma reactors used for microelectronics manufacturing.
- Evaporation and condensation phenomena.
- Astrophysical flow phenomena.

This chapter provides a description of the DSMC method. Firstly, the basic DSMC procedure is considered in §4.2. The relationship between the Boltzmann equation and the DSMC method is discussed in §4.3. A detailed discussion on DSMC molecular models appears in §4.4, with particular emphasis on the variable hard sphere model. Borgnakke-Larsen procedures for modelling internal energy exchange are considered in §4.5. It is shown that these procedures allow satisfaction of detailed balancing. Finally, a summary of validation efforts is given in §4.6. The application of the DSMC method to chemically reacting flows is considered separately in Chapters 6 and 7. Ionisation modelling is beyond

the scope of this study. This study concentrates on steady flow modelling procedures for the DSMC method. For aerospace applications, the assumption of steady flow conditions is by no means restrictive because the freestream conditions typically vary over time scales that are orders of magnitude longer than the time required for flowfields to reach steady state.

4.2 The standard DSMC procedure

The standard DSMC procedure is:

1. Determine the cell in which each simulator particle resides. This requires a spatial sorting algorithm. Where cells are further divided into subcells, the subcell must also be determined.

2. Select collision partners within each cell and perform intermolecular collisions with internal energy exchange and chemical reactions. This is a zero-dimensional calculation that is performed probabilistically.

3. Perform the collisionless particle move step for time Δt and enforce boundary conditions. The move step is performed deterministically.

4. Sample the flowfield.

The remainder of this section discusses the standard DSMC procedure, with the exception of chemical reactions.

The DSMC method depends on random numbers. True random numbers cannot be generated with a computer algorithm, and pseudo-random number generators are used. As noted by Bird [21], the DSMC method is tolerant of problems with pseudo-random number generators. However, the quality of the generator used in any DSMC study should be assessed. Some discussion on the generator used in this study appears in §D.1.

The DSMC method was originally developed using the dilute gas assumption in which molecules interact through binary collisions alone. For most applications in hypersonics, this assumption is appropriate. Standard DSMC procedures have been extended to dense gases by Alexander *et al.* [3].

4.2.1 Decoupling interval and division of physical space

The fundamental DSMC simplification is that the simulation of molecular collisions is decoupled from the simulation of molecular motions. The two processes are performed independently, separated by a decoupling interval or time step Δt. The time step must be set to a value substantially less than the local mean collision time. Garcia and Wagner [61] and Hadjiconstantinou [77, 78] showed that the transport coefficients depend on Δt, and that the error in the transport coefficients is of order $(\Delta t)^2$. Typically, $\Delta t \sim \tau/3$ is used.

Physical space is discretised into computational cells in which collisions are performed and from which flowfield samples are accumulated to calculate macroscopic flow conditions. The collision and sampling routines require the number of the cell in which each particle resides, which requires some form of spatial sorting algorithm. Cells may be further divided into subcells. Collisions are then performed only between particles within each subcell. This ensures that collision partners are near neighbours. Where subcells are used, the subcell number must also be determined.

The characteristic dimension Δx of each cell depends on the local mean free path λ and the local flow gradients. The local gradient length scale $l_{\text{grad}}(Q)$ is defined by Eq. 3.2. Since changes in the flow gradients depend on collisions that occur over the mean free path λ, l_{grad} will always be greater than λ. Where l_{grad} approaches λ, Δx should be substantially less than λ. This ensures that the simulation can accurately capture local flow gradients. Bird [21] recommends $\Delta x \sim \lambda/3$. Where $l_{\text{grad}} \gg \lambda$, then $\Delta x \sim l_{\text{grad}}/3$ is suitable. More discussion on this issue is given in §8.8. According to Alexander *et al.* [4, 5], viscosity and thermal conductivity are cell size dependent. For $\Delta x < \lambda/3$, the errors are small. Where Δx is small relative to λ, subcells are unnecessary.

The above requirements for Δt and Δx result in the computational expense of the DSMC method being proportional to ρ^N, where N is the flow dimensionality. This has, in practice, limited the method to transition regime flows. For near continuum flows, the mean collision time and mean free path are very small, and the DSMC method becomes extremely computationally expensive relative to continuum CFD solvers. These practical limitations on the DSMC method will become less important as computing costs decrease and more powerful DSMC algorithms are introduced.

In addition to the above criteria for Δt and Δx, Bird [13] notes that the ratio $\Delta x/\Delta t$ must not be large compared to the local sound speed a. This avoids the propagation of artificial disturbances at a speed $\sim\Delta x/\Delta t$. For $\Delta x = \lambda/3$ and $\Delta t = \tau/3$, Eqs. 2.39 and 2.41 can be used to show that

$$\Delta x/\Delta t \sim \bar{c} \approx 1.3a.$$

Therefore this additional criterion is satisfied.

4.2.2 Collision partner selection and collision simulation

In the DSMC method, simulating intermolecular collisions first requires identification of collision partners, followed by the actual collision calculation. Collision partners are selected probabilistically. This contrasts to molecular dynamics methods in which collisions are calculated deterministically. Usually, the no time-counter (NTC) technique of Bird [20] is employed to select collision partners. In this method, the number of particle pairs to test for collision in a given cell, denoted N_{pairs}, is calculated using

$$N_{\text{pairs}} = nN(\sigma g)_{\max}\Delta t/2.$$

Here, n is the time-averaged number density in the cell and N is the instantaneous number of particles in the cell. $(\sigma g)_{\max}$ is the maximum value of σg for the cell. This value is updated during the simulation when a larger value is found. An initial estimate of $(\sigma g)_{\max}$ is required at the start of the simulation. Here, an initial value of $1.5\langle\sigma g\rangle$ was used.

N_{pairs} is a pure number and has both integer and fractional parts. The factional part $N_{\text{frac}} = N_{\text{pairs}} - \lfloor N_{\text{pairs}} \rfloor$ can be considered probabilistically; if $R_f < N_{\text{frac}}$ then $N_{\text{frac}} = 1$, otherwise $N_{\text{frac}} = 0$. Alternatively, N_{frac} can be stored as a fractional remainder and then added to N_{pairs} at the next time step [8].

Particle positions in each cell are ignored when selecting collision partners, and all possible collision pairs have an equal probability of being selected. For a selected pair of particles, a collision is performed if

$$R_f < \sigma g/(\sigma g)_{\max}.$$

Clearly, the NTC method is an acceptance-rejection technique. Where subcells are used, the first collision partner is selected at random within the cell, and the second partner is then selected from the same subcell as the first partner. The NTC method gives the correct collision rate for any velocity distribution, in both pure gases and gas mixtures [21].

When collision partners are selected, intermolecular collisions are performed, with internal energy exchange and chemical reactions. This is a zero-dimensional calculation, and is performed probabilistically. When performing collisions, particle positions are ignored and only particle velocities are changed.

Calculating the post-collision velocity vector $\left(g'_x, g'_y, g'_z\right)$ using Eq. 2.2 depends on the deflection angle χ and the collision plane orientation ϵ. The deflection angle $\chi(g, b)$ depends on the molecular model, as discussed in §4.4. The miss distance b and the collision plane orientation ϵ are calculated using $b = R_f^{1/2} b_{\max}$ and $\epsilon = 2\pi R_f$. Here $b_{\max}$ corresponds to collisions with the minimum deflection angle $\chi_{\min} = \chi\left(g, b_{\max}\right)$.

To select possible collision pairs from a given cell, a list of the particles residing in the cell is required. This list array is constructed when the cell number of each particle is determined. Particles in the list array are arranged in order of cell and subcell number. To select a possible collision pair, a particle is selected at random from the portion of the list array for the current cell. A second particle is then selected from the portion of the list array for the same subcell as the first particle.

4.2.3 Particle move step

After the collision routine, particles are moved for time Δt and the boundary conditions are enforced. The move step is collisionless. In a three-dimensional Cartesian co-ordinate

system without body forces, particle positions after the move step are simply

$$\mathbf{x}' = \mathbf{x}_0 + \mathbf{v}\Delta t$$

where $\mathbf{x}_0 = (x_0, y_0, z_0)$ is the starting position and $\mathbf{v} = (v_x, v_y, v_z)$ is the particle velocity. In the (r, θ, z) cylindrical co-ordinate system used in axisymmetric simulations, a particle with starting radius r_0, radial velocity v_r and tangential velocity v_θ at time t moves to a new radial co-ordinate

$$r' = \left[(r_0 + v_r\Delta t)^2 + (v_\theta \Delta t)^2\right]^{\frac{1}{2}} \tag{4.1}$$

at time $t + \Delta t$. Using

$$x_r = r_0 + v_r\Delta t \quad \text{and} \quad x_\theta = v_\theta \Delta t, \tag{4.2}$$

Eq. 4.1 reduces to

$$r' = (x_r^2 + x_\theta^2)^{\frac{1}{2}}.$$

The new axial co-ordinate z' is simply

$$z' = z_0 + v_z\Delta t. \tag{4.3}$$

The new radial and tangential velocities are obtained from the transformations

$$v_r' = \left[v_r\,(r_0 + v_r\Delta t) + v_\theta^2\Delta t\right]/r' \quad \text{and} \quad v_\theta' = \left[v_\theta\,(r_0 + v_r\Delta t) - v_r v_\theta \Delta t\right]/r'$$

which, using Eqs. 4.2, reduce to

$$v_r' = \left(x_r v_r + x_\theta v_\theta\right)/r' \quad \text{and} \quad v_\theta' = \left(x_r v_\theta - x_\theta v_r\right)/r'$$

respectively. §C.2 contains further details on calculating the intersection points between particle trajectories and straight lines and circles in axisymmetric co-ordinates.

4.2.4 Boundary conditions

At flow boundaries, new particles entering the simulation domain must be generated. This involves sampling the velocity and internal energy of each entering particle, and also determining the location at which each particle crosses the boundary. Particles that leave the domain are simply deleted from the simulation. Upstream boundaries must be sufficiently far upstream such that they are in the freestream. For rarefied flows this can result in relatively large simulation domains, because the large mean free paths result in flowfield disturbances extending relatively large distances. Methods for generating the velocities of particles entering the simulation domain have been considered in detail by Lilley and Macrossan [109]. These procedures apply to both inflow and outflow boundaries and both subsonic and supersonic flows. They can also be applied to unsteady flows. At

supersonic outflow boundaries, the number of particles entering the simulation domain is very small, and can be ignored if the downstream boundary is sufficiently distant from regions of interest.

For an N-dimensional simulation, $N-1$ random numbers are required to determine the location at which an entering particle crosses the simulation boundary. In two-dimensional simulations, the location of a particle crossing a simulation boundary between $x_{\min}$ and $x_{\max}$ is simply $x_{\min}+R_f(x_{\max}-x_{\min})$. In axisymmetric simulations, the radial co-ordinate r of entering particles is distributed according to [21]

$$f(r) = 2r/\left(r_{\max}^2 - r_{\min}^2\right),$$

where $r_{\min}$ and $r_{\max}$ are the minimum and maximum radial co-ordinates of the region of interest. Radial co-ordinates r for entering particles are generated using

$$r = \left[r_{\min}^2 + R_f\left(r_{\max}^2 - r_{\min}^2\right)\right]^{\frac{1}{2}}. \tag{4.4}$$

In two-dimensional flows, axes of symmetry are replaced with a specularly reflecting surface. In axisymmetric simulations, particles do not cross the axis of symmetry.

If a particle strikes a solid surface, a scattering law is required. The two most common models are specular and diffuse reflection. For specular reflection, the velocity component normal to the surface is simply reversed. Components parallel to the surface do not change. For diffuse reflection, particles are reflected away from the surface in all directions with equal probability. The normal velocity component of a reflected particle, denoted v_n' is generated using

$$v_n' = (-\ln R_f)^{\frac{1}{2}}\, c_{\mathrm{mp}}\left(T_{\mathrm{wall}}\right).$$

Here $c_{\mathrm{mp}} = (2kT_{\mathrm{wall}}/m)^{1/2}$ is the most probable thermal speed in an equilibrium gas at the wall temperature T_{wall}. For steady flows, it is assumed that $(dT_{\mathrm{wall}}/dt)\,\Delta t$ is small, so T_{wall} may be assumed to be constant. Parallel velocity components are generated from a normal distribution and internal energies from appropriate Boltzmann distributions, again at the wall temperature. Engineering surfaces are usually assumed to be completely diffusely reflecting. However, at high impact energies, a significant fraction of collisions may be specular [21]. Examples of DSMC studies using a component of specular reflection are given by Dogra and Moss [54] and Boyd [38]. Under unsteady flow conditions, the time dependent nature of the flow boundary conditions must be considered when generating entering particles at flow boundaries, and when considering surface interactions. For unsteady flows where T_{wall} varies significantly, the modelled heat flux to the wall, and the thermal properties of the wall material can be used to calculate $T_{\mathrm{wall}}(t)$ during the simulation.

4.2.5 Particle weighting factors

Each particle in a DSMC calculation represents a very large number of real gas molecules. This number is the particle weighting factor W. Statistical problems can arise when simulating trace species, because they are represented by small numbers of simulator particles relative to the dominant species. Bird [14] introduced species-based weighting factors so that all species would be represented by a similar number of particles. Particular care is required to ensure that momentum and energy are conserved in collisions between particles with different weighting factors. A conservative species weighting scheme was proposed by Boyd [36] to accomplish this. This scheme was used by Wu *et al.* [153] to model chemical vapour deposition. Species-based weighting factors have not been used here.

In a typical DSMC calculation, number densities and cell volumes may vary by orders of magnitude. Consequently, the number of real molecules that must be simulated in each cell has large variations. To maintain a manageable number of particles in the simulation, different weighting factors are required for different cells. Cell-based weighting factors have been used here, such that all particles in a given cell have the same weighting factor. Ideally, cell-based weighting factors should be set so that all cells contain similar numbers of particles. In axisymmetric simulations, W generally increases with distance from the axis.

As a particle moves from one cell with a weighting factor W to a new cell with a different weighting factor W', the number of real molecules that it represents changes. The particle may therefore be either deleted or cloned so that it represents, on average, a constant number of real molecules. If $W' > W$, the particle has a probability of deletion, and the deletion criterion is $R_f > W/W'$. If $W' < W$, the particle has a probability of being cloned, and the required mean number of clones is $W/W' - 1$, which could be greater than unity. Therefore $N_{\text{clones}} = \lfloor W/W' - 1 \rfloor$ clones are made, and another clone is made if $R_f < W/W' - 1 - N_{\text{clones}}$. Cloned particles are not placed into the flow immediately. The first clone of a particle is delayed by three time steps. Further clones of a particle are introduced into the flow at intervals of three time steps.

These delays for cloned particles necessitate the use of an array containing the number of time steps that each particle has been delayed. If the delay value of a particle is greater than zero, it is decremented at the particle move step. No other computations are performed for delayed particles. Similar delay procedures are recommended by Bird [21], and appear to give accurate flowfields. However, the numerical effects of cloning particles, with their associated delays, have not been studied in detail. In unsteady flows, the effects of delaying cloned particles may cause numerical problems.

4.2.6 Flowfield sampling

In a typical steady flow DSMC calculation, the simulation domain will initially be filled with particles at the ambient conditions. The simulation will then be run for a period until the average cell conditions do not change with time, within statistical scatter. This is called steady state. The approach to steady state is required because the initial simulation conditions usually differ from the calculated steady state conditions. After steady state is attained, particle properties are sampled until a sufficiently large number of samples has been obtained. Sampling of some flowfield properties is undertaken during the approach to steady state, to obtain macroscopic quantities such as the time-averaged number density n used in the NTC method, or kinetic temperatures. The sampling arrays, discussed below, are reset periodically during the approach to steady state so that the macroscopic properties used in the simulation are updated regularly.

In an unsteady flow simulation, the DSMC calculation is repeated several times. The first several simulations should be used to obtain macroscopic quantities such as the time-averaged number density n for the NTC method. Subsequent simulations are then performed, and the quantities sampled in each cell during each time step are stored to recover the time dependent behaviour.

The sampling arrays contain the quantities

$$N, \quad \sum v_x, \quad \sum v_y, \quad \sum v_z, \quad \sum v_x^2, \quad \sum v_y^2, \quad \sum v_z^2, \quad \sum \epsilon_{\text{rot}} \quad \text{and} \quad \sum \epsilon_{\text{vib}}$$

for each species in each cell. The mean i velocity component in a cell containing N_{sp} species is calculated using

$$u_i = \left[\sum_{s=1}^{N_{\text{sp}}} \left(\sum v_i \right)_s m_s \right] \cdot \left(\sum_{s=1}^{N_{\text{sp}}} N_s m_s \right)^{-1}.$$

The density is obtained from

$$\rho = \frac{W}{V_c} \sum_{s=1}^{N_{\text{sp}}} N_s m_s.$$

Kinetic temperatures are calculated according to the formulae presented in §2.9.

Solid surfaces are divided into surface cells, and for each particle reflected from a surface cell, the momentum change $\Delta \mathbf{P} = W m \Delta \mathbf{v}$ and energy change

$$\Delta \epsilon = W \left[m\Delta(v^2)/2 + \Delta\epsilon_{\text{rot}} + \Delta\epsilon_{\text{rot}} \right]$$

are accumulated for the cell. The mean force on the surface cell is

$$\mathbf{F} = - \left(\Delta \mathbf{P} \right)_{\text{total}} / \Delta t_s,$$

where $(\Delta \mathbf{P})_{\text{total}}$ is the total momentum change for particles hitting the cell and Δt_s is the

total time covered by the sample. The total heat transfer to the cell is simply the sum of $\Delta\epsilon$ for all reflection events.

4.3 Relationship to the Boltzmann equation

The DSMC method was originally developed and applied in the absence of a formal mathematical proof that it provided a solution of the Boltzmann equation. This was an early criticism of the method, and there has been much debate about whether the DSMC method does provide a solution of the Boltzmann equation. It may be argued [21] that the DSMC method provides a physical, rather than mathematical, solution of the Boltzmann equation, because the physical reasoning used to establish the Boltzmann equation is similar to that used in DSMC procedures [13].

In the DSMC method, the velocity distribution function f is replaced by a representative set of simulator particles [61]. Physical space and time are discretised as described in §4.2.2. The decoupling of collisions and particle movements means that the DSMC method solves the Boltzmann equation in two steps. In the absence of body forces, the particle move step solves the collisionless Boltzmann equation

$$\frac{\partial(nf)}{\partial t} + \mathbf{v} \cdot \frac{\partial(nf)}{\partial \mathbf{x}} = 0.$$

The collision routine solves the collision term

$$\left[\frac{\partial(nf)}{\partial t}\right]_{\text{coll}}$$

in a probabilistic zero-dimensional calculation for each cell. The solution of the collision term is essentially a relaxation calculation. As $\Delta t \to 0$ and $\Delta x \to 0$, the DSMC procedure becomes more exact [21].

Several authors have discussed the relationship between the DSMC method and the Boltzmann equation. Summaries of early studies are given by Bird [21] and Ivanov and Gimelshein [88]. Wagner [151] has provided a formal proof that DSMC simulations converge to a solution of the time and spatially discretised Boltzmann equation in the limit of infinite simulator particles. However, this proof applies to a simple gas only. The DSMC method can incorporate models of rotational, vibrational and electronic excitation, chemical reactions, ionisation, radiation and surface interactions. Proof that the DSMC method solves the Boltzmann equation when such phenomena are present have not been provided.

4.4 DSMC molecular models

In the DSMC method, a molecular model is selected that attempts to reproduce the required transport properties over the temperature range of interest. In early DSMC calculations, various intermolecular potentials were used to model collisions. These included

the IPL, Lennard-Jones, Morse and Maitland-Smith potentials. The use of such potentials requires the calculation of the deflection angle $\chi(g, b)$ for each collision as a function of the relative speed and miss distance. Such calculations are difficult, and recourse to extensive tables is necessary when many collisions must be simulated. In an engineering context, the use of such intermolecular potentials is unnecessary [21], prompting the introduction of simpler phenomenological molecular models for use in DSMC simulations. This section summarises several available phenomenological models, with particular emphasis on the variable hard sphere model.

4.4.1 Variable hard sphere model

The variable hard sphere (VHS) model combines the viscosity cross-section $\sigma_\mu \propto g^{-4/\alpha}$ of IPL molecules with simple hard sphere scattering. Because $\sigma = 3\sigma_\mu/2$ for hard sphere scattering, VHS molecules have $\sigma \propto g^{-4/\alpha}$. The VHS collision cross-section for collisions between a particle of species A and a particle of species B can therefore be written

$$\sigma(g) = \sigma_r \left(g_r/g\right)^{2\upsilon}, \tag{4.5}$$

where $\upsilon = 2/\alpha$ and the reference values σ_r and g_r are constants characteristic of the A + B collision pair. This combination of total cross-section and hard sphere scattering was first used by Borgnakke and Larsen [26] and also by Erofeev and Perepukhov [56]. The VHS model was first formalised and studied in detail by Bird [18]. The parameter υ may be regarded as the deviation from hard sphere viscosity behaviour. Hard sphere and Maxwell-VHS molecules are simulated with $\upsilon = 0$ and $\frac{1}{2}$ respectively.

Scattering for hard sphere collisions is isotropic in the centre-of-mass reference frame, so the components of the post-collision velocity $\mathbf{g}^*$ are determined by selecting a random point from the surface of a sphere of radius $g^* = g$. Marsaglia [130] provided a computationally efficient method of generating such random points, as discussed in §D.2.

Using the Chapman-Enskog viscosity formula of Eq. 2.29 with $\sigma_\mu = 2\sigma/3$ for hard sphere scattering, the VHS viscosity expression

$$\mu_{\mathrm{A+B}} = \frac{15}{8} \frac{[\pi(2\tilde{m})kT]^{\frac{1}{2}}}{\Gamma(4-\upsilon)} \frac{(2kT/\tilde{m})^{\upsilon}}{\sigma_r g_r^{2\upsilon}} \tag{4.6}$$

is obtained, which shows the expected power law viscosity behaviour $\mu \propto T^{1/2+\upsilon}$. For a pure VHS gas,

$$\mu = \frac{15}{8} \frac{m(\pi RT)^{\frac{1}{2}}}{\Gamma(4-\upsilon)} \frac{(4RT)^{\upsilon}}{\sigma_r g_r^{2\upsilon}}. \tag{4.7}$$

The VHS parameters $\sigma_r g_r^{2\upsilon}$ and υ should be selected such that the resulting viscosity behaviour matches that of the gas being modelled, over the temperature range of interest. The parameter υ is obtained from the slope of $\log\mu(T)$ versus $\log T$, and $\sigma_r g_r^{2\upsilon}$ is obtained by specifying a reference viscosity $\mu_r = \mu_{\mathrm{A+B}}(T_r)$ at a reference temperature T_r. These

values are then used in the equation

$$\sigma_r g_r^{2\upsilon} = \frac{15\pi^{\frac{1}{2}}}{8}\frac{\tilde{m}/\mu_r}{\Gamma(4-\upsilon)}\left(\frac{2kT_r}{\tilde{m}}\right)^{\frac{1}{2}+\upsilon} \tag{4.8}$$

to give $\sigma_r g_r^{2\upsilon}$. The choice of a particular expression for g_r is arbitrary. Given an expression for g_r, the reference cross-section σ_r is obtained from Eq. 4.8. Bird [21] used

$$g_r^{2\upsilon} = (2kT_r/\tilde{m})^{\upsilon}/\Gamma(2-\upsilon),$$

which is the mean value of $g^{2\upsilon}$ in collisions at the reference temperature T_r. This gives

$$\sigma_r = \frac{15}{8}\frac{\left[\pi(2\tilde{m})kT_r\right]^{\frac{1}{2}}/\mu_r}{(2-\upsilon)(3-\upsilon)}.$$

Alternatively,

$$g_r = (2kT_r/\tilde{m})^{\frac{1}{2}} \tag{4.9}$$

may be used, which gives

$$\sigma_r = \frac{15\pi^{\frac{1}{2}}}{8}\frac{g_r\tilde{m}/\mu_r}{\Gamma(4-\upsilon)} = \frac{15}{8}\frac{\left[\pi(2\tilde{m})kT_r\right]^{\frac{1}{2}}/\mu_r}{\Gamma(4-\upsilon)}. \tag{4.10}$$

Here, Eqs. 4.9 and 4.10 will be used for g_r and σ_r. For a pure VHS gas,

$$g_r = (4RT_r)^{\frac{1}{2}} \quad \text{and} \quad \sigma_r = \frac{15}{8}\frac{m\,(\pi RT_r)^{\frac{1}{2}}/\mu_r}{\Gamma(4-\upsilon)}.$$

For VHS molecules, Eqs. 2.26 and 2.27 give

$$\pi d^2\Omega^{(1,1)\star} = \sigma_r\frac{\Gamma(3-\upsilon)}{2}\left(\frac{T_r}{T}\right)^{\upsilon} \qquad \pi d^2\Omega^{(2,2)\star} = \sigma_r\frac{\Gamma(4-\upsilon)}{6}\left(\frac{T_r}{T}\right)^{\upsilon}.$$

These give

$$A^\star = \Omega^{(2,2)\star}/\Omega^{(1,1)\star} = (3-\upsilon)/3.$$

The probability of a collision occurring between two VHS molecules is proportional to $\sigma g \propto g^{1-2\upsilon}$. This probability biases the equilibrium distribution of g in collisions from the overall distribution of g as given by Eq. 2.10. For VHS molecules, the resulting distribution of g in collisions is

$$\left[f(g)\right]_{\text{colls}} = \frac{2}{\Gamma(2-\upsilon)}\left(\frac{\tilde{m}}{2kT}\right)^{2-\upsilon} g^{3-2\upsilon}\exp\left(-\frac{\tilde{m}g^2}{2kT}\right).$$

The relative translational energy in collisions, denoted ϵ_g, is defined by

$$\epsilon_g \equiv \tilde{m}g^2/2.$$

For VHS molecules, the distribution of reduced relative translational energy in collisions, denoted $\tilde{\epsilon}_g \equiv \epsilon_g/(kT)$, is

$$f(\tilde{\epsilon}_g) = \tilde{\epsilon}_g^{\,1-\upsilon} \exp(-\tilde{\epsilon}_g) / \Gamma(2-\upsilon). \tag{4.11}$$

By comparison with the continuous Boltzmann distribution of Eq. 2.16, the effective number of translational DOF in collisions for VHS molecules is then

$$\zeta_g = 4 - 2\upsilon. \tag{4.12}$$

For hard sphere and Maxwell-VHS molecules, $\zeta_g = 4$ and 3 respectively. The mean value of $\tilde{\epsilon}_g$ is found by evaluating

$$\langle \tilde{\epsilon}_g \rangle = \int_0^\infty \tilde{\epsilon}_g f(\tilde{\epsilon}_g) d\tilde{\epsilon}_g = 2 - \upsilon, \quad \text{which gives} \quad \langle \epsilon_g \rangle = (2-\upsilon)kT.$$

The total energy in a collision between particles A and B, denoted ϵ_c, may be defined by

$$\epsilon_c \equiv \epsilon_g + (\epsilon_{\rm rot})_{\rm A} + (\epsilon_{\rm vib})_{\rm A} + (\epsilon_{\rm rot})_{\rm B} + (\epsilon_{\rm vib})_{\rm B}.$$

For independently distributed continuous energy modes, the distribution of reduced collision energy $\tilde{\epsilon}_c \equiv \epsilon_c/(kT)$ for VHS molecules can be obtained from Eq. 2.16 and is

$$f(\tilde{\epsilon}_c) = \tilde{\epsilon}_c^{\,1-\upsilon+\bar{\zeta}_{\rm int}} \exp(-\tilde{\epsilon}_c) / \Gamma\left(2-\upsilon+\bar{\zeta}_{\rm int}\right), \tag{4.13}$$

where

$$\bar{\zeta}_{\rm int} = \left[(\zeta_{\rm rot})_{\rm A} + (\zeta_{\rm vib})_{\rm A} + (\zeta_{\rm rot})_{\rm B} + (\zeta_{\rm vib})_{\rm B} \right]/2 \tag{4.14}$$

is the mean number of internal DOF in each of the two colliding particles A and B. The distribution of ϵ_g and any combination of continuous internal energy modes may be obtained by including only the internal modes of interest in $\bar{\zeta}_{\rm int}$.

The mean collision rate of a species A particle with particles of species B is given by

$$\begin{aligned} \nu_{\rm A+B} &= n_{\rm B} \langle \sigma g \rangle_{\rm A+B} = n_{\rm B} \int_0^\infty (\sigma g)_{\rm A+B} f(g) dg \\ &= n_{\rm B} \left(\sigma_r g_r^{2\upsilon}\right) \frac{2\Gamma(2-\upsilon)}{\pi^{\frac{1}{2}}} \left(\frac{\tilde{m}}{2kT}\right)^{\upsilon-\frac{1}{2}}. \end{aligned} \tag{4.15}$$

Here, $f(g)$ is from Eq. 2.10. Substituting Eq. 4.8 into Eq. 4.15 yields

$$\nu_{\rm A+B} = n_{\rm B} \frac{15}{2} \frac{kT_r/\mu_r}{(2-\upsilon)(3-\upsilon)} \left(\frac{T}{T_r}\right)^{\frac{1}{2}-\upsilon}. \tag{4.16}$$

For later work, it is convenient to define a parameter

$$\Xi \equiv \frac{15}{2}\frac{kT_r/\mu_r}{(2-\upsilon)(3-\upsilon)}, \tag{4.17}$$

which is a constant that includes the VHS parameters of the A + B collision pair and has units of m^3/s. Ξ may be regarded as a reference value of σg. Using this definition for Ξ, Eq. 4.16 becomes

$$\nu_{\mathrm{A+B}} = n_{\mathrm{B}}\,\Xi\left(\frac{T}{T_r}\right)^{\frac{1}{2}-\upsilon} \quad \text{and} \quad \langle\sigma g\rangle_{\mathrm{A+B}} = \Xi\left(\frac{T}{T_r}\right)^{\frac{1}{2}-\upsilon}. \tag{4.18}$$

In a mixture of VHS molecules, the overall mean collision rate is obtained by summing over all possible collision partners using Eq. 2.35. For a pure VHS gas,

$$\nu = \frac{15}{2}\frac{p/\mu}{(2-\upsilon)(3-\upsilon)}.$$

From Eq. 2.37, the number of collisions occurring between VHS molecules of species A and species B per unit volume per unit time is

$$\dot{n}_{\mathrm{colls}} = \frac{\Xi n_{\mathrm{A}} n_{\mathrm{B}}}{f_s}\left(\frac{T}{T_r}\right)^{\frac{1}{2}-\upsilon}. \tag{4.19}$$

From §2.7, the mean time between collisions τ is simply $\tau = 1/\nu$. For a pure VHS gas, the ratio of τ to the nominal collision rate of Eq. 2.40 is

$$\frac{\tau_{\mathrm{VHS}}}{\tau_{\mathrm{nom}}} = \frac{8(2-\upsilon)(3-\upsilon)}{15\pi} \approx 0.817 \quad \text{for} \quad \upsilon = 0.25.$$

Bird [21] gives expressions for calculating the mean free path in a mixture of VHS molecules. Firstly, the expression

$$(\lambda_p)_0 = \left(\sum_{q=1}^{N_{\mathrm{sp}}} f_{pq}\right)^{-1}$$

must be evaluated for each species, where

$$f_{pq} = \sigma_r \Gamma(2-\upsilon) n_q \left(\frac{T_r}{T}\right)^{\upsilon}\left(\frac{m_p}{\tilde{m}}\right)^{\frac{1}{2}}.$$

Here, the reduced mass $\tilde{m}$ and the VHS parameters σ_r, T_r and υ refer to collisions between particles of species p and q. The mean free path in the mixture $(\lambda_{\mathrm{VHS}})_{\mathrm{mix}}$ is then given by

$$(\lambda_{\mathrm{VHS}})_{\mathrm{mix}} = \sum_{p=1}^{N_{\mathrm{sp}}}\frac{n_p}{n}(\lambda_p)_0 = \sum_{p=1}^{N_{\mathrm{sp}}}\frac{n_p}{n}\left(\sum_{q=1}^{N_{\mathrm{sp}}} f_{pq}\right)^{-1}. \tag{4.20}$$

In a pure VHS gas, $N_{\rm sp} = 1$ and Eq. 4.20 reduces to

$$\lambda_{\rm VHS} = \frac{8(2-\upsilon)(3-\upsilon)}{15\pi^{1/2}} \frac{\beta\mu}{\rho} = \frac{1}{n}\left(\frac{2}{\pi}\right)^{\frac{1}{2}} \frac{g_r}{\Xi}\left(\frac{T}{T_r}\right)^{\upsilon}. \tag{4.21}$$

The ratio $\lambda_{\rm VHS}/\lambda_{\rm nom}$ is

$$\frac{\lambda_{\rm VHS}}{\lambda_{\rm nom}} = \frac{8(2-\upsilon)(3-\upsilon)}{15\pi} \frac{\mu_r}{\mu(T)}\left(\frac{T}{T_r}\right)^{\frac{1}{2}+\upsilon}.$$

Bird [19] has suggested that $\lambda_{\rm VHS}$ of Eq. 4.21 should be used as the definition of the mean free path in a real gas.

Although the VHS model approximates the potentials of real molecules with an IPL potential, it is still of considerable use in modelling high temperature flows because, as noted in §2.6.1, the IPL potential is accurate at high temperatures. At low temperatures, attractive intermolecular forces are significant and the IPL potential does not accurately describe most gases. Because of its accuracy at high temperatures, and its relative simplicity, the VHS model is the most common molecular model used in DSMC calculations. Most developments in DSMC procedures have been undertaken for the VHS model.

To the first Chapman-Enskog approximation, the VHS model matches the viscosity of IPL molecules, but gives hard sphere diffusion behaviour. In flows were diffusion is unimportant, such as many hypersonic flows, the VHS model is appropriate.

4.4.2 Other DSMC molecular models

In an attempt to match both the viscosity and diffusion behaviour of IPL molecules, Koura and Matsumoto [97] introduced the variable soft sphere (VSS) molecular model. The VSS model has the same $\sigma = \sigma(g)$ dependence as the VHS model, but scattering is anisotropic with the deflection angle given by

$$\chi = 2\arccos\left[(b/d)^{1/w}\right].$$

Here, w is an adjustable parameter that is constant for each species interaction. The resulting VSS deflection angle is closer to that of IPL molecules than the deflection angle for VHS molecules. When using the VSS model in DSMC calculations, $\cos\chi$ is generated using $\cos\chi = 2R_f^{1/w} - 1$. The VHS model has $w = 1$. The VSS model should be used where diffusion effects are significant.

For low temperature flows, a molecular model that includes the effects of long range attraction as well as short range repulsion should be considered. Kuščer [101] introduced a molecular model that has the collision cross-section of molecules obeying a Sutherland intermolecular potential, with hard sphere scattering. The collision cross-section is given

by

$$\sigma = \sigma_s \left(1 + \frac{6kT_s}{\tilde{m}g^2}\right),$$

where σ_s is a Sutherland cross-section and T_s is the Sutherland temperature that are constants for a particular gas, and are obtained from viscosity data. This Sutherland-VHS model gives the Sutherland viscosity behaviour of Eq. 2.32. The model has been used by Boyd [34] and Lilley and Macrossan [107, 108], and may be regarded as an early special case of the generalised hard sphere model described below.

The generalised hard sphere (GHS) model, introduced by Hassan and Hash [84], allows simple modelling of molecules with realistic intermolecular potentials. The GHS cross-section is given by the sum of N VHS terms such that

$$\sigma = \sum_{i=1}^{N} \sigma_i \left(g_r/g\right)^{2\upsilon_i}.$$

Here, σ_i and υ_i are constants that are obtained by matching the GHS viscosity to available viscosity data. The GHS model uses hard sphere scattering. The original development of the GHS model was for weak attractive potentials. Kunc *et al.* [100] extended the model for strong attractive potentials. Fan [57] introduced the generalised soft sphere model, which is the logical extension of the GHS model to capture realistic diffusion behaviour. Further details of the GHS model are given in §C.3.

Despite the improved modelling accuracy afforded by the GHS model, it is rarely used in favour of the more common VHS model in DSMC calculations. This is probably due to a combination of two factors. Firstly, as discussed in §4.4.1, the VHS model is sufficiently accurate at high temperatures, and the GHS model offers little improvement in accuracy over the VHS model under high temperature conditions. Secondly, as noted by Macrossan and Lilley [125], the GHS model has poor computational efficiency. This prompted the introduction of the modified GHS (MGHS) model [125], which is only slightly less efficient than the VHS model, but represents the low temperature viscosity behaviour of argon more accurately than both the VHS and GHS models. The MGHS model has the potential to model low temperature flows more accurately than the VHS model. Further details of the MGHS model are included in §C.4.

Macrossan [121, 122] introduced two new DSMC collision models in which the collision frequency is based on the local time-averaged macroscopic translational kinetic temperature $T_{\rm tr}$. The second method [122], called μ-DSMC, is more general than the earlier ν-DSMC method [121], and a brief description is given here. The μ-DSMC model depends on calculating a local VHS reference cross-section from any viscosity behaviour $\mu = \mu(T)$. Using Eqs. 4.7 and 4.9 the viscosity of a pure VHS gas is

$$\mu\left(T_{\rm tr}\right) = \frac{15}{8}\frac{m\left(\pi R T_{\rm tr}\right)^{\frac{1}{2}}}{\Gamma(4-\upsilon)}\frac{1}{\sigma_r}.$$

This viscosity $\mu(T_{\text{tr}})$ is used to establish a local reference cross-section using

$$\sigma_r(T_{\text{tr}}) = \frac{15}{8}\frac{m(\pi RT_{\text{tr}})^{\frac{1}{2}}}{\Gamma(4-v)}\frac{1}{\mu(T_{\text{tr}})}.$$

This reference cross-section is used for the VHS collision model in each cell. Standard NTC collision partner selection procedures are used. The important feature of the μ-DSMC model is that any viscosity law $\mu = \mu(T_{\text{tr}})$ can be used.

Macrossan [122, 118] performed conventional DSMC calculations with the VHS, Sutherland-VHS and GHS models, and compared the results to those obtained using the μ-DSMC method with power law, Sutherland and GHS viscosity behaviour. In general, there was good agreement between the results. Consequently, Macrossan claims that the μ-DSMC method allows any viscosity behaviour to be modelled accurately with the DSMC method. This is an important advantage, because it permits modelling of gases using experimentally measured viscosity, for which no conventional DSMC model may be available.

4.5 Modelling molecules with internal energy

In most DSMC calculations, rotational energy is a continuous variable and is therefore represented by a floating point number. The equilibrium distribution of rotational energy is given by Eq. 2.16 with $\zeta = \zeta_{\text{rot}}$. For diatomic molecules with $\zeta_{\text{rot}} = 2$, the equilibrium distribution reduces to the exponential distribution of Eq. 2.18. ϵ_{rot} can be sampled directly from this distribution using

$$\epsilon_{\text{rot}} = -\ln(R_f)\,kT. \tag{4.22}$$

For each simulator particle, ϵ_{rot} is stored.

Quantised vibration models are often used in DSMC calculations. The unbounded harmonic oscillator model is the most common, where the energy levels are given by Eq. 2.21. At equilibrium, the integer quantum level q of an unbounded harmonic oscillator is sampled using [21]

$$q = \lfloor -\ln(R_f)\,T/\Theta_{\text{vib}} \rfloor. \tag{4.23}$$

The integer level q is stored for each particle. For anharmonic oscillators, an acceptance-rejection method must be applied to sample q.

During collisions involving molecules with internal DOF, energy can be exchanged between the internal and translational energy modes. Several models have been proposed to capture such exchange processes with the DSMC method. The energy exchange method of Borgnakke and Larsen [25, 26] gives adequate accuracy with low computational expense, and versions of the method are almost exclusively applied in DSMC studies to model internal energy exchange. In the Borgnakke-Larsen (BL) method, post-collision energies for relaxing collisions are sampled from equilibrium energy distributions for the collision.

The BL method has been formulated to satisfy basic physical requirements, such as the conservation laws and detailed balancing. However, BL procedures do not capture the true physical behaviour at the molecular level. For example, most BL versions consider interactions between internal modes and the translational mode only, and ignore exchange between internal modes. Clearly, the BL method is a phenomenological approach to modelling internal energy exchange.

As for the calculation of intermolecular collisions discussed in §4.2.2, the calculation of internal energy exchange using the BL method involves two steps. Firstly, those collisions in which energy exchange occurs must identified, followed by the assignment of post-collision energies. In most applications of the BL method, a fraction ϕ of collisions are regarded as being inelastic and subject to BL energy exchange. For a given collision, energy exchange is performed when $R_f < \phi$. The remaining collisions are purely elastic with no internal energy exchange. Here, the total energy of the modes that participate in a BL exchange event is denoted $\epsilon_{\rm ex}$, and the total effective DOF of these modes is denoted $\zeta_{\rm ex}$.

The remainder of this section is concerned primarily with the details of BL procedures for non-reactive collisions. Firstly, various schemes for selecting those collisions in which BL energy exchange occurs are considered in §4.5.1. This is of considerable importance, as it allows the simulation to approximate a specified macroscopic relaxation rate. Specific procedures for continuous rotational energy and quantised vibrational energy are considered in §4.5.2 and §4.5.3 respectively. Energy exchange in reactive collisions is considered in §6.7.

4.5.1 Selecting particles for Borgnakke-Larsen energy exchange

In the BL method, collisions in which internal energy exchange occurs are selected such that the resulting macroscopic relaxation behaviour approximates the desired behaviour. Several schemes have been devised to select the fraction of relaxing collisions ϕ. These schemes have several subtle differences which are often not elucidated in the literature. This section gives a brief summary of the various particle selection schemes for the BL method, with details of the particular scheme adopted in this study.

In the first applications of the BL method [26], relaxation was performed on a collision pair basis, whereby the internal energy of both particles participating in a collision was subject to exchange with the translational mode in each inelastic collision. This method is suited only to pure gases with a single relaxing internal energy mode, because it does not allow for different relaxation rates for different modes and different species. When this selection scheme is applied to rotational relaxation, the energy participating in the exchange is $\epsilon_{\rm ex} = \epsilon_g + (\epsilon_{\rm rot})_{\rm A} + (\epsilon_{\rm rot})_{\rm B}$. For this selection scheme, Lumpkin *et al.* [115]

showed that a rotational relaxation probability

$$\phi_{\text{rot}} = \frac{1}{Z_{\text{rot}}}\left(1 + \frac{\zeta_{\text{rot}}}{\zeta_g}\right) \tag{4.24}$$

should be used to recover a desired macroscopic collision number Z_{rot}. Bird [21] gives further details on the application of this selection scheme.

The common versions of the BL method, where only a fraction of collisions are regarded as inelastic, are physically unrealistic. In reality, all collisions are inelastic to some extent. To capture more physically realistic behaviour, Larsen and Borgnakke [103] introduced a restricted exchange version of the BL method. In this version, all collisions are inelastic, but only a certain fraction of the collision energy is available for energy exchange. Again, relaxation was performed on a pair basis. Pullin [141] showed that this restricted exchange scheme did not satisfy detailed balancing, and proposed a modified version to overcome this problem. Despite the improved physical realism afforded by restricted exchange schemes, they are rarely used. The reasons for this poor acceptance are not clear.

Bird [21] discussed a more general relaxation scheme, where BL energy exchange is performed on a particle basis. In this scheme, several energy modes in either one or both particles may contribute to ϵ_{ex}. These are termed multiple relaxation events [75]. This particle based selection scheme allows different relaxation rates for different energy modes and different species. As described by Bird, this scheme is implemented by serial application of the BL method, in which each internal energy mode interacts independently with the translational mode.

Haas *et al.* [75] recommended a selection scheme in which relaxation was performed on a particle basis, and multiple relaxation events were prohibited. In this scheme,

$$\epsilon_{\text{ex}} = \epsilon_g + \epsilon_i,$$

where ϵ_i is the energy of the single internal mode subject to exchange. Prohibiting multiple relaxation events allows the relaxation rate for each mode of each species interaction to be preserved [75]. For collisions where relaxation occurs, the relaxing mode exchanges energy only with the relative translational energy ϵ_g of the collision pair. Calculating the BL exchange probability ϕ for this scheme is quite complicated. Gimelshein *et al.* [65] proposed a simpler scheme that also prohibits multiple relaxation events. This particle selection scheme has been adopted here, and is illustrated in Table 4.1.

The selection scheme of Gimelshein *et al.* [65] requires that the sum of all exchange probabilities, denoted $\sum \phi$, is less than unity. Boyd [28] plotted mean ϕ_{rot} and ϕ_{vib} values for nitrogen at various temperatures. Although these probabilities were intended for a different particle selection scheme, they do indicate that $\sum \phi < 1$. Gimelshein *et al.* claim that the assumption of $\sum \phi < 1$ is probably correct for most gases. Expressions for ϕ_{rot} and ϕ_{vib} in terms of the macroscopic collision numbers Z_{rot} and Z_{vib} are provided below.

Table 4.1: Relaxing particle selection scheme of Gimelshein *et al.* [65]. Here R_f^* is a single random fraction generated before selecting the relaxing particle.

Let $\phi_1 = (\phi_{\rm rot})_{\rm A}$	If $R_f^* < \phi_1$,	$\epsilon_{\rm ex} = \epsilon_g + (\epsilon_{\rm rot})_{\rm A}$
Let $\phi_2 = \phi_1 + (\phi_{\rm rot})_{\rm B}$	If $\phi_1 \le R_f^* < \phi_2$,	$\epsilon_{\rm ex} = \epsilon_g + (\epsilon_{\rm rot})_{\rm B}$
Let $\phi_3 = \phi_2 + (\phi_{\rm vib})_{\rm A}$	If $\phi_2 \le R_f^* < \phi_3$,	$\epsilon_{\rm ex} = \epsilon_g + (\epsilon_{\rm vib})_{\rm A}$
Let $\phi_4 = \phi_3 + (\phi_{\rm vib})_{\rm B}$	If $\phi_3 \le R_f^* < \phi_4$,	$\epsilon_{\rm ex} = \epsilon_g + (\epsilon_{\rm vib})_{\rm B}$
	If $R_f^* \ge \phi_4$,	perform elastic collision

For adiabatic rotational relaxation, Eq. 2.42 gives

$$\frac{d\bar{\epsilon}_{\rm rot}}{dt} = \frac{\bar{\epsilon}_{\rm rot}^* - \bar{\epsilon}_{\rm rot}}{\tau Z_{\rm rot}}. \tag{4.25}$$

Here, $\bar{\epsilon}_{\rm rot}$ is the mean rotational energy and $\bar{\epsilon}_{\rm rot}^* = \zeta_{\rm rot} k T_{\rm tr}/2$ is the instantaneous average energy per molecule at the translational temperature of the heat bath $T_{\rm tr}$. From Eqs. 2.43 and 2.48,

$$2\bar{\epsilon}_{\rm rot}^* / (k\zeta_{\rm rot}) = T_{\rm tr} = 2\bar{\epsilon}_{\rm tr} / (k\zeta_{\rm tr}), \quad \text{so} \quad \bar{\epsilon}_{\rm rot}^* = (\zeta_{\rm rot}/\zeta_{\rm tr})\,\bar{\epsilon}_{\rm tr}.$$

Substituting this into Eq. 4.25 gives

$$\frac{d\bar{\epsilon}_{\rm rot}}{dt} = \frac{(\zeta_{\rm rot}/\zeta_{\rm tr})\,\bar{\epsilon}_{\rm tr} - \bar{\epsilon}_{\rm rot}}{\tau Z_{\rm rot}}. \tag{4.26}$$

To a first order approximation, which is accurate if $\Delta t \ll \tau$,

$$\frac{d\bar{\epsilon}_{\rm rot}}{dt} \approx \frac{\bar{\epsilon}_{\rm rot}^{t+\Delta t} - \bar{\epsilon}_{\rm rot}^{t}}{\Delta t}, \tag{4.27}$$

where $\bar{\epsilon}_{\rm rot}^{t+\Delta t}$ is the mean rotational energy at time $t + \Delta t$. $\bar{\epsilon}_{\rm rot}^{t+\Delta t}$ is given by

$$\bar{\epsilon}_{\rm rot}^{t+\Delta t} = \left(\frac{\Delta t}{\tau}\right) \phi_{\rm rot} \left(\bar{\epsilon}_{\rm rot}^{t+\Delta t}\right)_{\rm relax} + \left[1 - \left(\frac{\Delta t}{\tau}\right) \phi_{\rm rot}\right] \bar{\epsilon}_{\rm rot}^{t}. \tag{4.28}$$

Here $\Delta t/\tau$ is the fraction of particles that have a collision during Δt. In the selection scheme of Gimelshein *et al.* [65], each particle in a collision has a probability $\phi_{\rm rot}$ of participating in BL energy exchange. During Δt the fraction of particles that relaxing is therefore $(\Delta t/\tau)\phi_{\rm rot}$, and the fraction of particles that do not have a relaxing collision is $1 - (\Delta t/\tau)\phi_{\rm rot}$. At time $t + \Delta t$, the mean rotational energy of those particles that have a relaxing collision during time Δt is denoted $\left(\bar{\epsilon}_{\rm rot}^{t+\Delta t}\right)_{\rm relax}$. The first term on the right of Eq. 4.28 is the contribution to $\bar{\epsilon}_{\rm rot}^{t+\Delta t}$ from the relaxing particles. The second term is the contribution to $\bar{\epsilon}_{\rm rot}^{t+\Delta t}$ from the particles that do not relax. Substituting Eq. 4.28 into Eq. 4.27 gives

$$\frac{d\bar{\epsilon}_{\rm rot}}{dt} \approx \frac{\phi_{\rm rot}}{\tau} \left[\left(\bar{\epsilon}_{\rm rot}^{t+\Delta t}\right)_{\rm relax} - \bar{\epsilon}_{\rm rot}^{t} \right]. \tag{4.29}$$

When a relaxing collision occurs, the BL method divides $\epsilon_{\rm ex}$ between the translational

mode and the participating rotational mode, such that the ratio $\left(\bar{\epsilon}_{\rm rot}^{t+\Delta t}\right)_{\rm relax}/\bar{\epsilon}_{\rm ex}^{t}$ is given by the ratio of the respective DOF [115]. Consequently,

$$\left(\bar{\epsilon}_{\rm rot}^{t+\Delta t}\right)_{\rm relax} = \left(\frac{\zeta_{\rm rot}}{\zeta_{\rm ex}}\right)\bar{\epsilon}_{\rm ex}^{t} = \left(\frac{\zeta_{\rm rot}}{\zeta_{\rm rot}+\zeta_g}\right)\left(\bar{\epsilon}_{\rm rot}^{t}+\bar{\epsilon}_g^{t}\right). \tag{4.30}$$

Substituting this into Eq. 4.29 gives

$$\frac{d\bar{\epsilon}_{\rm rot}}{dt} \approx \frac{\phi_{\rm rot}}{\tau}\left[\left(\frac{\zeta_{\rm rot}}{\zeta_{\rm rot}+\zeta_g}\right)\left(\bar{\epsilon}_{\rm rot}^{t}+\bar{\epsilon}_g^{t}\right)-\bar{\epsilon}_{\rm rot}^{t}\right] = \frac{\phi_{\rm rot}}{\tau}\left[\frac{\left(\zeta_{\rm rot}/\zeta_g\right)\bar{\epsilon}_g-\bar{\epsilon}_{\rm rot}}{\left(\zeta_{\rm rot}+\zeta_g\right)/\zeta_g}\right]. \tag{4.31}$$

Equating Eqs. 4.26 and 4.31, and using $\bar{\epsilon}_g = \left(\zeta_g/\zeta_{\rm tr}\right)\bar{\epsilon}_{\rm tr}$ which applies at equilibrium,

$$\frac{\left(\zeta_{\rm rot}/\zeta_{\rm tr}\right)\bar{\epsilon}_{\rm tr}-\bar{\epsilon}_{\rm rot}}{\tau Z_{\rm rot}} \approx \frac{\phi_{\rm rot}}{\tau}\left[\frac{\left(\zeta_{\rm rot}/\zeta_{\rm tr}\right)\bar{\epsilon}_{\rm tr}-\bar{\epsilon}_{\rm rot}}{\left(\zeta_{\rm rot}+\zeta_g\right)/\zeta_g}\right]$$

is obtained. Thus

$$\phi_{\rm rot} \approx \frac{1}{Z_{\rm rot}}\left(1+\frac{\zeta_{\rm rot}}{\zeta_g}\right). \tag{4.32}$$

This demonstrates that the particle selection scheme proposed by Gimelshein *et al.* [65] results in an expression for $\phi_{\rm rot}$ identical to that given by Lumpkin *et al.* [115] for pair relaxation in Eq. 4.24.

For the particle selection scheme of Gimelshein *et al.* [65], Eq. 4.32 is a new result, and must be verified. This has been achieved here by performing a zero-dimensional DSMC calculation of the rotational relaxation behaviour, and comparing the relaxation history to that provided by the exact solution of Eq. 2.45. The nitrogen parameters from Table B.1 were used. $Z_{\rm rot} = 5$ was used, which gives $\phi_{\rm rot} = 0.3149$. The initial translational temperature $T_{\rm tr}(0)$ was 1000 K and the initial rotational temperature $T_{\rm rot}(0)$ was 5000 K. The equilibrium temperature $T^* = T_{\rm tr}(\infty) = T_{\rm rot}(\infty)$ was 3400 K. The calculation contained 10^6 diatomic particles, and used a time step $\Delta t = \tau_{\rm VHS}/10$ where $\tau_{\rm VHS} = 1/\nu$ is the initial VHS collision time obtained from Eq. 4.18 with $T = T_{\rm tr}(0)$. Fig. 4.1 shows a plot of $\Delta\hat{\epsilon}_{\rm rot}$ versus the non-dimensional time $\hat{t}$. Here,

$$\Delta\hat{\epsilon}_{\rm rot} = \frac{T_{\rm rot}(t)-T^*}{T_{\rm rot}(0)-T^*}.$$

From Eq. 2.47, $\hat{t}$ is given by

$$\hat{t} = \int_0^t \frac{dt}{Z_{\rm rot}\tau(t)}.$$

By counting the number of collisions performed by the DSMC calculation during a time step s, denoted $N_{\rm colls}(s)$, Eq. 2.38 gives $\tau(s) = N\Delta t/\left[2N_{\rm colls}(s)\right]$, where N is the total number of particles. $\hat{t}$ is then given by

$$\hat{t}(s) = \frac{2}{Z_{\rm rot}N}\sum_{i=1}^{s} N_{\rm colls}(i).$$

The excellent agreement between the DSMC and exact solutions verifies that Eq. 4.32 is correct.

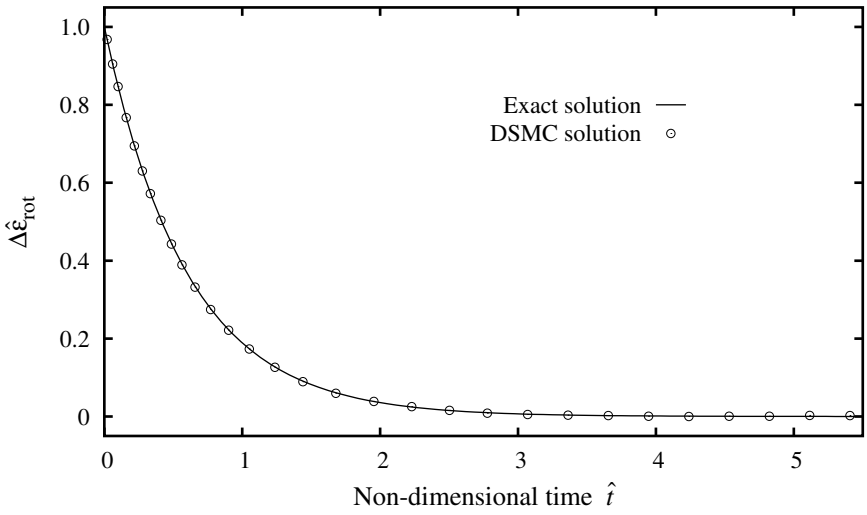

Figure 4.1: Exact and DSMC solutions of the relaxation history for the particle selection scheme of Gimelshein *et al.* [65].

Application of the preceding analysis to the vibrational mode is somewhat complicated by the temperature dependence of $\zeta_{\rm vib}$. For the selection scheme shown in Table 4.1, Gimelshein *et al.* [65] give

$$\phi_{\rm vib} = \frac{1}{Z_{\rm vib}} \frac{\zeta_{\rm vib}(T_{\rm tr})T_{\rm tr} - \zeta_{\rm vib}(T_{\rm vib})T_{\rm vib}}{\zeta_g(T_{\rm tr} - T')}, \tag{4.33}$$

where the temperature T' is found numerically from

$$\zeta_{\rm vib}(T_{\rm vib})T_{\rm vib} + \zeta_g T_{\rm tr} = \zeta_{\rm vib}(T')T' + \zeta_g T'. \tag{4.34}$$

In the above treatments, the implicit assumption is that the rotational relaxation occurs at a rate that far exceeds the vibrational relaxation rate, such that the two processes may be considered separately. When considering rotational relaxation, vibration is assumed to be frozen, and when considering vibrational relaxation, rotation is assumed to be at equilibrium. Where more than one relaxation process is proceeding, the selection schemes considered here may give macroscopic relaxation behaviour that does not match the target relaxation rate based on the collision numbers.

4.5.2 Rotational energy exchange

The following discussion gives the procedures used here to compute rotational energy exchange using the BL method. The derivation is similar to that of Haas *et al.* [76]. The particle selection scheme of Gimelshein *et al.* [65] has been used, in which multiple relaxation events are prohibited and the rotational mode of the relaxing particle exchanges

energy with the relative translational mode of the collision pair only. In this case, $\epsilon_{\rm ex}$ is

$$\epsilon_{\rm ex} = \epsilon_g + \epsilon_{\rm rot} = \epsilon'_g + \epsilon'_{\rm rot}, \quad \text{so} \quad \tilde{\epsilon}_{\rm ex} = \tilde{\epsilon}_g + \tilde{\epsilon}_{\rm rot} = \tilde{\epsilon}'_g + \tilde{\epsilon}'_{\rm rot}.$$

The post-collision rotational energy $\epsilon'_{\rm rot}$ may be written as a fraction $F_{\rm rot}$ of the participating energy, given by

$$F_{\rm rot} = \frac{\epsilon'_{\rm rot}}{\epsilon'_g + \epsilon'_{\rm rot}} = \frac{\epsilon'_{\rm rot}}{\epsilon_g + \epsilon_{\rm rot}} = \frac{\tilde{\epsilon}'_{\rm rot}}{\tilde{\epsilon}_g + \tilde{\epsilon}_{\rm rot}} = \frac{\tilde{\epsilon}'_{\rm rot}}{\tilde{\epsilon}_{\rm ex}}.$$

Note that $\tilde{\epsilon}'_g = \tilde{\epsilon}_{\rm ex}(1 - F_{\rm rot})$. In the BL method, $F_{\rm rot}$ is sampled from the equilibrium distribution $f(F_{\rm rot})$. The requirement is to obtain this distribution.

From Eq. 4.11, the equilibrium distribution of $\tilde{\epsilon}'_g$ for VHS molecules is

$$f\left(\tilde{\epsilon}'_g\right) = \left(\tilde{\epsilon}'_g\right)^{1-\upsilon} \exp\left(-\tilde{\epsilon}'_g\right) / \Gamma(2-\upsilon). \tag{4.35}$$

From Eq. 2.16, the equilibrium distribution of $\tilde{\epsilon}'_{\rm rot}$ is

$$f\left(\tilde{\epsilon}'_{\rm rot}\right) = \left(\tilde{\epsilon}'_{\rm rot}\right)^{\zeta_{\rm rot}/2-1} \exp\left(-\tilde{\epsilon}'_{\rm rot}\right) / \Gamma\left(\zeta_{\rm rot}/2\right). \tag{4.36}$$

Assuming that $f\left(\tilde{\epsilon}'_g\right)$ and $f\left(\tilde{\epsilon}'_{\rm rot}\right)$ are independent distributions, the joint distribution is

$$f(\tilde{\epsilon}'_g, \tilde{\epsilon}'_{\rm rot}) = \frac{\left(\tilde{\epsilon}'_g\right)^{1-\upsilon} \left(\tilde{\epsilon}'_{\rm rot}\right)^{\zeta_{\rm rot}/2-1} \exp\left(-\tilde{\epsilon}_{\rm ex}\right)}{\Gamma(2-\upsilon)\Gamma\left(\zeta_{\rm rot}/2\right)}.$$

This joint distribution must be transformed to a distribution over $F_{\rm rot}$ and $\tilde{\epsilon}_{\rm ex}$, according to the method presented in §A.2. The Jacobian J of the transformation is $J = -\tilde{\epsilon}_{\rm ex}$, giving $|J| = \tilde{\epsilon}_{\rm ex}$, so

$$\begin{aligned} f(F_{\rm rot}, \tilde{\epsilon}_{\rm ex}) &= \frac{\left(\tilde{\epsilon}'_g\right)^{1-\upsilon} \left(\tilde{\epsilon}'_{\rm rot}\right)^{\zeta_{\rm rot}/2-1} \exp\left(-\tilde{\epsilon}_{\rm ex}\right)}{\Gamma(2-\upsilon)\Gamma\left(\zeta_{\rm rot}/2\right)} \times \tilde{\epsilon}_{\rm ex} \\ &= \frac{\tilde{\epsilon}_{\rm ex}^{1-\upsilon+\zeta_{\rm rot}/2} \exp\left(-\tilde{\epsilon}_{\rm ex}\right)}{\Gamma(2-\upsilon)\Gamma\left(\zeta_{\rm rot}/2\right)} \left(\frac{\tilde{\epsilon}_{\rm ex} - \tilde{\epsilon}'_{\rm rot}}{\tilde{\epsilon}_{\rm ex}}\right)^{1-\upsilon} \left(\frac{\tilde{\epsilon}'_{\rm rot}}{\tilde{\epsilon}_{\rm ex}}\right)^{\zeta_{\rm rot}/2-1} \\ &= \frac{\tilde{\epsilon}_{\rm ex}^{1-\upsilon+\zeta_{\rm rot}/2} \exp\left(-\tilde{\epsilon}_{\rm ex}\right)}{\Gamma(2-\upsilon)\Gamma\left(\zeta_{\rm rot}/2\right)} \left(1 - F_{\rm rot}\right)^{1-\upsilon} F_{\rm rot}^{\zeta_{\rm rot}/2-1}. \end{aligned} \tag{4.37}$$

The distribution of $F_{\rm rot}$ alone is then obtained by integrating this joint distribution over $0 \leq \tilde{\epsilon}_{\rm ex} < \infty$ to give

$$f(F_{\rm rot}) = \int_0^\infty f(F_{\rm rot}, \tilde{\epsilon}_{\rm ex}) d\tilde{\epsilon}_{\rm ex} = \frac{\Gamma(2-\upsilon+\zeta_{\rm rot}/2)}{\Gamma(2-\upsilon)\Gamma(\zeta_{\rm rot}/2)} (1 - F_{\rm rot})^{1-\upsilon} F_{\rm rot}^{\zeta_{\rm rot}/2-1}. \tag{4.38}$$

In general, $F_{\rm rot}$ can be sampled from this beta distribution with the acceptance-rejection method. Gentle [62] summarises other more efficient methods for sampling from the beta

distribution. For diatomic molecules, $\zeta_{\rm rot} = 2$ and Eq. 4.38 reduces to

$$f(F_{\rm rot}) = (2-\upsilon)(1-F_{\rm rot})^{1-\upsilon}.$$

$F_{\rm rot}$ can be sampled directly from this distribution using

$$F_{\rm rot} = 1 - R_f^{1/(2-\upsilon)}, \quad \text{giving} \quad \epsilon'_{\rm rot} = \left[1 - R_f^{1/(2-\upsilon)}\right] \epsilon_{\rm ex}.$$

From Eq. 4.36, $\langle \tilde{\epsilon}'_{\rm rot} \rangle = \zeta_{\rm rot}/2$. By integrating Eq. 4.37 over the range $0 \leq F_{\rm rot} \leq 1$, the distribution of $\tilde{\epsilon}_{\rm ex}$ is

$$f\left(\tilde{\epsilon}_{\rm ex}\right) = \tilde{\epsilon}_{\rm ex}^{1-\upsilon+\zeta_{\rm rot}/2} \exp\left(-\tilde{\epsilon}_{\rm ex}\right) / \Gamma\left(2-\upsilon+\zeta_{\rm rot}/2\right) = \tilde{\epsilon}_{\rm ex}^{\zeta_{\rm ex}/2-1} \exp\left(-\tilde{\epsilon}_{\rm ex}\right) / \Gamma\left(\zeta_{\rm ex}/2\right).$$

This distribution has the form of Eq. 2.15 and provides $\langle \tilde{\epsilon}_{\rm ex} \rangle = 2 - \upsilon + \zeta_{\rm rot}/2 = \zeta_{\rm ex}/2$. The mean of the post-exchange rotational energy $\epsilon'_{\rm rot}$ used here is the same as the $\left(\bar{\epsilon}_{\rm rot}^{t+\Delta t}\right)_{\rm relax}$ notation used in §4.5.1. Therefore the ratio

$$\frac{\langle \tilde{\epsilon}'_{\rm rot} \rangle}{\langle \tilde{\epsilon}_{\rm ex} \rangle} = \frac{\langle \epsilon'_{\rm rot} \rangle}{\langle \epsilon_{\rm ex} \rangle} = \frac{\zeta_{\rm rot}}{\zeta_{\rm ex}}$$

confirms the earlier result of Lumpkin *et al.* [115] which was used to obtain Eq. 4.30.

The relative translational energy after rotational energy exchange is simply $\epsilon'_g = \epsilon_{\rm ex} - \epsilon'_{\rm rot}$. The relative speed after exchange is then

$$g' = \left(2\epsilon'_g/\tilde{m}\right)^{\frac{1}{2}}.$$

For hard sphere scattering, the direction of g' is randomly distributed on the unit sphere.

An internal energy exchange model must satisfy detailed balancing at equilibrium. The following discussion examines the issue of detailed balancing for the rotational energy exchange scheme presented above. Consider a total of $N_{\rm colls}$ collisions between particles of species A and B. The number of such collisions that result in rotational relaxation of the species A particle is $\phi_{\rm rot} N_{\rm colls}$, where $\phi_{\rm rot}$ is the rotational exchange probability for species A particles in A + B collisions. Here, $\phi_{\rm rot}$ may be a function of ϵ_g and $\epsilon_{\rm rot}$. The total number of relaxing collisions of class $\tilde{\epsilon}_g$ that are also of class $\tilde{\epsilon}_{\rm rot}$ is then

$$\left[N_{\rm relax}\right]_{\tilde{\epsilon}_g}^{\tilde{\epsilon}_{\rm rot}} = \phi_{\rm rot} N_{\rm colls} f\left(\tilde{\epsilon}_g\right) f\left(\tilde{\epsilon}_{\rm rot}\right) d\tilde{\epsilon}_{\rm rot} d\tilde{\epsilon}_g.$$

It is necessary to find the number of these relaxation events that result in relative translational energy $\tilde{\epsilon}'_g$ and rotational energy $\tilde{\epsilon}'_{\rm rot}$ after BL energy exchange. The number of relaxing collisions of class $\tilde{\epsilon}'_g$, $\tilde{\epsilon}'_{\rm rot}$ and $F_{\rm rot}$ is $\left[N_{\rm relax}\right]_{\tilde{\epsilon}_g}^{\tilde{\epsilon}_{\rm rot}} f\left(F_{\rm rot}\right) dF_{\rm rot}$. These collisions undergo BL exchange to give post-exchange rotational energy $\tilde{\epsilon}'_{\rm rot}$ and relative translational energy $\tilde{\epsilon}'_g$. Therefore, the number of relaxing collisions in classes $\tilde{\epsilon}_g$ and $\tilde{\epsilon}_{\rm rot}$ that result in

energies $\tilde{\epsilon}'_g$ and $\tilde{\epsilon}'_{\rm rot}$ after BL exchange is

$$[N_{\rm relax}]^{\tilde{\epsilon}_{\rm rot}\to\tilde{\epsilon}'_{\rm rot}}_{\tilde{\epsilon}_g\to\tilde{\epsilon}'_g} = \phi_{\rm rot} N_{\rm colls} f\left(\tilde{\epsilon}_g\right) f\left(\tilde{\epsilon}_{\rm rot}\right) f\left(F_{\rm rot}\right) dF_{\rm rot} d\tilde{\epsilon}_{\rm rot} d\tilde{\epsilon}_g. \tag{4.39}$$

Similarly, the number of relaxing collisions in classes $\tilde{\epsilon}'_g$ and $\tilde{\epsilon}'_{\rm rot}$ that result in energies $\tilde{\epsilon}_g$ and $\tilde{\epsilon}_{\rm rot}$ after BL energy exchange is

$$[N_{\rm relax}]^{\tilde{\epsilon}'_{\rm rot}\to\tilde{\epsilon}_{\rm rot}}_{\tilde{\epsilon}'_g\to\tilde{\epsilon}_g} = \phi'_{\rm rot} N_{\rm colls} f\left(\tilde{\epsilon}'_g\right) f\left(\tilde{\epsilon}'_{\rm rot}\right) f\left(F'_{\rm rot}\right) dF'_{\rm rot} d\tilde{\epsilon}'_{\rm rot} d\tilde{\epsilon}'_g. \tag{4.40}$$

For detailed balancing to apply, the expression

$$[N_{\rm relax}]^{\tilde{\epsilon}_{\rm rot}\to\tilde{\epsilon}' rot}_{\tilde{\epsilon}_g\to\tilde{\epsilon}'_g} = [N_{\rm relax}]^{\tilde{\epsilon}'_{\rm rot}\to\tilde{\epsilon}_{\rm rot}}_{\tilde{\epsilon}'_g\to\tilde{\epsilon}_g}$$

must be satisfied. Using Eqs. 4.39 and 4.40, this becomes

$$\phi_{\rm rot} f\left(\tilde{\epsilon}_g\right) f\left(\tilde{\epsilon}_{\rm rot}\right) f\left(F_{\rm rot}\right) dF_{\rm rot} d\tilde{\epsilon}_{\rm rot} d\tilde{\epsilon}_g = \phi'_{\rm rot} f\left(\tilde{\epsilon}'_g\right) f\left(\tilde{\epsilon}'_{\rm rot}\right) f\left(F'_{\rm rot}\right) dF'_{\rm rot} d\tilde{\epsilon}'_{\rm rot} d\tilde{\epsilon}'_g.$$

For a given exchange event with $\tilde{\epsilon}'_{\rm rot} = \tilde{\epsilon}_{\rm rot} + \Delta\tilde{\epsilon}$ and $\tilde{\epsilon}'_g = \tilde{\epsilon}_g - \Delta\tilde{\epsilon}$, the energy exchanged $\Delta\tilde{\epsilon}$ is constant, so $d\tilde{\epsilon}_g = d\tilde{\epsilon}'_g$ and $d\tilde{\epsilon}_{\rm rot} = d\tilde{\epsilon}'_{\rm rot}$. Also $F_{\rm rot} = F'_{\rm rot} + \Delta\tilde{\epsilon}/\tilde{\epsilon}_{\rm ex}$, so $dF_{\rm rot} = dF'_{\rm rot}$. The detailed balancing requirement then becomes

$$\phi_{\rm rot} f\left(\tilde{\epsilon}_g\right) f\left(\tilde{\epsilon}_{\rm rot}\right) f\left(F_{\rm rot}\right) = \phi'_{\rm rot} f\left(\tilde{\epsilon}'_g\right) f\left(\tilde{\epsilon}'_{\rm rot}\right) f\left(F'_{\rm rot}\right). \tag{4.41}$$

For constant $\phi_{\rm rot} = \phi'_{\rm rot}$, substituting the expressions for $f\left(\tilde{\epsilon}_g\right)$, $f\left(\tilde{\epsilon}_{\rm rot}\right)$ and $f\left(F_{\rm rot}\right)$ into Eq. 4.41 shows that detailed balancing is satisfied.

As noted in §2.8, the rotational collision number $Z_{\rm rot}$ generally increases with temperature. At the molecular level, $\phi_{\rm rot}$ should therefore decrease as the collision energy increases. To capture this behaviour, a number of variable-$\phi_{\rm rot}$ models have been proposed for the BL method [52, 53, 29]. For an energy dependent $\phi_{\rm rot} = \phi_{\rm rot}\left(\epsilon_g, \epsilon_{\rm rot}\right)$, a different form of $f\left(F_{\rm rot}\right)$ must be used to compensate for the biased selection of relaxing particles. From Eq. 4.41 the relation

$$\frac{f(F_{\rm rot})}{f(F'_{\rm rot})} = \frac{\phi_{\rm rot}\left(\epsilon'_g, \epsilon'_{\rm rot}\right)}{\phi_{\rm rot}\left(\epsilon_g, \epsilon_{\rm rot}\right)} \frac{f\left(\tilde{\epsilon}'_g\right) f\left(\tilde{\epsilon}'_{\rm rot}\right)}{f\left(\tilde{\epsilon}_g\right) f\left(\tilde{\epsilon}_{\rm rot}\right)} \tag{4.42}$$

must be satisfied for detailed balancing to hold. Following Abe [1], one possible solution for the biased distribution of $F_{\rm rot}$, denoted $f^*\left(F_{\rm rot}\right)$, is

$$f^*\left(F_{\rm rot}\right) \propto \phi_{\rm rot}\left(\epsilon'_g, \epsilon'_{\rm rot}\right) f\left(\tilde{\epsilon}'_g\right) f\left(\tilde{\epsilon}'_{\rm rot}\right).$$

Using Eqs. 4.35, 4.36 and 4.38, this becomes

$$\begin{aligned} f^*\left(F_{\rm rot}\right) &\propto \phi_{\rm rot}\left(\epsilon_g', \epsilon_{\rm rot}'\right)\left(1-F_{\rm rot}\right)^{1-\upsilon} F_{\rm rot}^{\zeta_{\rm rot}/2-1} \propto \phi_{\rm rot}\left(\epsilon_g', \epsilon_{\rm rot}'\right) f\left(F_{\rm rot}\right) \\ &\propto \phi_{\rm rot}\left[\epsilon_{\rm ex}\left(1-F_{\rm rot}\right), \epsilon_{\rm ex} F_{\rm rot}\right] f\left(F_{\rm rot}\right). \end{aligned}$$

Because $\epsilon_{\rm ex}$ is constant for a given exchange event, this shows that $f^*\left(F_{\rm rot}\right)$ depends on $F_{\rm rot}$ alone, as required. Selecting $F_{\rm rot}$ from this biased distribution using the acceptance-rejection method could involve considerable computational expense. Alternatively, Boyd [29] used the time-averaged $\phi_{\rm rot}$ for each cell. This effectively means that $\phi_{\rm rot}$ is constant in each cell, thereby satisfying detailed balancing. Other forms of $f^*\left(F_{\rm rot}\right)$ may exist that also satisfy Eq. 4.42. Also, a local $Z_{\rm rot}$ could be calculated in each cell from a local kinetic temperature to provide a local $\phi_{\rm rot}$. Variable-$\phi_{\rm rot}$ models have not been used here.

Boyd [33] introduced a version of the BL method for modelling rotational energy exchange between rigid rotor molecules with quantised rotational energies. Koura [95] proposed an energy exchange model for molecules with discrete rotational energy that does not use BL procedures.

4.5.3 Vibrational energy exchange

BL energy exchange procedures for molecules with continuous vibrational energy are similar to those for rotational energy, although consideration must be given to the effective number of vibrational DOF $\zeta_{\rm vib}$, which varies with temperature. Versions of BL procedures involving particles with quantised vibration have been proposed by Haas *et al.* [76] and Bergemann and Boyd [9]. A detailed derivation of the BL method of Bergemann and Boyd for a general quantised vibration model is presented here. The expressions are readily adapted for harmonic oscillators. The combination of harmonic oscillators and the BL exchange scheme of Bergemann and Boyd is often used in DSMC calculations.

When prohibiting multiple relaxation events, the energy available for exchange between translation and the vibrational mode of one particle in an inelastic collision is

$$\epsilon_{\rm ex} = \epsilon_g + \epsilon_{\rm vib}(q) = \epsilon_g' + \epsilon_{\rm vib}\left(q'\right) \quad \text{so} \quad \tilde{\epsilon}_{\rm ex} = \tilde{\epsilon}_g + \tilde{\epsilon}_{\rm vib}(q) = \tilde{\epsilon}_g' + \tilde{\epsilon}_{\rm vib}(q').$$

After BL energy exchange, the fraction of particles with vibrational energy level q' is obtained from From Eq. 2.19 and is

$$\Phi\left(q'\right) = \exp\left[-\tilde{\epsilon}_{\rm vib}(q')\right]/Q_{\rm vib} \quad \text{where} \quad q' = 0, 1, ..., q_{\rm max}.$$

Here, $q_{\rm max}$ is the maximum possible vibrational energy level, which depends on the vibration model. In the following discussion, $\tilde{\epsilon}_{\rm vib}^\star$ denotes the post-exchange vibrational energy in a continuous representation, as used in §2.5.2 and §A.3. In terms of the δ function, the

distribution of $\tilde{\epsilon}^{\star}_{\rm vib}$ is

$$f\left(\tilde{\epsilon}^{\star}_{\rm vib}\right) = \frac{\exp\left(-\tilde{\epsilon}^{\star}_{\rm vib}\right)}{Q_{\rm vib}}\,\delta\left[\tilde{\epsilon}^{\star}_{\rm vib} - \tilde{\epsilon}_{\rm vib}(q')\right] \quad \text{where} \quad q' = 0, 1, ..., q_{\rm max}.$$

The distribution of $\tilde{\epsilon}^{\star}_{\rm vib}$ for a given value of $\tilde{\epsilon}_{\rm ex}$ is found by evaluating the conditional distribution $f\left(\tilde{\epsilon}^{\star}_{\rm vib}|\tilde{\epsilon}_{\rm ex}\right)$ [152], which is given by

$$f\left(\tilde{\epsilon}^{\star}_{\rm vib}|\tilde{\epsilon}_{\rm ex}\right) = f\left(\tilde{\epsilon}_{\rm ex}, \tilde{\epsilon}^{\star}_{\rm vib}\right)/f\left(\tilde{\epsilon}_{\rm ex}\right).$$

From Eqs. A.9 and A.12,

$$f\left(\tilde{\epsilon}_{\rm ex}, \tilde{\epsilon}^{\star}_{\rm vib}\right) = \frac{\left(\tilde{\epsilon}_{\rm ex} - \tilde{\epsilon}^{\star}_{\rm vib}\right)^{1-\upsilon}\exp\left(-\tilde{\epsilon}_{\rm ex}\right)}{\Gamma(2-\upsilon)Q_{\rm vib}}\,\delta\left[\tilde{\epsilon}^{\star}_{\rm vib} - \tilde{\epsilon}_{\rm vib}(q')\right]$$

and

$$f\left(\tilde{\epsilon}_{\rm ex}\right) = \frac{\exp\left(-\tilde{\epsilon}_{\rm ex}\right)}{\Gamma(2-\upsilon)Q_{\rm vib}} \times S, \quad \text{where} \quad S = \sum_{q'=0}^{q_{\rm ex}}\left[\tilde{\epsilon}_{\rm ex} - \tilde{\epsilon}_{\rm vib}(q')\right]^{1-\upsilon}.$$

Here, $q_{\rm ex}$ is the maximum possible post-exchange vibrational energy level that corresponds to the exchange energy $\tilde{\epsilon}_{\rm ex}$, and is specified later. From above,

$$f\left(\tilde{\epsilon}^{\star}_{\rm vib}|\tilde{\epsilon}_{\rm ex}\right) = \left(\tilde{\epsilon}_{\rm ex} - \tilde{\epsilon}^{\star}_{\rm vib}\right)^{1-\upsilon}\delta\left[\tilde{\epsilon}^{\star}_{\rm vib} - \tilde{\epsilon}_{\rm vib}(q')\right]/S$$

which becomes

$$\Phi\left(q'|\tilde{\epsilon}_{\rm ex}\right) = \left[\tilde{\epsilon}_{\rm ex} - \tilde{\epsilon}_{\rm vib}(q')\right]^{1-\upsilon}/S. \tag{4.43}$$

Because $\tilde{\epsilon}_{\rm vib}$ increases monotonically from $\tilde{\epsilon}_{\rm vib}(0)$, the largest value of $\tilde{\epsilon}_{\rm ex} - \tilde{\epsilon}_{\rm vib}(q')$ occurs at $q' = 0$. Therefore this discrete distribution has a maximum $\Phi_{\rm max} = \left[\tilde{\epsilon}_{\rm ex} - \tilde{\epsilon}_{\rm vib}(0)\right]^{1-\upsilon}/S$. Using $\tilde{\epsilon}_{\rm vib}(0) = 0$, the ratio $\Phi/\Phi_{\rm max}$ is simply

$$\frac{\Phi}{\Phi_{\rm max}} = \left[\frac{\tilde{\epsilon}_{\rm ex} - \tilde{\epsilon}_{\rm vib}(q')}{\tilde{\epsilon}_{\rm ex}}\right]^{1-\upsilon} = \left[1 - \frac{\tilde{\epsilon}_{\rm vib}(q')}{\tilde{\epsilon}_{\rm ex}}\right]^{1-\upsilon} = \left[1 - \frac{\epsilon_{\rm vib}(q')}{\epsilon_{\rm ex}}\right]^{1-\upsilon}.$$

For unbounded harmonic oscillators, $\epsilon_{\rm vib}(q') = q'k\Theta_{\rm vib}$, so

$$\frac{\Phi}{\Phi_{\rm max}} = \left(1 - \frac{q'k\Theta_{\rm vib}}{\epsilon_{\rm ex}}\right)^{1-\upsilon}$$

as given by Bergemann and Boyd [9].

To sample q', test values of q' are generated according to $R_i\left(0, q_{\rm ex}\right)$ and are accepted if

$$R_f < \left[1 - \epsilon_{\rm vib}(q')/\epsilon_{\rm ex}\right]^{1-\upsilon}.$$

For harmonic oscillators, the acceptance criterion is

$$R_f < \left(1 - q'k\Theta_{\rm vib}/\epsilon_{\rm ex}\right)^{1-\upsilon}.$$

The maximum post-exchange vibrational level q_{ex} is required to sample q'. For anharmonic oscillators, the maximum possible vibrational level is the dissociation level q_d. If $\tilde{\epsilon}_{\text{ex}} > \tilde{\epsilon}_{\text{vib}}(q_d)$, then $q_{\text{ex}} = q_d$. Otherwise, q_{ex} is the quantum level with energy $\tilde{\epsilon}_{\text{vib}}(q_{\text{ex}})$ that is closest to $\tilde{\epsilon}_{\text{ex}}$ such that $\tilde{\epsilon}_{\text{vib}}(q_{\text{ex}}) < \tilde{\epsilon}_{\text{ex}}$. For unbounded harmonic oscillators,

$$q_{\text{ex}} = \left\lfloor \frac{\tilde{\epsilon}_{\text{ex}} T}{\Theta_{\text{vib}}} \right\rfloor = \left\lfloor \frac{\epsilon_{\text{ex}}}{k\Theta_{\text{vib}}} \right\rfloor. \tag{4.44}$$

For bounded harmonic oscillators

$$q_{\text{ex}} = \min\left(\left\lfloor \frac{\tilde{\epsilon}_{\text{ex}} T}{\Theta_{\text{vib}}} \right\rfloor, q_d \right) = \min\left(\left\lfloor \frac{\epsilon_{\text{ex}}}{k\Theta_{\text{vib}}} \right\rfloor, q_d \right).$$

Following arguments similar to those presented in §4.5.2, it can be shown that this BL exchange scheme satisfies detailed balancing. For a total of N_{colls} collisions, the number of vibrationally relaxing collisions of class $\tilde{\epsilon}_g$ that are also of class q is

$$\phi_{\text{vib}} N_{\text{colls}} \Phi(q) f(\tilde{\epsilon}_g)\, d\tilde{\epsilon}_g.$$

The number of these relaxing collisions that result in a post-relaxation vibrational energy level q' is

$$\phi_{\text{vib}} N_{\text{colls}} \Phi(q) f(\tilde{\epsilon}_g)\, \Phi\left(q' | \tilde{\epsilon}_{\text{ex}}\right) d\tilde{\epsilon}_g.$$

Similarly, the number of relaxing collisions of class $\tilde{\epsilon}'_g$ that are also of class q' that result in a post-relaxation vibrational energy level q is

$$\phi_{\text{vib}} N_{\text{colls}} \Phi\left(q'\right) f\left(\tilde{\epsilon}'_g\right) \Phi\left(q | \tilde{\epsilon}_{\text{ex}}\right) d\tilde{\epsilon}'_g.$$

Again, detailed balancing is satisfied when ϕ_{vib} is constant.

As noted in §2.8, the vibrational collision number Z_{vib} generally decreases as temperature increases. At the molecular level, ϕ_{vib} should therefore increase as the collision energy increases. In hypersonic flowfields, variations in Z_{vib} can be large. When simulating the hypersonic flow of a real gas, a variable-ϕ_{vib} model should therefore be used to capture such behaviour. As for rotational energy exchange, the implementation of a variable-ϕ_{vib} model must consider detailed balancing. Again, either a time-averaged ϕ_{vib} can be used for each cell [9], or as noted by Vijayakumar *et al.* [147], the method of Abe [1] can be used.

Lord [112] developed BL exchange procedures for anharmonic oscillators with the Morse potential. As noted above, the BL method is phenomenological and does not capture the detailed physical behaviour of vibrational energy exchange. Several alternative methods have been proposed to capture VT energy exchange more accurately at the molecular level. Boyd [31, 30] developed a level-to-level transition model for harmonic oscillators based on the Landau-Teller theory [102]. This model used a variable-ϕ_{vib} where

$\phi_{\text{vib}} = \phi_{\text{vib}}(\epsilon_g)$. Another level-to-level transition model that included both VT and VV transitions was introduced by Abe [2] for harmonic oscillators.

At high temperatures, multiple quantum level transitions become common. BL procedures do allow multiple quantum level transitions, but are phenomenological and are not based on the detailed physics of the exchange processes. Boyd [35], Koura [96] and Vijayakumar *et al.* [147] have proposed VT transfer models that capture multiple level transitions by considering the detailed physics of the exchange process. Gimelshein *et al.* [68] introduced a multiple level transition model for both VT and VV transfers.

The number of methods proposed for modelling vibrational energy exchange emphasises the importance of such processes in high temperature gas dynamics. The BL method remains the most common method for modelling VT energy transfer, which is probably due to its relative simplicity and computational efficiency relative to the alternative models. A comprehensive review of vibrational energy transfer models for DSMC calculations has not been performed.

According to Boyd [28], variable-ϕ models generally increase the degree of thermal and chemical non-equilibrium in a flowfield, as compared to constant ϕ models. This may be due to the decrease in ϕ_{rot} as temperature increases, which would increase the extent of rotational non-equilibrium. At high temperatures ϕ_{vib} increases, but it seems that the decreased rotational relaxation rate has a more marked effect on the extent of non-equilibrium than the accompanying increase in the vibrational relaxation rate. These significant effects should be captured when simulating high temperature reacting real gas flows, so variable-ϕ models are required.

4.6 Validating the DSMC method

Harvey and Gallis [81] have provided a comprehensive review of DSMC code validation studies for high speed rarefied flows. To date, most validation studies have been performed for flows without chemistry or ionisation. For such flows, the available experimental results suggest that accurate results can be obtained with the DSMC method. For reacting and ionising flows, there is little experimental data, and validation of the DSMC method for such flows is incomplete. Testing and validation efforts for chemically reacting flows are discussed briefly in §6.9.

CHAPTER 5

Molecular reaction dynamics

5.1 Introduction and summary

Under the extreme conditions posed by hypersonic flight, intermolecular collisions may be sufficiently energetic to result in chemical reactions and ionisation. In general, the probability of a chemical reaction occurring between two colliding reactant molecules A and B, denoted P_R, is a function of the collision energy and the internal states of the colliding molecules. This probability may be written

$$P_R = P_R\left[\epsilon_g, (\boldsymbol{\epsilon}_{\text{int}})_{\text{A}}, (\boldsymbol{\epsilon}_{\text{int}})_{\text{B}}, S\right], \tag{5.1}$$

where $\epsilon_g = \tilde{m}g^2/2$ is the relative translational energy and $(\boldsymbol{\epsilon}_{\text{int}})_{\text{A}}$ and $(\boldsymbol{\epsilon}_{\text{int}})_{\text{B}}$ represent the rotational, vibrational and electronic energy states of the colliding molecules A and B. The steric factor S accounts for the relative orientations of the collision partners, and reflects the fraction of collisions with effective orientations [157]. In general P_R is very low, such that the rate of reactive collisions is orders of magnitude lower than the collision rate. It is important to note that P_R is usually estimated from measured reaction rates. Actual calculation of P_R requires detailed quantum mechanical computations, which have been performed for simple reactions only.

The activation energy of a reaction, denoted ϵ_a, is the energy threshold that must be overcome to result in a chemical reaction. The characteristic reaction temperature Θ_a is defined by $\Theta_a \equiv \epsilon_a/k$. It is also useful to define a reduced activation energy by $\tilde{\epsilon}_a \equiv \epsilon_a/(kT) = \Theta_a/T$.

This chapter briefly discusses some aspects of molecular reaction dynamics. The symmetrical diatomic dissociating gas, which is of considerable interest in hypersonics, has been examined in particular detail. The dissociation of A_2 molecules in a mixture of A_2 molecules and A atoms is described by the net reaction

$$A_2 \rightleftharpoons A + A,$$

and proceeds via the two elementary reactions

$$\begin{aligned} &\text{Reaction 1:} \quad \mathrm{A_2 + A} \rightleftharpoons \mathrm{A + A + A} \quad \text{and} \\ &\text{Reaction 2:} \quad \mathrm{A_2 + A_2} \rightleftharpoons \mathrm{A + A + A_2}. \end{aligned}$$

The activation energy of the dissociation reaction is the bond dissociation energy [148], denoted here by ϵ_d. The characteristic dissociation temperature Θ_d is defined by $\Theta_d \equiv \epsilon_d/k$ and the reduced dissociation energy by $\tilde{\epsilon}_d \equiv \epsilon_d/(kT) = \Theta_d/T$.

5.2 The equilibrium constant

The equilibrium constant K^* for the symmetrical diatomic dissociating gas is given by

$$K^* = [\mathrm{A}]^{*2}/[\mathrm{A_2}]^*,$$

where $[s]^*$ denotes the molar concentration of species s at equilibrium. In this case, K^* has units of $\mathrm{kmol/m^3}$. The equilibrium constant can be obtained from statistical mechanics by evaluation of the molecular partition functions. In terms of the partition functions, denoted Q^{A} and Q^{AA} for atomic and diatomic molecules respectively, the equilibrium constant for a symmetrical diatomic gas is [21]

$$K^* = \frac{\left(Q^{\mathrm{A}}\right)^2}{Q^{\mathrm{AA}}} \frac{\exp\left(-\tilde{\epsilon}_d\right)}{V\mathcal{N}}.$$

Here V is the system volume. The most common form of the equilibrium constant is

$$K_c^*(T) = C^*(T/\Theta_a)^{\eta^*} \exp\left(-\Theta_a/T\right). \tag{5.2}$$

The dependence of K_c^* on T alone, as indicated by Eq. 5.2, is an approximation only. In reality K^* has a number density dependence, which is due to the effects of the electronic partition function. The effects are most significant under low density and high temperature conditions, as discussed by Gupta *et al.* [70] and Park [138]. Gupta *et al.* give curve fits of the form

$$\ln\left[K_{\mathrm{G}}^*(T,n)\right] = \sum_{i=0}^{5} G_i^*(n) Z^i \quad \text{where} \quad Z = \ln\left(10^4/T\right) \tag{5.3}$$

for the common reactions in air chemistry. The curve fit coefficients $G_i^*(n)$ have a number density dependence, and are tabulated for various reactions at a range of number densities [70]. Park [138] also gives a curve fit expression similar to Eq. 5.3.

5.3 Bimolecular reactions

Consider the general bimolecular reaction

$$\mathrm{A} + \mathrm{B} \rightarrow \text{products}, \tag{5.4}$$

which describes both dissociation and exchange reactions. By convention, the forward direction is the direction which the largest activation energy ϵ_a. Here, the rate of the forward reaction is denoted k^+, and the rate of the reverse reaction is denoted k^-.

The reaction rate describes the rate of change in the concentration of reactant species. If the general reaction of Eq. 5.4 describes the forward reaction direction in which species A is consumed, then the rate of change in the molar concentration of species A is

$$\frac{d[\mathrm{A}]}{dt} = -k^+[\mathrm{A}][\mathrm{B}].$$

For bimolecular reactions, k^+ has units of $\mathrm{m}^3/\mathrm{kmol/s}$. In terms of number densities,

$$\frac{dn_\mathrm{A}}{dt} = -\frac{k^+ n_\mathrm{A} n_\mathrm{B}}{\mathcal{N}}. \tag{5.5}$$

The modified Arrhenius rate equation

$$k^+ \propto T^{\eta^+} \exp\left[-\epsilon_a/(kT)\right]$$

is often used to approximate the forward rate k^+. Here, the convenient form

$$k^+ = C^+ \left(T/\Theta_a\right)^{\eta^+} \exp\left(-\Theta_a/T\right) \tag{5.6}$$

has been adopted, so that C^+ has the same units as k^+. Usually, the modified Arrhenius equation is simply called the Arrhenius equation. The Arrhenius equation is empirical, and the parameters C^+ and η^+ are obtained by correlation against experimental measurements. For the reactions of interest in hypersonics, these parameters are generally available in the literature for moderate temperatures. For the dissociating nitrogen system, some published rates are compared in §B.3.

Consider the general diatomic dissociation reaction

$$\mathrm{AB} + \mathrm{M} \rightarrow \mathrm{A} + \mathrm{B} + \mathrm{M}. \tag{5.7}$$

In a diatomic gas, the vibrational excitation and dissociation processes are strongly coupled, because dissociation occurs preferentially for those molecules in higher vibrational energy levels [150]. Here, this effect is called dissociation-vibration (DV) coupling. Where DV coupling is present, those molecules that dissociate have a high population of upper vibrational energy levels, relative to the equilibrium distribution of vibrational energy lev-

els. This biased distribution is due to the preferential dissociation of vibrationally excited molecules. Although DV coupling is known to be important for dissociation reactions, little quantitative information on the extent of coupling is actually available [150].

DV coupling significantly affects dissociation rates where vibrational non-equilibrium exists. For example, the dissociation rate immediately downstream of a strong shock is quite low despite the high translational temperature, because the downstream gas is in a vibrationally cold state. This produces a region in which there is minimal dissociation, called the dissociation incubation region. Actually determining the extent of this incubation region is somewhat subjective [82]. As collisions occur, energy is transferred to the vibrational mode, and significant dissociation then takes place. The delay in dissociation caused by DV coupling significantly affects the post-shock conditions. DV coupling results in the depletion of molecules with high vibrational energies. This depletion reduces the mean vibrational energy of the remaining diatomic molecules, and slows further vibrational energy exchange and thus further dissociation.

Numerous two-temperature reaction rate models have been introduced to capture DV coupling in macroscopic studies. A review has been conducted by Losev [114]. In hypersonic applications, the simple empirical two-temperature model of Park [137] is often used. This two-temperature model uses an effective temperature T_e, defined by

$$T_e \equiv T_{\text{vib}}^{1-s} T_{\text{tr+rot}}^{s} = \left(\frac{T_{\text{vib}}}{T_{\text{tr+rot}}} \right)^{1-s} T_{\text{tr+rot}} \tag{5.8}$$

where s is a constant that controls the extent of DV coupling. This effective temperature T_e replaces the thermodynamic temperature T in the Arrhenius rate of Eq. 5.6, to give the two-temperature rate

$$k_{2T}^{+}\left(T_{\text{tr+rot}}, T_{\text{vib}}, s\right) = C^{+}(T_e/\Theta_d)^{\eta^{+}} \exp\left(-\Theta_d/T_e\right). \tag{5.9}$$

The constant s in Eq. 5.8 typically ranges between 0.5 and 0.7. Lower s values correspond to higher degrees of DV coupling. When $s = 1$, T_{vib} has no direct effect on the reaction rate. Eq. 5.8 shows that T_e can be described in terms of the kinetic temperature of translation and rotation $T_{\text{tr+rot}}$ adjusted by the ratio $(T_{\text{vib}}/T_{\text{tr+rot}})^{1-s}$ that accounts for the DV coupling effect. Vibrationally cold flows have $T_{\text{vib}}/T_{\text{tr+rot}} < 1$, and vibrationally hot flows have $T_{\text{vib}}/T_{\text{tr+rot}} > 1$. At thermal equilibrium, $T_{\text{vib}} = T_{\text{tr+rot}} = T$, and the two-temperature rate reduces to the Arrhenius form of Eq. 5.6.

5.4 Recombination reactions

An atomic recombination reaction involves the formation of a diatomic molecule AB from the two atoms A and B. According to Kondrat'ev [93], upon collision between the atoms A and B, a quasi-molecule A·B forms, which will decompose spontaneously unless stabilised.

Stabilisation requires the removal of some energy, and can occur either by radiation or by collision with a third body M. Generally, stabilisation by collision occurs in air chemistry. Consequently, recombination reactions are generally considered to be termolecular, with the general form

$$\mathrm{AB} + \mathrm{M} \leftarrow \mathrm{A} + \mathrm{B} + \mathrm{M}. \tag{5.10}$$

For recombination reactions, $\epsilon_a = 0$ [148]. The recombination rate k^- describes the rate of change in the concentration of molecular species AB by

$$\frac{d[\mathrm{AB}]}{dt} = k^-[\mathrm{A}][\mathrm{B}][\mathrm{M}].$$

The units of k^- are $\mathrm{m}^6/\mathrm{kmol}^2/\mathrm{s}$. In terms of number densities,

$$\frac{dn_\mathrm{A}}{dt} = \frac{k^- n_\mathrm{A} n_\mathrm{B} n}{\mathcal{N}^2}, \tag{5.11}$$

where $n = n_\mathrm{M}$ is the total number density. K^*, k^+ and k^- are related through

$$K^* = k^+/k^-. \tag{5.12}$$

The recombination rate k^- is often calculated from $k^- = k^+/K^*$.

As noted in §5.3, if the forward dissociation reaction $\mathrm{AB}+\mathrm{M} \rightarrow \mathrm{A}+\mathrm{B}+\mathrm{M}$ exhibits DV coupling, then those AB molecules that dissociate have a higher population of the upper vibrational levels than the equilibrium distribution. Therefore, from detailed balancing considerations, the recombination of atoms A and B forms AB molecules in which upper vibrational energy levels are over-populated relative to the equilibrium distribution.

5.5 Reaction frequencies and mean probabilities

For the general bimolecular reaction $\mathrm{A} + \mathrm{B} \rightarrow$ products, the number of reaction events occurring per unit volume per unit time is obtained from Eq. 5.5 and is

$$\dot{n}_R^+ = k^+ n_\mathrm{A} n_\mathrm{B}/\mathcal{N}.$$

From Eq. 2.37, the number of collisions occurring between the reactant species A and B, per unit volume per unit time is

$$\dot{n}_\mathrm{colls} = n_\mathrm{A}\nu_{\mathrm{A+B}}/f_s = n_\mathrm{A} n_\mathrm{B}\langle\sigma g\rangle_{\mathrm{A+B}}/f_s,$$

where f_s is a symmetry factor that is two for like molecules and unity otherwise. The mean forward bimolecular reaction probability $\langle P_R^+\rangle$ is then

$$\langle P_R^+\rangle = \frac{\dot{n}_R^+}{\dot{n}_\mathrm{colls}} = \frac{k^+ f_s}{\langle\sigma g\rangle_{\mathrm{A+B}}\,\mathcal{N}}. \tag{5.13}$$

From Eq. 5.11, the number of reactions for the recombination reaction AB + M $\leftarrow$ A + B + M, per unit volume per unit time, is

$$\dot{n}_R^- = k^- n_\mathrm{A} n_\mathrm{B} n / \mathcal{N}^2.$$

For collisions between A and B atoms the mean recombination probability is then

$$\langle P_R^- \rangle = \frac{\dot{n}_R^-}{\dot{n}_\mathrm{colls}} = \frac{k^- n f_s}{\langle \sigma g \rangle_{\mathrm{A+B}} \mathcal{N}^2}. \tag{5.14}$$

It is apparent that $\langle P_R^- \rangle$ depends on the local number density n.

5.6 Details of the symmetrical diatomic dissociating gas

This section gives some further details of the symmetrical diatomic dissociation gas, with the unbounded harmonic oscillator vibration model. The extent of dissociation in a symmetrical diatomic gas is described by the dissociation fraction α. The dissociation fraction is defined as the mass fraction of the atomic species, and is given by

$$\alpha \equiv \frac{x_\mathrm{A}}{x_\mathrm{A} + 2x_{\mathrm{A}_2}} = \frac{x_\mathrm{A}}{2 - x_\mathrm{A}},$$

where x_s is the mole fraction of species s. Some useful expressions relating ρ, α and n are

$$n_\mathrm{A} = \rho\alpha/m_\mathrm{A}, \quad n_{\mathrm{A}_2} = \rho(1-\alpha)/m_{\mathrm{A}_2}, \quad n = \rho(1+\alpha)/m_{\mathrm{A}_2} \quad \text{and} \quad \alpha = n m_{\mathrm{A}_2}/\rho - 1.$$

From Vincenti and Kruger [148], the net rate of change of α due to dissociation and recombination via both reactions 1 and 2 is given by

$$\frac{d\alpha}{dt} = \dot{\alpha}(\alpha, T, \rho) = \left(k_1^+ \alpha + k_2^+ \frac{1-\alpha}{2} \right) \frac{\rho}{\mathcal{M}_\mathrm{A}} \left(1 - \alpha - \frac{2\rho}{\mathcal{M}_\mathrm{A} K^*} \alpha^2 \right). \tag{5.15}$$

Here, k_1^+ and k_2^+ are the forward reaction rates for reactions 1 and 2 respectively, as defined in Eqs. 5.1, and $\mathcal{M}_\mathrm{A}$ is the molar mass of the atomic species in kg/kmol. At equilibrium, $\dot{\alpha} = 0$ and Eq. 5.15 gives

$$\frac{\alpha^{*2}}{1-\alpha^*} = \frac{\mathcal{M}_\mathrm{A} K^*}{2\rho}.$$

Therefore

$$\alpha^* = \left[\left(\beta^2 + 4\beta \right)^{\frac{1}{2}} - \beta \right] / 2 \quad \text{where} \quad \beta = \mathcal{M}_\mathrm{A} K^* / (2\rho).$$

If recombination rates are negligible, $[\mathrm{A}_2]^* \to 0$. Therefore $K^* \to \infty$ and $\dot{\alpha}$ can be approximated by

$$\dot{\alpha} \approx \frac{\rho(1-\alpha)}{\mathcal{M}_\mathrm{A}} \left(k_1^+ \alpha + k_2^+ \frac{1-\alpha}{2} \right). \tag{5.16}$$

Using the fully diatomic state at absolute zero as the reference state and ignoring

electronic excitation, the specific internal energy of a partially dissociated symmetrical diatomic gas is

$$e = \alpha e_{\mathrm{A}} + (1-\alpha) e_{\mathrm{A}_2} + e_{\mathrm{cp}}, \tag{5.17}$$

where e_s is the specific internal energy of species s and e_{cp} is the specific chemical potential energy. Each dissociation event requires an amount of energy $\epsilon_d = k\Theta_d$, so the total chemical potential energy E_{cp} in the mixture is

$$E_{\mathrm{cp}} = N_{\mathrm{A}} \epsilon_d / 2 = N_{\mathrm{A}} k \Theta_d / 2,$$

where N_A is the number of A atoms and $N_{\mathrm{A}}/2$ is the total number of dissociation events that have occurred relative to the reference state. The specific chemical potential energy is then

$$e_{\mathrm{cp}} = \frac{E_{\mathrm{cp}}}{m_{\mathrm{A}} \left(N_{\mathrm{A}} + 2N_{\mathrm{A}_2}\right)} = \frac{\alpha k \Theta_d}{m_{\mathrm{A}_2}} = \alpha R \Theta_d,$$

where $R = k/m_{\mathrm{A}_2}$ is the specific gas constant of the diatomic species. Eq. 5.17 can then be written

$$e = \alpha e_{\mathrm{A}} + (1-\alpha) e_{\mathrm{A}_2} + \alpha R \Theta_d.$$

Only the translational mode contributes to the specific internal energy of the atomic species, so

$$e_{\mathrm{A}} = 3 R_{\mathrm{A}} T_{\mathrm{tr}} / 2 = 3 R T_{\mathrm{tr}}.$$

Translational, rotational and vibrational modes all contribute to the specific internal energy of the diatomic species, so

$$e_{\mathrm{A}_2} = 3RT_{\mathrm{tr}}/2 + RT_{\mathrm{rot}} + \zeta_{\mathrm{vib}} RT_{\mathrm{vib}}/2.$$

Here it has been assumed that rotation is fully excited. Typically, the characteristic time scale of reactions $\tau_{\mathrm{chem}} \sim 1/\dot{\alpha}$ is much larger than the mean collision time, and also the characteristic times of rotational and vibrational relaxation. It may therefore be assumed that the system is always quite close to thermal equilibrium, even when the chemical processes are not at equilibrium. At thermal equilibrium, $T_{\mathrm{tr}} = T_{\mathrm{rot}} = T_{\mathrm{vib}} = T$, so

$$e = \left[\frac{5 + \alpha + (1-\alpha)\zeta_{\mathrm{vib}}}{2}\right] RT + \alpha R \Theta_d. \tag{5.18}$$

For unbounded harmonic oscillators, Eq. 2.24 gives

$$\zeta_{\mathrm{vib}} = \frac{2\Theta_{\mathrm{vib}}/T}{\exp\left(\Theta_{\mathrm{vib}}/T\right) - 1},$$

so Eq. 5.18 can be rearranged to give

$$(Ax + B)\exp(1/x) - Ax + C = 0 \tag{5.19}$$

where x, A, B and C are non-dimensional parameters given by

$$x = T/\Theta_{\text{vib}}, \quad A = (5+\alpha)/2, \quad B = \left(\alpha\Theta_d - e/R\right)/\Theta_{\text{vib}} \quad \text{and} \quad C = 1-\alpha-B.$$

Eq. 5.19 can be solved numerically to obtain the temperature of a system at thermal equilibrium with a known specific internal energy e and dissociation fraction α. When using Newton's method [99] to solve Eq. 5.19, the $(n+1)$th estimate of x is given by

$$x_{n+1} = x_n - f(x)/f'(x),$$

where

$$f(x) = (Ax+B)\exp(1/x) - Ax + C \quad \text{and} \quad f'(x) = \exp(1/x)\left(A - A/x - B/x^2\right) - A.$$

The specific enthalpy h is given by

$$h = e + \frac{p}{\rho} = e + (1+\alpha)RT = \left[\frac{7+3\alpha+(1-\alpha)\zeta_{\text{vib}}}{2}\right]RT + \alpha R\Theta_d. \tag{5.20}$$

For a given h and α, T can be obtained by solving Eq. 5.19 numerically with

$$x = T/\Theta_{\text{vib}}, \quad A = (7+3\alpha)/2, \quad B = \left(\alpha\Theta_d - h/R\right)/\Theta_{\text{vib}} \quad \text{and} \quad C = 1-\alpha-B.$$

CHAPTER 6

Conventional DSMC chemistry models

6.1 Introduction and summary

As noted in Chapter 4, one important advantage of the DSMC method is that it permits modelling of gas flow phenomena at the molecular level. In principle, gas models with any degree of physical complexity can be used, including chemical reactivity. When simulating chemical reactions with the DSMC method, the reaction probability P_R is usually calculated at each collision in which the particle energies exceed a reaction energy threshold. A reaction is performed if $R_f < P_R$. Reaction simulation is therefore an integral part of the collision routine. Here the models used for calculating P_R are called conventional DSMC chemistry models.

The formulation of an accurate general function for P_R that includes the parameters incorporated in Eq. 5.1 depends on a detailed knowledge of the actual state-dependent reaction cross-sections. For the species typically of interest in hypersonics, knowledge of these cross-sections is very limited [81, 154]. Furthermore, if such cross-section were actually available, implementation in a DSMC code could impose a prohibitive computational overhead. Consequently, conventional DSMC chemistry models usually rely on an expression for P_R that plausibly approximates the expected real gas behaviour, within the limitations of mathematical tractability, numerical stability and computational efficiency, and recovers a suitable macroscopic rate in the equilibrium limit. Although conventional DSMC chemistry models simulate chemistry at the molecular level, the approach is clearly phenomenological in nature.

Several conventional DSMC chemistry models have been devised, and detailed reviews have been provided by Wadsworth and Wysong [150] and Boyd [38]. Ivanov and Gimelshein [88] also give a brief review. It is interesting to note that there have been relatively few developments in modelling chemistry with the DSMC method in the last decade. This may be due to the lack of detailed experimental data with which to validate the existing conventional DSMC chemistry models.

This chapter examines several conventional DSMC chemistry models for bimolecular and recombination reactions. The total collision energy (TCE) model, the vibrationally favoured dissociation (VFD) model, the threshold line dissociation (TLD) model and three

recombination models are considered in detail. Procedures for modelling reaction mechanics and detailed balancing issues are also discussed.

Conventional DSMC chemistry models have been developed primarily for the VHS collision model. In several of the treatments in this chapter, the fraction of reactive collisions for VHS molecules in binary collisions is required. This equals the mean bimolecular reaction probability, and is denoted $\langle P_R^+ \rangle_{\rm VHS}$. From Eq. 5.13, the mean bimolecular reaction probability is given by

$$\langle P_R^+ \rangle = \frac{\dot{n}_R^+}{\dot{n}_{\rm colls}} = \frac{k^+ f_s}{\langle \sigma g \rangle \mathcal{N}}.$$

For VHS molecules, Eq. 4.18 gives $\langle \sigma g \rangle = \Xi \left(T/T_r\right)^{\frac{1}{2}-\upsilon}$, so $\langle P_R^+ \rangle_{\rm VHS}$ is given by

$$\langle P_R^+ \rangle_{\rm VHS} = \frac{k^+ f_s}{\mathcal{N}\Xi} \left(\frac{T_r}{T}\right)^{\frac{1}{2}-\upsilon}. \tag{6.1}$$

6.2 Early DSMC chemistry models

The first application of a particle simulation method to model a chemically reacting flowfield was undertaken by Koura [94]. This study used a Monte Carlo method to examine non-equilibrium velocity distributions and reaction rates during zero-dimensional chemical relaxation. Although constant steric factors and structureless molecules were used, significant departures from equilibrium velocity distributions and reaction rates were observed.

Attempts at developing more detailed chemistry models for the DSMC method were made by Bird [14, 15]. In these early models, the forward reaction probability P_R^+ depended only on the relative translational energy in collisions ϵ_g, and was given by

$$P_R^+ \left(\epsilon_g\right) = \begin{cases} 0 & \text{for } \epsilon_g < \epsilon_a \\ \left(1 - \epsilon_a/\epsilon_g\right) \left(\epsilon_g/\epsilon_a - 1\right)^{\eta - \frac{1}{2}} & \text{for } \epsilon_g \geq \epsilon_a. \end{cases}$$

Here η is the Arrhenius temperature power from Eq. 5.6. This form of P_R^+ is similar to

$$\begin{aligned} P_R^+ &= 0 && \text{for } \epsilon_g < \epsilon^*, \\ P_R^+ &\propto \left(1 - \epsilon^*/\epsilon_g\right) \alpha \left(\epsilon_g - \epsilon^*\right) && \text{for } \epsilon_g \geq \epsilon^* \end{aligned}$$

as proposed by Light *et al.* [105] for the study of chemical kinetics. Here, ϵ^* is a threshold energy for the reaction, and the function α accounts for the deviation from hard sphere behaviour. Bird [15] simulated the flow of dissociating nitrogen downstream of a strong shock using this simple chemistry model. The DSMC calculations used the flow conditions from the shock tube experiments performed by Kewley and Hornung [91]. In the chemical relaxation region downstream of the shock, there was good agreement between the experimental density measurements and the DSMC predictions.

It must be noted that this shock case is not very useful for validating conventional DSMC chemistry models under non-equilibrium conditions, because the downstream gas

was essentially in a state of thermal equilibrium. Given that the derivation of the chemistry model depended on the recovery of the macroscopic rate equations, and that the rates employed were deduced by Kewley and Hornung [91] from the experimental results, it is not surprising that the DSMC solution of Bird [21] agreed with the experiments.

6.3 Total collision energy model

Bird [17] extended the early chemistry model with $P_R^+ = P_R^+(\epsilon_g)$ to include contributions from internal energy modes. It was assumed that all energy modes of the two particles A and B participating in a collision contributed to the probability of reaction, with no biasing towards any particular energy mode. Thus the form of P_R^+ depended only on the total collision energy

$$\epsilon_c = \epsilon_g + (\epsilon_{\text{int}})_{\text{A}} + (\epsilon_{\text{int}})_{\text{B}}\,.$$

This model is often called the total collision energy (TCE) chemistry model [74], and is the most common DSMC chemistry model [38, 154]. The TCE model was originally developed for the IPL potential, and was extended to the VHS model by Bird [18]. It was formulated to recover the Arrhenius rate equation of Eq. 5.6 at thermal equilibrium. As discussed below, when a quantised vibration model is used, the TCE model does not recover the Arrhenius rates.

In the TCE model, the form of $\left(P_R^+\right)_{\text{TCE}}$ is assumed to be

$$\begin{aligned}\left(P_R^+\right)_{\text{TCE}}(\epsilon_c) &= \beta_{\text{TCE}}\left(1-\frac{\epsilon_a}{\epsilon_c}\right)^{\chi_1}\left(\frac{\epsilon_c}{\epsilon_a}-1\right)^{\chi_2} = \beta_{\text{TCE}}\frac{(\epsilon_c-\epsilon_a)^{\chi_1+\chi_2}}{\epsilon_c^{\chi_1}\epsilon_a^{\chi_2}} \\ &= \beta_{\text{TCE}}\left(1-\frac{\tilde{\epsilon}_a}{\tilde{\epsilon}_c}\right)^{\chi_1}\left(\frac{\tilde{\epsilon}_c}{\tilde{\epsilon}_a}-1\right)^{\chi_2} = \beta_{\text{TCE}}\frac{(\tilde{\epsilon}_c-\tilde{\epsilon}_a)^{\chi_1+\chi_2}}{\tilde{\epsilon}_c^{\chi_1}\tilde{\epsilon}_a^{\chi_2}}\end{aligned} \tag{6.2}$$

for $\epsilon_c \geq \epsilon_a$. When $\epsilon_c < \epsilon_a$, $\left(P_R^+\right)_{\text{TCE}} = 0$. For mathematical tractability, Bird [17] used

$$\chi_1 = 1 - \upsilon + \bar{\zeta}_{\text{int}}, \tag{6.3}$$

where $\bar{\zeta}_{\text{int}}$ is the mean internal DOF in the colliding particles from Eq. 4.14. For the unbounded harmonic oscillator vibration model, for which ζ_{vib} is given by Eq. 2.24, $\bar{\zeta}_{\text{int}}$ and thus χ_1 depend on temperature only. The continuous equilibrium distribution of $\tilde{\epsilon}_c$ for VHS molecules from Eq. 4.13 becomes

$$f(\tilde{\epsilon}_c) = \tilde{\epsilon}_c^{\chi_1}\exp(-\tilde{\epsilon}_c)/\Gamma(\chi_1+1)\,. \tag{6.4}$$

§C.5 gives details of the method used to derive expressions for the non-dimensional parameters β_{TCE} and χ_2 in terms of the Arrhenius rate parameters C^+ and η^+ and the

VHS parameters. The resulting expressions are

$$\chi_2 = \eta^+ + \upsilon - \frac{1}{2} \quad \text{and} \quad \beta_{\text{TCE}} = \frac{C^+ f_s}{\mathcal{N}\Xi}\left(\frac{T_r}{\Theta_a}\right)^{\frac{1}{2}-\upsilon}\frac{\Gamma(\chi_1+1)}{\Gamma(\chi_1+\chi_2+1)}. \tag{6.5}$$

The VHS parameters υ, Ξ and T_r all refer to collisions between particles A and B. Eq. 4.14 shows that $\bar{\zeta}_{\text{int}}$ depends on ζ_{vib} of each particle participating in the collision. The effective number of vibrational DOF ζ_{int} can be assumed to be a constant value characteristic of the flowfield temperature [72]. Alternatively, using Eq. 2.24, $\bar{\zeta}_{\text{int}}$ could be calculated for each cell using the local vibrational temperature T_{vib} calculated from a time-averaged value of $\langle\epsilon_{\text{vib}}\rangle$. This alternative method was used by Lilley and Macrossan [110] and has been used in this study.

The TCE reaction probability $\left(P_R^+\right)_{\text{TCE}}$ is calculated for each collision pair with $\epsilon_c > \epsilon_a$. It is the probability of the collision resulting in a reaction. Here the TCE model has been used to model the dissociation of a symmetrical diatomic gas. In $A_2 + A_2$ collisions, either particle could be dissociated if $R_f < \left(P_R^+\right)_{\text{TCE}}$, but for simplicity the first collision partner is dissociated. In $A_2 + A$ collisions, the diatom dissociated if $R_f < \left(P_R^+\right)_{\text{TCE}}$, regardless of whether it is the first or second particle in the collision pair. This is an important point. For computational efficiency, Haas [71] suggested that $\left(P_R^+\right)_{\text{TCE}}$ should only be calculated if the first particle in the collision pair is diatomic. On average, this will be the case in only half of the $A_2 + A$ collisions. Therefore the TCE dissociation probability obtained above for $A_2 + A$ collisions must be doubled to compensate. This results in

$$\beta_{\text{TCE}} = \frac{2C^+}{\mathcal{N}\Xi}\left(\frac{T_r}{\Theta_a}\right)^{\frac{1}{2}-\upsilon}\frac{\Gamma(\chi_1+1)}{\Gamma(\chi_1+\chi_2+1)}$$

for both $A_2 + A_2$ and $A_2 + A$ collisions.

6.3.1 Advantages and disadvantages of the TCE model

The main advantages of the TCE model are that it is relatively simple and that it uses Arrhenius rate parameters that are generally available for the species of interest in hypersonics. However, the TCE model suffers from several disadvantages, as discussed below.

Apart from the fact that the form of $\left(P_R^+\right)_{\text{TCE}}$ was selected for mathematical tractability and computational efficiency, the most serious problem with the TCE model is that it does not include any biasing of $\left(P_R^+\right)_{\text{TCE}}$ for any particular energy mode. Consequently, the TCE model cannot capture the DV coupling behaviour that is important in dissociation reactions. This issue has prompted the introduction of conventional DSMC chemistry models that can capture DV coupling, as discussed in §6.4.

In common with the original TCE model of Bird [17, 18], the present implementation of the TCE model assumes that all internal energy modes of both colliding particles contribute to the total collision energy ϵ_c. As noted by Vincenti and Kruger [148], only some internal energy modes can contribute to the reaction. Hash and Hassan [83] used a

version of the TCE model in which half of the rotational and vibrational energy contributed to ϵ_c. A similar approach was used by Wadsworth and Wysong [150].

The expressions for β_{TCE} and χ_2 are derived using equilibrium energy distributions. The TCE model assumes that these same expressions can be used to calculate $\left(P_R^+\right)_{\text{TCE}}$ under non-equilibrium conditions. However, there is no way of verifying that this assumption is suitable.

The form of $\left(P_R^+\right)_{\text{TCE}}$ causes some numerical instabilities and physically unrealistic effects for certain values of χ_1 and χ_2. Consider Eq. 6.2, which may be written

$$\left(P_R^+\right)_{\text{TCE}} \propto (\epsilon_c - \epsilon_a)^{\chi_1+\chi_2}\, \epsilon_c^{-\chi_1}.$$

Firstly, when $\chi_1 + \chi_2 < 0$, then $\left(P_R^+\right)_{\text{TCE}} \to \infty$ as $\epsilon_c - \epsilon_a \to 0^+$ [43, 21]. This unbounded reaction probability is physically unrealistic. It exists when $\chi_1 + \chi_2 = \eta^+ + \bar{\zeta}_{\text{int}} + \frac{1}{2} < 0$. For reactions in high temperature air, $-3.5 \lesssim \eta^+ \lesssim 0$ [138], so this singularity can occur. Secondly, as $\epsilon_c \to \infty$, then $\left(P_R^+\right)_{\text{TCE}} \propto \epsilon_c^{\chi_2}$. For $\chi_2 > 0$, then $\left(P_R^+\right)_{\text{TCE}} \to \infty$ as $\epsilon_c \to \infty$. From Eq. 6.5, $\chi_2 = \eta^+ - 0.25$ for typical $\upsilon = 0.25$. For air chemistry, χ_2 is typically negative, so this problem with unbounded $\left(P_R^+\right)_{\text{TCE}}$ at high ϵ_c is usually avoided. Finally, when $\chi_2 < 0$ then $\left(P_R^+\right)_{\text{TCE}} \to 0$ as $\epsilon_c \to \infty$ [21]. This means that $\left(P_R^+\right)_{\text{TCE}}$ has a maximum at some ϵ_c value. According to Bird [21], this is realistic behaviour, although it might be expected that $\left(P_R^+\right)_{\text{TCE}}$ should approach unity in high energy collisions.

As noted by Gimelshein *et al.* [66, 67] and Lilley and Macrossan [110], the TCE model gives rates that differ significantly from the expected Arrhenius rates when a quantised vibration model is used. The differences arise because the TCE parameters χ_2 and β_{TCE} are derived by assuming that all molecular energy modes are distributed according to the continuous Boltzmann distribution of Eq. 2.16. However, when a quantised vibration model is used, the actual distribution of total collision energies differs from the assumed distribution, giving rates that differ from the expected Arrhenius rates. Gimelshein *et al.* [66, 67] examined this issue for bimolecular reactions, and proposed procedures to account for the use of discrete distributions and recover the desired Arrhenius rates at equilibrium.

6.3.2 An alternative version of the TCE model

Boyd and Stark [43] introduced an alternative form of P_R^+ for the TCE model, given by

$$P_R^+ = \beta \frac{k^+(T)}{\exp\left(-\tilde{\epsilon}_a\right)} \left(1 - \frac{\tilde{\epsilon}_a}{\tilde{\epsilon}_c}\right)^{\chi_1},$$

which explicitly includes the forward rate $k^+(T)$. Following the method used in §C.5 for obtaining β_{TCE}, it can be shown that

$$\beta = \frac{f_s}{\mathcal{N}\Xi} \left(\frac{T_r}{T}\right)^{\frac{1}{2}-\upsilon}$$

for this alternative form of P_R^+. Assuming that the thermodynamic temperature T can be replaced by an appropriate kinetic temperature T_k, this form of P_R^+ allows any rates $k^+(T_k)$ to be used. To use this method, the local kinetic temperature must be calculated for each cell, and presumably this would be a time-averaged kinetic temperature. According to Boyd and Stark [43], this imposes a small extra computational overhead.

Hassan and Hash [84] extended the TCE chemistry model to the GHS collision model. The resulting expression for P_R^+ includes additional terms. No DSMC studies using this GHS chemistry model appear in the refereed literature. This is probably because the GHS model is only required at low temperatures where flowfield chemistry is usually absent.

6.3.3 Mean reaction probabilities for nitrogen

It is instructive to examine the fraction of collisions in which the total collision energy ϵ_c exceeds the activation energy ϵ_a, the fraction of such collisions that result in a reaction, and the fraction of all collisions that result in a reaction. Although this analysis is performed here for an equilibrium gas composed of VHS molecules with the TCE chemistry model, the results are indicative of the behaviour of a real gas, and shows that few collisions result in a reaction. Nitrogen has been used as a test case, with the VHS parameters from Table B.1 and the dissociation rates of Kewley and Hornung [91] from Table B.3.

Firstly, the fraction of collisions in which ϵ_c exceeds ϵ_a is the same as the fraction with $\tilde{\epsilon}_c > \tilde{\epsilon}_a$. Here this fraction is denoted $F_{\tilde{\epsilon}_c>\tilde{\epsilon}_a}$. With $f(\tilde{\epsilon}_c)$ from Eq. 6.4,

$$F_{\tilde{\epsilon}_c>\tilde{\epsilon}_a} = \int_{\tilde{\epsilon}_a}^{\infty} f(\tilde{\epsilon}_c)\, d\tilde{\epsilon}_c = \frac{1}{\Gamma(\chi_1+1)} \int_{\tilde{\epsilon}_a}^{\infty} \tilde{\epsilon}_c^{\chi_1} \exp(-\tilde{\epsilon}_c)\, d\tilde{\epsilon}_c = \frac{\Gamma(\chi_1+1, \tilde{\epsilon}_a)}{\Gamma(\chi_1+1)}.$$

The distribution of $\tilde{\epsilon}_c$ for collisions with $\tilde{\epsilon}_c > \tilde{\epsilon}_a$ is given by re-normalising $f(\tilde{\epsilon}_c)$ and is

$$[f(\tilde{\epsilon}_c)]_{\tilde{\epsilon}_c>\tilde{\epsilon}_a} = \tilde{\epsilon}_c^{\chi_1} \exp(-\tilde{\epsilon}_c) / \Gamma(\chi_1+1, \tilde{\epsilon}_a), \quad \text{where} \quad \tilde{\epsilon}_a < \tilde{\epsilon}_c < \infty.$$

With the TCE model, the fraction of collisions with $\tilde{\epsilon}_c > \tilde{\epsilon}_a$ that result in a reaction is then

$$\begin{aligned} F^R_{\tilde{\epsilon}_c>\tilde{\epsilon}_a} &= \int_{\tilde{\epsilon}_a}^{\infty} \left(P_R^+\right)_{\mathrm{TCE}} [f(\tilde{\epsilon}_c)]_{\tilde{\epsilon}_c>\tilde{\epsilon}_a}\, d\tilde{\epsilon}_c \\ &= \frac{\beta_{\mathrm{TCE}}}{\Gamma(\chi_1+1, \tilde{\epsilon}_a)\, \tilde{\epsilon}_a^{\chi_2}} \int_{\tilde{\epsilon}_a}^{\infty} (\tilde{\epsilon}_c - \tilde{\epsilon}_a)^{\chi_1+\chi_2} \exp(-\tilde{\epsilon}_c)\, d\tilde{\epsilon}_c \\ &= \frac{\beta_{\mathrm{TCE}} \exp(-\tilde{\epsilon}_a)}{\tilde{\epsilon}_a^{\chi_2}} \frac{\Gamma(\chi_1+\chi_2+1)}{\Gamma(\chi_1+1, \tilde{\epsilon}_a)}. \end{aligned}$$

Here the definite integral was evaluated with Eq. A.1. The fraction of all collisions that result in a reaction is simply the mean VHS reaction probability $\langle P_R^+ \rangle_{\mathrm{VHS}}$ from Eq. 6.1. The product $F_{\tilde{\epsilon}_c>\tilde{\epsilon}_a} \times F^R_{\tilde{\epsilon}_c>\tilde{\epsilon}_a}$ gives $\langle P_R^+ \rangle_{\mathrm{VHS}}$, and verifies the above expressions for $F_{\tilde{\epsilon}_c>\tilde{\epsilon}_a}$ and $F^R_{\tilde{\epsilon}_c>\tilde{\epsilon}_a}$. For nitrogen, Fig. 6.1 shows $F_{\tilde{\epsilon}_c>\tilde{\epsilon}_a}$, $F^R_{\tilde{\epsilon}_c>\tilde{\epsilon}_a}$ and $\langle P_R^+ \rangle_{\mathrm{VHS}}$. Even at very high temperatures, the number of collisions resulting in reaction is ~1%.

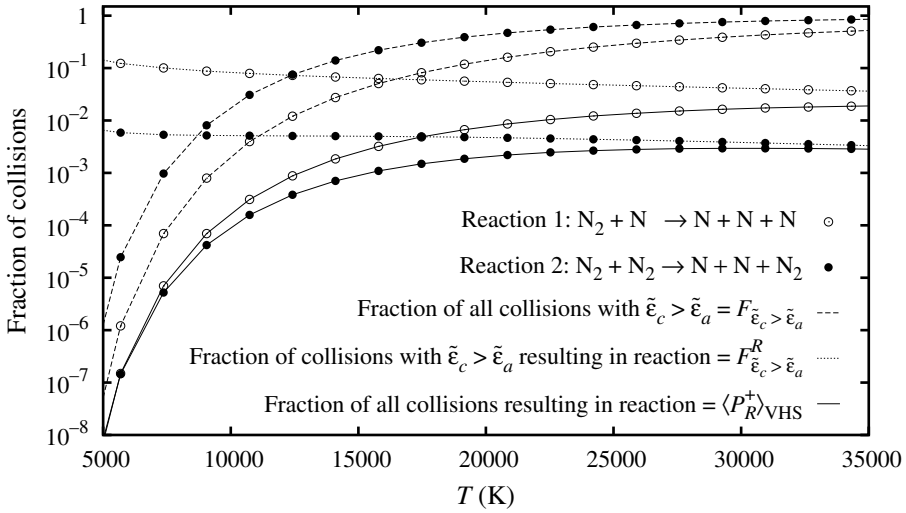

Figure 6.1: Mean reaction probabilities for nitrogen dissociation reactions with the TCE model at thermal equilibrium. The VHS parameters from Table B.1 and the rates of Kewley and Hornung [91] have been used. The activation energy ϵ_a is the dissociation energy $\epsilon_d = k\Theta_d = 113200k$.

6.4 Modelling dissociation-vibration coupling

The physical importance of dissociation-vibration (DV) coupling for the general dissociation reaction

$$\text{AB} + \text{M} \rightarrow \text{A} + \text{B} + \text{M}$$

was discussed in §5.3. To accurately model dissociating gas flows with the DSMC method, this behaviour must be captured, and several conventional chemistry models have been proposed. The various models have been compared by Wysong *et al.* [155, 154] and Wadsworth and Wysong [149, 150]. Here, the vibrationally favoured dissociation and threshold line dissociation models are considered in detail. Other models that can capture DV coupling are also discussed briefly in §6.6.

6.4.1 Vibrationally favoured dissociation model

Haas and Boyd [73, 74] proposed the vibrationally favoured dissociation (VFD) model in an attempt to capture DV coupling phenomena in diatomic gases. Different expressions for the VFD dissociation probability $\left(P_R^+\right)_{\text{VFD}}$ were proposed for anharmonic and harmonic oscillators. These expressions explicitly included a dependence on the vibrational energy of the particle AB being tested for dissociation. The VFD model attempts to recover the Arrhenius rate equation of Eq. 5.6 at thermal equilibrium. Only the version for unbounded harmonic oscillators is examined here, for which

$$\left(P_R^+\right)_{\text{VFD}} \propto \frac{\left(\epsilon_c - \epsilon_d\right)^{\psi}}{\epsilon_c^{\phi+\zeta_c/2-1}} \epsilon_{\text{vib}}^{\phi} \tag{6.6}$$

when $\epsilon_c \geq \epsilon_d$. When $\epsilon_c < \epsilon_a$, $\left(P_R^+\right)_{\rm VFD} = 0$. Here, $\epsilon_{\rm vib}$ is the vibrational energy of the diatomic molecule AB and ζ_c is the DOF in the total collision energy ϵ_c. The parameter ψ depends on the VHS parameters, the DOF of the colliding particles and the Arrhenius rate parameters. The free parameter ϕ controls the degree of DV coupling. For VHS molecules,

$$\begin{aligned} \phi + \zeta_c/2 - 1 &= \phi + \left[\zeta_g + (\zeta_{\rm rot})_{\rm AB} + (\zeta_{\rm vib})_{\rm AB} + (\zeta_{\rm rot})_{\rm M} + (\zeta_{\rm vib})_{\rm M}\right]/2 - 1 \\ &= \phi + \zeta_g/2 + \bar{\zeta}_{\rm int} - 1 \;=\; \phi + 1 - \upsilon + \bar{\zeta}_{\rm int} \\ &= \phi + \chi_1. \end{aligned}$$

Eq. 6.6 can be written in the convenient forms

$$\begin{aligned} \left(P_R^+\right)_{\rm VFD} &= \beta_{\rm VFD}\,\frac{(\epsilon_c/\epsilon_d - 1)^{\psi}}{(\epsilon_c/\epsilon_d)^{\phi+\chi_1}}\left(\frac{\epsilon_{\rm vib}}{\epsilon_d}\right)^{\phi} = \beta_{\rm VFD}\,\epsilon_d^{\chi_1-\psi}\,\frac{(\epsilon_c - \epsilon_d)^{\psi}}{\epsilon_c^{\phi+\chi_1}}\epsilon_{\rm vib}^{\phi} \\ &= \beta_{\rm VFD}\,\frac{(\tilde{\epsilon}_c/\tilde{\epsilon}_d - 1)^{\psi}}{(\tilde{\epsilon}_c/\tilde{\epsilon}_d)^{\phi+\chi_1}}\left(\frac{\tilde{\epsilon}_{\rm vib}}{\tilde{\epsilon}_d}\right)^{\phi} = \beta_{\rm VFD}\,\tilde{\epsilon}_d^{\chi_1-\psi}\,\frac{(\tilde{\epsilon}_c - \tilde{\epsilon}_d)^{\psi}}{\tilde{\epsilon}_c^{\phi+\chi_1}}\tilde{\epsilon}_{\rm vib}^{\phi} \end{aligned} \tag{6.7}$$

in which the parameter $\beta_{\rm VFD}$ is non-dimensional. The objective is to obtain expressions for $\beta_{\rm VFD}$ and ψ. These are derived in §C.6 and the results are

$$\begin{aligned} \psi &= \eta^+ + \upsilon - \frac{1}{2} + \chi_1 \;=\; \chi_1 + \chi_2 \quad \text{and} \\ \beta_{\rm VFD} &= \frac{C^+ f_s}{\mathcal{N}\Xi}\left(\frac{T_r}{\Theta_d}\right)^{\frac{1}{2}-\upsilon}\frac{\Gamma\left(\phi+\chi_1+1\right)\Gamma\left(\zeta_{\rm vib}/2\right)}{\Gamma\left(\phi+\zeta_{\rm vib}/2\right)\Gamma(\psi+1)}. \end{aligned} \tag{6.8}$$

When $\phi = 0$ there is no DV coupling, resulting in $\beta_{\rm VFD} = \beta_{\rm TCE}$ and $\left(P_R^+\right)_{\rm VFD} = \left(P_R^+\right)_{\rm TCE}$.

Here the VFD dissociation probability $\left(P_R^+\right)_{\rm VFD}$ is evaluated for each collision pair with $\epsilon_c > \epsilon_d$. In $A_2 + A_2$ collisions, $\epsilon_{\rm vib}$ of the first diatom is used to calculate $\left(P_R^+\right)_{\rm VFD}$. In $A_2 + A$ collisions, $\epsilon_{\rm vib}$ of the diatom is used. The diatom from which $\epsilon_{\rm vib}$ was obtained is then dissociated if $R_f < \left(P_R^+\right)_{\rm VFD}$.

The expression for $\beta_{\rm VFD}$ in Eq. 6.8 contains the factor

$$\Gamma\left(\zeta_{\rm vib}/2\right)/\Gamma\left(\phi + \zeta_{\rm vib}/2\right).$$

As $\zeta_{\rm vib} \to 0$, this factor approaches infinity and gives $\left(P_R^+\right)_{\rm VFD} \to \infty$, which is unrealistic. To avoid this singularity, Hash and Hassan [83] developed an alternative form of the VFD model in which the model parameters are derived using the condition that $\left(P_R^+\right)_{\rm VFD}$ must be bounded at unity. Unlike the original version of Haas and Boyd [73, 74], the DV coupling parameter ϕ can then be calculated explicitly and does not require calibration with experimental data. Hash and Hassan claim that this represents an improvement over the original VFD model. From a numerical perspective, this is certainly true. However, there is little evidence to suggest that the alternative $\left(P_R^+\right)_{\rm VFD}$ is actually more physically

realistic than the original form of Haas and Boyd [73, 74], because it was proposed for primarily numerical reasons and is not based on more rigorous physics than the original form.

When using quantised vibration models to simulate vibrationally cold reacting flows, many diatoms will be in the ground state with $\epsilon_{\text{vib}} = 0$. This gives $\left(P_R^+\right)_{\text{VFD}} = 0$ and results in very low reaction rates. Many flows of interest in hypersonics are vibrationally cold, so this is particularly problematic. The VFD version of Hash and Hassan [83] does not rectify this problem. For harmonic oscillators, the ground state energy $k\Theta_{\text{vib}}/2$ should be included in ϵ_{vib}, so $\epsilon_{\text{vib}} = \left(\frac{1}{2} + q\right) k\Theta_{\text{vib}}$. As shown in §8.5.7, using the VFD model with $\epsilon_{\text{vib}} = \left(\frac{1}{2} + q\right) k\Theta_{\text{vib}}$ instead of $\epsilon_{\text{vib}} = qk\Theta_{\text{vib}}$ gives more realistic dissociation rates.

6.4.2 Threshold line dissociation model

Based on the assumption of classical impulsive collisions, Macheret and Rich [117] and Macheret *et al.* [116] proposed the analytical threshold line concept for modelling dissociating diatomic molecules where $T_{\text{vib}} < T_{\text{tr+rot}}$. The threshold line model is based on the premise that dissociation can occur only when ϵ_g exceeds some threshold energy function ϵ_F. The threshold energy ϵ_F depends on the vibrational energy ϵ_{vib}. This model was adapted for conventional DSMC chemistry calculations by Boyd [37], and is known as the threshold line dissociation (TLD) model. The TLD dissociation probability $\left(P_R^+\right)_{\text{TLD}}$ considers translational, rotational and vibrational energy modes, and has distinctly different forms for low and high vibrational levels. This dependence on internal energy modes allows the threshold line model to include the effects of DV coupling, and some effects of high rotational energy. Different forms of ϵ_F and $\left(P_R^+\right)_{\text{TLD}}$ apply for low and high vibrational energies. The implementation of Boyd [37] is presented here for a symmetrical diatomic gas.

The demarcation between low and high vibrational energy levels depends on the parameter α, defined by

$$\alpha \equiv \left(\frac{m_{\text{A}}}{m_{\text{A}} + m'}\right)^2.$$

For a symmetrical diatomic gas, $m' = m_{\text{A}}$, so $\alpha = 0.25$ for both reactions 1 and 2. The threshold energy ϵ_F depends on ϵ_{vib}, and is given by

$$\epsilon_F = \begin{cases} \left[\epsilon_d^{*\frac{1}{2}} - (\alpha\epsilon_{\text{vib}})^{\frac{1}{2}}\right]^2 / (1-\alpha) & \text{for} \quad \epsilon_{\text{vib}} < \alpha\epsilon_d^* \\ \epsilon_d^* - \epsilon_{\text{vib}} & \text{for} \quad \epsilon_{\text{vib}} \geq \alpha\epsilon_d^*. \end{cases}$$

Here, ϵ_d^* is a modified dissociation energy, which accounts for the reduction in dissociation energy associated with the centrifugal effects of high rotational energy. The modified dissociation energy ϵ_d^* is given by

$$\epsilon_d^* = \epsilon_d - \epsilon_{\text{rot}} + \frac{2}{3}\left(\frac{\epsilon_{\text{rot}}^3}{6\epsilon_d}\right)^{\frac{1}{2}} \approx \epsilon_d - \epsilon_{\text{rot}} + 0.27217\left(\frac{\epsilon_{\text{rot}}^3}{\epsilon_d}\right)^{\frac{1}{2}}.$$

The use of this reduced dissociation energy is an important feature of the TLD model. The dissociation probability is evaluated when $\epsilon_g > \epsilon_F$ [150] and $\epsilon_c > \epsilon_d$. For low vibrational levels where $\epsilon_{\text{vib}} < \alpha\epsilon_d^*$, the TLD dissociation probability is

$$\begin{aligned}\left(P_R^+\right)_{\text{TLD}} &= A_{\text{TLD}}\left(\frac{8\sqrt{2}}{3\pi^2}\right)\frac{\left(\epsilon_g-\epsilon_F\right)^{3/2}}{\epsilon_F\left[\left(\sqrt{\epsilon_d^*}-\sqrt{\alpha\epsilon_{\text{vib}}}\right)\left(\sqrt{\epsilon_d^*}-2\sqrt{\epsilon_{\text{vib}}}+\sqrt{\alpha\epsilon_{\text{vib}}}\right)\right]^{1/2}} \\ &\approx 0.38211A_{\text{TLD}}\frac{\left(\epsilon_g-\epsilon_F\right)^{3/2}}{\epsilon_F\left[\left(\sqrt{\epsilon_d^*}-\sqrt{\alpha\epsilon_{\text{vib}}}\right)\left(\sqrt{\epsilon_d^*}-2\sqrt{\epsilon_{\text{vib}}}+\sqrt{\alpha\epsilon_{\text{vib}}}\right)\right]^{1/2}}.\end{aligned}$$

Here, A_{TLD} is a constant that is used to calibrate the TLD model against experimental reaction rate data. For high vibrational levels where $\epsilon_{\text{vib}} \geq \alpha\epsilon_d^*$, the TLD dissociation probability is

$$\begin{aligned}\left(P_R^+\right)_{\text{TLD}} &= A_{\text{TLD}}\left(\frac{1+\sqrt{\alpha}}{1-\sqrt{\alpha}}\right)^{\frac{1}{2}}\frac{\left(\epsilon_g-\epsilon_F\right)^2}{4\pi^2\epsilon_F^{3/2}\left(\epsilon_{\text{vib}}-\alpha\epsilon_d^*\right)^{1/2}} \\ &= A_{\text{TLD}}\frac{\sqrt{3}}{4\pi^2}\frac{\left(\epsilon_g-\epsilon_F\right)^2}{\epsilon_F^{3/2}\left(\epsilon_{\text{vib}}-\epsilon_d^*/4\right)^{1/2}} \\ &\approx 0.043873A_{\text{TLD}}\frac{\left(\epsilon_g-\epsilon_F\right)^2}{\epsilon_F^{3/2}\left(\epsilon_{\text{vib}}-\epsilon_d^*/4\right)^{1/2}}.\end{aligned}$$

Note that $\left(P_R^+\right)_{\text{TLD}}$ is a function of ϵ_g, ϵ_{rot} and ϵ_{vib}. Therefore the TLD model can capture both DV coupling and some effects of high rotational energy. The original threshold line model of Macheret and Rich [117] considered both diatom + atom and diatom + diatom collisions. For simplicity the expressions for diatom + atom collisions are used in DSMC calculations for all testing reactions for both diatom + atom and diatom + diatom collisions [37].

In this study, for $A_2 + A_2$ collisions, ϵ_{rot} and ϵ_{vib} from the first diatom in the collision pair were used to calculate $\left(P_R^+\right)_{\text{TLD}}$. For $A_2 + A$ collisions, ϵ_{rot} and ϵ_{vib} from the diatom were used. The tested diatom was then dissociated if $R_f < \left(P_R^+\right)_{\text{TLD}}$.

The above expressions for $\left(P_R^+\right)_{\text{TLD}}$ result in $\left(P_R^+\right)_{\text{TLD}} > 1$ at certain energies, which is physically unrealistic [37, 150, 154]. In such cases, a single dissociation event only is performed in most DSMC codes. To reduce the number of events with $\left(P_R^+\right)_{\text{TLD}} > 1$, Wadsworth and Wysong [150] suggested that the vibrational energy ϵ_{vib} should include the ground state energy $k\Theta_{\text{vib}}/2$. For harmonic oscillators, $\epsilon_{\text{vib}} = \left(\frac{1}{2}+q\right)k\Theta_{\text{vib}}$ should be used. As shown in §8.5.8 and §C.7, a large fraction of reaction events still have $\left(P_R^+\right)_{\text{TLD}} > 1$, even when the ground state energy is included. According to Wysong *et al.* [154], the occurrence of events with $\left(P_R^+\right)_{\text{TLD}} > 1$ is an important limitation of the TLD model.

6.5 Modelling recombination reactions

Recombination reactions require ternary collisions which are infrequent in a rarefied gas, and are therefore usually ignored in DSMC calculations. However, when studying systems that approach chemical equilibrium, such as the flow downstream of a strong shock, recombination reactions must be considered. Using Eqs. 5.14 and 4.18, the mean recombination probability for VHS molecules is

$$\langle P_R^- \rangle_{\text{VHS}} = \frac{\dot{n}_R^-}{\dot{n}_{\text{colls}}} = \frac{k^- f_s n}{\mathcal{N}^2 \Xi} \left(\frac{T_r}{T} \right)^{\frac{1}{2}-v} . \tag{6.9}$$

Early recombination models [14, 15] were based on assigning a lifetime to binary collisions. Ternary collisions were then calculated as a binary collision between the pair of particles in the initial binary collision and a third particle. This section considers the more recent recombination models of Boyd [32] and Bird [21].

6.5.1 TCER recombination model of Boyd [32]

Here, the DSMC recombination model of Boyd [32] has been used. In this model, a quasi-particle, consisting of two colliding atomic particles, is assumed to interact with a third body selected at random from the particles within the cell. Under equilibrium conditions, the distribution of reduced collision energy for the quasi-particle and the third body, denoted $\tilde{\epsilon}_3$, is

$$f(\tilde{\epsilon}_3) = \tilde{\epsilon}_3^{5/2+\zeta_3/2-v} \exp(-\tilde{\epsilon}_3) / \Gamma(7/2 + \zeta_3/2 - v)$$

where ζ_3 is the number of internal DOF in the third body [32]. Boyd [32] proposed the recombination probability

$$P_R^- = (n/n_r) (\epsilon_3/\epsilon_d)^\kappa = (n/n_r) (\tilde{\epsilon}_3/\tilde{\epsilon}_d)^\kappa , \tag{6.10}$$

where $1/n_r$ and κ are constants dependent on the VHS parameters of the atomic species, the equilibrium constant K^* and Arrhenius rate parameters. As for the TCE model, this form of P_R^- plausibly approximates real gas behaviour, with consideration of mathematical tractability. Because $P_R^- = P_R^-(\epsilon_3)$, this recombination model may be regarded as an extension of the TCE model to include termolecular reactions, and is called the TCER model here.

Proceeding in a manner similar to that used in §C.5 and §C.6, the mean TCER re-

combination probability $\langle P_R^- \rangle$ is

$$\begin{aligned}\langle P_R^- \rangle &= \int_0^\infty P_R^- \left(\tilde{\epsilon}_3\right) f\left(\tilde{\epsilon}_3\right) d\tilde{\epsilon}_3 \\ &= \frac{n/\left(n_r \tilde{\epsilon}_d^{\,\kappa}\right)}{\Gamma\left(7/2+\zeta_3/2-\upsilon\right)} \int_0^\infty \tilde{\epsilon}_3^{\,5/2+\zeta_3/2-\upsilon+\kappa} \exp\left(-\tilde{\epsilon}_3\right) d\tilde{\epsilon}_3 \\ &= \frac{n}{n_r}\left(\frac{T}{\Theta_d}\right)^\kappa \frac{\Gamma(7/2+\zeta_3/2-\upsilon+\kappa)}{\Gamma(7/2+\zeta_3/2-\upsilon)},\end{aligned}$$

where $\tilde{\epsilon}_d = \Theta_d/T$ has been used. Here the lower integration limit is zero because the activation energy is zero for recombination reactions [148]. Using Eqs. 5.12 and 6.9 the common form of the equilibrium constant K_c^* from Eq. 5.2,

$$k^- = \frac{k^+}{K_c^*} = \frac{C^+}{C^*}\left(\frac{T}{\Theta_d}\right)^{\eta^+-\eta^*} = \frac{1}{n_r}\frac{\mathcal{N}^2\Xi}{f_s}\left(\frac{T}{\Theta_d}\right)^\kappa \left(\frac{T}{T_r}\right)^{\frac{1}{2}-\upsilon} \frac{\Gamma(7/2+\zeta_3/2-\upsilon+\kappa)}{\Gamma(7/2+\zeta_3/2-\upsilon)}.$$

Equating temperature powers provides

$$\kappa = \eta^+ + \upsilon - \frac{1}{2} - \eta^* = \chi_2 - \eta^*, \tag{6.11}$$

and equating the leading constants gives

$$\frac{1}{n_r} = \frac{C^+}{C^*}\frac{f_s}{\mathcal{N}^2\Xi}\left(\frac{T_r}{\Theta_d}\right)^{\frac{1}{2}-\upsilon} \frac{\Gamma\left(7/2+\zeta_3/2-\upsilon\right)}{\Gamma\left(7/2+\zeta_3/2-\upsilon+\kappa\right)}.$$

The VHS parameters Ξ, T_r and υ all refer to collisions between the two atomic particles, and C^+ and η^+ are the forward Arrhenius rate parameters for the recombination reaction under consideration. The parameter $1/n_r$ has units of m^3, as expected.

It is important to note that the TCER model is limited to the common form of the equilibrium constant K_c^* of Eq. 5.2, which depends on temperature only. Other more accurate forms of the equilibrium constant, such those of Gupta *et al.* [70] and Park [138], are not mathematically convenient for use in this recombination model [41, 42].

The TCER recombination probability includes the local number density n. This is a macroscopic property, and during a DSMC calculation it is obtained from the time-averaged number of particles in each cell. Strictly, the TCER model is not a conventional chemistry model, because it requires this macroscopic information to calculate the reaction probability, rather than information from the colliding molecules alone.

When $\kappa < 0$, which is often the case for recombination reactions in air chemistry, the TCER model gives $P_R^- \to \infty$ as $\epsilon_3 \to 0$. This singularity is encountered more frequently where the local number density is high, and is of some concern because such conditions usually prevail where significant recombination occurs.

As discussed for the TCE model in §6.3, the use of a quantised vibration model can affect the recombination rates realised in a DSMC computation. This applies to recombination reactions where the third body has vibrational DOF. In such cases, the distribution

of ϵ_3 actually occurring in the simulation differs from the assumed continuous Boltzmann distribution $f(\tilde{\epsilon}_3)$ used in the above derivation of the TCER parameters $1/n_r$ and κ. This effect, and the singularity for $\epsilon_3 \to 0$, result in the TCER model giving a recombination rate that differs significantly from the expected Arrhenius recombination rate $k^- = k^+/K_c^*$.

6.5.2 Recombination model of Bird [21]

Bird [21] proposed a recombination model in which P_R^- depended on the relative translational energy ϵ_g of the two colliding atoms and the local number density. In this model, P_R^- had the form

$$P_R^- = (n/n_r)(\epsilon_g/\epsilon_d)^\kappa = (n/n_r)(\tilde{\epsilon}_g/\tilde{\epsilon}_d)^\kappa,$$

which is similar to that proposed by Boyd [32] in Eq. 6.10. If recombination occurred, a third body was selected at random from those in the cell to remove energy. The energy of this third body was not used in calculating P_R^-. The distribution of ϵ_g for VHS molecules is given by Eq. 4.11, so the mean recombination probability is

$$\begin{aligned}\langle P_R^- \rangle &= \frac{n/\left(n_r \tilde{\epsilon}_d^\kappa\right)}{\Gamma(2-\upsilon)} \int_0^\infty \tilde{\epsilon}_g^\kappa f(\tilde{\epsilon}_g) d\tilde{\epsilon}_g = \frac{n/\left(n_r \tilde{\epsilon}_d^\kappa\right)}{\Gamma(2-\upsilon)} \int_0^\infty \tilde{\epsilon}_g^{1-\upsilon+\kappa} \exp\left(-\tilde{\epsilon}_g\right) d\tilde{\epsilon}_g \\ &= \frac{n}{n_r} \left(\frac{T}{\Theta_d}\right)^\kappa \frac{\Gamma(2-\upsilon+\kappa)}{\Gamma(2-\upsilon)}.\end{aligned}$$

Equating this expression with $\langle P_R^- \rangle_{\text{VHS}}$ from Eq. 6.9 gives κ as in Eq. 6.11 and

$$\frac{1}{n_r} = \frac{C^+}{C^*} \frac{f_s}{\mathcal{N}^2 \Xi} \left(\frac{T_r}{\Theta_d}\right)^{\frac{1}{2}-\upsilon} \frac{\Gamma(2-\upsilon)}{\Gamma(2-\upsilon+\kappa)}.$$

Again, this recombination model requires the local number density, so it is not strictly a conventional chemistry model.

6.5.3 Equilibrium collision theory

Bird [21] proposed a conventional DSMC chemistry model for reverse reactions that uses molecular partition functions to calculate P_R^-. Bird claims that this model can lead to exact equilibrium conditions. Different forms of P_R^- are employed for bimolecular and termolecular reverse reactions. For the termolecular recombination reaction AB + M $\leftarrow$ A + B + M, the recombination probability in each cell is set to $P_R^- = \langle P_R^- \rangle_{\text{VHS}} = nF(T)$, where n is the local number density and F depends on temperature only. Eq. 6.9 provides

$$P_R^- = nF(T) = \frac{k^- f_s n}{\mathcal{N}^2 \Xi} \left(\frac{T_r}{T}\right)^{\frac{1}{2}-\upsilon}, \quad \text{which gives} \quad k^- = \frac{F(T)\mathcal{N}^2 \Xi}{f_s} \left(\frac{T}{T_r}\right)^{\frac{1}{2}-\upsilon}.$$

In terms of the partition functions, the equilibrium constant K^* is given by

$$K^* = \frac{Q^{\mathrm{A}} Q^{\mathrm{B}}}{V_c Q^{\mathrm{AB}}} \frac{\exp\left(-\Theta_d/T\right)}{\mathcal{N}},$$

where V_c is the cell volume [21]. Using this expression for K^* and the Arrhenius form of k^+ from Eq. 5.6,

$$k^- = \frac{k^+}{K^*} = C^+ \mathcal{N} \left(\frac{T}{\Theta_d}\right)^{\eta^+} \frac{V_c Q^{\mathrm{AB}}}{Q^{\mathrm{A}} Q^{\mathrm{B}}}.$$

Equating the two expressions for k^- provides $F(T)$ from which

$$P_R^- = nF(T) = \frac{nC^+ f_s}{\mathcal{N}\Xi} \left(\frac{T}{\Theta_d}\right)^{\eta^+} \left(\frac{T_r}{T}\right)^{\frac{1}{2}-\upsilon} \frac{V_c Q^{\mathrm{AB}}}{Q^{\mathrm{A}} Q^{\mathrm{B}}}$$

is obtained. When a recombination event occurs, a third body is selected at random to remove energy from the recombining atoms [21].

This recombination model requires the cell temperature to evaluate the partition functions, as well as the local number density. Under non-equilibrium conditions, a kinetic temperature calculated from time-averaged flowfield samples should be used. Again, these are macroscopic values, so this recombination model is not strictly a conventional chemistry model.

6.6 Other conventional DSMC chemistry models

Several other conventional chemistry models have been proposed for the DSMC method. This section briefly discusses some of these models.

6.6.1 Quasi-classical trajectory calculations

The quasi-classical trajectory (QCT) method is a procedure for calculating molecular trajectories that considers the quantisation of reactant molecules, but in which the course of the reaction is treated classically [87]. The QCT method allows calculation of detailed state-specific reaction cross-sections, and can therefore capture important phenomena such as DV coupling in dissociating gases. DSMC chemistry calculations using QCT results have been performed by Boyd *et al.* [39] for the $\mathrm{N_2 + O \rightarrow N + NO}$ exchange reaction, and by Wadsworth and Wysong [150] for the $\mathrm{H_2 + H \rightarrow H + H + H}$ dissociation reaction. To perform QCT calculation, a potential surface for the interacting molecules is required. For collisions involving more than three atoms, potential surfaces are not generally available. This has effectively limited the application of the QCT method for many reactions of interest in hypersonics.

6.6.2 Generalised collision energy model

Boyd *et al.* [39] introduced the generalised collision energy (GCE) model, which is a further generalisation of the VFD model to include a bias for reaction due to rotational energy, in addition to vibrational energy. The TCE and VFD models are special cases of this GCE model. The GCE model uses adjustable parameters to control the contribution to P_R^+ from internal energy modes. For the $N_2 + O \rightarrow N + NO$ exchange reaction, Boyd *et al.* obtained values for these adjustable parameters by calibration against QCT results. The reaction cross-sections then provided by the GCE model were in reasonable agreement with those provided by the QCT calculations.

6.6.3 Exact available energy model

Bird [22, 21] proposed the exact available energy (EAE) model for dissociation reactions, in which vibrational energy exchange and dissociation processes are closely related. Diatoms are dissociated if BL vibrational energy exchange results in a post-exchange vibrational energy ϵ'_{vib} larger than the dissociation energy ϵ_d. The EAE model may regarded as an extension of BL procedures to predict dissociation [150]. The model does not explicitly include adjustable parameters, so the accuracy of this model clearly depends on the physical accuracy of both the vibration model and the vibrational energy exchange scheme. The EAE model has been used by Carlson and Bird [45], Wysong *et al.* [155], Wadsworth and Wysong [149, 150] and Lord [111, 112, 113]. Like the TCE model, the EAE model depends only on the total energy of collision, and does not include effects of DV coupling [149, 150].

The EAE model is simple to implement in a DSMC code. After BL energy exchange, diatoms with $\epsilon'_{\text{vib}} > \epsilon_d$ are simply dissociated into constituent atoms. The internal energy of the dissociating diatom can be used for the relative translational energy ϵ'_g of the two product atoms. The actual DSMC implementation of the EAE model does not directly depend on the vibration model. However the resulting reaction rates do depend on the vibration model and vibrational energy exchange procedures. The EAE model was originally introduced for a continuous vibrational energy distribution with ζ_{vib} effective vibrational DOF. Versions for anharmonic oscillators were used by Bird [21] and Carlson and Bird [45]. Lord [111] considered a version using the Morse potential for vibrational energy levels.

The macroscopic dissociation rates realised by the EAE model at thermal equilibrium can be calculated numerically. Three possible methods are given in §C.8. The calculations have been performed for VHS harmonic oscillators with a constant exchange probability $\phi_{\text{vib}} = 0.1$ and the BL exchange model of Bergemann and Boyd [9] where multiple relaxation events are prohibited and relaxing particles are selected according to the scheme of Gimelshein *et al.* [65]. For nitrogen, this version of the EAE model results in macroscopic dissociation rates that are accurately approximated by a rate equation of the Arrhenius

form. However, the calculated dissociation rates are about two orders of magnitude lower than published rates. Even by increasing the exchange probability ϕ_{vib}, it seems that this version of the EAE model cannot achieve the published rates. It is possible that better agreement with the published rates could be achieved by using an anharmonic vibration model and a variable-ϕ_{vib} exchange probability.

6.6.4 Maximum entropy models

It has been observed experimentally that energy distributions in reaction products deviate from equilibrium distributions. Levine and Bernstein [104] examined these deviations, and formulated the maximum entropy model that describes the post-reaction energy distributions as a perturbation away from microscopic equilibrium. The perturbation is described in terms of maximal parameters λ_i. The probability of an energy state appearing in the reaction products equals the probability of this energy state causing the reverse reaction. Using the principle of microscopic reversibility, this can be used to determine the reaction probability for a collision between reactant molecules.

Marriott and Harvey [128], Koura [96] and Gallis and Harvey [59, 58, 60] have proposed conventional DSMC chemistry models based on maximum entropy concepts. These models use a single adjustable maximal parameter λ to control the extent of DV coupling. Gallis and Harvey developed the model for chemistry in air and the Martian atmosphere. These maximum entropy models have not been adopted widely, because it seems that the results obtained do not differ significantly from those obtained with other conventional DSMC chemistry models [38].

6.7 Reaction mechanics and detailed balancing

The conventional chemistry models discussed in this chapter give the probability P_R of a reaction occurring. In these models, P_R is calculated for every collision between reactant particles with $\epsilon_c > \epsilon_a$. A reaction is performed when $R_f < P_R$. Computing a reacting event involves changing the reactant species to product species and setting the post-reaction energies for the product particles. This section considers procedures for setting post-reaction energies, and discusses the associated issue of detailed balancing.

The topic of post-reaction energy disposal has received little attention in the literature [38]. The proportional energy partitioning scheme of Haas [71, 72] was used here to distribute post-reaction energy amongst the various energy modes of reaction products. In this scheme, all energy modes of the reactant particles are adjusted by a factor which represents the proportional change in the total collision energy ϵ_c due to the reaction.

For the dissociation reaction AB + M $\rightarrow$ A + B + M, the post-reaction total energy is $\epsilon_c' = \epsilon_c - \epsilon_d$ and the energy adjustment factor is

$$\Psi_\epsilon^+ \equiv \epsilon_c'/\epsilon_c = 1 - \epsilon_d/\epsilon_c.$$

Energy is partitioned before the reaction is performed. Firstly, the adjusted energies are calculated for the reactant particles AB and M using

$$\epsilon'_g = \Psi^+_\epsilon \epsilon_g, \quad (\epsilon_{\text{int}})'_{\text{AB}} = \Psi^+_\epsilon (\epsilon_{\text{int}})_{\text{AB}} \quad \text{and} \quad (\epsilon_{\text{int}})'_{\text{M}} = \Psi^+_\epsilon (\epsilon_{\text{int}})_{\text{M}}.$$

The adjusted relative speed g' of particles AB and M is then given by

$$g' = \left(2\epsilon'_g/\tilde{m}\right)^{\frac{1}{2}} = \left(\Psi^+_\epsilon\right)^{\frac{1}{2}} g.$$

The direction of g' is randomly distributed on the unit sphere. The adjusted internal energy of the dissociating AB particle $(\epsilon_{\text{int}})'_{\text{AB}}$ is manifested as relative translational energy of the dissociated A and B atoms. The relative speed of the dissociated atoms is

$$g'_{\text{A+B}} = \left[2\left(\epsilon_{\text{int}}\right)'_{\text{AB}}/\tilde{m}\right]^{1/2}.$$

The direction of this $g'_{\text{A+B}}$ is randomly distributed on the unit sphere. If particle M is diatomic, the adjusted internal energy $(\epsilon_{\text{int}})'_{\text{M}}$ must be partitioned between rotational and vibrational modes. For unbounded harmonic oscillators, the post-reaction vibrational energy level q' is obtained using $R_i\left(0, q'_{\max}\right)$ where $q'_{\max} = \left\lfloor \left(\epsilon_{\text{int}}\right)'_{\text{M}}/(k\Theta_{\text{vib}}) \right\rfloor$. The post-reaction rotational energy is then $(\epsilon_{\text{rot}})'_{\text{M}} = (\epsilon_{\text{int}})'_{\text{M}} - q' k\Theta_{\text{vib}}$.

Where reverse reactions such as recombination occur, detailed balancing should be considered when performing post-reaction energy disposal. However, satisfying detailed balancing using conventional DSMC chemistry models can be difficult, particularly when P^+_R has a complicated form as in the TLD model. This is further complicated by the frequent use of quantised vibration models. No general method has been proposed to ensure satisfaction of detailed balancing when using such conventional chemistry models. Fortunately recombination reactions are generally very infrequent in rarefied flows, so problems associated with violating detailed balancing are usually insignificant and can often be ignored.

The recombination energy partitioning scheme presented here applies to the TCER model, for the recombination reaction AB + M $\leftarrow$ A + B + M. The post-reaction energy is $\epsilon'_c = \epsilon_c + \epsilon_d$ and the energy adjustment factor is

$$\Psi^-_\epsilon \equiv \epsilon'_c/\epsilon_c = 1 + \epsilon_d/\epsilon_c.$$

It is assumed that the relative translational energy $(\epsilon_g)_{\text{A+B}}$ of the atomic particles is manifested as the internal energy of the new diatom. The internal energy of the new diatom is

$$(\epsilon_{\text{int}})'_{\text{AB}} = \Psi^-_\epsilon (\epsilon_g)_{\text{A+B}}.$$

$(\epsilon_{\text{int}})'_{\text{AB}}$ is partitioned into rotational and vibrational energy using the procedure discussed above for dissociation reactions. If particle M is diatomic, its internal energy $(\epsilon_{\text{int}})'_{\text{M}}$ is

also calculated with this method. The relative translational energy of the A · B quasi-particle and the third body M, denoted ϵ_g, is used to calculate the post-reaction relative translational energy ϵ'_g of the new AB diatom and particle M using $\epsilon'_g = \Psi_\epsilon^- \epsilon_g$. The post-reaction relative speed g' of the AB and M particles is then given by

$$g' = \left(2\epsilon'_g/\tilde{m}\right)^{\frac{1}{2}} = \left(\Psi_\epsilon^-\right)^{\frac{1}{2}} g,$$

where g is the initial relative translational speed of the A · B quasi-particle and M. Again, the direction of g' is randomly distributed on the unit sphere.

In DSMC computations where equilibrium conditions are approached, the problems associated with violating the detailed balancing requirement become apparent. They are manifested as different kinetic temperatures in different energy modes. It is clear that conventional DSMC chemistry models require further development to alleviate the detailed balancing issue. As noted in Chapter 7, decoupled chemistry methods do not suffer from these problems with detailed balancing.

For each dissociation event, a new particle must be added to the cell. In this study, the new particle was added during the collision routine, and was therefore available for subsequent collisions in that cell during the time step. The new particle could be inserted into the particle list array, but this necessitates changing the positions of many particles in the list array, and therefore imposes excessive computational expense. Instead, a second list array was used here, which contained only new atomic particles created by dissociation events in the current cell and the current time step. The selection routine then included this second list array when selecting possible collision partners. The additional computational expense associated with using the second list array is negligible.

The procedure for each recombination event simply involves the deletion of a particle from the list array. In such cases, the last particle in the list is copied to the position of the deleted particle.

6.8 A simplified conventional DSMC chemistry model

Cercignani *et al.* [46] examined the hypersonic flow of rarefied reacting air over a flat plate at various angles of attack. A simplified DSMC chemistry model was used, which considered oxygen dissociation only and ignored nitrogen dissociation and the exchange reactions. For all collisions with $\epsilon_c > \epsilon_d$, $P_R^+ = 1$ was used. The results obtained were compared to the DSMC results of Dogra and Moss [54], which were obtained with a full air chemistry model. The coefficients of pressure, skin friction, heat transfer and drag agreed to within 5%. The study of Cercignani *et al.* indicates that the details of chemical reaction processes may not be significant in the calculation of the aerodynamic coefficients of engineering interest. It is noted however, that the flow investigated by Cercignani *et al.* was relatively simple, and devoid of the complex shock-shock and shock-boundary

layer interactions that may occur in flows about more complex geometries. In such flows, the details of the chemical reaction models could have a significant influence on the flow characteristics of interest.

6.9 Testing and validating DSMC chemistry models

The most rigorous test for a conventional DSMC chemistry model is to compare the predicted reaction cross-sections to those obtained from detailed state-specific quantum calculations validated by experimental data. For most reactions of interest in hypersonics, quantum calculations have not been performed and experimental state-specific reaction cross-section data is virtually non-existent [81, 154]. The QCT calculations reported by Wadsworth and Wysong [150] for the $H_2 + H \rightarrow H + H + H$ reaction and Boyd *et al.* [39] for the $N_2 + O \rightarrow NO + N$ reaction, plus the experimental results reported by Wysong *et al.* [154] for the $Ar_2^+ + Ar \rightarrow Ar^+ + 2Ar$ reaction, all indicate that conventional DSMC chemistry models provide reaction cross-sections that are of the correct order.

In the absence of detailed reaction cross-section data, the most basic test to which a DSMC chemistry model can be subjected is the simulation of chemistry under thermal equilibrium conditions and the measurement of the resulting simulated reaction rates [149]. At equilibrium, the model should provide rates that reproduce known rates with reasonable accuracy. Most DSMC chemistry models satisfy this test, because most models have been formulated specifically to recover known rates at equilibrium.

Harvey and Gallis [81] have reviewed validation efforts for DSMC chemistry models. Experimental validation requires measurements of a non-equilibrium reacting flowfield. Actually generating such flowfields is difficult. Another problem is the acquisition of accurate, detailed flowfield measurements under such conditions. Although the few available experimental results suggest that DSMC chemistry models are reasonably accurate, the models and post-reaction energy distribution procedures have not yet been rigorously validated for non-equilibrium conditions [81]. Experimental density measurements of the flow downstream of strong shocks in nitrogen, obtained by Kewley and Hornung [91] and reported by Bird [15], have been used to test DSMC chemistry models [15, 32, 110]. This case is considered in §8.4.

CHAPTER 7

Decoupled chemistry methods

7.1 Introduction and summary

This chapter is concerned with decoupled chemistry methods for DSMC calculations, with attention given to the macroscopic chemistry method [110]. In decoupled chemistry methods, chemical reactions are decoupled from the collision routine, and are performed as a separate independent process. This decoupling is similar to the fundamental DSMC assumption where particle motions and intermolecular collisions are decoupled [7]. For dissociation reactions, decoupling collisions and reactions may have some physical basis, because collision-induced dissociation of a diatom occurs after excitation by collision with a second molecule. Decoupled chemistry methods have been considered by several authors, as discussed below.

Boyd *et al.* [40] used a decoupled chemistry method, called the overlay method, that excluded trace species from the DSMC calculation, and modelled each trace species concentration by solving a macroscopic diffusion equation with a chemical source term. These separate calculations used local flow conditions, obtained from the DSMC calculation of the dominant chemical species. This overlay method was specifically intended to simulate the chemistry of trace species.

Bartel *et al.* [8] applied the decoupled approach to capture chemistry in a six species chlorine plasma reactor, where the trace species dominate the system behaviour of interest. Using conventional DSMC chemistry procedures to model the system gave incorrect and physically unrealistic results, due to the large statistical scatter associated with the low reaction frequencies and small numbers of trace species particles. In this decoupled method, the number of reaction events required in a cell was calculated from the macroscopic reaction rate k^+ and number densities. Presumably, k^+ was calculated using a local kinetic temperature. The decoupled chemistry routine was invoked after the collision routine to perform the required number of reactions. For the bimolecular reaction $\mathrm{A} + \mathrm{B} \rightarrow \mathrm{C} + \mathrm{D}$, the change in the number of species A particles ΔN_A during a time step was given by

$$\Delta N_\mathrm{A} = -\left(N_\mathrm{A} - R_\mathrm{A}\right) n_\mathrm{B} k^+ \Delta t / \mathcal{N}.$$

Here R_A is the accumulated fractional remainder of ΔN_A from the previous time step. The

number density of species B n_B was a macroscopic property computed directly from the assumption of local charge neutrality. The numbers of species C and D particles created were then

$$\Delta N_C = -\Delta N_A W_{A,B}/W_{C,D} + R_C \quad \text{and} \quad \Delta N_D = -\Delta N_A W_{A,B}/W_{C,D} + R_D$$

respectively. Here $W_{A,B}$ is the species dependent weighting factor for species A and B, which is much larger than the weighting factor $W_{C,D}$ for the trace species C and D. The fractional remainders R_A, R_C and R_D were used to reduce the effects of statistical fluctuations. In this decoupled method the production and consumption of product and reactant particles could essentially occur independently during a time step. However, on average, the rates of consumption and production were correct. Bartel *et al.* [8] did not discuss methods for selecting reacting particles or performing post-reaction energy disposal.

Bartel [7] considered a similar decoupled chemistry scheme in which species B particles were present in the simulation. Some methods for selecting reacting A and B particles were considered. For each reaction event, possible reactant particles were randomly selected from those within in the cell, and a reaction was performed if the energy of the particles exceeded the energy threshold for the reaction. Presumably, the detailed reaction mechanics were calculated using a method similar to that of Haas [71, 72] as discussed in §6.7. As an alternative scheme, Bartel [7] suggested that reacting particles could be selected using a scheme analogous to the NTC method [20] for selecting collision partners. This alternative selection scheme is investigated in §7.4.

Another decoupled method, called the macroscopic chemistry method, was introduced by Lilley and Macrossan [110]. The fundamental premise of the macroscopic method is that chemical reactions are infrequent events, and provided that the macroscopic reaction rate is maintained, the microscopic details of reaction events have a minimal influence on the flowfield properties of engineering interest. Therefore little effort is made to accurately model the details of reaction processes at the molecular level. The macroscopic method was developed for the symmetrical diatomic dissociating gas and applied to nitrogen.

In the macroscopic method, no attempt is made to select a collision partner when simulating dissociation events. For each dissociation event, a single diatom is selected from those in the cell according to a simple selection rule, and is dissociated into two atoms. Similarly, no attempt is made to select a third body when simulating recombination events. For each recombination event, two atoms are selected at random and are recombined into a single diatom. The dissociation energy is accounted for by adjusting the thermal velocities of all particles in the cell. Details of the macroscopic method are given in §7.2.

The procedures adopted to select reacting particles in the macroscopic method are fundamentally different to those used in the earlier decoupled method of Bartel [7]. In the method of Bartel, reactions events were performed only when the total energy of

the selected reactant particles exceeded a reaction energy threshold. It appears that this decoupled method attempts to correctly model the reacting gas behavior at the molecular level. The macroscopic method does not attempt to capture the microscopic details of reaction processes. However, as shown by the results presented by Lilley and Macrossan [110, 106] and in Chapter 8, the macroscopic method produces flowfields in reasonable agreement with those obtained using conventional collision-based DSMC chemistry models which do attempt to model reactions at the molecular level.

It should be noted that decoupled approach used in the macroscopic method may not be suitable for modelling flowfield radiation, which depends strongly on the concentration and internal states of radiating species.

7.2 Details of the macroscopic chemistry method

When using the macroscopic method, the prime concern is to obtain the correct macroscopic reaction rate. For the symmetrical diatomic gas, the requirement is to determine the net change in the number of diatoms, denoted ΔN_{A_2}, in each cell at each time step. The procedure used here to calculate ΔN_{A_2} is discussed in §7.2.1. When ΔN_{A_2} has been calculated, some selection rule is required to select reacting particles in each cell. Two possible selection methods are given in §7.2.2. Reaction mechanics for the macroscopic method are discussed §7.2.3, and the procedure for adjusting thermal velocities to account for the dissociation energy is given in §7.2.4. Some discussion on the DSMC implementation of the macroscopic method is provided in §7.2.5, and comments on detailed balancing in §7.2.6.

7.2.1 Calculating the required number of reaction events

Consider the dissociation fraction α at the start of some zero-dimensional process, given by

$$\alpha = N_A / (N_A + 2N_{A_2})$$

where N_s is the number of species s particles. After a time Δt during which chemistry occurs, the new dissociation fraction is

$$\alpha' = N'_A / \left(N'_A + 2N'_{A_2}\right)$$

where N'_s is the new number of species s particles. The atom conservation equation

$$C = N_A + 2N_{A_2} = N'_A + 2N'_{A_2}$$

allows these dissociation fractions to be expressed as $\alpha = N_A/C$ and $\alpha' = N'_A/C$. The change in the number of atomic particles is

$$\Delta N_A = N'_A - N_A = C\left(\alpha' - \alpha\right).$$

Using $\Delta N_A = -2\Delta N_{A_2}$, the net change in the number of diatoms is given by

$$\Delta N_{A_2} = -\left(N_A/2 + N_{A_2}\right)\left(\alpha' - \alpha\right). \tag{7.1}$$

A simple Euler method can be used to estimate α' according to

$$\alpha' \approx \alpha + \dot{\alpha}\Delta t.$$

Substituting this into Eq. 7.1 gives

$$\Delta N_{A_2} \approx -\left(N_A/2 + N_{A_2}\right)\dot{\alpha}\Delta t.$$

If the time interval Δt is a DSMC time step, this should be a good approximation because DSMC time steps are small compared to the mean collision time and hence the characteristic reaction time $1/\dot{\alpha}$. From Eq. 5.15, $\dot{\alpha} = \dot{\alpha}\left(\alpha, T, \rho\right)$. Because ρ and α depend on N_A and N_{A_2}, $\Delta N_{A_2} = \Delta N_{A_2}\left(N_A, N_{A_2}, T\right)$. Under non-equilibrium conditions, T may be replaced by an appropriate kinetic temperature T_k. This kinetic temperature could be, for example, the overall kinetic temperature T_{kin} given in §2.9.4.

In the macroscopic method, flowfield samples are used to calculate the time-averaged quantities $\bar{N}_A$, $\bar{N}_{A_2}$ and $\bar{T}_k$ in each cell. These are used to calculate $\bar{\rho}$, $\bar{\alpha}$ and then $\dot{\alpha}$ in each cell. ΔN_{A_2} is then calculated using

$$\Delta N_{A_2} = -\left(\bar{N}_A/2 + \bar{N}_{A_2}\right)\dot{\alpha}\Delta t. \tag{7.2}$$

Time-averaged rather than instantaneous values are used, because the required mean number of reaction events, given by

$$\left\langle \Delta N_{A_2} \right\rangle = \Delta N_{A_2}\left(\bar{N}_A, \bar{N}_{A_2}, \bar{T}_k\right)$$

differs from the mean instantaneous value of

$$\left\langle \Delta N_{A_2}\left(N_A, N_{A_2}, T_k\right) \right\rangle.$$

Also, using time-weighted rather than instantaneous samples is more computationally efficient, because flowfield conditions must be calculated less often. For unsteady flows, the macroscopic method could be implemented by using stored time-averaged properties obtained for each cell from several successive DSMC simulations of the unsteady flow.

Sampling procedures for such flows are discussed in §4.2.6.

In the above expressions, ΔN_{A_2} depends on a single kinetic temperature T_k only. However, the macroscopic method is not limited to a single temperature rate equation for the forward rate k^+. Other forms of k^+ can be used, and these may be any empirical or theoretical function of the local macroscopic flow conditions. For example, the two-temperature rate model of Park [137], given in §5.3, can be used to capture the effects of DV coupling. This model uses the vibrational kinetic temperature T_{vib} and the kinetic temperature of translation and vibration $T_{\text{tr+vib}}$ which are calculated from time-averaged flowfield samples.

The macroscopic method is not limited to the common equilibrium constant $K^* = K_c^*(T)$ as given by Eq. 5.2. Other forms of K^* that are any function of the macroscopic conditions can be used. One example is $K^* = K_{\text{G}}^*(T, n)$ as given in Eq. 5.3. As noted in §6.5, such complicated forms of K^* may not be mathematically convenient for use in some conventional DSMC recombination models.

If recombination reactions must be considered when using the macroscopic method with the two-temperature model [137], then the equilibrium constant K^* must be evaluated at the effective temperature T_e in order to calculate $\dot{\alpha}$. According to Park [138], K^* may be approximated using

$$K_e^* \approx K_c^*\left(T_e\right).$$

When using K_{G}^*, then K^* should be approximated with

$$K_e^* \approx K_{\text{G}}^*\left(T_e, n\right).$$

The macroscopic method simulates the net number of reaction events only. For net dissociation $\Delta N_{A_2} < 0$, and for net recombination $\Delta N_{A_2} > 0$. Where chemical equilibrium exists $\Delta N_{A_2} = 0$, so no reaction events will be computed. When considering both dissociation and recombination, $\dot{\alpha}$ is calculated with Eq. 5.15. This accounts for the change in α due to both dissociation and recombination events. If recombination is negligible, Eq. 5.16 can be used to approximate $\dot{\alpha}$.

A cumulative total of ΔN_{A_2}, denoted $\sum \Delta N_{A_2}$, is maintained for each cell. At every time step, $\sum \Delta N_{A_2}$ is updated according to the value of ΔN_{A_2} calculated using Eq. 7.2 with stored time-weighted average values of N_{A}, N_{A_2} and $\dot{\alpha}$. When $|\sum \Delta N_{A_2} > 0.5|$, sufficient reaction events are performed to bring $\sum \Delta N_{A_2}$ back into the range $[-0.5, 0.5]$. The limits of ± 0.5 are used so that the mean value of $\sum \Delta N_{A_2}$ in each cell during the simulation is close to zero. In a small fraction of cases where there are insufficient particles in the cell to perform the required number of reaction events, all of the available particles are consumed and $\sum \Delta N_{A_2}$ is adjusted according to the number of events actually performed.

7.2.2 Methods for selecting reacting particles

When performing a dissociation event, a diatom is selected at random from those within the cell, and a dissociation probability P_s is calculated according to the selection rule. The diatom is dissociated if $R_f < P_s$. This is an acceptance-rejection method that continues until the required number of diatoms $|\Delta N_{A_2}|$ have been dissociated in the cell. Two possible methods have been considered for selecting dissociating diatoms in this study.

Firstly, Lilley and Macrossan [110] used the selection probability

$$P_s = \epsilon_{\text{int}} / \left(\epsilon_{\text{int}}\right)_{\text{max}} .$$

Here, $\epsilon_{\text{int}} = \epsilon_{\text{rot}} + \epsilon_{\text{vib}}$ is the internal energy of a randomly selected diatom and $\left(\epsilon_{\text{int}}\right)_{\text{max}}$ is the maximum instantaneous value of ϵ_{int} in the cell. $\left(\epsilon_{\text{int}}\right)_{\text{max}}$ is found before the diatom selection routine starts. This selection method approximates the selection of dissociating diatoms in the conventional TCE method, where particles with higher internal energies are more likely to dissociate.

For diatoms with DV coupling, the dissociation probability should depend primarily on the vibrational energy. Diatoms in higher vibrational energy levels should be more likely to dissociate. Following this logic, Lilley and Macrossan [106] proposed the diatom selection probability

$$P_s = \frac{1}{q_d}\left(\frac{1}{2} + q\right)$$

for harmonic oscillators with DV coupling. The $\frac{1}{2}$ added to q accounts for the ground state energy. This removes the minor difficulties that occur in vibrationally cold flows where q is often zero, resulting in an inefficient diatom selection routine. q_d is the vibrational energy level immediately below the dissociation limit.

For net recombination, two atomic particles are selected from the cell for each recombination event. Here, the process for selecting recombining atoms was random and independent of energy.

In a small fraction of cases, there may be insufficient particles in the cell to perform the required number of dissociation or recombination events. In such cases, all of the available particles are consumed, and $\sum \Delta N_{A_2}$ is adjusted according to the number of events actually performed.

7.2.3 Reaction mechanics

For dissociation events, it is assumed that all internal energy ϵ_{int} in the dissociating diatom is manifested as the relative translational energy of the two atoms after the dissociation event. The relative speed of the atoms is therefore

$$g' = \left(2\epsilon_{\text{int}}/\tilde{m}\right)^{\frac{1}{2}} .$$

The direction of the post-reaction relative velocity vector $\mathbf{g}'$ is random. The centre-of-mass velocity of the two atomic particles is the same as the velocity of the original diatom.

For recombination events, it is assumed that the relative translational energy $\epsilon_g = \tilde{m}g^2/2$ of the two atoms is manifested as the internal energy of the new diatom. The vibrational energy level is set to that closest to $\epsilon_g/2$ such that $\epsilon_{\text{vib}} \leq \epsilon_g$. The rotational energy is then simply $\epsilon_{\text{rot}} = \epsilon_g - \epsilon_{\text{vib}}$. The velocity of the new diatom equals the centre-of-mass velocity of the two atoms before the recombination event.

7.2.4 Accounting for the dissociation energy

The net change in chemical potential energy E_{cp} due to ΔN_{A_2} reaction events is

$$\Delta E_{\text{cp}} = -\Delta N_{\text{A}_2} \epsilon_d.$$

In the macroscopic method, ΔE_{cp} is the net energy that must be removed from the cell by adjusting the thermal velocities of all particles in the cell. For net dissociation, $\Delta N_{\text{A}_2} < 0$ so $\Delta E_{\text{cp}} > 0$ and the thermal velocities will be reduced. This reduces the local translational kinetic temperature, as expected. For net recombination, the thermal velocities will increase. The thermal velocities of all particles are adjusted by a factor Ψ_c. The new thermal velocity of particle p, denoted $\mathbf{c}'_p$, is given by

$$\mathbf{c}'_p = \Psi_c \, \mathbf{c}_p.$$

An expression for Ψ_c will be derived later. The new thermal speed c'_p is then

$$c'_p = |\mathbf{c}'_p| = \Psi_c |\mathbf{c}_p| = \Psi_c c_p.$$

The adjusted velocity of particle p is then given by

$$\begin{aligned} \mathbf{v}'_p &= \mathbf{c}'_p + \bar{\mathbf{v}} = \Psi_c \, \mathbf{c}_p + \bar{\mathbf{v}} \\ &= \Psi_c \left(\mathbf{v}_p - \bar{\mathbf{v}} \right) + \bar{\mathbf{v}} \\ &= \Psi_c \mathbf{v}_p + \left(1 - \Psi_c \right) \bar{\mathbf{v}}. \end{aligned} \tag{7.3}$$

This velocity adjustment changes the thermal velocities only. The centre-of-mass velocity of the particles does not change and momentum conservation is satisfied. In the execution of the macroscopic chemistry method, Eq. 7.3 is the most efficient formula for adjusting velocities because $\left(1 - \Psi_c \right) \bar{\mathbf{v}}$ is constant in each cell.

To find the expression for Ψ_c, the total translational thermal energies of all particles in the cell before and after the adjustment of velocities must be considered. The initial thermal energy of particle p is

$$\left(\epsilon_{\text{tr}} \right)_p = m_p c_p^2 / 2.$$

The adjusted thermal energy for particle p is then

$$(\epsilon_{\rm tr})'_p = m\left(c'_p\right)^2/2 = m\left(\Psi_c c_p\right)^2/2 = \Psi_c^2\left(\epsilon_{\rm tr}\right)_p .$$

The total translational thermal energy of all particles before adjustment, denoted $E_{\rm tr}$, is

$$E_{\rm tr} = \sum_{p=1}^{N_p} \left(\epsilon_{\rm tr}\right)_p ,$$

where N_p is the number of particles in the cell. The total translational thermal energy after adjustment is

$$E'_{\rm tr} = \sum_{p=1}^{N_p} \left(\epsilon'_{\rm tr}\right)_p = \Psi_c^2 \sum_{p=1}^{N_p} \left(\epsilon_{\rm tr}\right)_p = \Psi_c^2\, E_{\rm tr}.$$

The change in chemical potential energy $\Delta E_{\rm cp}$ is the energy that must be removed from the particles, so $E'_{\rm tr} = E_{\rm tr} - \Delta E_{\rm cp}$. Therefore $\Psi_c^2\, E_{\rm tr} = E_{\rm tr} - \Delta E_{\rm cp}$ and

$$\Psi_c = \left(1 - \frac{\Delta E_{\rm cp}}{E_{\rm tr}}\right)^{\frac{1}{2}} .$$

For dissociation $\Delta E_{\rm cp} > 0$ giving $\Psi_c < 1$. For recombination $\Psi_c > 1$.

In a small fraction of dissociation events, the translational thermal energy present in the cell may be less than the required change in chemical potential energy. In such cases, the thermal velocities are all set to zero, and the remaining translational thermal energy $\Delta E_{\rm cp} - E_{\rm tr}$ to be removed from the cell is stored. This remaining thermal energy is removed from the thermal velocities when the next reaction is calculated.

For each cell, the thermal velocity adjustments are quite computationally expensive. However, because reaction events are infrequent, few cells have reactions in any given time step, and the velocity adjustment procedure does not appear to slow the overall DSMC simulation significantly.

7.2.5 DSMC implementation of the macroscopic method

The macroscopic method is executed after the collision routine. This involves calculating $\Delta N_{\rm A_2}$ in each cell from stored time-average quantities, and then performing the required number of reaction events. Because the reactions are performed after the collision routine, there is no requirement to adjust the particle list array to add new atomic particles created by dissociation events and remove atomic particles for recombination events.

7.2.6 Satisfaction of detailed balancing

The macroscopic chemistry method considers net changes in composition only. At equilibrium, there is no net change in composition, so no reactions are performed. Consequently, at equilibrium, detailed balancing is not an issue for the macroscopic chemistry method.

In this respect, the macroscopic method is similar to continuum CFD solvers, which do not explicitly consider detailed balancing.

7.3 Extension to more complex reacting gas mixtures

The decoupled approach to DSMC chemistry modelling was applied to a complex reacting chlorine plasma system by Bartel *et al.* [8] and Bartel [7]. Similarly, the macroscopic chemistry method can be extended to a complex gas mixture with many species and many chemical reactions. For example, the common net reactions in high temperature air, ignoring ionisation and charge exchange reactions, are the dissociation reactions

$$\mathrm{N_2} \rightleftharpoons \mathrm{N} + \mathrm{N}, \quad \mathrm{O_2} \rightleftharpoons \mathrm{O} + \mathrm{O} \quad \text{and} \quad \mathrm{NO} \rightleftharpoons \mathrm{N} + \mathrm{O}$$

and the atom exchange reactions

$$\mathrm{N} + \mathrm{O_2} \rightleftharpoons \mathrm{NO} + \mathrm{O} \quad \text{and} \quad \mathrm{N_2} + \mathrm{O} \rightleftharpoons \mathrm{NO} + \mathrm{N}.$$

In a manner similar to the symmetrical diatomic gas considered above, the required number of reaction events can be calculated for each net reaction with a simple Euler method. For species A in the net reaction A + B $\rightarrow$ products, the new number density of species A, denoted n'_{A}, is given by

$$n'_{\mathrm{A}} = n_{\mathrm{A}} + \frac{dn_{\mathrm{A}}}{dt}\Delta t.$$

Using Eq. 5.5 this becomes

$$n'_{\mathrm{A}} = n_{\mathrm{A}} - \frac{k^+ n_{\mathrm{A}} n_{\mathrm{B}}}{\mathcal{N}}\Delta t.$$

Using $n_{\mathrm{A}} = N_{\mathrm{A}} W / V_c$, where N_{A} is the number of simulator particles of species A, W is the cell-based weighting factor and V_c is the cell volume,

$$N_{\mathrm{A}} - N'_{\mathrm{A}} = \frac{k^+ N_{\mathrm{A}} N_{\mathrm{B}} W \Delta t}{\mathcal{N} V_c}.$$

For the net reaction A + B $\rightarrow$ products, $N_{\mathrm{A}} - N'_{\mathrm{A}}$ reaction events are performed. As in §7.2.1, time-averaged numbers of particles $\bar{N}_{\mathrm{A}}$ and $\bar{N}_{\mathrm{B}}$ should be used rather than the instantaneous numbers N_{A} and N_{B}. k^+ is calculated using an appropriate macroscopic rate equation with local time-averaged kinetic temperatures. For the net reaction A + B $\rightarrow$ products, the mean number of reaction events that must be performed in a DSMC cell during a time step Δt, denoted $\langle N_R^+ \rangle_{\mathrm{A+B}}$, is

$$\langle N_R^+ \rangle_{\mathrm{A+B}} = \frac{k^+ \bar{N}_{\mathrm{A}} \bar{N}_{\mathrm{B}} W \Delta t}{\mathcal{N} V_c} + R. \tag{7.4}$$

Here R is either a random fraction $R = R_f$ or the fractional remainder from a previous time

step. Note that Eq. 7.4 applies when A $\neq$ B and A = B. Methods used to select reacting particles and distribute energy after reaction events may differ for each net reaction.

7.4 Particle selection method suggested by Bartel [7]

Bartel [7] suggested that decoupled chemistry methods could use procedures analogous to the NTC method of Bird [20] to select reacting particles. Details of this method were not actually provided by Bartel. Here, a possible version of this selection method is proposed for the bimolecular reaction A+B $\rightarrow$ products. The requirement is to obtain an expression for the number of A + B pairs that must be tested for reaction, based on the macroscopic reaction rate k^+.

Here it is assumed that the selection probability P_s for reaction has the form

$$P_s = Af, \tag{7.5}$$

where A is a constant and f is some function of the energy modes of the participating particles. Here f could have the form of P_R^+ from one of the conventional collision-based DSMC chemistry models considered in Chapter 6. This allows a biased selection probability, which may be of use when modelling DV coupling.

For the case where A $\neq$ B, the total number of possible reacting pairs that are available for testing, from a total of $\bar{N}_\mathrm{A}$ particles of species A and $\bar{N}_\mathrm{B}$ particles of species B is $\bar{N}_\mathrm{A}\bar{N}_\mathrm{B}$. If all of these possible pairs are tested, then the fraction of pairs that react is the mean reaction probability, given by

$$\langle P_s \rangle = \frac{\langle N_R^+ \rangle_{\mathrm{A+B}}}{\bar{N}_\mathrm{A}\bar{N}_\mathrm{B}}.$$

From Eq. 7.5, $\langle P_s \rangle = A\langle f \rangle$, so

$$\frac{\langle N_R^+ \rangle_{\mathrm{A+B}}}{\bar{N}_\mathrm{A}\bar{N}_\mathrm{B}} = A\langle f \rangle \quad \text{and} \quad A = \frac{\langle N_R^+ \rangle_{\mathrm{A+B}}}{\bar{N}_\mathrm{A}\bar{N}_\mathrm{B}\langle f \rangle}. \tag{7.6}$$

Rather than test all possible pairs, a fraction $\beta < 1$ will be tested, and the constant A increased to $A' = A/\beta$ so that the mean number of reactions actually performed remains unchanged. The number of pairs tested is then $N_\mathrm{pairs}^{\mathrm{A}\neq\mathrm{B}} = \beta\bar{N}_\mathrm{A}\bar{N}_\mathrm{B}$ and an adjusted reaction probability

$$P_s' = (A/\beta)f = A'f$$

is used to select reacting pairs. Optimum computational efficiency is achieved when the maximum probability $(P_s')_\mathrm{max} = 1 = A'f_\mathrm{max}$. This provides $\beta = Af_\mathrm{max}$, so

$$N_\mathrm{pairs}^{\mathrm{A}\neq\mathrm{B}} = \beta\bar{N}_\mathrm{A}\bar{N}_\mathrm{B} = Af_\mathrm{max}\bar{N}_\mathrm{A}\bar{N}_\mathrm{B} \tag{7.7}$$

possible A + B pairs should be tested for reaction. The reaction selection probability is

then

$$P_s' = f/f_{\max}.$$

This shows that the value of A is not actually required in the DSMC calculation, so the value of $f_{\max}$ corresponding to $(P_s')_{\max} = 1$ is not calculated. The value of $f_{\max}$ used to calculate P_s' is simply the maximum value of f encountered during the simulation. By substituting Eqs. 7.6 and 7.4 into Eq. 7.7,

$$N_{\text{pairs}}^{\text{A}\neq\text{B}} = \langle N_R^+ \rangle_{\text{A+B}} \left(\frac{f_{\max}}{\langle f \rangle} \right) = \left(\frac{k^+ \bar{N}_{\text{A}} \bar{N}_{\text{B}} W \Delta t}{\mathcal{N} V_c} + R \right) \left(\frac{f_{\max}}{\langle f \rangle} \right). \tag{7.8}$$

For the case where A = B, the number of possible reaction pairs is $\bar{N}_{\text{A}} \left(\bar{N}_{\text{A}} - 1 \right) /2$. Following the arguments used above, the number of possible pairs to be tested for reaction is given by

$$N_{\text{pairs}}^{\text{A=B}} = A f_{\max} \bar{N}_{\text{A}} \left(\bar{N}_{\text{A}} - 1 \right) /2.$$

In this case

$$A = \frac{\langle N_R^+ \rangle_{\text{A+B}}}{\langle f \rangle} \frac{2}{\bar{N}_{\text{A}} \left(\bar{N}_{\text{A}} - 1 \right)}.$$

These equations give

$$N_{\text{pairs}}^{\text{A=B}} = \langle N_R^+ \rangle_{\text{A+B}} \left(\frac{f_{\max}}{\langle f \rangle} \right) = \left(\frac{k^+ \bar{N}_{\text{A}}^2 W \Delta t}{\mathcal{N} V_c} + R \right) \left(\frac{f_{\max}}{\langle f \rangle} \right),$$

which is identical to Eq. 7.8 with $\bar{N}_{\text{A}} = \bar{N}_{\text{B}}$.

In this method, $f_{\max}$ must be stored for each reaction in each cell. $\langle f \rangle$ should be recalculated at each time step, using a cumulative total f, denoted $\sum f$, and the number of samples in $\sum f$. $\sum f$ and the number of samples accumulated must also be stored for each reaction in each cell. During the approach to steady state, $\langle f \rangle$ will vary, and the total f should be periodically set to zero and the sampling of f restarted.

CHAPTER 8

Simulation results

8.1 Introduction and summary

This chapter presents the results of DSMC chemistry calculations performed to test the macroscopic chemistry method. The emphasis has been placed on comparing the results obtained with the macroscopic method to those obtained with conventional collision-based DSMC chemistry models, rather than code validation. This approach was adopted through necessity, because of the very limited amount of experimental data available for validating DSMC chemistry models, as discussed in §6.9. In this respect, this study uses the same approach as most published DSMC chemistry studies. Zero-dimensional chemical relaxation, a strong one-dimensional shock and axisymmetric flows over a blunt circular cylinder have been used as test cases. For the shock case, the experimental density measurements of Kewley and Hornung [91] have been used to test the macroscopic method. The zero-dimensional and axisymmetric cases have not been investigated experimentally. They have been considered here because they exhibit flow phenomena of specific interest in this study, as noted in §8.3 and §8.5. All simulations were performed using C codes written specifically for this study. Consequently, some emphasis has been placed on providing details of the DSMC procedures used in the simulations.

In this chapter, the notation $k^+_{\mathrm{Arr}}(T_{\mathrm{kin}})$ refers to dissociation rates of the Arrhenius form from Eq. 5.6, calculated using the overall kinetic temperature T_{kin}. The notation $k^+_{2T}(T_{\mathrm{tr+rot}}, T_{\mathrm{vib}}, s)$ refers to dissociation rates calculated using the two-temperature rate model of Park [137] from Eq. 5.9.

DSMC calculations have been performed using the macroscopic method with dissociation rates of the form $k^+_{\mathrm{Arr}}(T_{\mathrm{kin}})$ and $k^+_{2T}(T_{\mathrm{tr+rot}}, T_{\mathrm{vib}}, s)$. Calculations have also been performed with the equilibrium constants $K^* = K^*(T)$ and $K^* = K^*_{\mathrm{G}}(T, n)$. The use of these forms of k^+ and K^* demonstrate the flexibility of the macroscopic method. In principle, the macroscopic method can use any forms of k^+ and K^*, and these may be any empirical or theoretical function of the macroscopic flow conditions. It is shown that the macroscopic method provides results in reasonable agreement with those provided by conventional DSMC chemistry models.

8.2 Gas model used in simulations

All simulation results reported in this chapter used the same dissociating nitrogen model. The high temperature viscosity parameters for collisions involving N_2 and N molecules, and the resulting VHS parameters are given in Table B.1. The unbounded harmonic oscillator vibration model with $\Theta_{\text{vib}} = 3390$ K was used. The equilibrium constants and dissociation rates are provided in §B.2 and §B.3.

For simplicity, constant rotational and vibrational energy exchange probabilities were used in BL energy exchange procedures. The particle selection logic of Gimelshein *et al.* [65], which prohibits multiple relaxation events, was employed. The rotational energy exchange probability was $\phi_{\text{rot}} = 0.3$. From Eq. 4.32, this gives $Z_{\text{rot}} \approx 4.50$ for $N_2 + N_2$ collisions and $Z_{\text{rot}} \approx 4.53$ for $N_2 + N$ collisions. Both values are slightly lower than $Z_{\text{rot}} = 5$ often used for N_2 relaxation. The vibrational exchange probability was $\phi_{\text{vib}} = 0.01$. Fig. 8.9 in §8.4.4 shows the Z_{vib} profile through a strong shock resulting from this constant ϕ_{vib}. This profile differs from the expected behaviour as discussed in §2.8 where Z_{vib} usually decreases with increasing temperature. It is recognised that these constant exchange probabilities do not produce the relaxation behaviour expected of a real gas. However, considering the comparative nature of this study, this departure from real gas behaviour is unimportant.

8.3 Zero-dimensional chemical relaxation

The first test case considered the constant volume relaxation of pure atomic nitrogen at relatively high density and low initial temperature. The following solutions were examined:

1. Conventional DSMC chemistry procedures, using the conventional TCER recombination model. The TCE model was used for dissociation reactions that occur as the relaxation calculation approaches equilibrium.

2. Macroscopic method with $k^+ = k^+_{\text{Arr}}(T_{\text{kin}})$ and $K^* = K^*_c(T)$ from Eq. B.2. The diatom selection probability was $P_s = \epsilon_{\text{int}} / (\epsilon_{\text{int}})_{\text{max}}$ as discussed in §7.2.2.

3. Macroscopic method with $k^+ = k^+_{\text{Arr}}(T_{\text{kin}})$ and $K^* = K^*_{\text{G}}(T, n)$ from Eq. B.3. The diatom selection probability was $P_s = \epsilon_{\text{int}} / (\epsilon_{\text{int}})_{\text{max}}$ as discussed in §7.2.2.

4. Runge-Kutta solution with $K^* = K^*_c(T)$ from Eq. B.2.

5. Runge-Kutta solution with $K^* = K^*_{\text{G}}(T, n)$ from Eq. B.3.

This test case permits comparison between the solutions provided by the conventional TCER and TCE models and the macroscopic method. From Eq. 5.12, it is apparent that the equilibrium constant K^* effectively controls the recombination behaviour, so this case can be used to test the effects of different forms of K^* with the macroscopic method. The

Runge-Kutta calculations were performed to provide an exact solution of the relaxation behaviour for comparison with the three DSMC solutions.

The initial conditions are shown in Table 8.1. These conditions result in rapid recombination rates. Similar conditions may exist near the stagnation region of hypersonic flow over a blunt body with a cold wall. The nitrogen dissociation rates of Kewley and Hornung [91] were used in all solutions. The final equilibrium conditions depend on the form of K^*. These equilibrium conditions were obtained numerically using an iterative method to find the root of Eq. 5.19, and are included in Table 8.1.

Table 8.1: Initial conditions and calculated equilibrium conditions for constant volume chemical relaxation of atomic nitrogen at density $\rho = 0.2$ kg/m^3.

Initial conditions	Calculated equilibrium conditions	
	Using K_c^* from Eq. B.2	Using K_G^* from Eq. B.3
$\alpha_0 = 1$	$\alpha^* = 0.778$	$\alpha^* = 0.768$
$T_0 = 1000$ K	$T^* = 9164$ K	$T^* = 9520$ K
$n_0 = 8.60 \times 10^{24}$/m^3	$n^* = 7.64 \times 10^{24}$/m^3	$n^* = 7.60 \times 10^{24}$/m^3
$(\tau_{\rm VHS})_0 = 2.352 \times 10^{-10}$ s	$\tau^*_{\rm VHS} = 1.553 \times 10^{-10}$ s	$\tau^*_{\rm VHS} = 1.546 \times 10^{-10}$ s

8.3.1 DSMC solutions

Initially, the DSMC simulation contained 10^5 atomic simulator particles. This number decreased as recombination occurred. The initial time step $(\Delta t)_0$ was

$$(\Delta t)_0 = \frac{(\tau_{\rm VHS})_0}{4} = \frac{1}{4}\frac{1}{n\Xi}\left(\frac{T_r}{T}\right)^{\frac{1}{2}-\upsilon} = 5.882 \times 10^{-11} \text{ s},$$

where $(\tau_{\rm VHS})_0 = 1/\nu_{\rm VHS}$ comes from Eq. 4.18. The collision rate changes during the calculation, so the time step was adjusted for subsequent time steps so that $\Delta t \sim \tau_{\rm VHS}/4$ throughout the entire simulation. This was achieved by counting the number of collisions actually performed by the DSMC calculation, denoted $N_{\rm colls}^{\rm DSMC}$, and then adjusting Δt to $\Delta t'$ at the end of every time step according to

$$\Delta t' = \left(N_{\rm colls}^{\rm required} \Big/ N_{\rm colls}^{\rm DSMC}\right) \Delta t.$$

Using $N_{\rm colls} = N\nu\Delta t/2$ from Eq. 2.38, the required number of collisions $N_{\rm colls}^{\rm required}$ is

$$N_{\rm colls}^{\rm required} = \frac{N}{2}\frac{\Delta t}{\tau_{\rm VHS}}.$$

Using $\Delta t = \tau_{\rm VHS}/4$,

$$\Delta t' = N \Big/ \left(8N_{\rm colls}^{\rm DSMC}\right) \Delta t.$$

The $T_{\rm kin}$ and α relaxation histories obtained from the DSMC calculations are shown in

Fig. 8.1. These histories show that the solution obtained with the conventional TCER and TCE models does not attain the calculated equilibrium conditions shown in Table 8.1. This can be attributed to the fact that the DSMC implementation of the conventional TCER and TCE models does not actually realise the Arrhenius rates, as these models intend. The reasons for this are discussed in §6.5.1 and §6.3.1 respectively. The macroscopic method attains the calculated equilibrium conditions. The relaxation histories in Fig. 8.1 show that different forms of K^* result in markedly different relaxation behaviour.

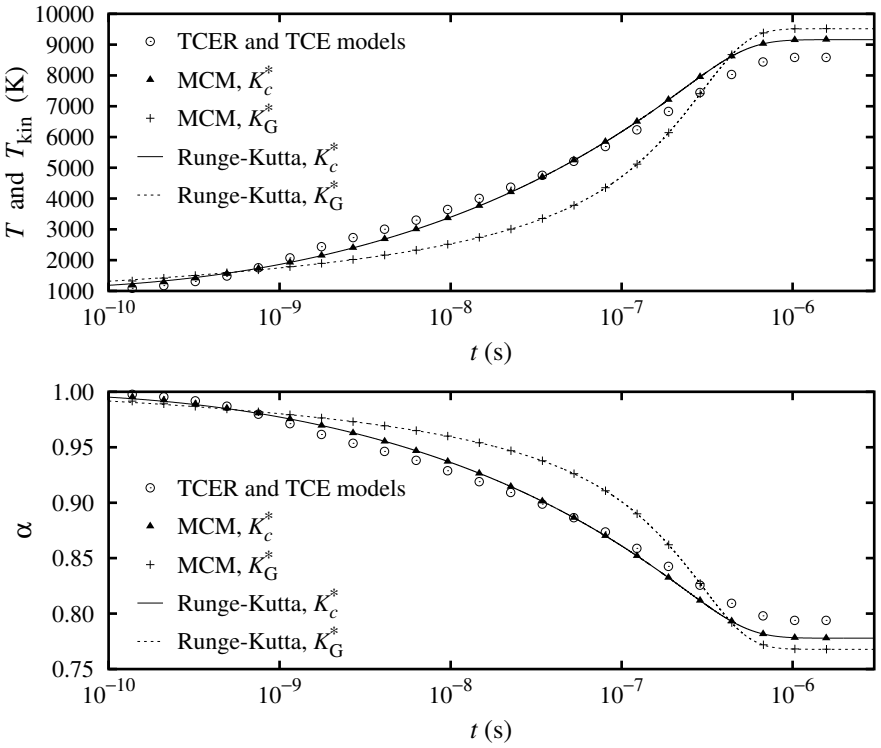

Figure 8.1: Relaxation histories of temperature T and dissociation fraction α for zero-dimensional relaxation calculations. The relaxation histories obtained with the conventional TCER and TCE models do not reach the calculated equilibrium conditions shown in Table 8.1, whereas those obtained with the Runge-Kutta method and the macroscopic method do reach the calculated equilibrium conditions.

During the DSMC calculations using the conventional TCER and TCE models, the number of reactions with $P_R > 1$ was recorded. For the TCER model, 4.97% of recombination events for the reaction $\mathrm{N_2 + N \leftarrow N + N + N}$ had $P_R^- > 1$. For the reaction $\mathrm{N_2 + N_2 \leftarrow N + N + N_2}$, 4.93% of recombination events had $P_R^- > 1$. In these simulations, the TCE model did not give any dissociation reactions with $\left(P_R^+\right)_{\mathrm{TCE}} > 1$.

8.3.2 Runge-Kutta solutions

By assuming thermal equilibrium conditions, relaxation histories of T and α were obtained by applying a fourth-order Runge-Kutta method, as given by Kreyszig [99]. In this Runge-Kutta method, the dissociation fraction at the end of the Runge-Kutta time step $(\Delta t)_{\mathrm{RK}}$, denoted α', was estimated by firstly evaluating four intermediate values of the dissociation

fraction. These intermediate values, denoted α_i, were evaluated using

$$\begin{aligned}
\alpha_1 &= (\Delta t)_{\mathrm{RK}}\ \dot{\alpha}\big[\alpha, T, \rho\big], \\
\alpha_2 &= (\Delta t)_{\mathrm{RK}}\ \dot{\alpha}\big[\alpha + \alpha_1/2, T(\alpha + \alpha_1/2, e), \rho\big], \\
\alpha_3 &= (\Delta t)_{\mathrm{RK}}\ \dot{\alpha}\big[\alpha + \alpha_2/2, T(\alpha + \alpha_2/2, e), \rho\big] \quad \text{and} \\
\alpha_4 &= (\Delta t)_{\mathrm{RK}}\ \dot{\alpha}\big[\alpha + \alpha_3, T(\alpha + \alpha_3, e), \rho\big].
\end{aligned}$$

Evaluating the intermediate dissociation fractions α_2, α_3 and α_4 required the thermodynamic temperature at dissociation fractions of $\alpha + \alpha_1/2$, $\alpha + \alpha_2/2$ and $\alpha + \alpha_3$. These intermediate temperatures $T(\alpha + \alpha_1/2, e)$, $T(\alpha + \alpha_2/2, e)$ and $T(\alpha + \alpha_3, e)$ were obtained by numerical solution of Eq. 5.19. The specific internal energy e was given by Eq. 5.18. The Runge-Kutta time step was

$$(\Delta t)_{\mathrm{RK}} = \frac{1}{\dot{\alpha}} \frac{|\alpha_0 - \alpha^*|}{N_{\mathrm{steps}} - 500}$$

where $N_{\mathrm{steps}} = 5000$ was the number of time steps used for the Runge-Kutta solution. The dissociation fraction at the end of the time step α' was calculated from

$$\alpha' = \alpha + (\alpha_1 + 2\alpha_2 + 2\alpha_3 + \alpha_4)/6.$$

To avoid numerical instabilities, a constant $(\Delta t)_{\mathrm{RK}}$ was used when α was within 0.1% of the equilibrium value α^*.

The Runge-Kutta solutions for T and α relaxation are shown in Fig. 8.1. The relaxation histories obtained using the macroscopic method with both K_c^* and K_{G}^* are in good agreement with those provided by the exact Runge-Kutta solution. This shows that the macroscopic method can include a number density dependent form of K^*. The results obtained using the conventional TCER and TCE models deviate from the exact Runge-Kutta relaxation behaviour.

8.4 Strong shock in dissociating nitrogen

This section describes one-dimensional DSMC calculations of the chemical relaxation region downstream of a strong shock in nitrogen. These calculations were performed to compare solutions provided by conventional DSMC chemistry models and the macroscopic method. These solutions are also compared to the experimental density measurements of Kewley and Hornung [91]. The macroscopic method with $k^+ = k^+_{\mathrm{Arr}}(T_{\mathrm{kin}})$, $k^+ = k^+_{2T}(T_{\mathrm{tr+rot}}, T_{\mathrm{vib}}, s)$, $K^* = K_c^*(T)$ and $K^* = K_{\mathrm{G}}^*(T, n)$ has been examined. The following five shock calculations were performed:

1. Conventional DSMC chemistry procedures, using the TCE model for dissociation reactions and the TCER recombination model. The parameters β_{TCE}, χ_2, n_r and κ

were obtained from the nitrogen dissociation rates of Kewley and Hornung [91] and $K^* = K_c^*(T)$ from Eq. B.2.

2. Macroscopic method with $k^+ = k^+_{\text{Arr}}(T_{\text{kin}})$, the nitrogen dissociation rates of Kewley and Hornung [91] and $K^* = K_c^*(T)$ from Eq. B.2. Dissociating diatoms were selected according to method A where $P_s = \epsilon_{\text{int}} / (\epsilon_{\text{int}})_{\max}$.

3. Macroscopic method with $k^+ = k^+_{\text{Arr}}(T_{\text{kin}})$, the nitrogen dissociation rates of Park [138] and $K^* = K_c^*(T)$ from Eq. B.2. Dissociating diatoms were selected according to method A where $P_s = \epsilon_{\text{int}} / (\epsilon_{\text{int}})_{\max}$.

4. Macroscopic method with $k^+ = k^+_{2T}(T_{\text{tr+rot}}, T_{\text{vib}}, 0.5)$ and $k^+ = k^+_{2T}(T_{\text{tr+rot}}, T_{\text{vib}}, 0.7)$ to capture DV coupling. The nitrogen dissociation rates of Park [138] and $K^* = K_c^*(T)$ from Eq. B.2 were used. Dissociating diatoms were selected according to method B where $P_s = \left(\frac{1}{2} + q\right)/33$. A shock calculation was also performed using the rates of Park with $k^+ = k^+_{\text{Arr}}(T_{\text{kin}})$.

5. Macroscopic method with $k^+ = k^+_{\text{Arr}}(T_{\text{kin}})$, the nitrogen dissociation rates of Kewley and Hornung [91] and $K^* = K^*_{\text{G}}(T, n)$ from Eq. B.3. Dissociating diatoms were selected according to method A where $P_s = \epsilon_{\text{int}} / (\epsilon_{\text{int}})_{\max}$.

8.4.1 Shock conditions

The highest enthalpy flow conditions in the experiments of Kewley and Hornung [91], as reported by Bird [15], have been simulated. The upstream conditions are shown in Table 8.2. The upstream viscosity μ_1, used to calculate the upstream nominal mean free path $\lambda_1 = 2\mu_1/(\rho_1 \bar{c}_1)$, is that recommended by Cole and Wakeham [51].

The equilibrium downstream conditions were obtained with an adaption of the method used by Macrossan [120]. In one dimension, the mass, momentum and energy conservation equations for a symmetrical diatomic gas are

$$X_1 = \rho u, \quad X_2 = \rho u^2 \rho (1+\alpha) RT \quad \text{and} \quad X_3 = u^2/2 + h \tag{8.1}$$

respectively, where $X_{1,2,3}$ denotes the conserved quantities. For a symmetrical diatomic dissociating gas in thermal equilibrium with the unbounded harmonic oscillator vibration model, the specific enthalpy is given by Eq. 5.20. For a particular α value, the equation

$$\frac{X_2 - X_1 \left[2(X_3 - h) + (1-\alpha)RT\right]}{\left[2(X_3 - h)\right]^{1/2}} = 0$$

was solved numerically to obtain T. This gives h and allows evaluation of u using the last of Eqs. 8.1. Next, $\dot{\alpha} = \dot{\alpha}(\alpha, T, \rho)$ was evaluated according to Eq. 5.15, with suitable expressions for the dissociation rates k_1^+, k_2^+ and K^*. If $\dot{\alpha} > 0$ then α was increased, otherwise α was decreased. The procedure was terminated when successive α values

Table 8.2: Flow conditions of Kewley and Hornung [91], as reported by Bird [15], and calculated downstream conditions. Here $\lambda_1 = 2\mu_1/(\rho_1 \bar{c}_1)$ is the nominal upstream mean free path from Eq. 2.39, and λ_{VHS} is the VHS mean free path from Eq. 4.21.

Upstream conditions	Equilibrium downstream conditions	
	Using K_c^* from Eq. B.2	Using K_{G}^* from Eq. B.3
$u_1 = 7.31$ km/s	$\rho^*/\rho_1 = 14.72$	$\rho^*/\rho_1 = 14.43$
$M_1 = 20.71$	$T^*/T_1 = 25.62$	$T^*/T_1 = 26.23$
$\rho_1 = 7.48 \times 10^{-3}$ kg/m^3	$\alpha^* = 0.486$	$\alpha^* = 0.479$
$T_1 = 300$ K	$n^*/n_1 = 21.88$	$n^*/n_1 = 21.34$
$\alpha_1 = 0$	$\Delta x/\lambda_{\text{VHS}}^* = 0.327$	$\Delta x/\lambda_{\text{VHS}}^* = 0.318$
$n_1 = 1.608 \times 10^{23}$/m^3	$\Delta t/\tau_{\text{VHS}}^* = 0.332$	$\Delta t/\tau_{\text{VHS}}^* = 0.326$
$\mu_1 = 17.90$ μPa·s		
$\bar{c}_1 = 476.1$ m/s		
$\lambda_1 = 10.052$ μm		
$(\lambda_{\text{VHS}})_1 = 7.029$ μm	Rankine-Hugoniot conditions downstream of a	
$\Delta x/(\lambda_{\text{VHS}})_1 = 0.0475$	vibrationally and chemically frozen shock	
$\Delta t/(\tau_{\text{VHS}})_1 = 0.00741$	$\rho_2/\rho_1 = 5.93, \quad T_2/T_1 = 84.34$	

differed by less than 10^{-6}. The resulting equilibrium downstream conditions are included in Table 8.2, for both $K^* = K_c^*(T)$ and $K^* = K_{\text{G}}^*(T, n)$ from Eqs. B.2 and B.3 respectively. These equilibrium conditions differ slightly from those of Bird [15].

Kewley and Hornung [91] measured densities downstream of this shock with a Mach-Zehnder interferometer. These densities have been obtained from the figures presented by Bird [15], and are contained in Table 8.3. Lilley and Macrossan [110] estimated the errors associated with these experimental values. The approximate errors in ρ/ρ_1 and x/λ_1 are ± 0.63 and ± 8 respectively.

Table 8.3: Experimental density measurements of Kewley and Hornung [91], obtained from data plotted by Bird [15]. The x co-ordinate has been normalised using the upstream nominal mean free path $\lambda_1 = 10.052$ μm from Table 8.2.

x (mm)	0	0.158	0.373	0.473	0.855	1.141
x/λ_1	0	15.7	37.1	47.1	85.1	113.5
ρ/ρ_1	7.29	9.26	11.92	12.55	13.49	14.85

8.4.2 Shock simulation details

The shock simulation domain extended a distance of $380\,(\lambda_{\text{VHS}})_1 \approx 265.7\lambda_1$ from $-41\lambda_1$ to $225\lambda_1$. It contained 8000 equally sized cells, each with 6 subcells. As will be shown in §8.4.3, downstream equilibrium conditions were not quite achieved in some calculations. However, for computational efficiency, the simulation was not extended. The DSMC

time step was $\Delta t = (\tau_{\rm VHS})_1 / 135 \approx 1.094 \times 10^{-10}$ s. The ratios $\Delta x / (\lambda_{\rm VHS})_1$, $\Delta x / \lambda^*_{\rm VHS}$, $\Delta t / (\tau_{\rm VHS})_1$ and $\Delta t / \tau^*_{\rm VHS}$ included in Table 8.2 show that both Δx and Δt were sufficiently small for DSMC calculations.

At the start of the simulation, the domain was split into upstream and downstream regions with lengths x_1 and x^* respectively. Using target of 1.176×10^6 simulator particles, these distances were used to calculate the weighting factor $W = (x_1 n_1 + x^* n^*)/1.176 \times 10^6$, which was the same for all cells. The initial upstream cells were then filled with particles at the upstream conditions, and initial downstream cells were filled with particles at the calculated equilibrium downstream conditions. During the simulation, the shock stabilisation routine [21] was invoked when the total number of particles differed by more than 12×10^3 from the initial number of 1.176×10^6. Steady state was assumed to have been reached after a time $5\,(x_1/u_1 + x^*/u^*)$, which required 185,634 time steps.

The velocities of particles entering the simulation domain across the upstream boundary were generated using the method of Lilley and Macrossan [109]. The downstream piston [21] was used for the downstream boundary.

The sampling interval was $7\Delta t$. For the upstream flow, the ratio $7u_1\Delta t/\Delta x \approx 16.8$, which means that the upstream flow travelled more than the requisite one cell width between samples. For the downstream flow, $7u^*\Delta t/\Delta x \approx 1.14$. During the approach to steady state, five flowfield samples were used to calculate the required time-averaged flow conditions in each cell. Therefore the conditions were recalculated only once in every 35 time steps, which is a minimal computational overhead. After the time-averaged conditions were recalculated, the sampling arrays were cleared. When steady state had been achieved, time-averaged conditions were still recalculated once every five sample periods, but the sampling arrays were not cleared. The simulations were run until 5000 flowfield samples were obtained, which required a total of 220,628 time steps. As shall be shown in Fig. 8.8, the mean numbers of particles in the upstream and downstream flows were about 9 and 195 respectively. Therefore the upstream and downstream sample sizes were approximately 45×10^3 and 975×10^3 respectively. The shock stabilisation routine [21] was invoked before each sample was recorded.

8.4.3 Shock simulation results

Downstream density profiles obtained using the TCE and TCER models and the macroscopic method are shown in Fig. 8.2. The origin of the x-axis has been set to the point where $\rho/\rho_1 = 5.93$, which is the frozen Rankine-Hugoniot density ratio given in Table 8.2. The x co-ordinate was normalised using the nominal upstream mean free path $\lambda_1 = 10.052$ μm from Table 8.2. The experimental density measurements obtained by Kewley and Hornung [91] are included in Fig. 8.2, with the error estimates of Lilley and Macrossan [110]. Both DSMC solutions give reasonable agreement with the experimental results. Also, there is good agreement between the results of the TCE and TCER models and the

macroscopic method. It could be argued that this agreement was expected, because the flow was close to thermal equilibrium in the chemical relaxation region downstream of the shock, and that this case is not a rigorous test of the macroscopic method. A comparison of the solutions within the shock, were highly non-equilibrium conditions exist, is a more rigorous test.

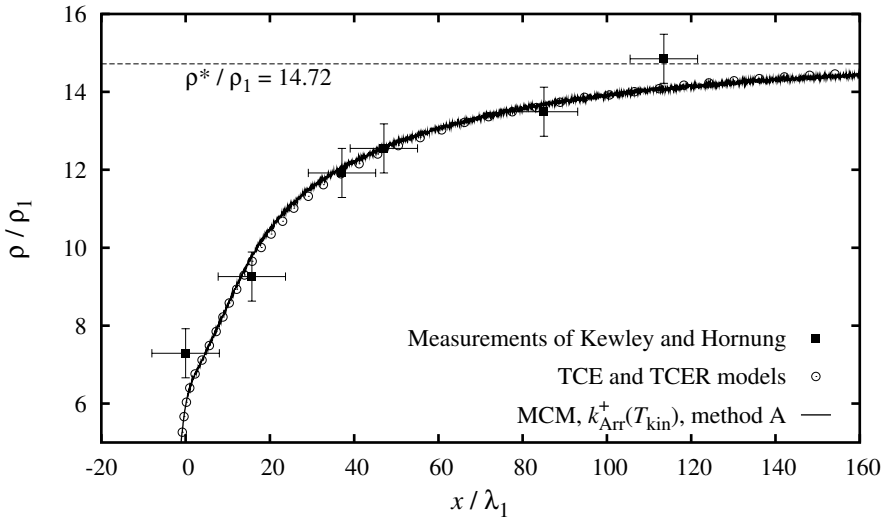

Figure 8.2: Profiles of density ratio ρ/ρ_1 downstream of strong shock in nitrogen, calculated using the TCE and TCER models and the macroscopic method. The nitrogen dissociation rates of Kewley and Hornung [91] were used, as given in Table B.3. The experimental density measurements of Kewley and Hornung, as reported by Bird [15], are included with approximate error bars [110].

Normalised profiles of ρ, the various kinetic temperature and α within the shock are given in Fig. 8.3. The normalised density $\hat{\rho}$ is defined by

$$\hat{\rho} \equiv (\rho - \rho_1) \,/\, (\rho^* - \rho_1)\,,$$

and likewise for the kinetic temperatures and α. The origin of the x-axis was set as in Fig. 8.2. At the origin, $\hat{\rho} = 0.359$. The profiles show that non-equilibrium conditions prevail within the shock. Despite the non-equilibrium conditions, there is still good agreement between the profiles provided by the TCE and TCER models and the macroscopic method.

For the same shock conditions, Lilley and Macrossan [110] used larger cells $\Delta x/\lambda^*_{\rm VHS} \approx 0.654$ and a longer time step $\Delta t/\tau^*_{\rm VHS} \approx 0.6$. Despite the fact that these are larger than recommended for DSMC calculations, the detailed shock structure reported by Lilley and Macrossan is essentially identical to that shown in Fig. 8.3.

For the shock calculated with the TCE and TCER models, profiles of $\hat{\rho}$, $\hat{\alpha}$ and $\hat{T}_{\rm kin}$ near the downstream limit of the simulation domain are shown in Fig. 8.4. For clarity, a 51-point moving filter was applied to smooth the profiles, with a reduced number of points near the downstream boundary. Despite the scatter, it is apparent that the solution obtained using the TCE and TCER models gives profiles that overshoot the calculated

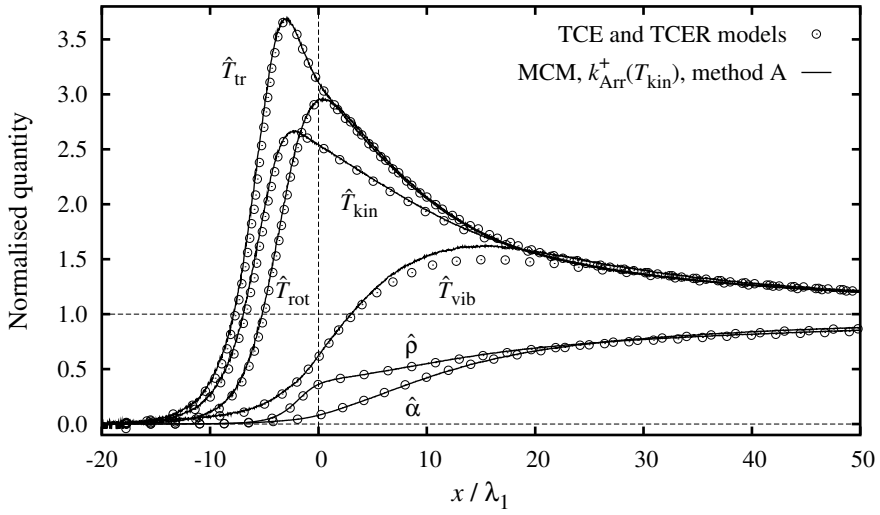

Figure 8.3: Profiles of normalised quantities $\hat{\rho}$, $\hat{T}_{\rm tr}$, $\hat{T}_{\rm rot}$, $\hat{T}_{\rm vib}$, $\hat{T}_{\rm kin}$ and $\hat{\alpha}$ within a strong shock in nitrogen, calculated using the TCE and TCER models and the macroscopic method. The nitrogen dissociation rates of Kewley and Hornung [91] were used, as given in Table B.3.

downstream equilibrium conditions at $x/\lambda_1 \approx 212$. This contrasts with the expected behaviour where the profiles should approach the calculated equilibrium downstream conditions asymptotically. This failure to achieve the expected downstream conditions is a consequence of the difference between the Arrhenius rates and the actual rates realised by the DSMC implementation of the TCE and TCER models, as discussed in §6.3.1 and §6.5.1. The downstream profiles calculated with the macroscopic method are also shown in Fig. 8.4, and show that the expected behaviour where the profiles approach the calculated equilibrium downstream conditions asymptotically.

During the shock solution with the TCE and TCER models, the number of reactions with $P_R > 1$ was recorded. For dissociation reactions 1 and 2 calculated with the TCE model, the respective percentages of events with $\left(P_R^+\right)_{\rm TCE} > 1$ were 0.041% and 0.012%. For the recombination reactions calculated with the TCER model, the respective percentages of events with $P_R^- > 1$ were 3.01% and 4.91%.

The α profiles calculated using the two-temperature model $k^+ = k^+_{2T}\left(T_{\rm tr+rot}, T_{\rm vib}, s\right)$ and the rates of Park [138] are shown in Fig. 8.5. The profile calculated using $k^+ = k^+_{\rm Arr}\left(T_{\rm kin}\right)$ is also shown. These profiles show that the two-temperature model can capture the delay in dissociation expected from DV coupling, as compared to the single temperature rate with $k^+ = k^+_{\rm Arr}\left(T_{\rm kin}\right)$. For these calculations, the downstream profiles of ρ/ρ_1 are shown in Fig. 8.6. It appears that the two-temperature rate with $s = 0.5$ gives better agreement with the experimental measurements of Kewley and Hornung [91] than $s = 0.7$. Note that the profiles in Fig. 8.6 differ slightly from those of Lilley and Macrossan [110], due to the use of method B to select dissociation diatoms instead of method A.

Fig. 8.2 shows that DSMC solutions obtained using the rates of Kewley and Hornung [91], without any consideration of DV coupling, give reasonable agreement with the experimental results. This suggests that these rates implicitly include the effects of DV

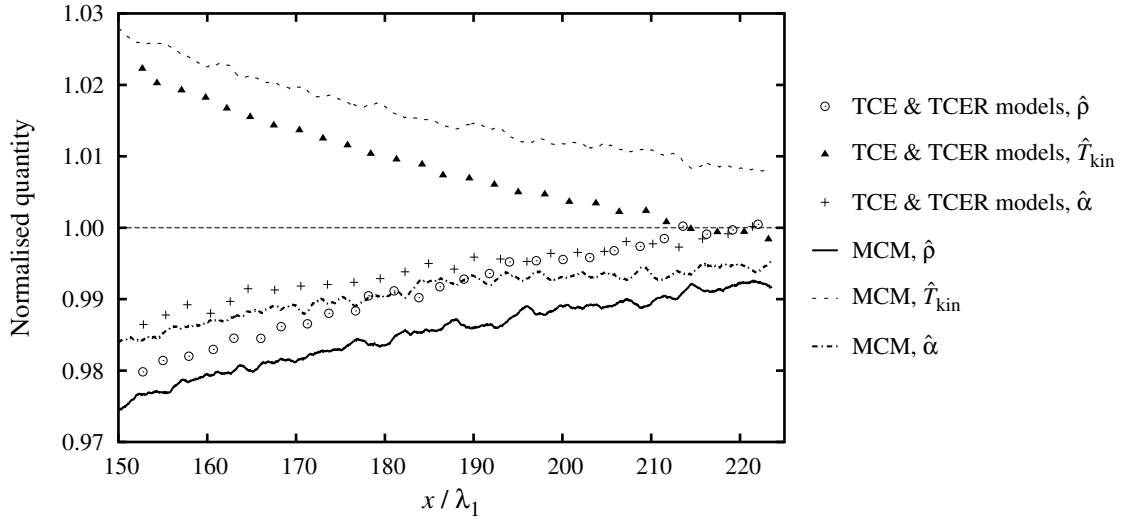

Figure 8.4: Profiles of normalised conditions $\hat{\rho}$, $\hat{T}_{\text{kin}}$ and $\hat{\alpha}$ downstream of a strong shock in nitrogen. Some smoothing has been applied for clarity, as detailed in §8.4.3. The solution obtained with the macroscopic method displays the expected behaviour in which the profiles approach the calculated equilibrium conditions asymptotically. The profiles obtained with the TCE and TCER models do not achieve the equilibrium downstream conditions, because they overshoot the calculated equilibrium state at $x/\lambda_1 \approx 212$, rather than approach the equilibrium state asymptotically.

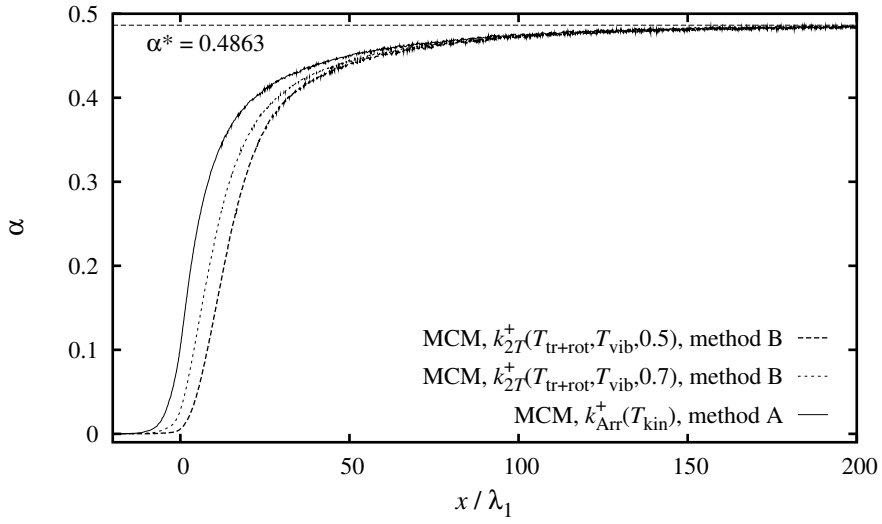

Figure 8.5: Profiles of α downstream of strong shock in nitrogen, calculated using the macroscopic method with the two-temperature model [137]. The nitrogen dissociation rates of Park [138] were used, as given in Table B.3.

coupling downstream of the shock, and therefore apply only where there is a high degree of vibrational non-equilibrium [32]. For conditions near thermal equilibrium, Boyd [32] recommends the rates of Byron [44].

As shown in Fig. B.7, the difference between $K_c^*(T)$ and $K_{\text{G}}^*(T,n)$ is largest at high temperatures and low densities, which are the conditions of interest in hypersonic rarefied flows. Because K^* effectively controls the recombination rate, and because the recombination rate is low within the shock, the use of K_{G}^* rather than K_c^* should have a minimal effect on the internal shock structure. The profiles from the calculations using the macro-

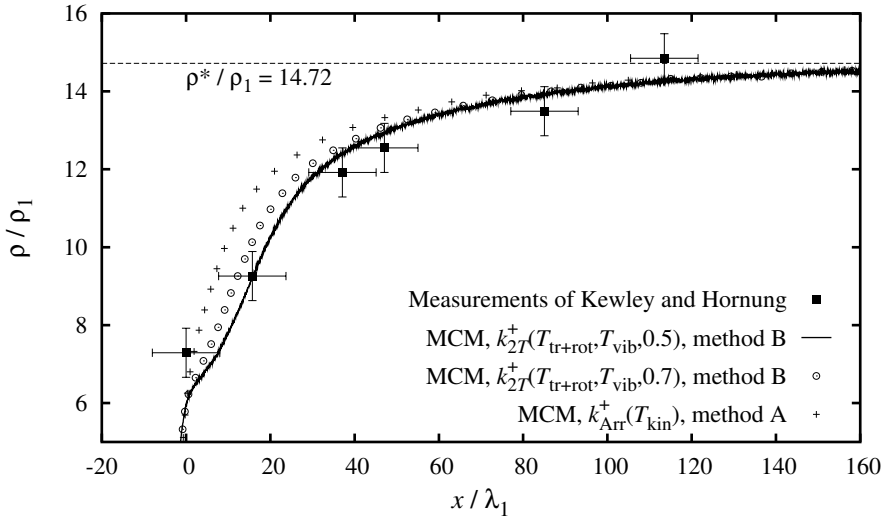

Figure 8.6: Profiles of density ratio ρ/ρ_1 downstream of strong shock in nitrogen, calculated using the macroscopic method. The nitrogen dissociation rates of Park [138] were used, as given in Table B.3. The experimental density measurements of Kewley and Hornung [91], as reported by Bird [15], are included with approximate error bars [110].

scopic method with K_c^* and K_G^* are shown in Fig. 8.7. In this representation, $\hat{T}_{kin}$ and $\hat{\alpha}$ are plotted versus $\hat{\rho}$ to emphasise differences between the profiles within the shock, where the density gradient is high. The results in Fig. 8.7 were normalised using the downstream conditions calculated with K_c^*. These results confirm that under conditions that are primarily dissociative, such as those within a strong shock, the number density dependence of K^* has little effect on the macroscopic flowfield.

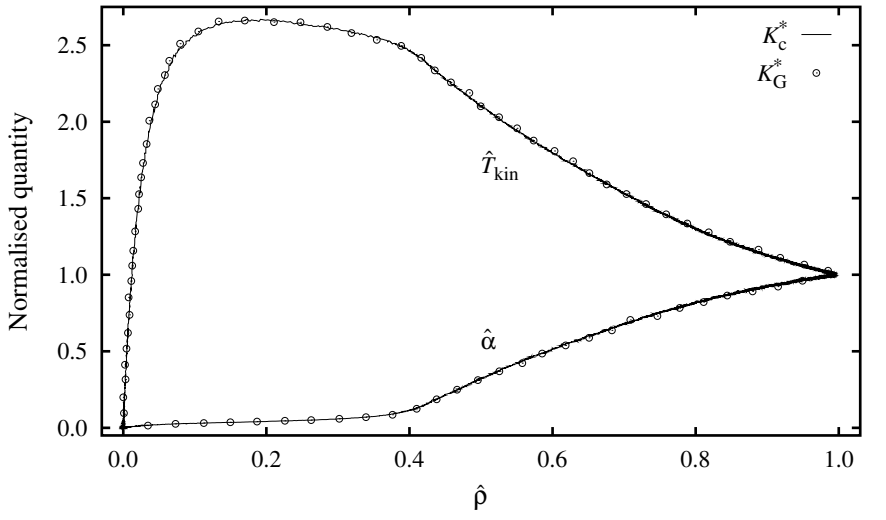

Figure 8.7: Comparison of $\hat{T}_{kin}$ and $\hat{\alpha}$ within shock, calculated using the macroscopic method with both $K_c^*(T)$ and $K_G^*(T,n)$. $\hat{T}_{kin}$ and $\hat{\alpha}$ are plotted versus $\hat{\rho}$ to emphasise differences where the density gradient is high.

The mean number of particles per cell $\bar{N}$ during steady state sampling is shown in Fig. 8.8 for the solution obtained using the TCE and TCER models. In the upstream flow, $\bar{N} \approx 9$. This is lower than the minimum $10 \lesssim \bar{N} \lesssim 20$ recommended by Bird [21]. $\bar{N}$

increases rapidly through the shock, so it can be argued that the relatively small $\bar{N} \approx 9$ in the upstream flow will not cause significant errors.

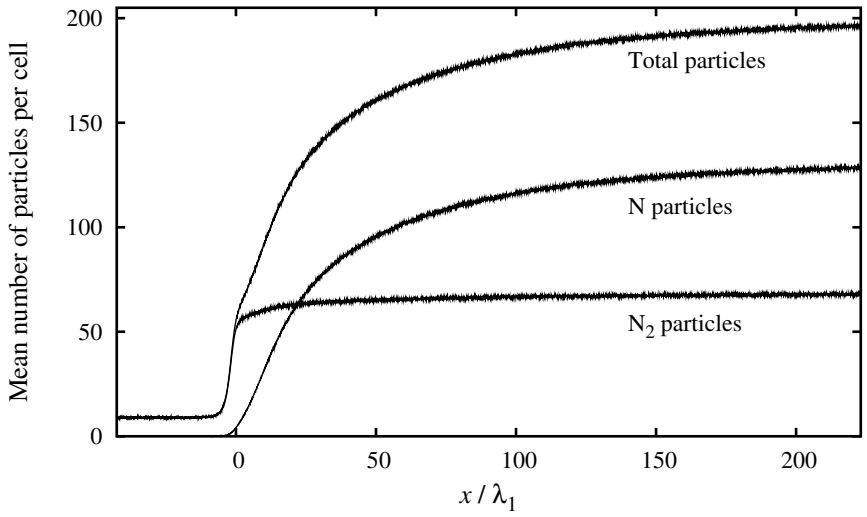

Figure 8.8: Mean number of particles per cell for shock simulations performed with the TCE and TCER models.

8.4.4 Vibrational relaxation number in shock

As noted in §8.2, using a constant $\phi_{\text{vib}} = 0.01$ in the BL vibrational energy exchange procedure results in unrealistic temperature dependent vibrational relaxation behaviour. This is due to the temperature dependence of ζ_{vib}. Using the kinetic temperatures through the shock, as computed with the TCE and TCER models, the vibrational relaxation numbers Z_{vib} have been calculated for $N_2 + N_2$ and $N_2 + N$ collisions. Gimelshein *et al.* [65] give a method for finding Z_{vib}, as given by Eqs. 4.33 and 4.34. The profiles of Z_{vib}, presented in Fig. 8.9, show an increase in Z_{vib} through the shock as the temperature increases. This is opposite to the expected behaviour discussed in §2.8 where Z_{vib} generally decreases with temperature. Although this effect is physically unrealistic, it does not detract from the testing of the macroscopic chemistry method. The small difference in the two curves shown in Fig. 8.9 is due to the different ζ_g values for each collision.

8.5 Blunt cylinder in rarefied dissociating nitrogen

This section examines the flow of hypersonic rarefied dissociating nitrogen over an axisymmetric blunt cylinder. The main purpose of the simulations was to test the performance of the macroscopic method against the conventional collision-based DSMC chemistry models under thermal non-equilibrium conditions. §8.5.1 gives the flow conditions, and details of the DSMC code are discussed in §8.5.2. The following blunt cylinder calculations were performed:

- Flow without chemistry

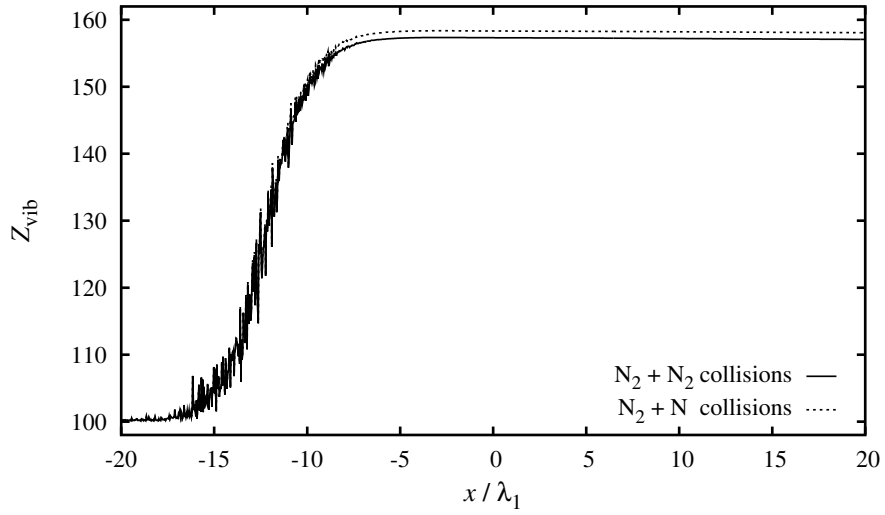

Figure 8.9: Profile of Z_{vib} through strong shock in dissociating nitrogen resulting from a constant $\phi_{\text{vib}} = 0.01$. The shock was calculated using the TCE and TCER models. Only $-20 \leq x/\lambda_1 \leq 20$ is shown, where steep flow gradients exist.

- Conventional TCE model for dissociation reactions. The TCE parameters β_{TCE} and χ_2 were obtained from the nitrogen dissociation rates of Kewley and Hornung [91]. Initially, a simulation was performed using the TCE model with the TCER model for recombination reactions. The TCER parameters κ and n_r were calculated using $K_c^*(T)$ from Eq. B.2. This initial simulation showed that recombination events were extremely rare in this case. For computational efficiency, recombination events were therefore ignored in subsequent blunt cylinder simulations. This flow was considered by Lilley and Macrossan [110, 106].

- Macroscopic method with $k^+ = k^+_{\text{Arr}}(T_{\text{kin}})$ and the nitrogen dissociation rates of Kewley and Hornung [91]. When recombination events are ignored $K^* \to \infty$, so Eq. 5.16 was used to calculate $\dot{\alpha}$. Dissociating particles were selected according to method A where $P_s = \epsilon_{\text{int}} / (\epsilon_{\text{int}})_{\text{max}}$. This flow was considered by Lilley and Macrossan [110, 106].

- Macroscopic method with $k^+ = k^+_{2T}(T_{\text{tr+rot}}, T_{\text{vib}}, s)$ using $s = 0.5$ and 0.7 and the nitrogen dissociation rates of Kewley and Hornung [91]. Again, recombination events were ignored by using Eq. 5.16 to calculate $\dot{\alpha}$. These calculations were performed to demonstrate that the macroscopic method can capture the expected effects of DV coupling, which include increased surface heat fluxes and reduced dissociation rates. Both method A with $P_s = \epsilon_{\text{int}} / (\epsilon_{\text{int}})_{\text{int}}$ and method B with $P_s = \left(\frac{1}{2} + q\right)/33$ were used to select dissociating diatoms. This flow was also considered by Lilley and Macrossan [106].

- Conventional VFD model, as presented in §6.4.1. The VFD parameters β_{VFD} and ψ were obtained from the nitrogen dissociation rates of Kewley and Hornung [91]. ϕ

values of 0, 0.1, 0.5, 1, 2, 3 and 4 were used to test the extent to which ϕ can control DV coupling. Recombination reactions were also ignored in these calculations. Calculations were performed using both $\epsilon_{\text{vib}} = qk\Theta_{\text{vib}}$, as proposed in the original VFD model [73, 74] and $\epsilon_{\text{vib}} = \left(\frac{1}{2} + q\right) k\Theta_{\text{vib}}$. As will be shown in §6.4.1, the latter form avoids the low reaction rates obtain when using the VFD model with a quantised vibration model in vibrationally cold flows.

- Conventional TLD model, as presented in §6.4.2. Following Boyd [37], $(A_{\text{TLD}})_1 = 14$ and $(A_{\text{TLD}})_2 = 5$ were used for reactions 1 and 2 respectively. Recombination reactions were ignored. This case was also considered by Lilley and Macrossan [106].

- Macroscopic method using the fitted TLD rates for nitrogen, as calculated in §C.7. For reactions 1 and 2 in nitrogen, the curve fits

$$\begin{aligned} k_1^+ &\approx 2.0 \times 10^{12} (T/122000)^{-1.1} \exp(-122000/T) \quad \text{m}^3/\text{kmol/s} \quad \text{and} \\ k_2^+ &\approx 9.5 \times 10^{11} (T/120500)^{-1.3} \exp(-120500/T) \quad \text{m}^3/\text{kmol/s} \end{aligned}$$

accurately approximate the calculated rates. To capture the effects of DV coupling, the two-temperature model $k^+ = k_{2T}^+ (T_{\text{tr+rot}}, T_{\text{vib}}, s)$ was used. Here $s = 0.9$ was used, which was found by running test simulations with various s values. Both method A with $P_s = \epsilon_{\text{int}} / (\epsilon_{\text{int}})_{\text{max}}$ and method B with $P_s = \left(\frac{1}{2} + q\right) /33$ were used to select dissociating diatoms. This case was examined to demonstrate that the macroscopic method can capture the TLD flowfield with reasonable accuracy. This case was also considered by Lilley and Macrossan [106].

Results for these simulations are presented and discussed in §8.5.3 to §8.5.9.

The general flowfield features observed in the flow over a blunt cylinder will be similar to those for other blunt entry bodies. For hypersonic flows over blunt cylinders where $\text{Kn} \gtrsim 0.01$, the shock wave merges with the thick viscous boundary layer [79], and a monotonic density increase is observed along the stagnation streamline up to the face [81] such that no discrete shock exists. Such flows have a significant region of thermal non-equilibrium and a thick shock layer with an extensive stagnation region. The density at the cylinder face is orders of magnitude higher than ρ_∞, particularly if the body has a cold wall. The high densities result in a high collision rate such that local thermal equilibrium conditions prevail near the body. According to Bird [21], a cold wall decreases the shock stand-off distance relative to that for an adiabatic wall. Experimental and computational studies of hypersonic rarefied flow over a blunt cylinder have been reported by Metcalf *et al.* [132], Pullin *et al.* [142], Macrossan [119], Davis *et al.* [53], Harvey [79], Dominy [55], Harvey *et al.* [80], Gilmore and Harvey [64], Marriott [127] and Bird [21].

8.5.1 Freestream conditions, surface properties and rarefaction parameters

To test the various DSMC chemistry models, a rarefied reacting flowfield is required. High altitude atmospheric entry at superorbital speeds produces such flowfields. Higher density freestream conditions usually result in extensive flowfield chemistry, but require long computation times when using the DSMC method. Lower densities give less chemistry but can be computed quickly. The requirement is to select freestream conditions that result in flowfields with a significant degree of dissociation that can still be computed within a convenient time using the DSMC method.

To characterise the extent of dissociation in the blunt cylinder flow, it is useful to examine an approximate Damköhler number Da for the flow, defined by

$$\mathrm{Da} \equiv t_{\mathrm{flow}}/t_{\mathrm{chem}}.$$

Here,

$$t_{\mathrm{flow}} = r_c/u_2 \quad \text{and} \quad t_{\mathrm{chem}} = 1/\dot{\alpha}$$

were used to obtain Da, where u_2 is the flow speed downstream of a normal shock. For frozen chemistry Da $= 0$, and for equilibrium chemistry Da $\to \infty$. A cylinder radius $r_c = 0.5$ metres was used.

Here, $\dot{\alpha}$ was calculated with the temperature downstream of a vibrationally and chemically frozen normal shock, with the nitrogen dissociation rates of Kewley and Hornung [91] and $K^* = K_c^*(T)$ from Eq. B.2. This approximate Damköhler number is related to the reaction rate parameter R_p of Macrossan *et al.* [124] by $\mathrm{Da} = 1/(2R_p)$. Atmospheric conditions at altitudes of 90 km, 95 km and 100 km, with $u_\infty = 10$ km/s, were used for ρ_∞ and T_∞, as shown in Table 8.4.

Table 8.4: Temperatures, densities and approximate Damköhler numbers at various altitudes. The calculations used the nitrogen dissociation rates of Kewley and Hornung [91] and $K^* = K_c^*(T)$ from Eq. B.2. The cylinder radius $r_c = 0.5$ metres.

Altitude (km)	Source	ρ_∞ (kg/m^3)	T_∞ (K)	Da
90	Gerhart *et al.* [63]	3.17×10^{-6}	180.7	0.186
95	Mean of values at 90 km and 100 km	1.835×10^{-6}	195.35	0.108
100	Seinfeld and Pandis [144]	4.99×10^{-7}	210	0.029

The approximate Damköhler numbers shown in Table 8.4 indicate that significant non-equilibrium chemistry will occur at altitudes of 90 km and 95 km. At 100 km, chemistry will be practically frozen. The freestream conditions at 95 km altitude were selected for the blunt cylinder calculations, because this case requires less computation time than the 90 km case. These freestream conditions are the same as those used by Lilley and Macrossan

[110, 106]. The stagnation enthalpy is $h_0 = h_\infty + u_\infty^2/2 \approx 50.2$ MJ/kg. The ratio of h_0 to the specific dissociation energy $R_{N_2}\Theta_d$ is about 1.5, which shows that the flow energy is sufficient for significant dissociation.

Table 8.5: Freestream conditions for blunt cylinder calculations. The subscript 2 refers to Rankine-Hugoniot conditions behind a vibrationally and chemically frozen shock at $M_\infty = 35.1$. Here $\mu_\infty = \mu_r(T_\infty/T_r)^{1/2+\upsilon}$ is the freestream viscosity for VHS molecules calculated with T_r, μ_r and υ for N_2 from Table B.1.

ρ_∞	=	1.835×10^{-6} kg/m^3	μ_∞	=	11.16 μPa·s
T_∞	=	195.4 K	$(\lambda_{VHS})_\infty$	=	2.563×10^{-2} m
u_∞	=	10 km/s	Kn_∞	=	0.026
α_∞	=	0	B_∞	=	0.91
p_∞	=	0.106 Pa	Ch	=	0.66
M_∞	=	35.10	T_2/T_∞	=	240.5
n_∞	=	3.944×10^{19}/m^3	ρ_2/ρ_∞	=	5.98

A hot wall at $T_{wall} = 1000$ K was used. This gave densities in the stagnation region that were lower than those resulting from a cold wall at $T_{wall} \sim 300$ K. This avoided the long computation times required when performing DSMC calculations for high density flows. Fully diffuse reflection was assumed.

For this flow, the rarefaction parameters Kn_∞, B_∞ and Ch, as introduced in Chapter 3, are shown in Table 8.5. Here Kn_∞ and B_∞ were calculated with Eqs. 3.1 and 3.6 respectively, with the mean free path for VHS molecules $(\lambda_{VHS})_\infty$ from Eq. 4.21. The length scale was the cylinder diameter $2r_c = 1$ metre. Cheng's parameter Ch was calculated with Eq. 3.7. In calculating Ch, it was assumed that $T^* = (T_{wall} + T_2)/2$, where T^* is the temperature characteristic of the shock layer. The viscosity at this temperature $\mu^*(T^*)$ was evaluated with a power law viscosity relation which applies for VHS molecules. The parameters T_r, μ_r and υ for N_2 from Table B.1 were used to calculate μ^*. From the classification schemes discussed in §3.5, Kn_∞, B_∞ and Ch all show that the flow was rarefied and that significant departures from equilibrium conditions are expected. The freestream Reynolds number $\mathrm{Re}_\infty = \rho_\infty u_\infty (2r_c)/\mu_\infty = 1644$, which is in the laminar regime.

8.5.2 Blunt cylinder simulation details

The simulation geometry is shown in Fig. 8.10. The simulation domain contained of two rectangular regions and two radial regions. The grid details are summarised below. The simulation contained 60,601 cells in total.

- Region 1 was a rectangular region that contained 180×200 cells in the $z \times r$ directions. Cells were spaced equally in the r direction. A geometric progression in cell sizes was used in the z direction, with smaller cell sizes near the cylinder. The ratio of

adjacent Δz values was 1.0152.

- Region 2 was a radial region that contained 180×90 cells in the $d \times \theta$ directions, where d denotes the radial direction and θ the angular direction. The region was centred at $(0, r_c)$, but started at a distance of $r_c/100$ from this centre to accommodate region 4. Cells were spaced equally in the θ direction. A geometric progression in cell sizes was used in the d direction, and the ratio of adjacent Δd values was 1.01.

- Region 3 was a rectangular region that contained 70×120 cells in the $z \times r$ directions. Geometric progressions in cell sizes were used in both directions. The ratio of adjacent cell sizes was 1.01 in both the z and r directions.

- Region 4 was a small radial region that contained a single cell. The region was the upper left quadrant centred at $(0, r_c)$ with a radius $r_c/100$. This region was used to avoid the very small cell sizes associated with extending region 2 to the cylinder edge at $(0, r_c)$.

- The cylinder face was divided into 200 surface cells, spaced equally between 0 and r_c. These cells were aligned with the cells in region 1.

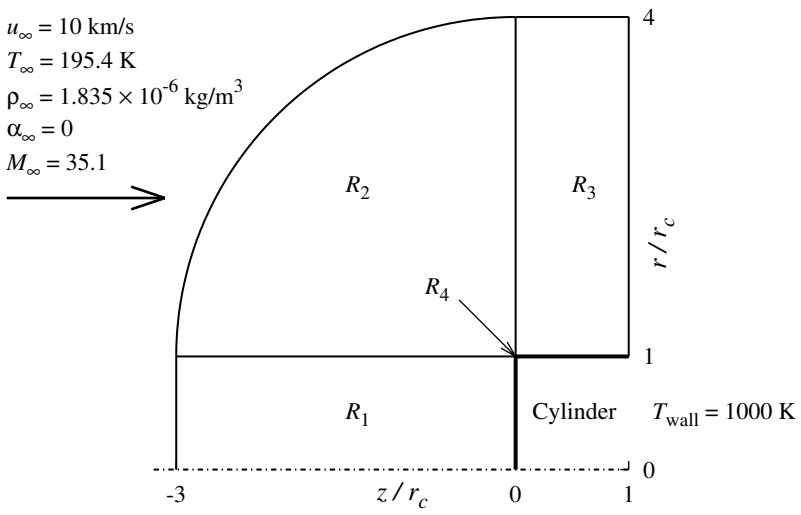

Figure 8.10: Blunt cylinder simulation geometry. The cylinder radius $r_c = 0.5$ metres. Flow is from left to right. R_i denotes region i.

The blunt cylinder calculations used the time step

$$\Delta t = \tau_2/8 = 3.743 \times 10^{-7} \text{ s},$$

where τ_2 is the mean VHS collision time behind a vibrationally and chemically frozen shock at $M_\infty = 35.10$. The sample period was $7\Delta t$. During the approach to steady state, macroscopic properties were recalculated for every 5 flowfield samples.

Cell-based weighting factors were used. These weighting factors were calculated so that the mean number of particles $\bar{N}$ in each cell during steady state was close to 20.

This is the upper end of the recommended range $10 \lesssim \bar{N} \lesssim 20$ [21]. To obtain the weighting factors, a non-reacting simulation was first performed with cell-based weighting factors proportional to the radial distance of the cell centroid from the axis. These initial weighting factors, the mean number of particles in each cell at steady state and the final conditions in each cell were written to a file at the end of the simulation. For subsequent simulations, these weighting factors and particle numbers were read by the program, and the weighting factor for each cell was then calculated using

$$W_{\text{new}} = W_{\text{saved}} N_{\text{saved}} / N_{\text{target}}.$$

$N_{\text{target}} = 20$ was used. The saved final conditions from the first simulation were used to generate the initial particles in each cell, assuming equilibrium velocity and internal energy distributions. Cell-based weighting factors were adjusted by rounding $\ln W_{\text{new}}$ to the nearest 0.2 and then recalculating W_{new}. This meant that adjacent cells with close weighting factors had W_{new} adjusted to the same value. This saved some computation time, because particles were tested less often for cloning or deletion, because they moved into a cell with a different weighting factor less often. Cloned particles were delayed as discussed in §4.2.5. Subcells were not used in the blunt cylinder simulations.

The method of Lilley and Macrossan [109] was used to generate the z velocities of particles entering the simulation domain across the upstream and top boundaries. Some care was required to calculate the positions of particles entering the domain across the circular boundary of region 2. Firstly, the radial co-ordinate of the particle r_e was generated using Eq. 4.4, where $r_{\min}$ and $r_{\max}$ refer to the minimum and maximum radial co-ordinates of the cell boundary, respectively. The z co-ordinate of the entry point is then $z_e = -\left(r_c^2 - r_e^2\right)^{1/2}$. The z co-ordinate of the new particle was then given by $R_f \Delta t v_z - z_e$. This may place the particle in a cell different to the cell through which it entered the simulation domain. In such cases, standard routines were used for cloning and deletion. Particles entering the domain across the downstream boundary were ignored.

For all blunt cylinder calculations, the total number of particles in the simulation and the total energy of all particles was plotted to determine the number of time steps required to attain steady state. An example is given in Fig. 8.25 in §8.5.4. The time required to achieve steady state was about $10 \times 4r_c/u_\infty$, where $4r_c$ is the length of the simulation domain in the z direction. This required 5384 time steps. 5000 flowfield samples were obtained at steady state, so the final sample size was about 10^5 particles per cell. The simulation continued for a total of 40378 time steps.

8.5.3 Flow without chemistry

For the blunt cylinder flowfield without chemistry, the stagnation streamline profiles of ρ/ρ_∞, T_z/T_∞, T_r/T_∞, T_θ/T_∞, T_{tr}/T_∞, T_{rot}/T_∞ and T_{vib}/T_∞ are shown in Fig. 8.11. The conditions along the stagnation streamline are approximated by the conditions in the

row of cells adjacent to the axis. The profiles show the behaviour expected for a non-equilibrium blunt body flowfield. In particular, the disparate kinetic temperature profiles illustrate the expected high degree of non-equilibrium between the various molecular energy modes.

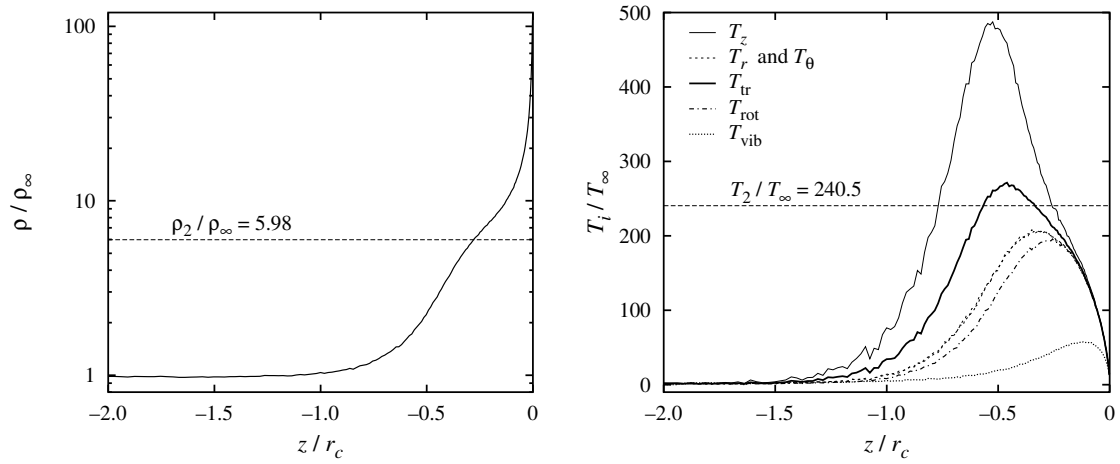

Figure 8.11: Stagnation streamline profiles of ρ/ρ_∞ and kinetic temperatures for non-reacting blunt cylinder simulation. The upstream simulation domain is only shown from $z/r_c = -2$.

Force and heat transfer coefficients may be defined by

$$C_{F_i} \equiv \frac{F_i / \left(\pi r_c^2\right)}{\rho_\infty u_\infty^2 / 2} \quad \text{and} \quad C_H \equiv \frac{\dot{Q}}{\rho_\infty u_\infty^3 / 2}$$

respectively, where F_i is a force acting on the surface and $\dot{Q}$ is the heat transfer rate. During steady state, the total momentum and heat transferred to the cylinder face were recorded, and used to calculate F_i and $\dot{Q}$. The drag coefficient C_D is associated with the normal force $D = F_z$. $(C_F)_r$ and $(C_F)_\theta$ are the force coefficients in the r and θ directions respectively. For the blunt cylinder case without flowfield chemistry, the drag and heat transfer coefficients are shown in Table 8.6. Profiles of $(C_F)_i$ and C_H across the face are shown in Fig. 8.12. Near the axis, the gradients in $(C_F)_i$ and C_H are small, which indicates that axis problems associated with the use of cell-based weighting factors [21] are not apparent in the code developed for this study.

An indication of the extent of translational non-equilibrium can be obtained by comparing the theoretical number of collisions to the number actually performed by the DSMC computation at steady state, denoted $N_{\text{colls}}^{\text{DSMC}}$. From Eq. 4.19, the number of collisions that should occur between particles of species A and particles of species B during a sampling interval $(\Delta t)_s$ is

$$N_{\text{colls}}^{\text{theory}} \approx \frac{\Xi \bar{N}_\text{A} \bar{N}_\text{B}}{f_s} \left(\frac{T_{\text{tr}}}{T_r}\right)^{\frac{1}{2}-\upsilon} \frac{W(\Delta t)_s}{V_c},$$

where $\bar{N}_s$ is the mean number of species s particles in the cell during $(\Delta t)_s$, W is the cell-based weighting factor and V_c is the cell volume. For the non-reacting blunt cylinder

Table 8.6: Surface fluxes and relative CPU requirements for blunt cylinder calculations. For method A, dissociating diatoms were selected with probability $P_s = (\epsilon_{\rm int})_{\rm max}/\epsilon_{\rm int}$. For method B, dissociating diatoms were selected with probability $P_s = \left(\frac{1}{2} + q\right) k\Theta_{\rm vib}$. CPU requirements are discussed in §8.9.

Chemistry model	Rate data	C_D	C_H	Relative CPU time
No chemistry	–	1.772	0.289	1
Conventional TCE model	Kewley & Hornung	1.772	0.233	1.05
MCM, $k^+_{\rm Arr}(T_{\rm kin})$, method A	Kewley & Hornung	1.770	0.234	1.06
MCM, $k^+_{2T}(T_{\rm tr+rot}, T_{\rm vib}, 0.5)$, method A	Kewley & Hornung	1.772	0.275	0.98
MCM, $k^+_{2T}(T_{\rm tr+rot}, T_{\rm vib}, 0.5)$, method B	Kewley & Hornung	1.772	0.279	0.96
MCM, $k^+_{2T}(T_{\rm tr+rot}, T_{\rm vib}, 0.7)$, method A	Kewley & Hornung	1.771	0.259	1.04
MCM, $k^+_{2T}(T_{\rm tr+rot}, T_{\rm vib}, 0.7)$, method B	Kewley & Hornung	1.770	0.261	1.01
Conventional VFD model, $\phi = 0$	Kewley & Hornung	1.772	0.232	1.10
Conventional VFD model, $\phi = 0.1$	Kewley & Hornung	1.772	0.236	1.04
Conventional VFD model, $\phi = 0.5$	Kewley & Hornung	1.770	0.253	1.05
Conventional VFD model, $\phi = 1$	Kewley & Hornung	1.771	0.264	1.04
Conventional VFD model, $\phi = 2$	Kewley & Hornung	1.772	0.271	1.04
Conventional VFD model, $\phi = 3$	Kewley & Hornung	1.770	0.273	1.00
Conventional VFD model, $\phi = 4$	Kewley & Hornung	1.770	0.274	1.03
Conventional TLD model	–	1.788	0.163	1.21
MCM, $k^+_{\rm Arr}(T_{\rm kin})$, method A	Fitted TLD rates	1.792	0.143	1.33
MCM, $k^+_{2T}(T_{\rm tr+rot}, T_{\rm vib}, 0.9)$, method A	Fitted TLD rates	1.787	0.155	1.26
MCM, $k^+_{2T}(T_{\rm tr+rot}, T_{\rm vib}, 0.9)$, method B	Fitted TLD rates	1.787	0.158	1.28

calculations, Fig. 8.13 shows the collision rate ratio $\theta \equiv N^{\rm DSMC}_{\rm colls}/N^{\rm theory}_{\rm colls}$ for $N_2 + N_2$ collisions. The results show near-equilibrium conditions in the freestream and near the body, and non-equilibrium conditions within the diffuse shock, as expected.

Fig. 8.14 shows contours of the mean number of particles per cell. As required, the mean number was close to 20 [21]. The pattern of contours in Fig. 8.14 is a direct result of the procedure used to round $W_{\rm new}$ to improve computational efficiency, as described in §8.5.2. Note that the gaps between regions 1 and 2 and between regions 2 and 3 that appear in this and later contour plots are an artifact of the data presentation method, and did not actually exist in the DSMC calculation. Fig. 8.15 shows contours of the ratio $\Delta t/\tau_{\rm VHS}$ in each cell. The mean VHS collision time $\tau_{\rm VHS} = 1/\nu_{\rm VHS}$ was calculated using Eqs. 4.18 and 2.35 with the local translational kinetic temperature $T_{\rm tr}$ instead of T. Fig. 8.16 shows contours of the ratio $(\Delta x)_{\rm max}/\lambda_{\rm VHS}$. For each cell, a local VHS mean free path $\lambda_{\rm VHS}$ was calculated using Eq. 4.20 with $T_{\rm tr}$ instead of T. Here, $(\Delta x)_{\rm max}$ is the maximum cell dimension.

As noted in §4.2.1, the ratios $(\Delta x)_{\rm max}/\lambda_{\rm VHS}$ and $\Delta t/\tau_{\rm VHS}$ should both be less than 1/3. Figs. 8.15 and 8.16 show that these criteria are violated near the cylinder face. The criterion $(\Delta x)_{\rm max}/\lambda_{\rm VHS} < 1/3$ is also violated in the freestream. The violations near the

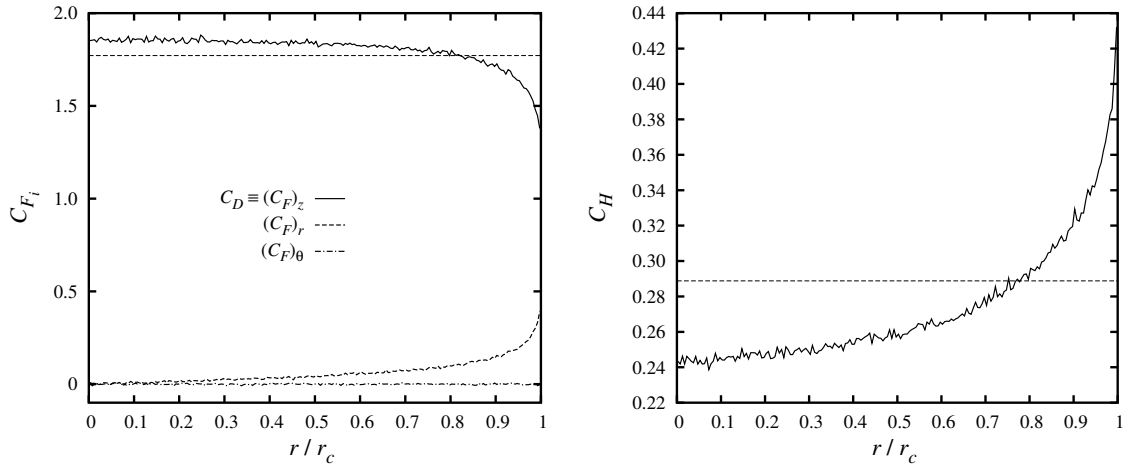

Figure 8.12: Profiles of force coefficients $(C_F)_i$ and heat transfer coefficients C_H across cylinder face for non-reacting flow. The force coefficient in the axial direction $(C_F)_z$ is the drag coefficient C_D. The face was divided into 200 equally sized surface cells.

face are due to the high densities and hence high collision rates and small mean free paths in that region. The region with $\Delta t/\tau_{\rm VHS} > 1/3$ is limited to a zone about $0.035 r_c$ from the cylinder face. More discussion on the issue of $(\Delta x)_{\rm max}/\lambda_{\rm VHS}$ is given in §8.8. The cell sizes and time step could be reduced with an attendant increase in computational expense, but for the purposes of this study, these problems have been ignored. The effects introduced by the locally large time step and cell sizes should be limited to the small zone near the cylinder face.

As noted in §4.2.2, the NTC method for collision partner selection requires that $(\sigma g)_{\rm max}$ for each cell be updated during simulation when a value higher than the stored value is found. This updating process has a small effect on the collision rate for the time step in which the update occurs. Fig. 8.17 shows the mean number of $(\sigma g)_{\rm max}$ updates per cell per simulation time step. After steady state was attained, $(\sigma g)_{\rm max}$ was updated infrequently, and the resulting effects on the collision rate should therefore have been negligible.

8.5.4 Solution using conventional TCE model

The stagnation streamline profiles of ρ/ρ_∞, $T_{\rm tr}/T_\infty$, $T_{\rm rot}/T_\infty$, $T_{\rm vib}/T_\infty$ and α calculated using the TCE model are shown in Fig. 8.18. The coefficients C_D and C_H for this case are shown in Table 8.6. Chemistry has a small effect on C_D but decreases C_H significantly, as expected from the general behaviour discussed in §3.1.

Contour plots of ρ/ρ_∞, $T_{\rm tr}/T_\infty$, $T_{\rm rot}/T_\infty$, $T_{\rm vib}/T_\infty$, $T_{\rm kin}/T_\infty$ and α are shown in Figs. 8.19 to 8.24. The ρ/ρ_∞ contours in Fig. 8.19 show some structure in the freestream flow where none should exist. The cause of this structure is not clear, but possible sources could be the boundary conditions or the particle cloning process. Similar freestream structure is also apparent in the results from the MONACO code at the University of Michigan, which was used to perform axisymmetric DSMC calculations similar to those reported

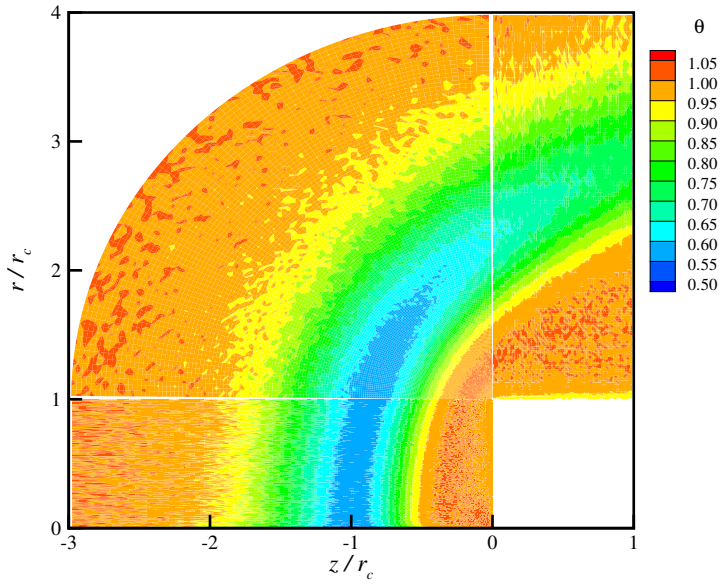

Figure 8.13: Contours of collision rate ratio $\theta \equiv N_{\text{colls}}^{\text{DSMC}}/N_{\text{colls}}^{\text{theory}}$ for non-reacting blunt cylinder flowfield.

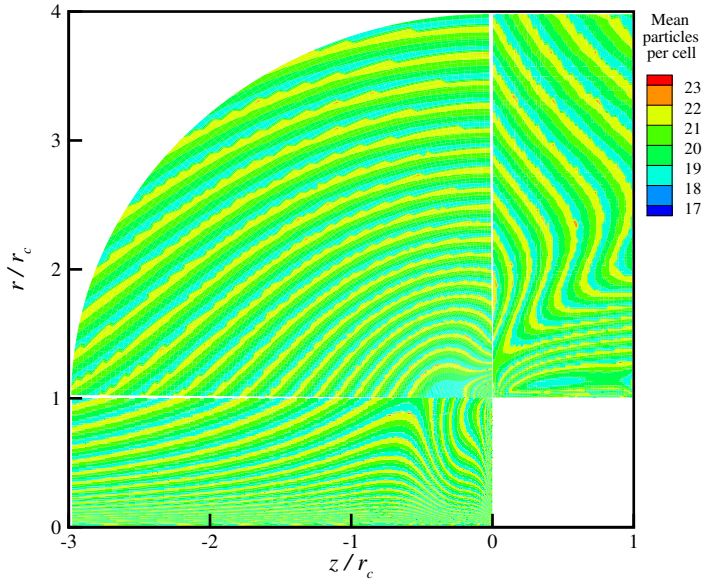

Figure 8.14: Mean number of particles per cell for non-reacting blunt cylinder flowfield.

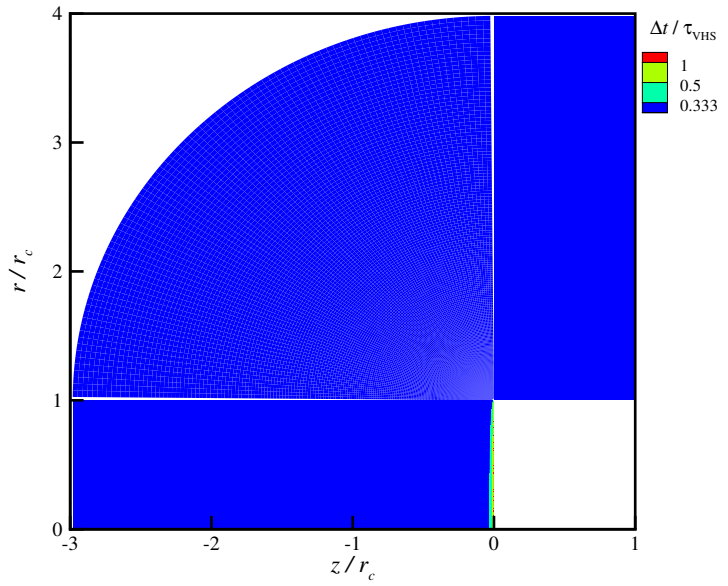

Figure 8.15: Ratio $\Delta t/\tau_{\mathrm{VHS}}$ for non-reacting blunt cylinder flowfield. The contour intervals emphasise regions with $\Delta t/\tau_{\mathrm{VHS}} > 1/3$.

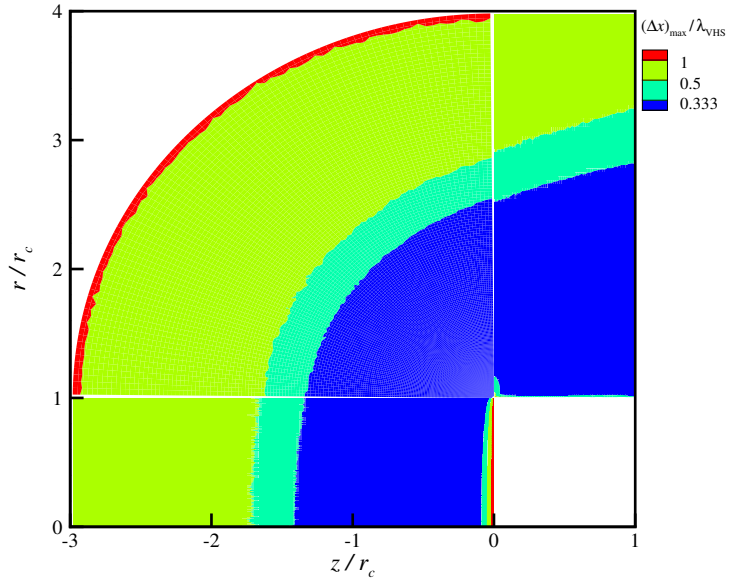

Figure 8.16: Ratio $(\Delta x)_{\mathrm{max}}/\lambda_{\mathrm{VHS}}$ for non-reacting blunt cylinder flowfield. The contour intervals emphasise regions with $(\Delta x)_{\mathrm{max}}/\lambda_{\mathrm{VHS}} > 1/3$.

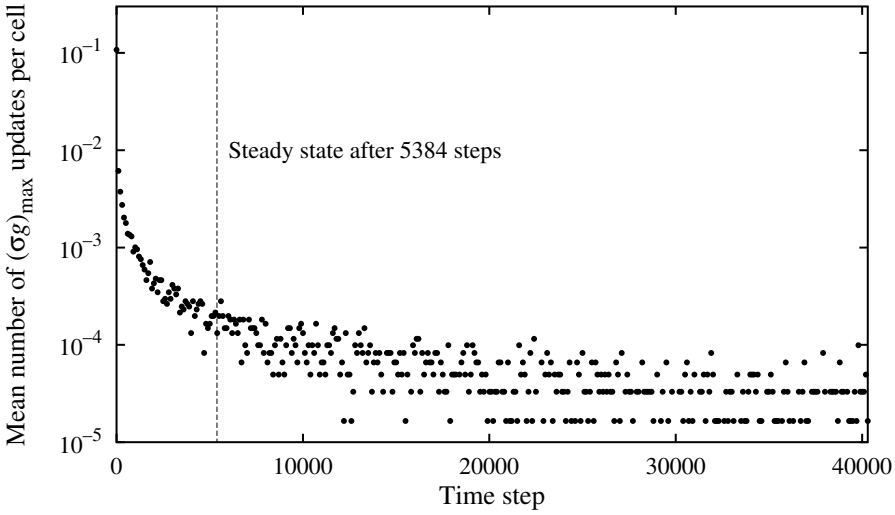

Figure 8.17: Mean number of updates of $(\sigma g)_{\max}$ per cell for non-reacting blunt cylinder simulation. Only one point per 100 is shown for clarity. When the number of updates was zero, 1.1×10^{-5} was plotted.

here. Given that the amplitude of the freestream density fluctuations was less than 1%, it is unlikely that the freestream structure will affect the results, and so it may be deemed insignificant. Fig. 8.20 shows that $T_{\rm tr}$ begins to rise a distance $z/r_c \sim 3$ from the cylinder. This shows that the effects of the blunt body persist a long distance upstream in rarefied flow. In Fig. 8.22, the tracks visible in the freestream are due to individual N_2 particles with vibrational energy level $q_{\rm vib} > 0$ that have moved upstream during the simulation. One such particle can give $T_{\rm vib}/T_\infty > 1$, which is clearly visible within the rest of the freestream that has $T_{\rm vib}/T_\infty \approx 0$.

Fig. 8.25 shows the total number of particles and the total energy of all particles in the simulation for the TCE solution. This plot demonstrates that steady state conditions were attained after about 5000 time steps. In this case, sampling commenced after 5384 time steps.

Figs. 8.26 and 8.27 show the mean number of particles per cell and $(\Delta x)_{\max}/\lambda_{\rm VHS}$ for the TCE solution. Except for the limited zone near the cylinder face and the freestream, the criterion $(\Delta x)_{\max}/\lambda_{\rm VHS} \lesssim 1/3$ is satisfied. A discussion on the issue of $(\Delta x)_{\max}/\lambda_{\rm VHS}$ is given in §8.8. Contours of the ratio $\Delta t/\tau_{\rm VHS}$ were similar to those shown in Fig. 8.15, except that the zone with $\Delta t/\tau_{\rm VHS} > 1/3$ extended to a distance $0.05 r_c$ from the cylinder face.

The results shown in Fig. 8.18 and Table 8.6 were calculated using a grid that differed from that used by Lilley and Macrossan [110]. Furthermore, in the calculations reported here, there were about 20 particles in every cell. In the calculations of Lilley and Macrossan, there were fewer particles per cell. In fact, within the shock, some cells had an mean of less than two particles per cell. Despite these differences, the results reported here are essentially identical to those of Lilley and Macrossan [110].

Bird [21] noted that specular reflection becomes significant at high impact energies.

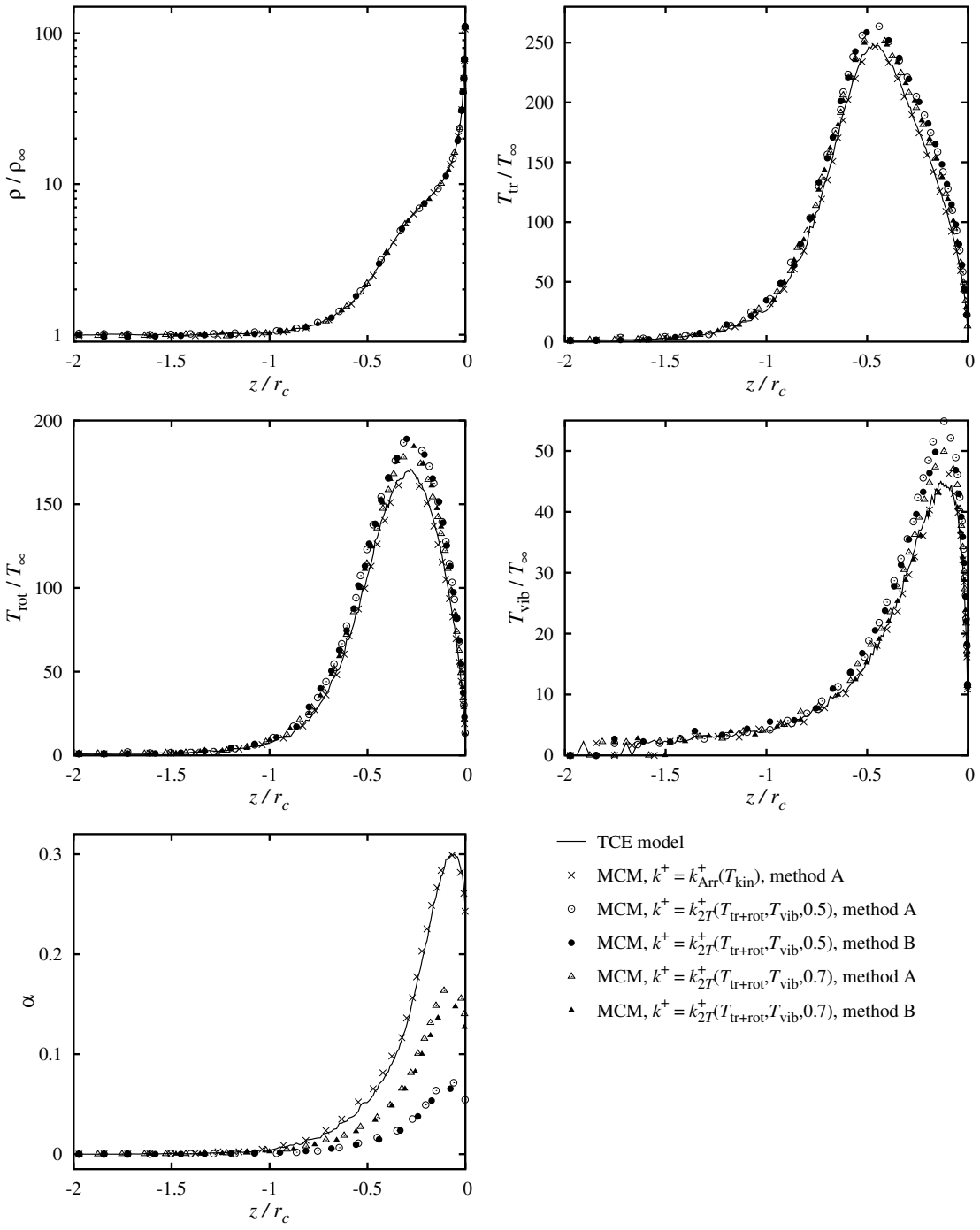

Figure 8.18: Stagnation streamline profiles for blunt cylinder flow, calculated using the conventional TCE model and the macroscopic method with $k^+ = k^+_{\mathrm{Arr}}(T_{\mathrm{kin}})$ and $k^+ = k^+_{2T}(T_{\mathrm{tr+rot}}, T_{\mathrm{vib}}, s)$. The dissociation rates of Kewley and Hornung [91] were used in all cases. The upstream simulation domain is only shown from $z/r_c = -2$.

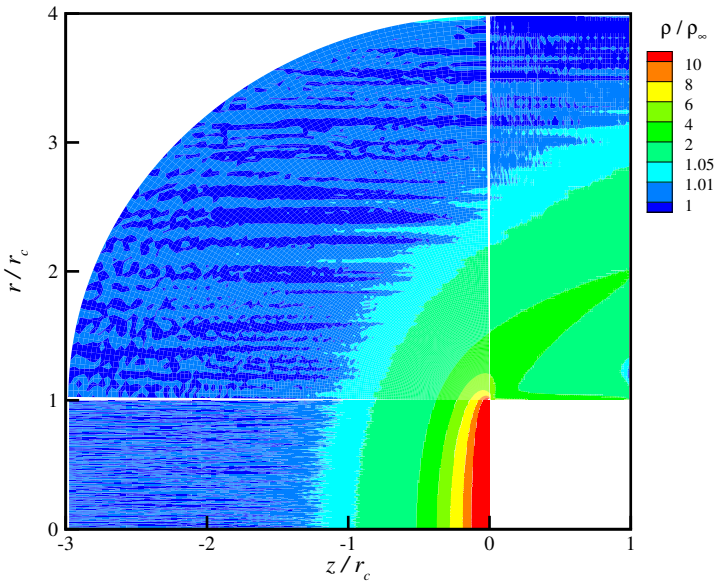

Figure 8.19: ρ/ρ_∞ contours for TCE solution of blunt cylinder flow. Fluctuations in the freestream are exaggerated by the small contour intervals. The structure visible in the freestream is discussed in §8.5.4.

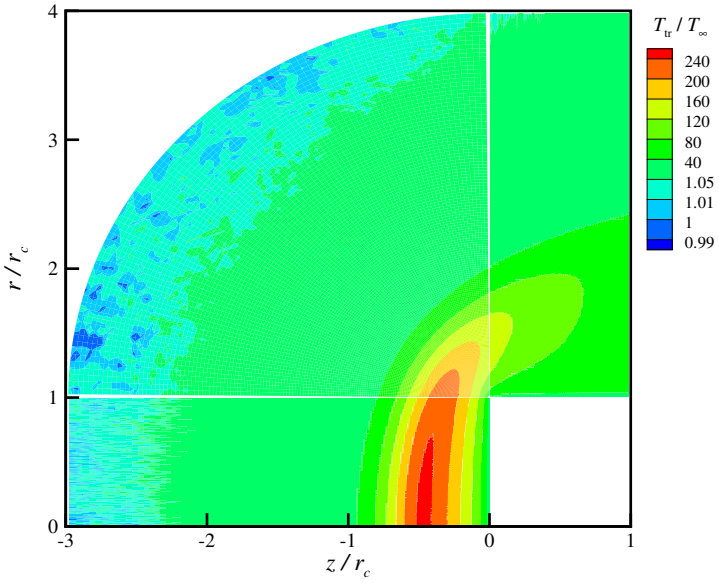

Figure 8.20: $T_{\rm tr}/T_\infty$ contours for TCE solution of blunt cylinder flow. Fluctuations in the freestream are exaggerated by the small contour intervals.

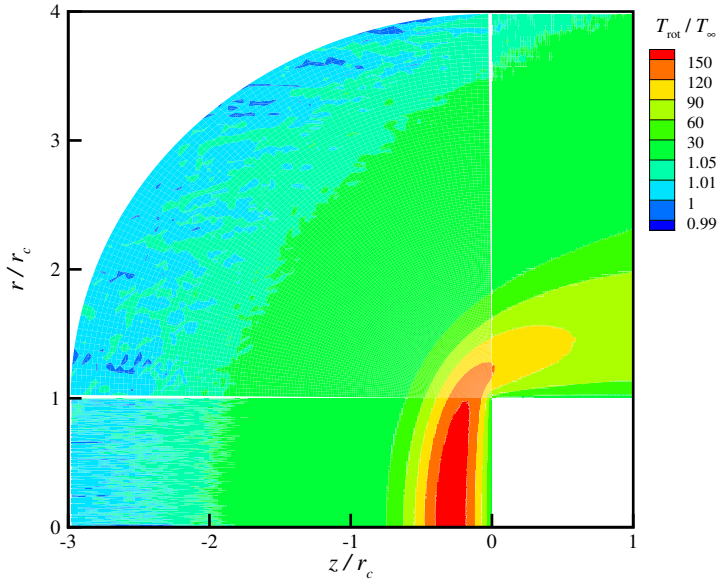

Figure 8.21: $T_{\rm rot}/T_\infty$ contours for TCE solution of blunt cylinder flow. Fluctuations in the freestream are exaggerated by the small contour intervals.

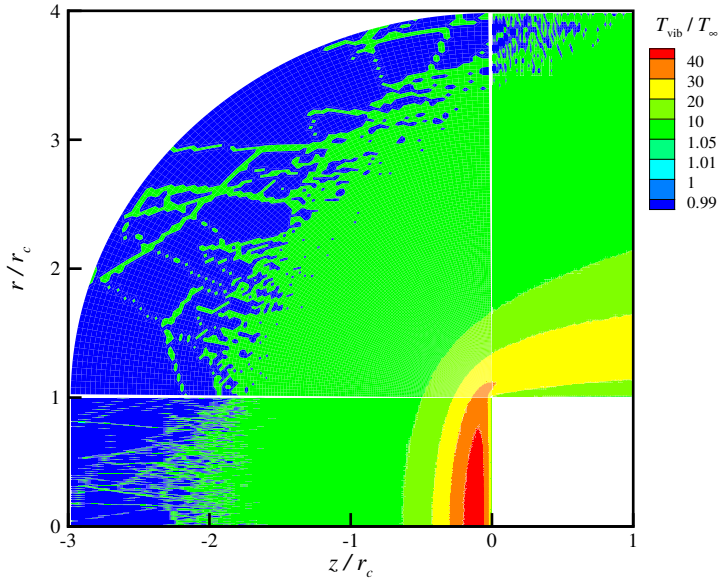

Figure 8.22: $T_{\rm vib}/T_\infty$ contours for TCE solution of blunt cylinder flow. Fluctuations in the freestream are exaggerated by the small contour intervals. The tracks visible in the freestream are discussed in §8.5.4.

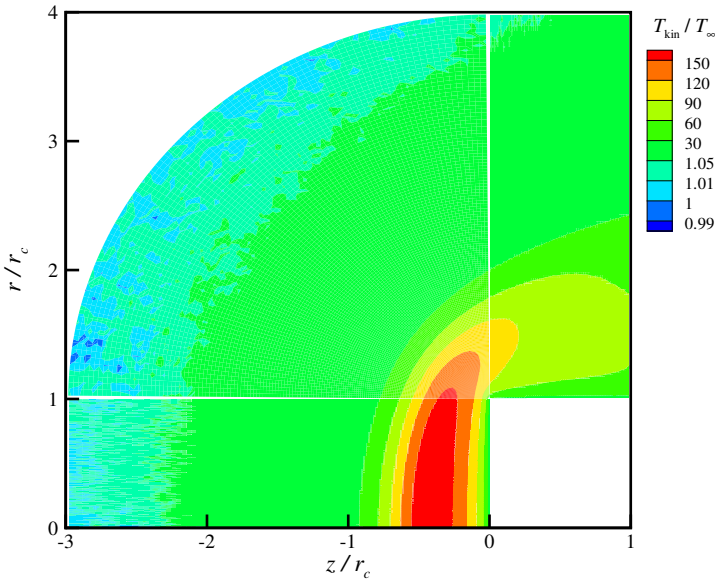

Figure 8.23: T_{kin}/T_∞ contours for TCE solution of blunt cylinder flow. Fluctuations in the freestream are exaggerated by the small contour intervals.

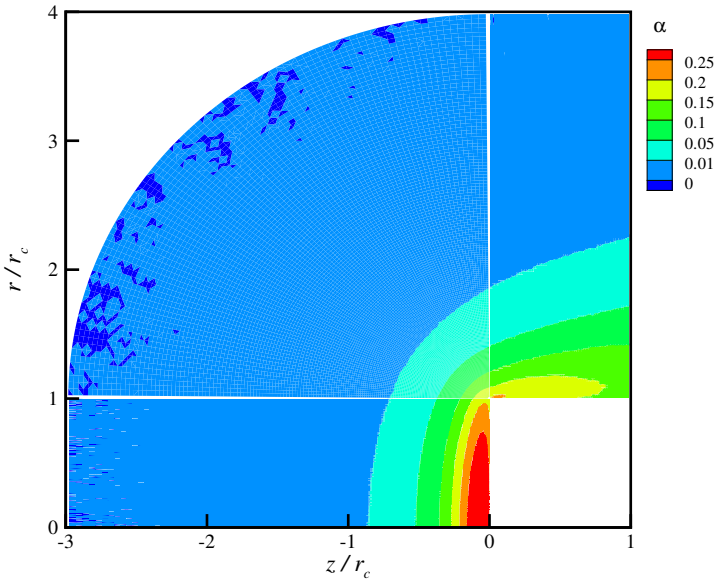

Figure 8.24: Dissociation fraction α contours for TCE solution of blunt cylinder flow. Fluctuations in the freestream are exaggerated by the small contour intervals.

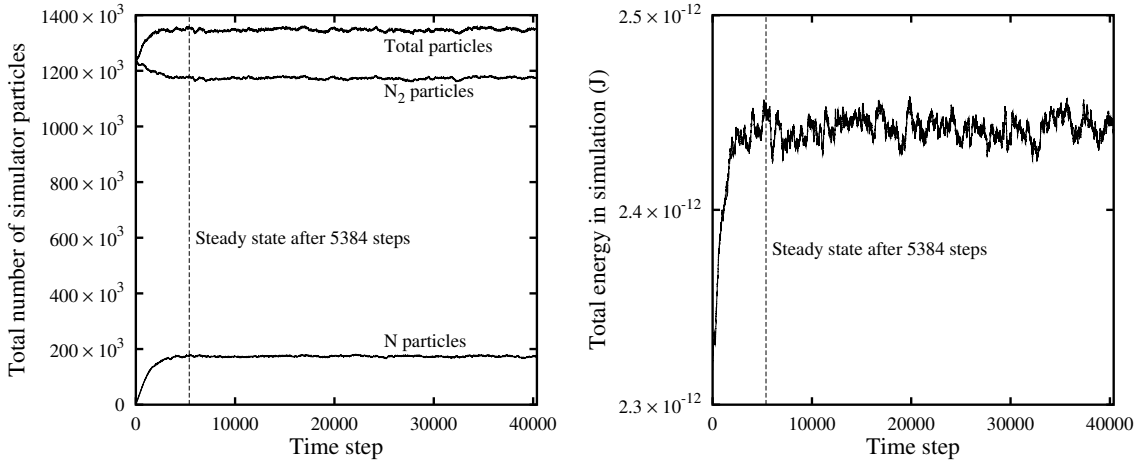

Figure 8.25: Demonstration of approach to steady state for TCE solution of blunt cylinder flow. The numerical scatter after steady state conditions were attained is ~1%.

When surface impact energies are more than several electron volts, the usual assumption of diffuse reflection should be critically reviewed. During the TCE solution, the axial velocities v_z of $\sim 10^6$ particles hitting the cylinder face were recorded. Fig. 8.28 shows the energy distribution of these surface collisions. It is apparent that most surface collisions occurred at energies much less than 1 eV. The assumption of diffuse reflection used here therefore appears suitable. It seems that specular reflection should only be considered in highly rarefied hypersonic flow where many molecules hit the surface with $v_z \sim u_\infty$.

During the TCE calculations, only 0.36% of dissociation events for reaction 1 had $\left(P_R^+\right)_{\mathrm{TCE}} > 1$. For reaction 2, only 0.057% of dissociation events had $\left(P_R^+\right)_{\mathrm{TCE}} > 1$. This shows that the occurrence of events with $\left(P_R^+\right)_{\mathrm{TCE}} > 1$ is not a serious problem for the TCE model.

8.5.5 Solution using macroscopic method with $k^+ = k^+_{\mathbf{Arr}}\left(T_{\mathbf{kin}}\right)$

The stagnation streamline profiles obtained using the macroscopic method with $k^+ = k^+_{\mathrm{Arr}}\left(T_{\mathrm{kin}}\right)$ are shown in Fig. 8.18. The coefficients C_D and C_H are included in Table 8.6. There is good agreement between the results obtained using the TCE model and the macroscopic method. Similar results were reported by Lilley and Macrossan [110, 106].

8.5.6 Solution using macroscopic method with $k^+ = k^+_{2T}\left(T_{\mathbf{tr+rot}}, T_{\mathbf{vib}}, s\right)$

For the calculations using the two-temperature rates, C_D and C_H are shown in Table 8.6. The stagnation streamline profiles are included in Fig. 8.18. It appears that the macroscopic method with the two-temperature model can capture the expected DV coupling behaviour, in that dissociation rates decrease and C_H increases relative to case with $k^+ = k^+_{\mathrm{Arr}}\left(T_{\mathrm{kin}}\right)$ which does not capture DV coupling. Also, C_H increases as s decreases as expected. In these cases, it appears that the method for selecting dissociating particles

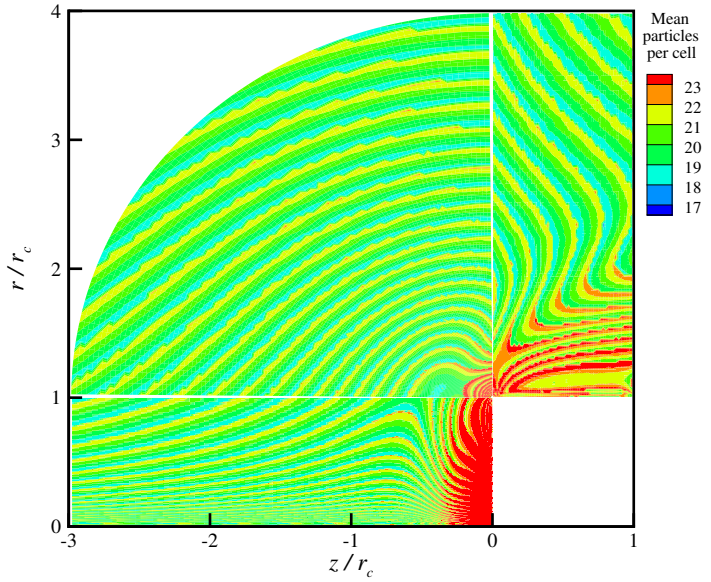

Figure 8.26: Mean number of particles per cell for TCE solution of blunt cylinder flow.

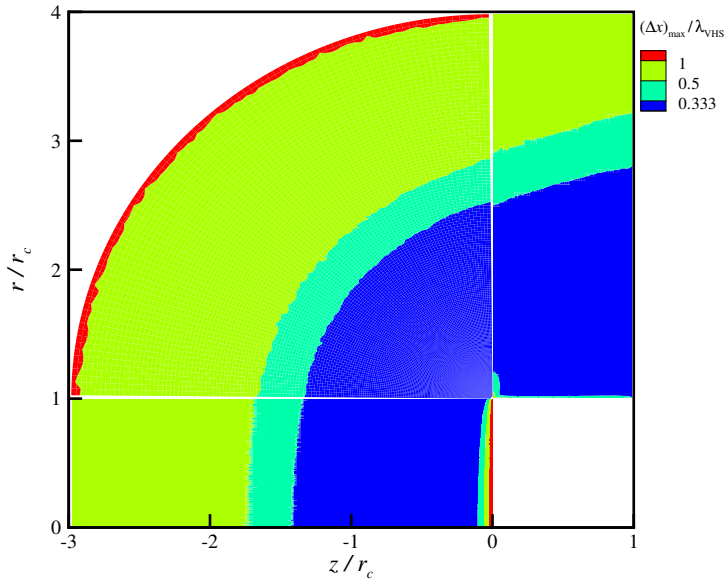

Figure 8.27: Ratio $(\Delta x)_{\max}/\lambda_{\mathrm{VHS}}$ for TCE solution of blunt cylinder flow. The contour intervals emphasise regions with $(\Delta x)_{\max}/\lambda_{\mathrm{VHS}} > 1/3$.

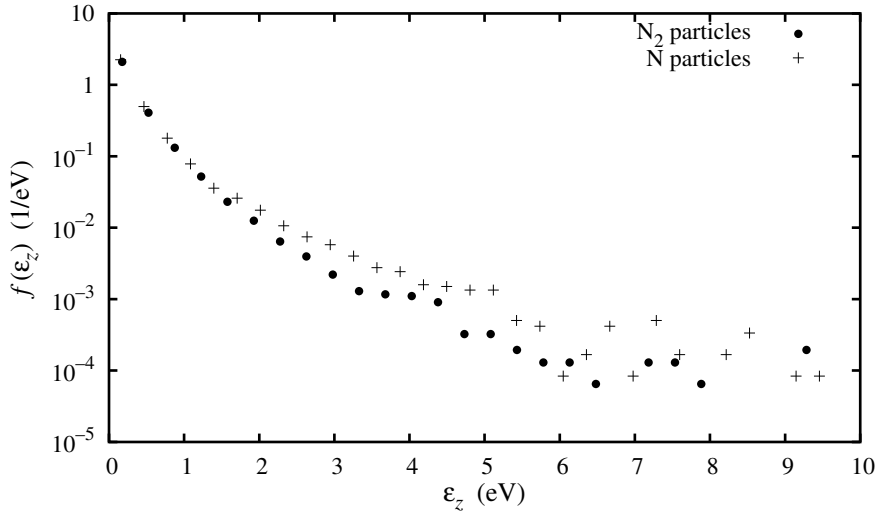

Figure 8.28: Distributions of translational energy in the axial direction $\epsilon_z = mv_z^2/2$ for particles hitting the cylinder face during the TCE solution. Note that 1 eV = 1.60×10^{-19} J.

has little effect on the either the flowfield or C_H.

8.5.7 Solution using conventional VFD model

For the blunt cylinder calculations performed using the VFD model with $\epsilon_{\text{vib}} = qk\Theta_{\text{vib}}$, the C_D and C_H values are included in Table 8.7. As expected, the results for $\phi = 0$ are very close to those obtained using the TCE model. Using $\phi > 0$ has the expected effect on the heat flux, in that C_H increases relative to the $\phi = 0$ case. However, ϕ gave minimal control over DV coupling. The coefficients obtained using $\epsilon_{\text{vib}} = \left(\frac{1}{2} + q\right) k\Theta_{\text{vib}}$ are also shown in Table 8.7. These results show a more significant variation of C_H with ϕ, and indicate this method for calculating ϵ_{vib} should be used when implementing the VFD model. For comparison with other chemistry methods, the VFD results with $\epsilon_{\text{vib}} = \left(\frac{1}{2} + q\right) k\Theta_{\text{vib}}$ are also included in Table 8.6.

Table 8.7: Summary of blunt cylinder results using the VFD model.

ϕ		0	0.1	0.5	1	2	3	4
$\epsilon_{\text{vib}} = qk\Theta_{\text{vib}}$								
C_D		1.772	1.773	1.771	1.771	1.771	1.770	1.770
C_H		0.232	0.270	0.269	0.271	0.273	0.273	0.276
% of events with	Reaction 1:	0.36%	0.051%	0.13%	0.39%	2.5%	7.5%	13.4%
$\left(P_R^+\right)_{\text{VFD}} > 1$	Reaction 2:	0.06%	0.008%	0.028%	0.069%	0.23%	0.55%	1.3%
$\epsilon_{\text{vib}} = \left(\frac{1}{2} + q\right) k\Theta_{\text{vib}}$								
C_D		1.772	1.772	1.770	1.771	1.772	1.770	1.770
C_H		0.232	0.236	0.253	0.264	0.271	0.273	0.274
% of events with	Reaction 1:	0.36%	0.37%	0.31%	0.42%	2.6%	8.0%	14.0%
$\left(P_R^+\right)_{\text{VFD}} > 1$	Reaction 2:	0.06%	0.12%	0.19%	0.17%	0.24%	0.56%	1.4%

Fig. 8.29 shows the stagnation streamline profiles of α obtained using the VFD model with $\epsilon_{\text{vib}} = \left(\frac{1}{2} + q\right) k\Theta_{\text{vib}}$. The α profiles obtained using the macroscopic method with $k^+ = k^+_{2T}\left(T_{\text{tr+rot}}, T_{\text{vib}}, 0.7\right)$ are included. These profiles, and the C_H values included in Table 8.6, indicate that the VFD model with $0.5 \lesssim \phi \lesssim 1$ results in a flowfield similar to the two-temperature model of Park [137] with $s \approx 0.7$.

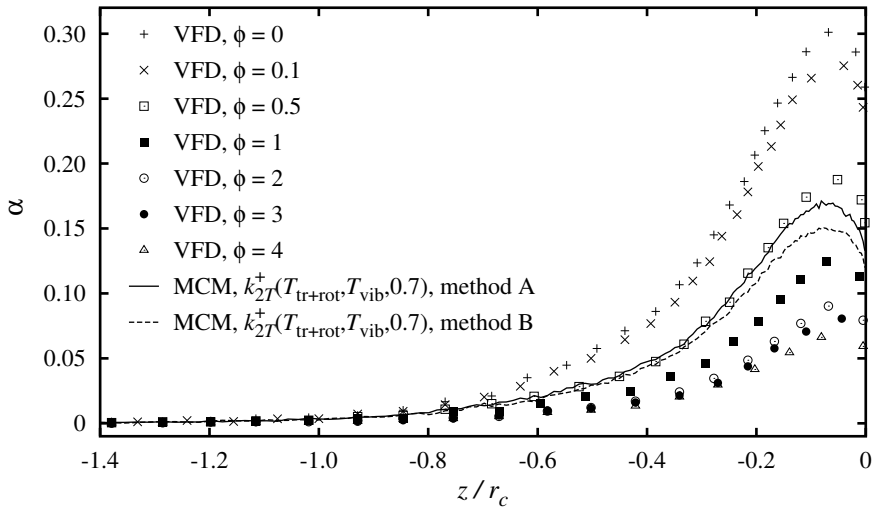

Figure 8.29: Stagnation streamlines of α for VFD calculations using $\epsilon_{\text{vib}} = \left(\frac{1}{2} + q\right) k\Theta_{\text{vib}}$, compared to results from macroscopic method using $k^+ = k^+_{2T}\left(T_{\text{tr+rot}}, T_{\text{vib}}, 0.7\right)$. The upstream simulation domain is shown from $z/r_c = -1.4$ only.

As noted in §6.4.1, $\left(P_R^+\right)_{\text{VFD}} > 1$ can occur when using the VFD model. The percentages reaction events with $\left(P_R^+\right)_{\text{VFD}} > 1$ are included in Table 8.7. It appears that the VFD version with $\epsilon_{\text{vib}} = \left(\frac{1}{2} + q\right) k\Theta_{\text{vib}}$ results in slightly more instances of $\left(P_R^+\right)_{\text{VFD}} > 1$ than the version with $\epsilon_{\text{vib}} = qk\Theta_{\text{vib}}$.

8.5.8 Solution using conventional TLD model

For the calculations performed using the conventional TLD model, the coefficients C_D and C_H are included in Table 8.6. The stagnation streamline profiles are shown in Fig. 8.30. In this case, dissociation proceeds to a greater extent than in the former cases, so C_H is lower. Similar results were reported by Lilley and Macrossan [106].

During the TLD calculations, the numbers of reaction events with $\left(P_R^+\right)_{\text{TLD}} > 1$ was recorded. For reactions 1 and 2, the respective percentages of events with $\left(P_R^+\right)_{\text{TLD}} > 1$ were 43.7% and 70.1%. As noted in §6.4.2, the existence of events with $\left(P_R^+\right)_{\text{TLD}} > 1$ is an important limitation of the TLD model.

Fig. 8.31 shows that the mean number of particles per cell was close to 20, as recommended by Bird [21]. Contours of the ratio $(\Delta x)_{\max}/\lambda_{\text{VHS}}$ are shown in Fig. 8.32. The region where $(\Delta x)_{\max}/\lambda_{\text{VHS}} > 1/3$ is larger than that shown for the non-reacting and TCE cases, as shown in Figs. 8.16 and 8.27. This is because the TLD solution results in a smaller λ_{VHS}, due to the higher number densities arising from extensive dissociation. More dis-

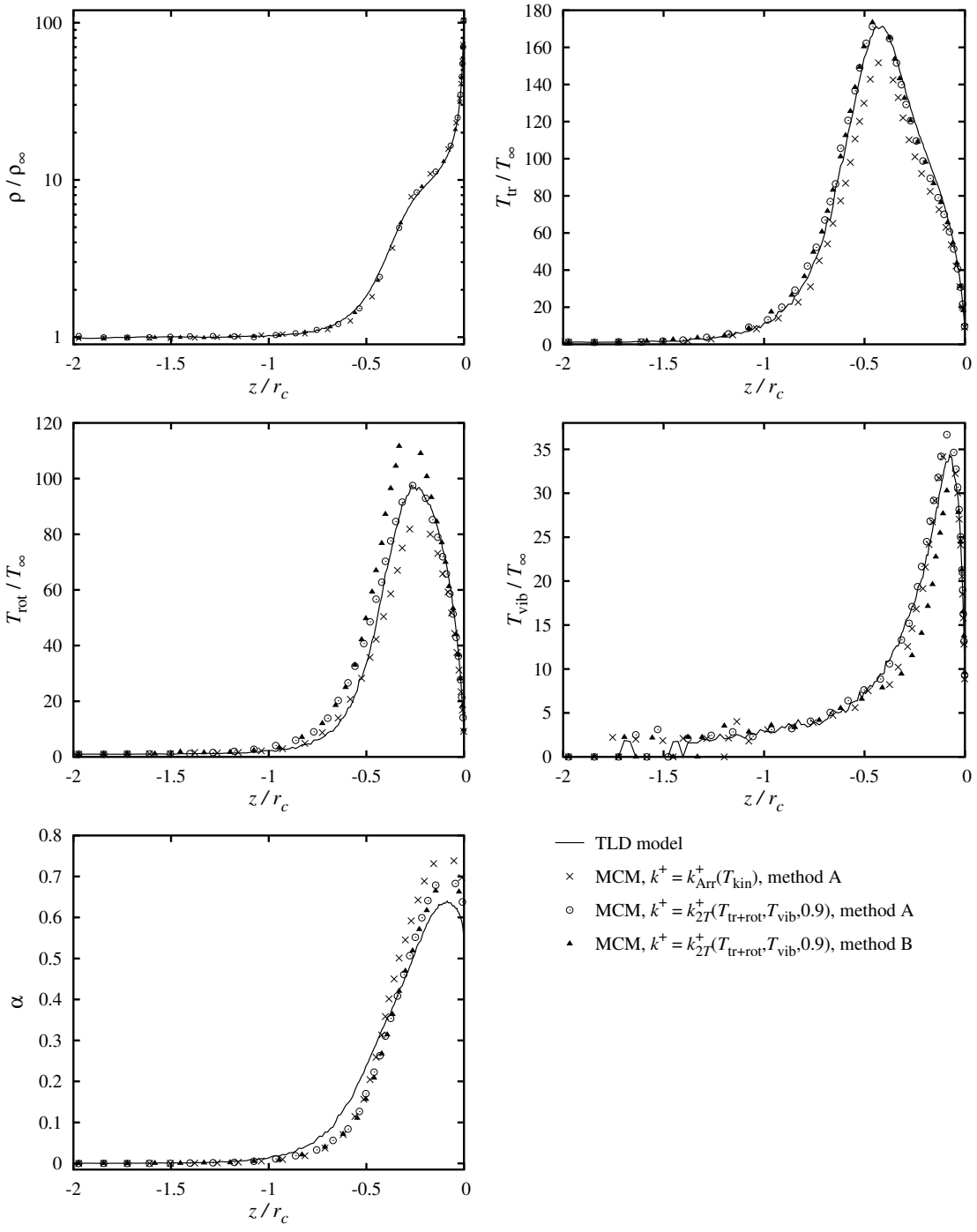

Figure 8.30: Stagnation streamline profiles for blunt cylinder flow, calculated using the conventional TLD model and the macroscopic method with the fitted TLD rates. The upstream simulation domain is only shown from $z/r_c = -2$.

cussion on the issue of $(\Delta x)_{\max}/\lambda_{\text{VHS}}$ is given in §8.8. Contours of the ratio $\Delta t/\tau_{\text{VHS}}$ were similar to those shown in Fig. 8.15, except that the zone with $\Delta t/\tau_{\text{VHS}} > 1/3$ extended to a distance $0.08r_c$ from the cylinder face.

8.5.9 Solution using macroscopic method with fitted TLD rates

For the macroscopic method using the fitted TLD rates, the coefficients C_D and C_H are included in Table 8.6. The stagnation streamline profiles are shown in Fig. 8.30. The agreement between these results and those obtained using the conventional TLD model is generally reasonable. Similar results were reported by Lilley and Macrossan [106].

From Fig. 8.30, there are minor differences in the results obtained when using methods A and B to select dissociating diatoms. Further investigations are required to determine the best method for selecting dissociating diatoms. The similar results obtained for the two different selection methods confirms the original premise of the macroscopic method, in that the details of the reaction processes have little influence on the macroscopic conditions.

8.6 Discussion on the macroscopic chemistry method

The macroscopic method offers several significant advantages over conventional DSMC chemistry models. The most important advantage is that it can use any macroscopic rate expressions, and these may be any empirical or theoretical function of the local macroscopic flow conditions. This has been demonstrated by the examples presented in this chapter. The macroscopic method allows DSMC chemistry calculations to be performed using reaction rates for which no conventional DSMC chemistry model exists. Importantly, the macroscopic method allows the large amount of literature on macroscopic reaction rates, as used in continuum studies, to be applied directly to DSMC chemistry studies [106]. The ability to use any rate expressions offers considerable flexibility for modelling reacting flows with the DSMC method.

Most conventional DSMC chemistry models have been developed for the VHS collision model only. Although the existing conventional models could be applied to other collision models, the resulting reaction rates will differ from the expected rates, due to the different collision rates relative to the VHS model. The macroscopic method permits simple chemistry modelling with any DSMC collision model, including realistic potentials, such that the desired macroscopic reaction rates are recovered.

As noted above, conventional DSMC chemistry models often have $P_R > 1$, which is physically unrealistic. The occurrence of events with $P_R > 1$ certainly results in reduced reaction rates relative to the expected rates. However, there may be more subtle effects introduced by $P_R > 1$ that are not immediately obvious. The macroscopic method does not suffer from any singularities or numerical instabilities.

The macroscopic method may offer advantages over conventional DSMC chemistry models in hybrid codes that employ both continuum solvers in near-equilibrium regions

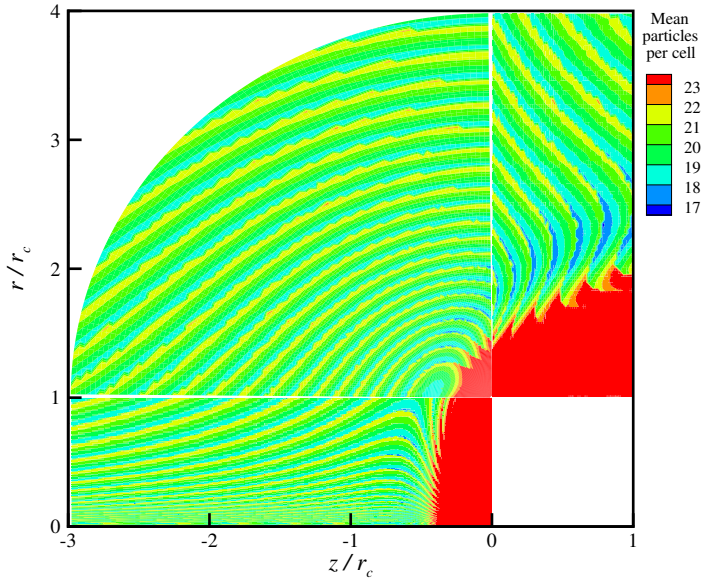

Figure 8.31: Mean number of particles per cell for TLD solution of blunt cylinder flow.

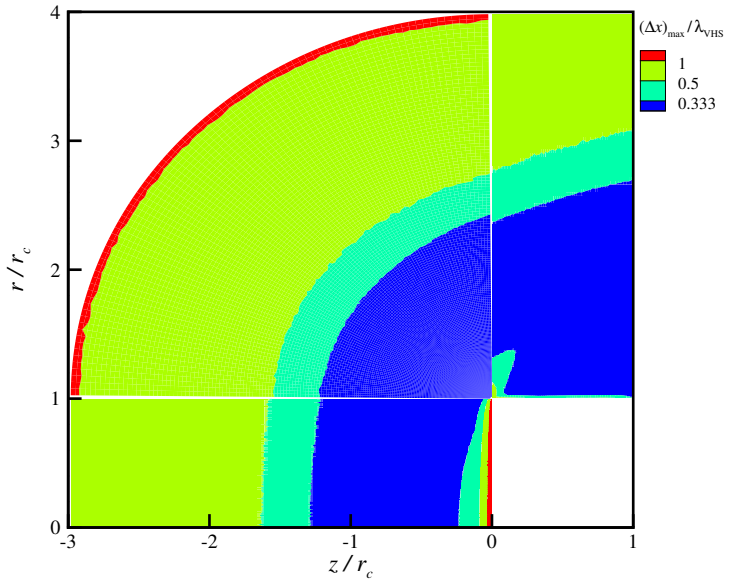

Figure 8.32: Ratio $(\Delta x)_{\max}/\lambda_{\mathrm{VHS}}$ for TLD solution of blunt cylinder flow. The contour intervals emphasise regions with $(\Delta x)_{\max}/\lambda_{\mathrm{VHS}} > 1/3$.

and the DSMC method in non-equilibrium regions. The macroscopic method allows the same chemistry model to be used throughout the entire simulation domain, because the rate model used in continuum regions can be used directly in the DSMC regions.

For the TLD case considered in §8.5.8, it could be argued that using the macroscopic method instead of the conventional TLD model offers no advantages, because the TLD model is already available and calculating the macroscopic TLD rates requires some effort. This is true for the TLD case, because it was examined here to provide a comparison case between a conventional chemistry model and the macroscopic method. However, the important point is that the macroscopic method can use any macroscopic rates, without the need to develop expressions for the reaction probability P_R at the molecular level. Again, this allows DSMC chemistry calculations to be performed using reaction rates for which no conventional DSMC chemistry model exists.

The methods A and B used in this study to select dissociating particles could be regarded as being quite arbitrary, and therefore a disadvantage. Bartel *et al.* [8] and Bartel [7] suggested methods that could be used to implement the decoupled approach whilst allowing individual reaction events to be modelled with any desired level of physical detail. One such method, which is analogous to the NTC method for selecting collision partners, is discussed in §7.4.

8.7 Discussion on using macroscopic information in DSMC calculations

The macroscopic chemistry method differs from the conventional approach to DSMC calculations in that macroscopic information derived from all energy modes in a cell, rather than from individual collisions as they occur, is used to determine the reaction rate [110]. This use of macroscopic information is not limited to the macroscopic chemistry method, and several examples of DSMC procedures that use macroscopic information exist, as listed below.

- The NTC method for selecting collision partners, as discussed in §4.2.2, depends on the local macroscopic number density to calculate the number of possible collision pairs to test for collision.

- In flows where temperature dependent relaxation behaviour must be captured, rotational and vibrational relaxation numbers in each cell can be calculated from local kinetic temperatures. This approach has been suggested by Bird [21].

- As noted in §4.5.2 and §4.5.3, variable-ϕ models for calculating the BL rotational and vibrational energy exchange probability can use a time-averaged ϕ value for each cell. This is macroscopic property, because it is obtained from all exchange events in a cell.

- Using the TCE and VFD chemistry models with quantised vibration models requires some method to calculate the effective vibrational DOF ζ_{vib}. Here, a cell-based ζ_{vib} was used. This ζ_{vib} was calculated from the local kinetic temperature, which a macroscopic property obtained from a time-averaged vibrational energy per molecule.

- The version of the TCE model proposed by Boyd and Stark [43] depends on a local kinetic temperature to calculate a reaction rate which is then used directly to calculate P_R^+.

- The three recombination models discussed in §6.5 all require the local number density to calculate the recombination probability P_R^-. The equilibrium collision theory of Bird [21], presented in §6.5.3, also requires the local kinetic temperature to evaluate the partition functions. Although these recombination models are generally considered to be conventional chemistry models, they do in fact rely on local macroscopic information.

- The simplified DSMC collision models of Macrossan [121, 122], discussed in §4.4.2, use local kinetic temperatures to calculate the collision rates to recover any desired viscosity law.

One justification for these macroscopic approaches is that they work effectively. This suggests that the microscopic details of collision processes are relatively unimportant. Another justification is that these methods do not rely on the physical details of collision processes at the molecular level. In general, such details are poorly known. These methods use available macroscopic near equilibrium information about reaction rates, relaxation rates and viscosity laws, but make no detailed assumptions about how the gas behaves far from equilibrium, or how individual collisions proceed. The same near-equilibrium information is usually used to formulate conventional collision-based DSMC procedures, with the hope that the models will behave realistically under non-equilibrium conditions. Clearly, it would be good if the conventional collision-based procedures behaved realistically under non-equilibrium conditions. However, there is often no data to confirm the accuracy of the collision-based procedures under non-equilibrium conditions. In the absence of such data, it can be argued that the methods using macroscopic data provide a similar level of modelling accuracy as the conventional collision-based DSMC procedures [110].

8.8 Discussion on the DSMC cell size criterion

The importance of the $(\Delta x)_{\max}/\lambda_{\text{VHS}} \lesssim 1/3$ criterion can be critically examined by considering the relationship between local flow gradients and cell size. From Eq. 3.2, gradient length scales $l_{\text{grad}}(Q)$ can be obtained. Along the stagnation streamline, the ratios $\Delta z/l_{\text{grad}}(Q)$ describe how quickly the gradients change within a cell. Where $\Delta z/l_{\text{grad}}(Q)$ is small, the cell size is small relative to the flow gradients and it is postulated that the

DSMC cell size criterion $\Delta z/\lambda \lesssim 1/3$ can be violated with little effect on the flowfield. The argument supporting this is as follows.

Imagine two adjacent cells, each of which has $\Delta z/\lambda = 1/3$. Where the flow gradients are small, disturbances are small, so the velocity distribution must be similar in both cells. This occurs in either near-equilibrium flow, or in non-equilibrium flow where the collision rate is low. Because these cells have similar conditions, they could be replaced by a single cell of size $\Delta z/\lambda \approx 2/3$ with little effect on the flowfield. It therefore follows that cells with $\Delta z/\lambda > 1/3$ can be used where the flow gradients are small.

For the TLD solution, the profile of $\Delta z/\lambda_{\mathrm{VHS}}$ along the stagnation streamline is shown in Fig. 8.33. This shows that the $\Delta z/\lambda < 1/3$ criterion is violated for $z/r_c \lesssim -1.3$ and for $z/r_c \gtrsim -0.25$. For the TLD solution, the length scales $l_{\mathrm{grad}}(Q)$ were calculated at the centre of each cell along the stagnation streamline for $Q = \lambda_{\mathrm{VHS}}$, ρ, T_{tr} and α. For all cells but the first and last cell, the local Q profile was obtained by fitting a parabola to the Q values in the cell and the two adjacent cells. This procedure is described in §A.4. For the first and last cells, the gradient was based on Q in the cell and the adjacent cell, and was assumed to be linear. The resulting profiles of $\Delta z/l_{\mathrm{grad}}(Q)$ are shown in Fig. 8.34. If the scatter in the region $-2 \lesssim z/r_c \lesssim -1$ is ignored, then $\Delta z/l_{\mathrm{grad}}(Q)$ is only large near the cylinder face. In the freestream, the flow gradients are small and the violations of the $(\Delta x)_{\max}/\lambda_{\mathrm{VHS}} < 1/3$ criterion are not important.

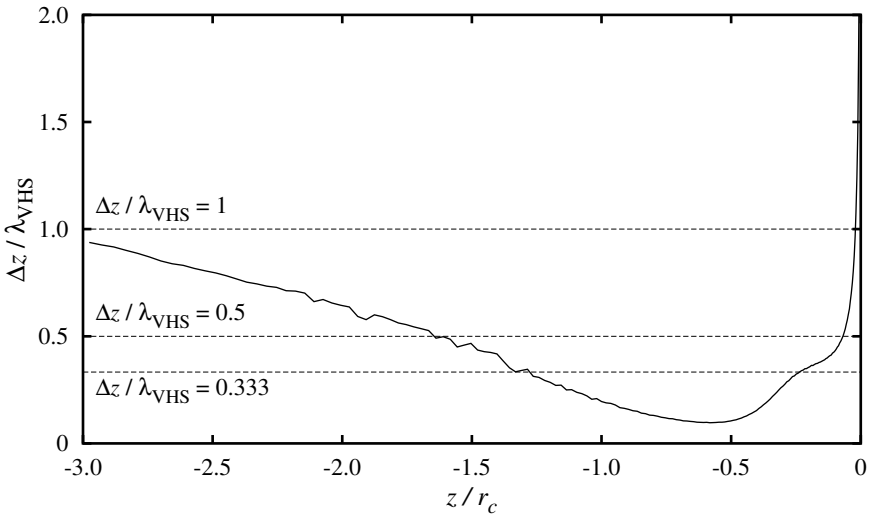

Figure 8.33: Profiles of $\Delta z/\lambda_{\mathrm{VHS}}$ along stagnation streamline for TLD solution of blunt cylinder flow.

8.9 CPU requirements

The DSMC results presented in this chapter were obtained by running codes on a Linux cluster consisting of 66 nodes. Each node contained two AMD Opteron 248 processors. These processors each had a nominal clock speed of 2.2 GHz. Each job was run on a single

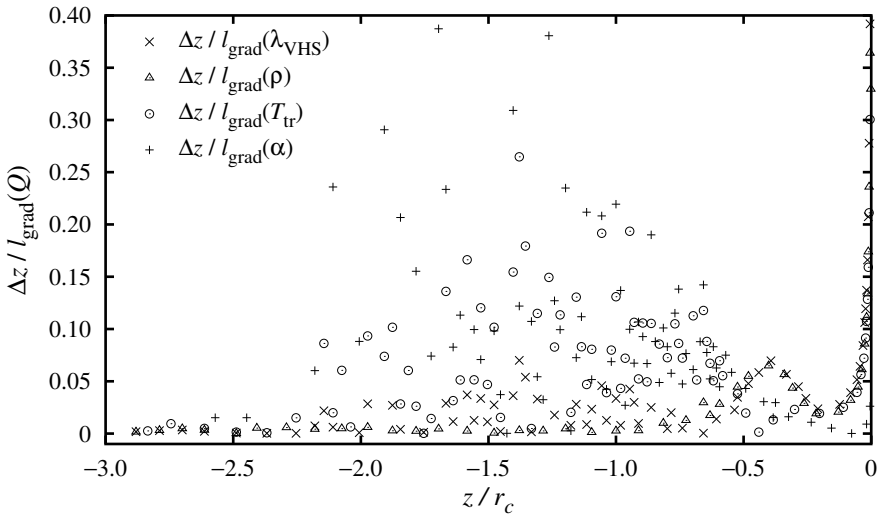

Figure 8.34: Profiles of $\Delta z/l_{\rm grad}(Q)$ along stagnation streamline for $Q = \lambda_{\rm VHS}$, ρ, $T_{\rm tr}$ and α for TLD solution of blunt cylinder flow. In all cases a reduced number of points have been shown for clarity.

dedicated processor. The codes were compiled using the GNU C compiler `gcc` with the `-O3` flag for maximum optimisation.

The relative CPU times for the shock calculations and blunt cylinder calculations are shown in Tables 8.8 and 8.6 respectively. The results suggest that the CPU requirements of the macroscopic method are similar to those of conventional DSMC chemistry models. It is important to note that the C codes used in this study were not optimised for computational efficiency, and that substantial improvements in efficiency may be possible for all chemistry models examined here.

Table 8.8: CPU requirements for DSMC shock calculations reported in §8.4.

Chemistry model	Rate data	K^*	Relative CPU time
Conventional TCE & TCER models	Kewley & Hornung	$K_c^*(T)$	1
MCM, $k^+_{\rm Arr}(T_{\rm kin})$, method A	Kewley & Hornung	$K_c^*(T)$	0.85
MCM, $k^+_{\rm Arr}(T_{\rm kin})$, method A	Kewley & Hornung	$K_{\rm G}^*(T,n)$	0.76
MCM, $k^+_{\rm Arr}(T_{\rm kin})$, method A	Park	$K_c^*(T)$	0.80
MCM, $k^+_{2T}(T_{\rm tr+rot}, T_{\rm vib}, 0.5)$, method B	Park	$K_c^*(T)$	0.83
MCM, $k^+_{2T}(T_{\rm tr+rot}, T_{\rm vib}, 0.7)$, method B	Park	$K_c^*(T)$	0.87

CHAPTER 9

Summary and conclusions

The main objective of this study was to develop a decoupled chemistry method for DSMC calculations of non-equilibrium reacting flow. This decoupled method has been called the macroscopic chemistry method, and has been developed for a symmetrical diatomic dissociating gas. To test the macroscopic method, zero-dimensional chemical relaxation, a strong one-dimensional shock and flow over a blunt axisymmetric cylinder were examined. The results obtained with the macroscopic method were compared to solutions obtained with conventional collision-based DSMC chemistry models. The results of the shock calculations were also compared to experimental density measurements. Nitrogen was used in all cases.

The zero-dimensional case considered the chemical relaxation of pure atomic nitrogen at high density and initial low temperature. For both the common form of the equilibrium constant $K^* = K_c^*(T)$ and the form of Gupta *et al.* [70] where $K^* = K_{\mathrm{G}}^*(T, n)$, the macroscopic method gave results in good agreement with exact solutions provided by a Runge-Kutta technique. The use of these different forms of K^* demonstrates that the macroscopic method can use any macroscopic information to calculate reaction rates. A DSMC solution using conventional chemistry models gave poor agreement with the Runge-Kutta solution using $K_c^*(T)$. This poor agreement occurred because the parameters used in the conventional models were derived by assuming that all energy modes were distributed according to a continuous Boltzmann distribution. Because a quantised vibration model was used, the actual energy distributions occurring in the DSMC calculations differed from the continuous distribution. This resulted in actual reaction rates that differed substantially from the expected rates.

The shock structure was calculated using conventional chemistry models and the macroscopic method. The conventional calculations used the TCE model for dissociation reactions and the TCER model for recombination reactions. Both the conventional and macroscopic solutions gave downstream density profiles that were in reasonable agreement with the experimental density measurements of Kewley and Hornung [91]. Within the shock, where highly non-equilibrium conditions prevail, there was good agreement between the results provided by the conventional models and the macroscopic method. This shows that the macroscopic method can capture non-equilibrium reacting flowfields

with a level of accuracy similar to that provided by the conventional models. The solution using the macroscopic method approached the calculated downstream equilibrium conditions. When using the conventional models, the downstream equilibrium conditions were not attained. This was due the difference between the actual rates realised by the the conventional chemistry models and the expected rates, which was again caused by the use of a quantised vibration model.

Shock calculations were also performed using the macroscopic method with the two-temperature rate model of Park [137]. This empirical model accounts for the DV coupling effect which is an important phenomenon in non-equilibrium flows. The solution obtained with the two-temperature model resulted in the expected decrease in the dissociation rate and an attendant decrease in the downstream density, relative to the case without DV coupling. The downstream density profiles were also reasonably close to the experimental results of Kewley and Hornung [91]. Again, the use of a two-temperature dissociation model demonstrates that the macroscopic method can employ reaction rates calculated from any macroscopic information.

Blunt cylinder calculations were performed using the several conventional DSMC chemistry models and the macroscopic method. This flow exhibited strongly non-equilibrium conditions within the merged shock layer. Again, there was good agreement between the results provided by the macroscopic method and the conventional TCE model despite the non-equilibrium conditions. To capture DV coupling, the two-temperature model of Park [137] was again used. As expected, this rate model decreased dissociation rates and increased surface heat fluxes, compared to the case without DV coupling. The blunt cylinder flowfield was also calculated with the conventional TLD model that also captures DV coupling. The macroscopic rates realised by the TLD model at thermal equilibrium were calculated with a Monte Carlo sampling technique, and then used in the macroscopic method to calculate the blunt cylinder flowfield. This calculation used the two-temperature model to account for DV coupling effects. The resulting flowfield was in reasonable agreement with that obtained using the conventional TLD model. This demonstrates that the macroscopic method can give a flowfield close to that calculated using the conventional collision-based TLD model, which was formulated specifically to capture DV coupling.

Several blunt cylinder calculations were performed using the conventional VFD model with various values of the parameter ϕ which controls the extent of DV coupling. The results showed that the vibrational energy should include the ground state vibrational energy. Without this ground state energy, the parameter ϕ afforded little control over the extent of DV coupling.

Again, the most important advantage of the macroscopic method is that it can use any macroscopic information to calculate the reaction rates. The rates may be any empirical or theoretical function of this macroscopic information. Using the macroscopic method removes the need to develop reaction probabilities at the molecular level for use in conventional collision-based DSMC chemistry models. The macroscopic method allows simple

chemistry modelling with any DSMC collision model, for which no conventional chemistry model may be available. The accuracy and flexibility of the macroscopic method demonstrate that it has significant potential for modelling non-equilibrium reacting flow with the DSMC method.

In addition to DSMC chemistry procedures, this study considered several other aspects of non-equilibrium gas dynamics and the DSMC method. Methods for characterising non-equilibrium reacting flows were reviewed. The basic DSMC method was described, with particular emphasis on the VHS collision model and BL energy exchange schemes. A method for obtaining the VHS parameters for collisions involving particles of different species was introduced. It was shown that BL procedures satisfy detailed balancing for constant exchange probabilities when using the relaxing particle selection scheme of Gimelshein *et al.* [65]. A detailed review of several conventional collision-based DSMC chemistry models was also provided. Detailed derivations of viscosity and collision rate expressions for the GHS [84] and MGHS [125] collision models have been provided. These expressions are more general than those provided by Macrossan and Lilley [125].

Bibliography

[1] Abe, T., "Direct simulation Monte Carlo method for internal-translational energy exchange in nonequilibrium flow," *Rarefied gas dynamics: Theory and simulations. Proceedings of the 18th International Symposium*, edited by B. D. Shizgal and D. P. Weaver, Vol. 159 of *Progress in Astronautics and Aeronautics*, AIAA, Washington, 1994, pp. 103–113.

[2] Abe, T., "Inelastic collision model for vibrational-translational and vibrational-vibrational energy transfer in the direct simulation Monte Carlo method," *Phys. Fluids*, Vol. 6, No. 9, September 1994, pp. 3175–3179.

[3] Alexander, F. J., Garcia, A. L., and Alder, B. J., "A consistent Boltzmann algorithm," *Phys. Rev. Lett.*, Vol. 74, No. 26, 26th June 1995, pp. 5212–5215.

[4] Alexander, F. J., Garcia, A. L., and Alder, B. J., "Cell size dependence of transport coefficients in stochastic particle algorithms," *Phys. Fluids*, Vol. 10, No. 6, June 1998, pp. 1540–1542.

[5] Alexander, F. J., Garcia, A. L., and Alder, B. J., "Erratum: *Cell size dependence of transport coefficients in stochastic particle algorithms* [Phys. Fluids 10, 1540 (1998)]," *Phys. Fluids*, Vol. 12, No. 3, March 2000, pp. 731.

[6] Anderson, J. D., *Hypersonic and high temperature gas dynamics*, McGraw-Hill, New York, 1989.

[7] Bartel, T. J., "Modelling neutral and plasma chemistry with DSMC," *Rarefied gas dynamics: Proceedings of the 23rd International Symposium*, edited by A. D. Ketsdever and E. P. Muntz, American Institute of Physics, New York, 2003, pp. 849–856.

[8] Bartel, T. J., Johannes, J. E., and Furlani, T. R., "Trace chemistry modelling with DSMC in chemically reacting plasmas," *AIAA Paper 98-2753*, AIAA, Washington, June 1998.

[9] Bergemann, F. and Boyd, I. D., "New discrete vibrational energy model for the direct simulation Monte Carlo method," *Rarefied Gas Dynamics: Experimental techniques and physical systems. Proceedings of the 18th International Symposium*, edited by B. D. Shizgal and D. P. Weaver, Vol. 158 of *Progress in Astronautics and Aeronautics*, AIAA, Washington, 1994, pp. 174–183.

[10] Bhatnagar, P. L., Gross, E. P., and Krook, M., "A model for collision processes in gases. I. Small amplitude processes in charged and neutral one-component systems," *Phys. Rev.*, Vol. 94, No. 3, 1954, pp. 511–525.

[11] Bird, G. A., "Approach to translational equilibrium in a rigid sphere gas," *Phys. Fluids*, Vol. 6, 1963, pp. 1518–1519.

[12] Bird, G. A., "Breakdown of translational and rotational equilibrium in gaseous expansions," *AIAA J.*, Vol. 8, No. 11, November 1970, pp. 1998–2003.

[13] Bird, G. A., "Direct simulation and the Boltzmann equation," *Phys. Fluids*, Vol. 13, No. 11, November 1970, pp. 2676–2681.

[14] Bird, G. A., *Molecular gas dynamics*, Clarendon Press, Oxford, 1976.

[15] Bird, G. A., "Direct molecular simulation of a dissociating diatomic gas," *J. Comp. Phys.*, Vol. 25, 1977, pp. 353–365.

[16] Bird, G. A., "Monte Carlo simulation of gas flows," *Ann. Rev. Fluid Mech.*, Vol. 10, 1978, pp. 11–31.

[17] Bird, G. A., "Simulation of multi-dimensional and chemically reacting flows," *Rarefied gas dynamics: Proceedings of the 11th International Symposium*, edited by R. Campargue, Vol. 1, Commissariat à l'Energie Atomique, Paris, 1979, pp. 365–388.

[18] Bird, G. A., "Monte-Carlo simulation in an engineering context," *Rarefied gas dynamics: Proceedings of the 12th International Symposium*, edited by S. S. Fisher, Vol. 74 of *Progress in Astronautics and Aeronautics*, Part I, AIAA, New York, 1981, pp. 239–255.

[19] Bird, G. A., "Definition of mean free path for real gases," *Phys. Fluids*, Vol. 26, No. 11, November 1983, pp. 3222–3223.

[20] Bird, G. A., "Perception of numerical methods in rarefied gasdynamics," *Rarefied gas dynamics: Theoretical and computational techniques. Proceedings of the 16th International Symposium*, edited by E. P. Muntz, D. Weaver, and D. Campbell, Vol. 118 of *Progress in Astronautics and Aeronautics*, AIAA, Washington, 1989, pp. 211–226.

[21] Bird, G. A., *Molecular gas dynamics and the direct simulation of gas flows*, Clarendon Press, Oxford, 1994.

[22] Bird, G. A., "New chemical reaction model for direct simulation Monte Carlo studies," *Rarefied gas dynamics: Theory and simulations. Proceedings of the 18th International Symposium*, edited by B. D. Shizgal and D. P. Weaver, Vol. 159 of *Progress in Astronautics and Aeronautics*, AIAA, Washington, 1994, pp. 185–196.

[23] Bird, G. A., "Recent advances and current challenges for DSMC," *Computers Math. Applic.*, Vol. 35, No. 1/2, 1998, pp. 1–14.

[24] Bird, G. A., "Forty years of DSMC, and now?" *Rarefied gas dynamics: Proceedings of the 22nd International Symposium*, edited by T. J. Bartel and M. A. Gallis, American Institute of Physics, New York, 2001, pp. 372–380.

[25] Borgnakke, C. and Larsen, P. S., "Statistical collision model for Monte Carlo simulations of polyatomic gas," Tech. Rep. AFM 73-08, Department of Fluid Mechanics, Technical University of Denmark, Lyngby, Denmark, 1973.

[26] Borgnakke, C. and Larsen, P. S., "Statistical collision model for Monte Carlo simulation of polyatomic gas mixture," *J. Comp. Phys.*, Vol. 18, No. 4, August 1975, pp. 405–420.

[27] Box, G. E. P. and Muller, M. E., "A note on the generation of random normal deviates," *The Annals of Mathematical Statistics*, Vol. 29, 1958, pp. 610–611.

[28] Boyd, I. D., "Rotational and vibrational nonequilibrium effects in rarefied hypersonic flow," *J. Thermophys.*, Vol. 4, No. 4, October 1990, pp. 478–484.

[29] Boyd, I. D., "Rotational-translational energy transfer in rarefied nonequilibrium flows," *Phys. Fluids A*, Vol. 2, No. 3, March 1990, pp. 447–452.

[30] Boyd, I. D., "Analysis of vibrational-translational energy transfer using the direct simulation Monte Carlo method," *Phys. Fluids A*, Vol. 3, No. 7, July 1991, pp. 1785–1791.

[31] Boyd, I. D., "Monte Carlo study of vibrational relaxation processes," *Rarefied Gas Dynamics: Proceedings of the 17th International Symposium*, edited by A. E. Beylich, VCH, Weinheim, Germany, 1991, pp. 792–799.

[32] Boyd, I. D., "Analysis of vibration-dissociation-recombination processes behind strong shock waves of nitrogen," *Phys. Fluids A*, Vol. 4, No. 1, January 1992, pp. 178–185.

[33] Boyd, I. D., "Relaxation of discrete rotational energy distributions using a Monte Carlo method," *Phys. Fluids A*, Vol. 5, No. 9, September 1993, pp. 2278–2288.

[34] Boyd, I. D., "Temperature dependence of rotational relaxation in shock waves of nitrogen," *J. Fluid Mech.*, Vol. 246, January 1993, pp. 343–360.

[35] Boyd, I. D., "Particle simulation of vibrational relaxation," *Rarefied gas dynamics: Theory and simulations. Proceedings of the 18th International Symposium*, edited by B. D. Shizgal and D. P. Weaver, Vol. 159 of *Progress in Astronautics and Aeronautics*, AIAA, Washington, 1994, pp. 78–86.

[36] Boyd, I. D., "Conservative species weighting scheme for the direct simulation Monte Carlo method," *J. Thermophys. Heat Transfer*, Vol. 10, No. 4, October–December 1996, pp. 579–585.

[37] Boyd, I. D., "A threshold line dissociation model for the direct simulation Monte Carlo method," *Phys. Fluids*, Vol. 8, No. 5, May 1996, pp. 1293–1300.

[38] Boyd, I. D., "Nonequilibrium chemistry modeling in rarefied hypersonic flows," *Chemical dynamics in extreme environments*, edited by R. A. Dressler, World Scientific, Singapore, 2001, pp. 81–137.

[39] Boyd, I. D., Bose, D., and Candler, G. V., "Monte Carlo modeling of nitric oxide formation based on quasi-classical trajectory calculations," *Phys. Fluids*, Vol. 9, No. 4, April 1997, pp. 1162–1170.

[40] Boyd, I. D., Candler, G. V., and Levin, D. A., "Dissociation modeling in low density hypersonic flows of air," *Phys. Fluids*, Vol. 7, No. 7, July 1995, pp. 1757–1763.

[41] Boyd, I. D. and Gökçen, T., "Evaluation of thermochemical models for particle and continuum simulations of hypersonic flow," *J. Thermophys. Heat Transfer*, Vol. 7, No. 3, July–September 1993, pp. 406–411.

[42] Boyd, I. D. and Gökçen, T., "Computation of axisymmetric and ionized hypersonic flow using particle and continuum methods," *AIAA J.*, Vol. 32, No. 9, September 1994, pp. 1828–1835.

[43] Boyd, I. D. and Stark, J. P. W., "Direct simulation of chemical reactions," *J. Thermophys.*, Vol. 4, No. 3, July 1990, pp. 391–393.

[44] Byron, S., "Shock-tube measurement of the rate of dissociation of nitrogen," *J. Chem. Phys.*, Vol. 44, No. 4, 15th February 1966, pp. 1378–1388.

[45] Carlson, A. B. and Bird, G. A., "Implementation of a vibrationally linked chemical reaction model for DSMC," *Rarefied gas dynamics: Proceedings of the 19th International Symposium*, edited by J. K. Harvey and G. Lord, Vol. 1, Oxford University Press, New York, 1995, pp. 434–440.

[46] Cercignani, C., Frezzotti, A., and Sibilla, S., "Hypersonic rarefied flows DSMC analysis by a simplified chemical model," *Meccanica*, Vol. 30, No. 1, 1995, pp. 93–104.

[47] Chapman, S. and Cowling, T. G., *The mathematical theory of non-uniform gases*, Cambridge University Press, Cambridge, 3rd ed., 1970.

[48] Cheng, H. K., "Hypersonic shock-layer theory of the stagnation region at low Reynolds number," *Proceedings of the 1961 Heat Transfer and Fluid Mechanics Institute*, Heat Transfer and Fluid Mechanics Institute, 1961, pp. 161–175.

[49] Cheng, H. K. and Emanuel, G., "Perspective on hypersonic nonequilibrium flow," *AIAA J.*, Vol. 33, No. 3, March 1995, pp. 385–400.

[50] Cheng, R. C. H. and Feast, G. M., "Some simple gamma variate generators," *Applied Statistics*, Vol. 28, No. 3, 1979, pp. 290–295.

[51] Cole, W. A. and Wakeham, W. A., "The viscosity of nitrogen, oxygen and their binary mixtures in the limit of zero density," *J. Phys. Chem. Ref. Data*, Vol. 14, No. 1, 1985, pp. 209–226.

[52] Davis, J., *An experimental study to evaluate and develop the direct-simulation method as applied to rarefied hypersonic flow fields*, PhD thesis, Imperial College, University of London, 1978.

[53] Davis, J., Dominy, R. G., Harvey, J. K., and Macrossan, M. N., "An evaluation of some collision models used for Monte Carlo calculations of diatomic rarefied hypersonic flows," *J. Fluid Mech.*, Vol. 135, October 1983, pp. 355–371.

[54] Dogra, V. K. and Moss, J. N., "Hypersonic rarefied flow about plates at incidence," *AIAA J.*, Vol. 29, No. 8, August 1991, pp. 1250–1258.

[55] Dominy, R. G., *Rarefied hypersonic shock wave and blunt body flows*, PhD thesis, Imperial College, University of London, 1987.

[56] Erofeev, A. I. and Perepukhov, V. A., "Hypersonic rarefied flow about a flat plate by the direct simulation method," *Rarefied gas dynamics: Proceedings of the 11th International Symposium*, edited by R. Campargue, Commissariat à l'Energie Atomique, Paris, 1979, pp. 417–426.

[57] Fan, J., "A generalized soft-sphere model for Monte-Carlo simulation," *Phys. Fluids*, Vol. 14, No. 12, December 2002, pp. 4399–4405.

[58] Gallis, M. A. and Harvey, J. K., "Maximum entropy analysis of chemical reaction energy dependence," *J. Thermophys. Heat Transfer*, Vol. 10, No. 2, April–June 1996, pp. 217–223.

[59] Gallis, M. A. and Harvey, J. K., "Modelling of chemical reactions in hypersonic rarefied flow with the direct simulation Monte Carlo method," *J. Fluid Mech.*, Vol. 312, 10th April 1996, pp. 149–172.

[60] Gallis, M. A. and Harvey, J. K., "The modeling of chemical reactions and thermochemical nonequilibrium in particle simulation computations," *Phys. Fluids*, Vol. 10, No. 6, June 1998, pp. 1344–1358.

[61] Garcia, A. L. and Wagner, W., "Time step truncation error in direct simulation Monte Carlo," *Phys. Fluids*, Vol. 12, No. 10, October 2000, pp. 2621–2633.

[62] Gentle, J. E., *Random number generation and Monte Carlo methods*, Springer-Verlag, New York, 1998.

[63] Gerhart, P. M., Gross, R. J., and Hochstein, J. I., *Fundamentals of fluids mechanics*, Addison-Wesley Publishing Company, Reading, 2nd ed., 1992.

[64] Gilmore, M. R. and Harvey, J. K., "Effects of Mach number, T_{wall}, T_{∞}, and thermal accommodation coefficient on flow around bluff bodies in the rarefied regime," *Rarefied gas dynamics: Space science and engineering. Proceedings of the 18th International Symposium*, edited by B. D. Shizgal and D. P. Weaver, Vol. 160 of *Progress in Astronautics and Aeronautics*, AIAA, Washington, 1993, pp. 308–322.

[65] Gimelshein, N. E., Gimelshein, S. F., and Levin, D. A., "Vibrational relaxation rates in the direct simulation Monte Carlo method," *Phys. Fluids*, Vol. 14, No. 12, December 2002, pp. 4452–4455.

[66] Gimelshein, S. F., Gimelshein, N. E., Levin, D. A., Ivanov, M. S., and Markelov, G. N., "Modeling of rarefied hypersonic flows over spacecraft in Martian atmosphere using the DSMC method," *AIAA Paper 2002-2759*, AIAA, Washington, June 2002.

[67] Gimelshein, S. F., Gimelshein, N. E., Levin, D. A., Ivanov, M. S., and Wysong, I. J., "On the use of chemical reaction rates with discrete internal energies in the direct simulation Monte Carlo method," *Phys. Fluids*, Vol. 16, No. 7, July 2004, pp. 2442–2451.

[68] Gimelshein, S. F., Ivanov, M. S., Markelov, G. N., and Gorbachev, Y. E., "Statistical simulation of nonequilibrium rarefied flows with quasiclassical vibrational energy transfer models," *J. Thermophys. Heat Transfer*, Vol. 12, No. 4, October–December 1998, pp. 489–495.

[69] Grimmett, G. R. and Stirzaker, D. R., *Probability and random processes*, Oxford University Press, New York, 3rd ed., 2001.

[70] Gupta, R. N., Yos, J. M., Thompson, R. A., and Lee, K.-P., *A review of reaction rates and thermodynamic and transport properties for an 11-species air model for chemical and thermal nonequilibrium calculations to 30 000 K*, NASA, Washington, 1990, NASA reference publication 1232.

[71] Haas, B. L., *Thermochemistry models applicable to a vectorized particle simulation*, PhD thesis, Stanford University, 1991.

[72] Haas, B. L., "Models of energy-exchange mechanics applicable to a particle simulation of reactive flow," *J. Thermophys. Heat Transfer*, Vol. 6, No. 2, April–June 1992, pp. 200–207.

[73] Haas, B. L. and Boyd, I. D., "Models for vibrationally-favored dissociation applicable to a particle simulation," *AIAA Paper 91-0774*, AIAA, Washington, January 1991.

[74] Haas, B. L. and Boyd, I. D., "Models for direct Monte Carlo simulation of coupled vibration-dissociation," *Phys. Fluids A*, Vol. 5, No. 2, February 1993, pp. 478–489.

[75] Haas, B. L., Hash, D. B., Bird, G. A., Lumpkin, F. E., and Hassan, H. A., "Rates of thermal relaxation in direct simulation Monte Carlo methods," *Phys. Fluids*, Vol. 6, No. 6, June 1994, pp. 2191–2201.

[76] Haas, B. L., McDonald, J. D., and Dagum, L., "Models of thermal relaxation mechanics for particle simulation methods," *J. Comp. Phys.*, Vol. 107, No. 2, August 1993, pp. 348–358.

[77] Hadjiconstantinou, N. G., "Analysis of discretization in the direct simulation Monte Carlo," *Phys. Fluids*, Vol. 12, No. 10, October 2000, pp. 2634–2638.

[78] Hadjiconstantinou, N. G., "Timestep dependence of transport coefficients in the direct simulation Monte Carlo," *Rarefied gas dynamics: Proceedings of the 22nd International Symposium*, edited by T. J. Bartel and M. A. Gallis, American Institute of Physics, New York, 2001, pp. 381–387.

[79] Harvey, J. K., "Direct simulation Monte Carlo method and comparison with experiment," *Thermophysical aspects of re-entry flows*, edited by J. N. Moss and C. D. Scott, Vol. 103 of *Progress in Astronautics and Aeronautics*, AIAA, Washington, 1986, pp. 25–43.

[80] Harvey, J. K., Celenligil, M. C., Dominy, R. G., and Gilmore, M. R., "Flat-ended circular cylinder in hypersonic rarefied flow," *J. Thermophys.*, Vol. 6, No. 1, January–March 1992, pp. 35–43.

[81] Harvey, J. K. and Gallis, M. A., "Review of code validation studies in high-speed low-density flows," *J. Spacecraft Rockets*, Vol. 37, No. 1, January–February 2000, pp. 8–20.

[82] Hash, D. B. and Hassan, H. A., "Direct simulation with vibration-dissociation coupling," *J. Thermophys. Heat Transfer*, Vol. 7, No. 4, October–December 1993, pp. 680–686.

[83] Hash, D. B. and Hassan, H. A., "Monte Carlo simulation of entry in the Martian atmosphere," *J. Thermophys. Heat Transfer*, Vol. 7, No. 2, April–June 1993, pp. 228–232.

[84] Hassan, H. A. and Hash, D. B., "A generalized hard-sphere model for Monte Carlo simulation," *Phys. Fluids A*, Vol. 5, No. 3, March 1993, pp. 738–744.

[85] Hinshelwood, C. N., *The kinetics of chemical change*, Clarendon Press, Oxford, 1940.

[86] Hirschfelder, J. O., Curtiss, C. F., and Bird, R. B., *Molecular theory of gases and liquids*, John Wiley & Sons, New York, 1954.

[87] International Union of Pure and Applied Chemistry, *Compendium of chemical terminology*, Blackwell Science, Oxford, 2nd ed., 1997, Compiled by Alan D. McNaught and Andrew Wilkinson.

[88] Ivanov, M. S. and Gimelshein, S. F., "Computational hypersonic rarefied flows," *Ann. Rev. Fluid Mech.*, Vol. 30, 1998, pp. 469–505.

[89] Jeans, J. H., *The dynamical theory of gases*, Dover Publications, New York, 4th ed., 1954.

[90] Kestin, J., Knierim, K., Mason, E. A., Najafi, B., Ro, S. T., and Waldman, M., "Equilibrium and transport properties of the noble gases and their mixtures at low density," *J. Phys. Chem. Ref. Data*, Vol. 13, No. 1, 1984, pp. 229–303.

[91] Kewley, D. J. and Hornung, H. G., "Free-piston shock-tube study of nitrogen dissociation," *Chem. Phys. Lett.*, Vol. 25, 15th April 1974, pp. 531–536.

[92] Knuth, D. E., *The art of computer programming*, Vol. 2: Seminumerical algorithms, Addison-Wesley, Reading, 3rd ed., 1997.

[93] Kondrat'ev, V. N., *Chemical kinetics of gas reactions*, Pergamon Press, Oxford, 1964, Translated from the Russian by J. M. Crabtree and S. N. Carruthers. Translation edited by N. B. Slater.

[94] Koura, K., "Nonequilibrium velocity distributions and reaction rates in fast highly exothermic reactions," *J. Chem. Phys.*, Vol. 59, No. 2, 15th July 1973, pp. 691–697.

[95] Koura, K., "Statistical inelastic cross-section model for the Monte Carlo simulation of molecules with discrete internal energy," *Phys. Fluids A*, Vol. 4, No. 8, August 1992, pp. 1782–1788.

[96] Koura, K., "A set of model cross sections for the Monte Carlo simulation of rarefied real gases: Atom-diatom collisions," *Phys. Fluids*, Vol. 6, No. 10, October 1994, pp. 3473–3486.

[97] Koura, K. and Matsumoto, H., "Variable soft sphere molecular model for inverse-power-law or Lennard-Jones potential," *Phys. Fluids A*, Vol. 3, No. 10, October 1991, pp. 2459–2465.

[98] Koura, K. and Matsumoto, H., "Variable soft sphere molecular model for air species," *Phys. Fluids A*, Vol. 4, No. 5, May 1992, pp. 1083–1085.

[99] Kreyszig, E., *Advanced engineering mathematics*, John Wiley & Sons, New York, 6th ed., 1988.

[100] Kunc, J. A., Hash, D. B., and Hassan, H. A., "The GHS interaction model for strong attractive potentials," *Phys. Fluids*, Vol. 7, No. 5, May 1995, pp. 1173–1175.

[101] Kuščer, I., "A model for rotational energy exchange in polyatomic gases," *Physica A*, Vol. 158, 1989, pp. 784–800.

[102] Landau, L. and Teller, E., "Zur Theorie der Schalldispersion," *Physikalische Zeitschrift der Sowjetunion*, Vol. 10, No. 1, 1936, pp. 34–43.

[103] Larsen, P. S. and Borgnakke, C., "Statistical collision model for simulating polyatomic gas with restricted energy exchange," *Rarefied gas dynamics: Proceedings of the 9th International Symposium*, edited by M. Becker and M. Fiebig, DFVLR-Press, Porz-Wahn, West Germany, 1974, Paper A7.

[104] Levine, R. D. and Bernstein, R. B., *Molecular reaction dynamics and chemical reactivity*, Oxford University Press, New York, 1987.

[105] Light, J. C., Ross, J., and Shuler, K. E., "Rate coefficients, reactions cross sections and microscopic reversibility," *Kinetic processes in gases and plasmas*, edited by A. R. Hochstim, Academic Press, New York, 1969, pp. 281–320.

[106] Lilley, C. R. and Macrossan, M. N., "Modeling dissociation-vibration coupling with the macroscopic chemistry method," *Rarefied gas dynamics: Proceedings of the 24th International Symposium*, American Institute of Physics, New York, In press.

[107] Lilley, C. R. and Macrossan, M. N., "An investigation of a Sutherland molecular model for DSMC simulations," Tech. Rep. 09/2002, Department of Mechanical Engineering, The University of Queensland, Brisbane, July 2002.

[108] Lilley, C. R. and Macrossan, M. N., "DSMC calculations of shock structure with various viscosity laws," *Rarefied gas dynamics: Proceedings of the 23rd International Symposium*, edited by A. D. Ketsdever and E. P. Muntz, American Institute of Physics, New York, 2003, Included on CD-ROM.

[109] Lilley, C. R. and Macrossan, M. N., "Methods for implementing the stream boundary condition in DSMC computations," *Int. J. Numer. Meth. Fluids*, Vol. 42, No. 12, 30th August 2003, pp. 1363–1371.

[110] Lilley, C. R. and Macrossan, M. N., "A macroscopic chemistry method for the direct simulation of gas flows," *Phys. Fluids*, Vol. 16, No. 6, June 2004, pp. 2054–2066.

[111] Lord, R. G., "Modelling dissociation of diatomic molecules using the Morse potential," *Rarefied gas dynamics: Proceedings of the 20th International Symposium*, edited by C. Shen, Peking University Press, Beijing, 1997, pp. 180–185.

[112] Lord, R. G., "Modeling vibrational energy exchange of diatomic molecules using the Morse interatomic potential," *Phys. Fluids*, Vol. 10, No. 3, March 1998, pp. 742–746.

[113] Lord, R. G., "Models of collisional dissociation," *Rarefied gas dynamics: Proceedings of the 23rd International Symposium*, edited by A. D. Ketsdever and E. P. Muntz, American Institute of Physics, New York, 2003, pp. 291–295.

[114] Losev, S. A., "Two-temperature chemical kinetics in gas dynamics," *AIAA Paper 96-2026*, AIAA, Washington, June 1996.

[115] Lumpkin, F. E., Haas, B. L., and Boyd, I. D., "Resolution of differences between collision number definitions in particle and continuum simulations," *Phys. Fluids A*, Vol. 3, No. 9, September 1991, pp. 2282–2284.

[116] Macheret, S. O., Fridman, A. A., Adamovich, I. V., Rich, J. W., and Treanor, C. E., "Mechanisms of nonequilibrium dissociation of diatomic molecules," *AIAA Paper 94-1984*, AIAA, Washington, 1994.

[117] Macheret, S. O. and Rich, J. W., "Nonequilibrium dissociation rates behind strong shock waves: Classical model," *Chem. Phys.*, Vol. 174, No. 1, 15th July 1993, pp. 25–43.

[118] Macrossan, M. N., "A fast simulation method with arbitrary viscosity law," *Rarefied gas dynamics: Proceedings of the 24th International Symposium*, American Institute of Physics, New York, In press.

[119] Macrossan, M. N., *Diatomic collision models used in the Monte-Carlo direct simulation method applied to rarefied hypersonic flows*, PhD thesis, Imperial College, University of London, 1983.

[120] Macrossan, M. N., "The equilibrium flux method for the calculation of flows with non-equilibrium chemical reactions," *J. Comp. Phys.*, Vol. 80, No. 1, January 1989, pp. 204–231.

[121] Macrossan, M. N., "ν-DSMC: A fast simulation method for rarefied flow," *J. Comp. Phys.*, Vol. 173, No. 2, 1st November 2001, pp. 600–619.

[122] Macrossan, M. N., "μ-DSMC: A general viscosity method for rarefied flow," *J. Comp. Phys.*, Vol. 185, No. 2, 1st March 2003, pp. 612–627.

[123] Macrossan, M. N., "Scaling parameters in rarefied flow and the breakdown of the Navier-Stokes equations," Tech. Rep. 09/2004, Division of Mechanical Engineering, The University of Queensland, Brisbane, 2004.

[124] Macrossan, M. N., Chiu, H.-H., and Mee, D. J., "A test facility for hypervelocity rarefied flows," *Rarefied gas dynamics: Proceedings of the 22nd International Symposium*, edited by T. J. Bartel and M. A. Gallis, American Institute of Physics, New York, 2001, pp. 772–779.

[125] Macrossan, M. N. and Lilley, C. R., "Modified generalized hard sphere collision model for direct simulation Monte Carlo calculations," *J. Thermophys. Heat Transfer*, Vol. 17, No. 2, April–June 2003, pp. 289–291.

[126] Macrossan, M. N. and Lilley, C. R., "Viscosity of argon at temperatures >2000 K from measured shock thickness," *Phys. Fluids*, Vol. 15, No. 11, November 2003, pp. 3452–3457.

[127] Marriott, P. M., *Non-equilibrium chemical reactions in the simulation of hypersonic rarefied flows*, PhD thesis, Imperial College, University of London, 1994.

[128] Marriott, P. M. and Harvey, J. K., "New approach for modelling energy exchange and chemical reactions in the direct simulation Monte Carlo method," *Rarefied Gas Dynamics: Proceedings of the 17th International Symposium*, edited by A. E. Beylich, VCH, Weinheim, Germany, 1991, pp. 784–791.

[129] Marsaglia, G., "Improving the polar method for generating a pair of normal random variables," Tech. Rep. D1-82-0203, Boeing Scientific Research Laboratories, Seattle, Washington, September 1962.

[130] Marsaglia, G., "Choosing a point from the surface of a sphere," *The Annals of Mathematical Statistics*, Vol. 43, No. 2, 1972, pp. 645–646.

[131] Meador, W. E., Miner, G. A., and Heinbockel, J. H., *Vibrational relaxation in hypersonic flow fields*, NASA, Washington, September 1993, NASA Technical Paper 3367.

[132] Metcalf, S. C., Coleman, G. T., and Berry, C. J., "Heat transfer to bluff faced and hemispherical faced cylinders between continuum and free molecular flow limits," *Rarefied gas dynamics: Proceedings of the 9th International Symposium*, edited by M. Becker and M. Fiebig, DFVLR-Press, Porz-Wahn, West Germany, 1974, pp. D16.1–D16.11.

[133] Millikan, R. C. and White, D. R., "Systematics of vibrational relaxation," *J. Chem. Phys.*, Vol. 39, No. 12, 15th December 1963, pp. 3209–3213.

[134] Muntz, E. P., "Rarefied gas dynamics," *Ann. Rev. Fluid Mech.*, Vol. 21, 1989, pp. 387–417.

[135] Oran, E. S., Oh, C. K., and Cybyk, B. Z., "Direct simulation Monte Carlo: Recent advances and applications," *Ann. Rev. Fluid Mech.*, Vol. 30, 1998, pp. 403–441.

[136] Park, C., "Problems of rate chemistry in the flight regimes of aeroassisted orbital transfer vehicles," Vol. 96 of *Progress in Astronautics and Aeronautics*, AIAA, New York, 1985, pp. 511–537.

[137] Park, C., "Assessment of two-temperature kinetic model for ionizing air," *AIAA Paper 87-1574*, AIAA, Washington, 1987.

[138] Park, C., *Nonequilibrium hypersonic aerothermodynamics*, John Wiley & Sons, New York, 1990.

[139] Parker, J. G., "Rotational and vibrational relaxation in diatomic gases," *Phys. Fluids*, Vol. 2, No. 4, July–August 1959, pp. 449–462.

[140] Present, R. D., *Kinetic theory of gases*, McGraw-Hill Book Company, New York, 1958.

[141] Pullin, D. I., "Kinetic models for polyatomic molecules with phenomenological energy exchange," *Phys. Fluids*, Vol. 21, No. 2, February 1978, pp. 209–216.

[142] Pullin, D. I., Davis, J., and Harvey, J. K., "Monte Carlo calculations of the rarefied transition flow past a bluff faced cylinder," *Rarefied gas dynamics: Proceedings of the 10th International Symposium*, edited by L. Potter, Vol. 51 of *Progress in Astronautics and Aeronautics*, AIAA, New York, 1979, pp. 379–391.

[143] Schaaf, S. A. and Chambré, P. L., "Flow of rarefied gases," *High speed aerodynamics and jet propulsion*, edited by H. W. Emmons, Vol. 3, Princeton University Press, 1958, Section H.

[144] Seinfeld, J. H. and Pandis, S. N., *Atmospheric chemistry and physics*, John Wiley & Sons, New York, 1998.

[145] The Chemical Rubber Publishing Company, *CRC handbook of chemistry and physics*, CRC Press, Boca Raton, Florida, 82nd ed., 2001.

[146] Tsien, H.-S., "Superaerodynamics, mechanics of rarefied gases," *Journal of the Aeronautical Sciences*, Vol. 13, December 1946, pp. 653–664.

[147] Vijayakumar, P., Sun, Q., and Boyd, I. D., "Vibrational-translational energy exchange models for the direct simulation Monte Carlo method," *Phys. Fluids*, Vol. 11, No. 8, August 1999, pp. 2117–2126.

[148] Vincenti, W. G. and Kruger, C. H., *Introduction to physical gas dynamics*, John Wiley & Sons, New York, 1965.

[149] Wadsworth, D. C. and Wysong, I. J., "Examination of DSMC chemistry models: Role of vibrational favoring," *Rarefied gas dynamics: Proceedings of the 20th International Symposium*, edited by C. Shen, Peking University Press, Beijing, 1997, pp. 174–179.

[150] Wadsworth, D. C. and Wysong, I. J., "Vibrational favoring effect in DSMC dissociation models," *Phys. Fluids*, Vol. 9, No. 12, December 1997, pp. 3873–3884.

[151] Wagner, W., "A convergence proof for Bird's direct simulation Monte Carlo method for the Boltzmann equation," *J. Statist. Phys.*, Vol. 6g, No. 3–4, 1992, pp. 1011–1044.

[152] Walpole, R. E. and Myers, R. H., *Probability and statistics for engineers and scientists*, Macmillan Publishing Company, New York, 4th ed., 1989.

[153] Wu, J.-S., Hsiao, W.-J., Lian, Y.-Y., and Tseng, K.-C., "Assessment of conservative weighting scheme in simulating chemical vapour deposition with trace species," *Int. J. Numer. Meth. Fluids*, Vol. 43, No. 1, 10th September 2003, pp. 93–114.

[154] Wysong, I. J., Dressler, R. A., Chiu, Y. H., and Boyd, I. D., "Direct simulation Monte Carlo dissociation model evaluation: Comparison to measured cross sections," *J. Thermophys. Heat Transfer*, Vol. 16, No. 1, January–March 2002, pp. 83–93.

[155] Wysong, I. J., Wadsworth, D. C., Weaver, D. P., and Campbell, D. H., "Influence of vibrational nonequilibrium on chemically reacting rarefied flows: Toward experimental verification of DSMC models," *AIAA Paper 96-2023*, AIAA, Washington, June 1996.

[156] Yun, K.-S., Weissman, S., and Mason, E. A., "High-temperature transport properties of dissociating nitrogen and dissociating oxygen," *Phys. Fluids*, Vol. 5, No. 6, June 1962, pp. 672–678.

[157] Zumdahl, S. S., *Chemistry*, D.C. Heath and Company, Lexington, 2nd ed., 1989.

APPENDIX A

Mathematical miscellanea

A.1 Some useful integrals

The complete gamma function $\Gamma(m+1)$ is defined by

$$\Gamma(m+1) = \int_0^\infty x^m \exp(-x) dx.$$

The solution

$$\int_a^\infty (x-a)^m \exp(-x) dx = \Gamma(m+1)\exp(-a) \tag{A.1}$$

has application in this study. The incomplete gamma function $\Gamma(m+1,\alpha)$ is defined by

$$\Gamma(m+1,\alpha) = \int_\alpha^\infty x^m \exp(-x) dx.$$

Incomplete gamma functions in the form

$$\int_\omega^\infty x^a \exp\left(-bx^2\right) dx = \left[2b^{(a+1)/2}\right]^{-1} \Gamma\left(\frac{a+1}{2}, b\omega^2\right) \tag{A.2}$$

and

$$I_n(\omega) \equiv \int_\omega^\infty x^n \exp\left(-x^2\right) dx \quad \text{where} \quad n \in \mathsf{Z}$$

appear in this study. Integrals of the form I_n are encountered when evaluating viscosity and collision rate expressions for the modified generalised hard sphere model. In terms of the incomplete gamma function,

$$I_n(\omega) = \frac{1}{2}\int_{\omega^2}^\infty y^{(n-1)/2} \exp(-y) dy = \frac{1}{2}\Gamma\left(\frac{n+1}{2}, \omega^2\right).$$

By applying the reduction formula $\Gamma(m+1,\alpha) = m\Gamma(m,\alpha) + \alpha^m \exp(-\alpha)$ and $\Gamma\left(\frac{1}{2},\omega^2\right) = \pi^{\frac{1}{2}} - \pi^{\frac{1}{2}}\mathrm{erf}(\omega) = \pi^{\frac{1}{2}}\mathrm{erfc}(\omega)$, it can be shown that

$$I_2(\omega) = \frac{\pi^{\frac{1}{2}}}{4}\mathrm{erfc}(\omega) + \frac{\omega\exp\left(-\omega^2\right)}{2}, \tag{A.3}$$

$$I_3(\omega) = \frac{\exp\left(-\omega^2\right)}{2}\left(1+\omega^2\right), \tag{A.4}$$

$$I_6(\omega) = \frac{15\pi^{\frac{1}{2}}}{16}\operatorname{erfc}(\omega) + \omega\exp\left(-\omega^2\right)\left(\frac{15}{8} + \frac{5}{4}\omega^2 + \frac{1}{2}\omega^4\right) \quad \text{and} \tag{A.5}$$

$$I_7(\omega) = \frac{\exp\left(-\omega^2\right)}{2}\left(6 + 6\omega^2 + 3\omega^4 + \omega^6\right). \tag{A.6}$$

Note that

$$I_2(0) = \frac{\pi^{\frac{1}{2}}}{4}, \quad I_3(0) = \frac{1}{2}, \quad I_6(0) = \frac{15\pi^{\frac{1}{2}}}{16} \quad \text{and} \quad I_7(0) = 3.$$

For this study, it is also convenient to define

$$I'_n(\omega) = \int_0^{\omega} x^n \exp\left(-x^2\right) dx = I_n(0) - I_n(\omega). \tag{A.7}$$

A solution of the beta function that has application in this study is

$$\int_0^a (a-x)^m x^n dx = \frac{\Gamma(m+1)\Gamma(n+1)}{\Gamma(m+n+2)} a^{m+n+1}. \tag{A.8}$$

A.2 Joint distribution functions

Consider two statistically independent continuous distributions $f_{x_1}(x_1)$ and $f_{x_2}(x_2)$. The joint distribution is given by $f_x(x_1, x_2) = f_{x_1} f_{x_2}$. A transformation of variables in the joint distribution from x_1, x_2 to $y_1(x_1, x_2), y_2(x_1, x_2)$ requires consideration of the Jacobian determinant $J(y_1, y_2)$. Following Grimmett and Stirzaker [69], the joint distribution of y_1 and y_2 is

$$f_y(y_1, y_2) = f_x\left[x_1(y_1, y_2), x_2(y_1, y_2)\right] \left|J(y_1, y_2)\right|,$$

where

$$J(y_1, y_2) = \frac{\partial(x_1, x_2)}{\partial(y_1, y_2)} = \begin{vmatrix} \dfrac{\partial x_1}{\partial y_1} & \dfrac{\partial x_2}{\partial y_1} \\ \dfrac{\partial x_1}{\partial y_2} & \dfrac{\partial x_2}{\partial y_2} \end{vmatrix} = \frac{\partial x_1}{\partial y_1}\frac{\partial x_2}{\partial y_2} - \frac{\partial x_1}{\partial y_2}\frac{\partial x_2}{\partial y_1}.$$

For

$$y_1 = ax_1 + bx_2 \quad \text{and} \quad y_2 = cx_1 + dx_2$$

where a, b, c and d are constants, it can be shown that

$$J = (ad - bc)^{-1}.$$

For a joint distribution $f(x, y)$, the marginal distribution of x can be obtained with

$$h(x) = \int_R f(x, y) dy,$$

where R is the range of y. The marginal distribution of y is obtained similarly.

A.3 Energy distributions for quantised vibrational energy

From Eq. 2.20, the continuous distribution of the reduced vibrational energy $\tilde{\epsilon}_{\rm vib}(q)$ is given by

$$f\left(\tilde{\epsilon}^{\star}_{\rm vib}\right) = \frac{\exp\left(-\tilde{\epsilon}^{\star}_{\rm vib}\right)}{Q_{\rm vib}}\,\delta\left[\tilde{\epsilon}^{\star}_{\rm vib} - \tilde{\epsilon}_{\rm vib}(q)\right] \quad \text{where} \quad q = 0, 1, ..., q_{\rm max}.$$

Here, $\tilde{\epsilon}^{\star}_{\rm vib}$ is the reduced vibrational energy in a continuous representation and $q_{\rm max}$ is the maximum possible vibrational energy level, which depends on the vibration model. It is useful to derive the distribution of $\tilde{\epsilon}_t = \tilde{\epsilon} + \tilde{\epsilon}_{\rm vib}(q)$ where $\tilde{\epsilon}$ is some reduced energy distributed according to the continuous Boltzmann distribution

$$f\left(\tilde{\epsilon}\right) = \tilde{\epsilon}^{\,\phi} \exp\left(-\tilde{\epsilon}\right) / \Gamma(\phi + 1).$$

The joint distribution of $\tilde{\epsilon}$ and $\tilde{\epsilon}^{\star}_{\rm vib}$ is

$$f\left(\tilde{\epsilon}, \tilde{\epsilon}^{\star}_{\rm vib}\right) = \frac{\tilde{\epsilon}^{\,\phi} \exp\left(-\tilde{\epsilon}_t\right)}{\Gamma(\phi+1) Q_{\rm vib}}\,\delta\left[\tilde{\epsilon}^{\star}_{\rm vib} - \tilde{\epsilon}_{\rm vib}(q)\right] \quad \text{where} \quad q = 0, 1, ..., q_{\rm max}.$$

The joint distribution of $\tilde{\epsilon}_t$ and $\tilde{\epsilon}^{\star}_{\rm vib}$ is found by transforming this distribution as discussed in §A.2. In this case, $x_1 = \tilde{\epsilon}$, $x_2 = \tilde{\epsilon}^{\star}_{\rm vib}$, $y_1 = \tilde{\epsilon}_t$ and $y_2 = \tilde{\epsilon}^{\star}_{\rm vib}$, giving a Jacobian $J = 1$. Therefore,

$$f\left(\tilde{\epsilon}_t, \tilde{\epsilon}^{\star}_{\rm vib}\right) = \frac{\left(\tilde{\epsilon}_t - \tilde{\epsilon}^{\star}_{\rm vib}\right)^{\phi} \exp\left(-\tilde{\epsilon}_t\right)}{\Gamma(\phi+1) Q_{\rm vib}}\,\delta\left[\tilde{\epsilon}^{\star}_{\rm vib} - \tilde{\epsilon}_{\rm vib}(q)\right] \quad \text{where} \quad q = 0, 1, ..., q_t. \tag{A.9}$$

Here, q_t is the quantum level with reduced energy $\tilde{\epsilon}_{\rm vib}\left(q_t\right)$ that is closest to $\tilde{\epsilon}_t$ such that $\tilde{\epsilon}_{\rm vib}\left(q_t\right) < \tilde{\epsilon}_t$. However if $\tilde{\epsilon}_t > \tilde{\epsilon}_{\rm vib}\left(q_{\rm max}\right)$, then $q_t = q_{\rm max}$ must be used. The distribution of $\tilde{\epsilon}_t$ alone is therefore

$$\begin{aligned} f\left(\tilde{\epsilon}_t\right) &= \frac{\exp\left(-\tilde{\epsilon}_t\right)}{\Gamma(\phi+1) Q_{\rm vib}} \int_0^{\tilde{\epsilon}_t} \left(\tilde{\epsilon}_t - \tilde{\epsilon}^{\star}_{\rm vib}\right)^{\phi} \delta\left[\tilde{\epsilon}^{\star}_{\rm vib} - \tilde{\epsilon}_{\rm vib}(q)\right] d\tilde{\epsilon}^{\star}_{\rm vib} \\ &= \frac{\exp\left(-\tilde{\epsilon}_t\right)}{\Gamma(\phi+1) Q_{\rm vib}} \sum_{q=0}^{q_t} \left[\tilde{\epsilon}_t - \tilde{\epsilon}_{\rm vib}(q)\right]^{\phi}. \end{aligned} \tag{A.10}$$

For bounded harmonic oscillators, $\tilde{\epsilon}_{\rm vib}(q) = q\Theta_{\rm vib}/T$, giving

$$q_t = \min\left(\left\lfloor \frac{\tilde{\epsilon}_t T}{\Theta_{\rm vib}} \right\rfloor, q_d\right) = \min\left(\left\lfloor \frac{\epsilon_t}{k\Theta_{\rm vib}} \right\rfloor, q_d\right).$$

For unbounded harmonic oscillators,

$$q_t = \left\lfloor \frac{\tilde{\epsilon}_t T}{\Theta_{\rm vib}} \right\rfloor = \left\lfloor \frac{\epsilon_t}{k\Theta_{\rm vib}} \right\rfloor.$$

As an example, consider the distribution of internal energy $\tilde{\epsilon}_{\rm int}$ in unbounded harmonic

oscillator molecules. In this case, the rotational energy $\tilde{\epsilon}_{\rm rot}$ is distributed according to Eq. 2.18, so $\phi = 0$. From Eq. A.10, the distribution of total internal energy $\tilde{\epsilon}_{\rm int} = \tilde{\epsilon}_{\rm rot} + \tilde{\epsilon}_{\rm vib}$ is given by

$$f\left(\tilde{\epsilon}_{\rm int}\right) = \frac{\exp\left(-\tilde{\epsilon}_{\rm int}\right)}{Q_{\rm vib}} \sum_{q=0}^{q_t} 1 = \frac{\exp\left(-\tilde{\epsilon}_{\rm int}\right)}{Q_{\rm vib}} (q_t + 1) = \frac{\exp\left(-\tilde{\epsilon}_{\rm int}\right)}{Q_{\rm vib}} \left\lfloor \frac{\tilde{\epsilon}_{\rm int} T}{\Theta_{\rm vib}} + 1 \right\rfloor . \qquad \text{(A.11)}$$

This result can be checked by sampling $\tilde{\epsilon}_{\rm rot}$ and $\tilde{\epsilon}_{\rm vib}$ from equilibrium distributions and comparing the resulting sampled distribution of $\tilde{\epsilon}_{\rm int}$ to the theoretical distribution of Eq. A.11. The results of such a comparison are shown in Fig. A.1 and confirm that Eq. A.11 is correct.

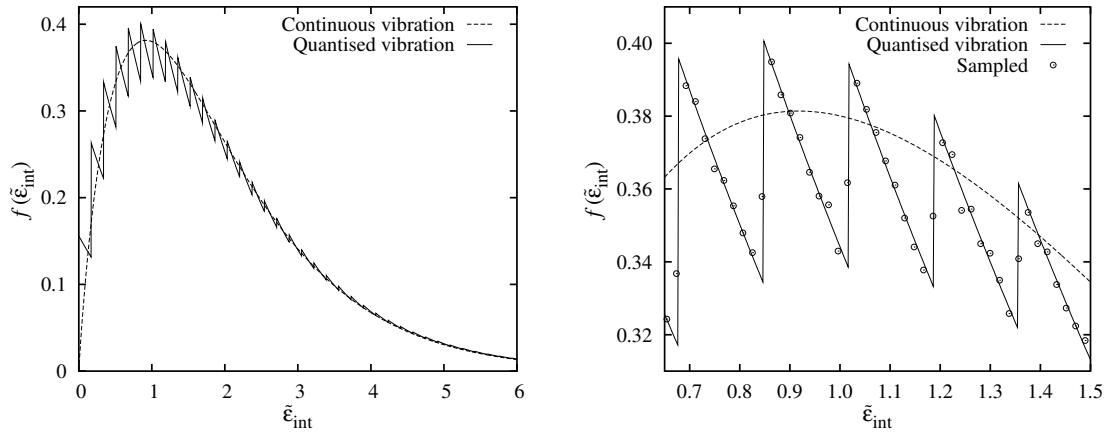

(a) Theoretical distributions.

(b) Detail of theoretical distributions compared to sampled distribution of $\tilde{\epsilon}_{\rm int}$.

Figure A.1: Distribution of reduced internal energy $\tilde{\epsilon}_{\rm int}$ for diatomic molecules with a continuous rotational energy distribution and the unbounded harmonic oscillator vibration model at $T/\Theta_{\rm vib} = 5.90$.

As a second example, consider the equilibrium distribution of $\tilde{\epsilon}_t = \tilde{\epsilon}_g + \tilde{\epsilon}_{\rm vib}(q)$ for VHS molecules with quantised vibrational energy. From Eq. 4.11, the distribution of reduced relative translational energy in collisions $\tilde{\epsilon}_g$ is

$$f(\tilde{\epsilon}_g) = \tilde{\epsilon}_g^{1-\upsilon} \exp\left(-\tilde{\epsilon}_g\right) / \Gamma\left(2-\upsilon\right).$$

For this example, $\phi = 1 - \upsilon$ and Eq. A.10 gives

$$f\left(\tilde{\epsilon}_t\right) = \frac{\exp\left(-\tilde{\epsilon}_t\right)}{\Gamma(2-\upsilon) Q_{\rm vib}} \times S \quad \text{where} \quad S = \sum_{q=0}^{q_t} \left[\tilde{\epsilon}_t - \tilde{\epsilon}_{\rm vib}(q)\right]^{1-\upsilon}. \qquad \text{(A.12)}$$

Note that S is constant for a given $\tilde{\epsilon}_t$.

This distribution has been calculated for both unbounded and bounded harmonic oscillators. This example used $\upsilon = 0.25$ and $q_d = 33$. These theoretical distributions are

shown in Fig. A.2. Sampled values of $\tilde{\epsilon}_g$ and $\tilde{\epsilon}_{\rm vib}(q)$ were used to obtain a sampled distribution of $\tilde{\epsilon}_t$. These sampled distributions are also shown in Fig. A.2 and demonstrate that Eq. A.12 is correct.

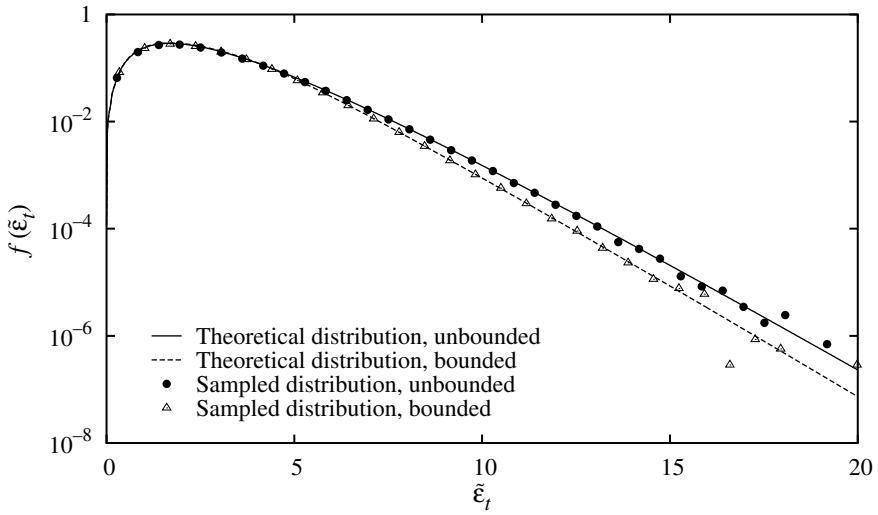

Figure A.2: Comparison of theoretical and sampled distributions of $\tilde{\epsilon}_t = \tilde{\epsilon}_g + \tilde{\epsilon}_{\rm vib}(q)$ for VHS molecules with $\upsilon = 0.25$ at $T/\Theta_{\rm vib} = 8.85$. For the bounded harmonic oscillators, $q_d = 33$.

A.4 Parabolic curve fit

Consider the three points (x_1, y_1), (x_2, y_2) and (x_3, y_3) as shown in Fig. A.3. The parabola $y = ax^2 + bx + c$ passing through these points can be obtained by specifying

$$\mathbf{y} = \begin{pmatrix} y_1 \\ y_2 \\ y_3 \end{pmatrix}, \quad \mathbf{Z} = \begin{pmatrix} x_1^2 & x_1 & 1 \\ x_2^2 & x_2 & 1 \\ x_3^2 & x_3 & 1 \end{pmatrix} \quad \text{and} \quad \mathbf{v} = \begin{pmatrix} a \\ b \\ c \end{pmatrix} \tag{A.13}$$

and then solving $\mathbf{v} = \mathbf{Z}^{-1}\mathbf{y}$. The gradient at the point (x_2, y_2) is then $2ax_2 + b$.

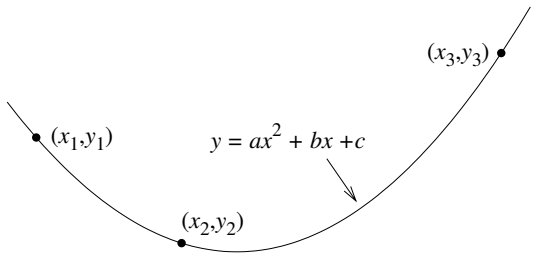

Figure A.3: Parabola $y = ax^2 + bx + c$ fitted to the points (x_1, y_1), (x_2, y_2) and (x_3, y_3).

APPENDIX **B**

Physical data for nitrogen

This appendix contains viscosity, equilibrium and reaction rate data for the dissociating nitrogen system. The collisions $N_2 + N_2$, $N_2 + N$ and $N + N$ occur in this system.

B.1 Viscosity and VHS parameters

The CRC Handbook of Chemistry and Physics [145] recommends the use of the curve fits given by Cole and Wakeham [51] for the viscosity of molecular nitrogen and oxygen mixtures. Over the temperature range 110 K $< T <$ 2100 K, Cole and Wakeham give

$$\begin{aligned} \ln\left[\Omega^{(2,2)\star}(T^*)\right] &= 0.41132 - 0.40972\ln T^* + 0.0228\,(\ln T^*)^2 + 0.0365\,(\ln T^*)^3 \\ &\quad - 0.00857\,(\ln T^*)^4 \end{aligned}$$

for diatomic nitrogen, where $T^* = T/104.2$. This $\Omega^{(2,2)\star}$ was used in Eq. 2.28 with $d = 3.632$ Å [51] to obtain the recommended viscosity, which is shown in Fig. B.1. This recommended viscosity is within 2% of 11 sets of experimental data in the temperature range 110 K $< T <$ 2100 K. Fig. B.1 also shows the viscosity obtained by extrapolating the curve fit beyond 2100 K.

For the major species present in high temperature air, Gupta *et al.* [70] give expressions for $\Omega^{(1,1)\star}$ and $\Omega^{(2,2)\star}$ in the form

$$\ln\left[\pi d^2 \Omega^{(j,j)\star}\right] = \sum_{i=0}^{3} G_i^{(j,j)} (\ln T)^i , \tag{B.1}$$

where j corresponds to 1 or 2 for $\Omega^{(1,1)\star}$ or $\Omega^{(2,2)\star}$ respectively. For collisions in the dissociating nitrogen system, the curve fit coefficients $G_i^{(j,j)}$ are given in Table B.1. These coefficients have been used to calculate $\pi d^2 \Omega^{(2,2)\star}$, and then the characteristic viscosity μ_{A+B} using Eq. 2.29. The resulting viscosity behaviour for the $N_2 + N_2$, $N_2 + N$ and $N + N$ systems is shown in Figs. B.1 to B.3. Fig. B.1 indicates that the viscosity fit of Cole and Wakeham [51] is inaccurate when extrapolated above $T \sim 4000$ K, because the viscosity rises rapidly. Consequently, the viscosity fits of Gupta *et al.* have been used here. The viscosity data of Yun *et al.* [156] for atomic nitrogen is also shown in Fig. B.3.

Power law viscosity relations have been fitted to the data of Gupta *et al.* [70] for 1000

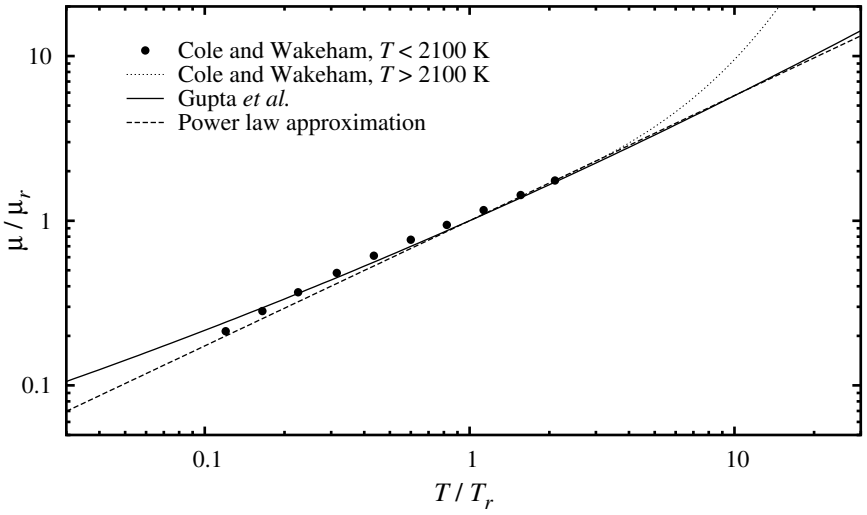

Figure B.1: Viscosity of pure diatomic nitrogen using the values recommended by Cole and Wakeham [51], the curve fit of Gupta *et al.* [70] and the power law viscosity relation $\mu/\mu_r = (T/T_r)^{0.76}$. Here $\mu_r = 38.61$ μPa·s and $T_r = 1000$ K. The data of Cole and Wakeham is accurate for temperatures below the limit of reliable experimental data at $T \approx 2100$ K. For $T > 2100$ K, the extrapolated viscosity is shown.

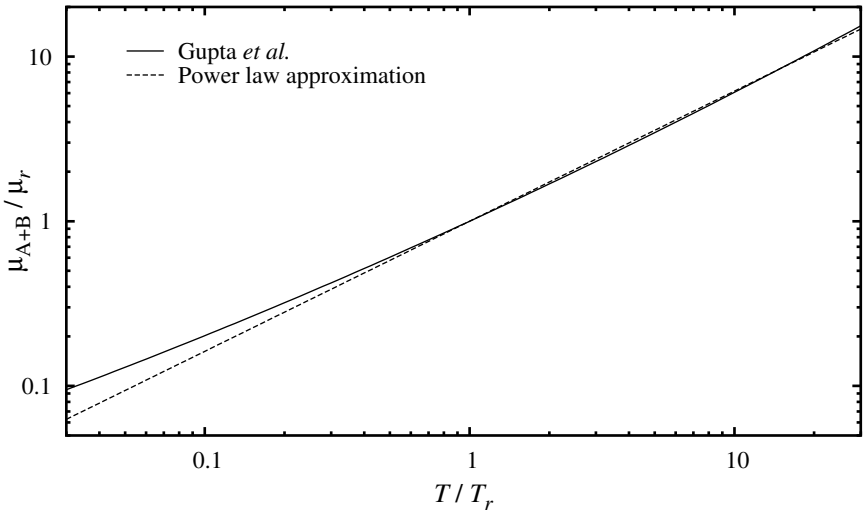

Figure B.2: Characteristic viscosity μ_{A+B} for collisions between N_2 and N molecules. The curve fit of Gupta *et al.* [70] and the power law viscosity relation $\mu/\mu_r = (T/T_r)^{0.79}$ are shown. Here $\mu_r = 36.87$ μPa·s and $T_r = 1000$ K.

K $< T <$ 20000 K and are also shown in Figs. B.1 to B.3. The T_r, μ_r and v values have been used to obtain the VHS collision parameters, which are included in Table B.1. Fig. B.4 shows the differences between the power law viscosities and the predictions of Gupta *et al.* over the temperature range 1000 K $< T <$ 30000 K. Up to 20000 K, the differences were less than 5%. These power law viscosities, and the resulting VHS model parameters, are therefore considered to be sufficiently accurate at high temperatures. The cross-species collision cross-sections, given by Koura and Matsumoto [98] for the VSS model, can also be used for the VHS model.

Table B.1: Curve fit coefficients from Gupta *et al.* [70] for calculating $\pi d^2\Omega^{(1,1)\star}$ and $\pi d^2\Omega^{(2,2)\star}$ according to Eq. B.1, and VHS parameters for collisions in the dissociating nitrogen system. For these collisions, $G_3^{(1,1)} = 0$ and $G_3^{(2,2)} = 0$. The VHS parameters were calculated from the power law viscosity $\mu/\mu_r = (T/T_r)^{1/2+\upsilon}$ fitted to the viscosity correlation of Gupta *et al.* at high temperatures. In all cases, $T_r = 1000$ K was used. The mass of nitrogen atoms has been calculated using $\mathcal{M}_N/\mathcal{N} = 14.01/\mathcal{N} = 2.3264 \times 10^{-26}$ kg. Here $\mathcal{M}_N$ is the molar mass of nitrogen atoms in kg/kmol.

Properties	Collision partners		
	$N_2 + N_2$	$N_2 + N$	$N + N$
$G_0^{(1,1)}$	-41.0253	-41.9462	-41.0065
$G_1^{(1,1)}$	-0.1182	0.0119	-0.0572
$G_2^{(1,1)}$	-0.0112	-0.0194	-0.0033
$G_0^{(2,2)}$	-41.9617	-41.8735	-41.7265
$G_1^{(2,2)}$	0.0683	0.0239	-0.0960
$G_2^{(2,2)}$	-0.0203	-0.0190	-0.0118
μ_r (μPa·s)	38.61	36.87	44.75
υ	0.26	0.29	0.28
σ_r (m^2)	4.991×10^{-19}	4.421×10^{-19}	3.118×10^{-19}
g_r (m/s)	1089.5	1334.3	1540.7
Ξ (m^3/s)	5.625×10^{-16}	6.061×10^{-16}	4.946×10^{-16}

Both accurate and approximate formulae for calculating the viscosity of binary mixtures were presented in §2.6.2. The nitrogen viscosity correlations of Gupta *et al.* [70] have been used to compare these accurate and approximate formulae. The results are shown in Fig. B.5. For various dissociation fractions, the approximate formula gives viscosity up to 4.5% higher than the accurate formula.

B.2 Equilibrium constants

The equilibrium constant for the net nitrogen dissociation reaction $N_2 \rightleftharpoons N + N$ is often represented using the common form of the equilibrium constant K_c^* given by Eq. 5.2. For this form, Vincenti and Kruger [148] provide

$$K_c^* = 1.8 \times 10^4 \exp\left(-\Theta_d/T\right) \text{ kmol/m}^3. \tag{B.2}$$

For nitrogen, the characteristic dissociation temperature $\Theta_d = 113200$ K [91]. As given in Eq. 5.3, Gupta *et al.* [70] represented K^* by the curve fit

$$\ln\left[K_G^*(T,n)\right] = \sum_{i=0}^{5} G_i^*(n) Z^i \quad \text{where} \quad Z = \ln\left(10^4/T\right). \tag{B.3}$$

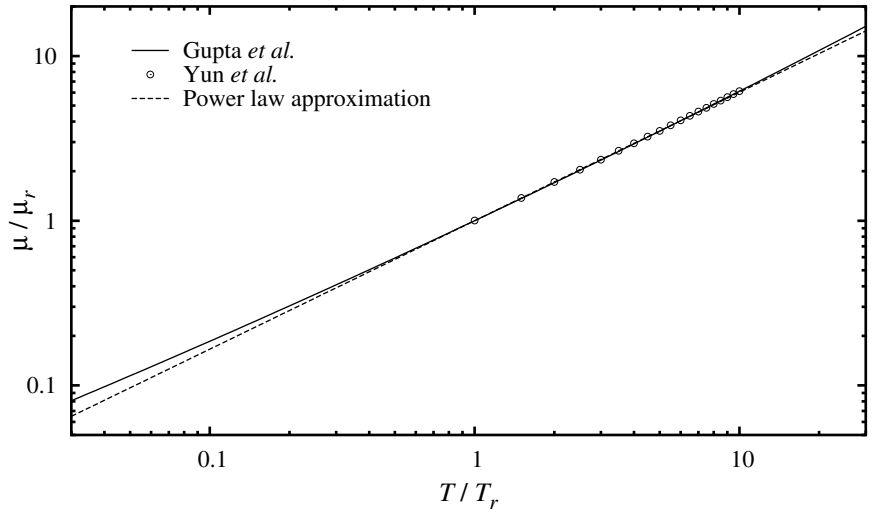

Figure B.3: Viscosity of pure atomic nitrogen calculated using the curve fit of Gupta *et al.* [70] and the power law viscosity relation $\mu/\mu_r = (T/T_r)^{0.78}$. Here $\mu_r = 44.75$ μPa·s and $T_r = 1000$ K.

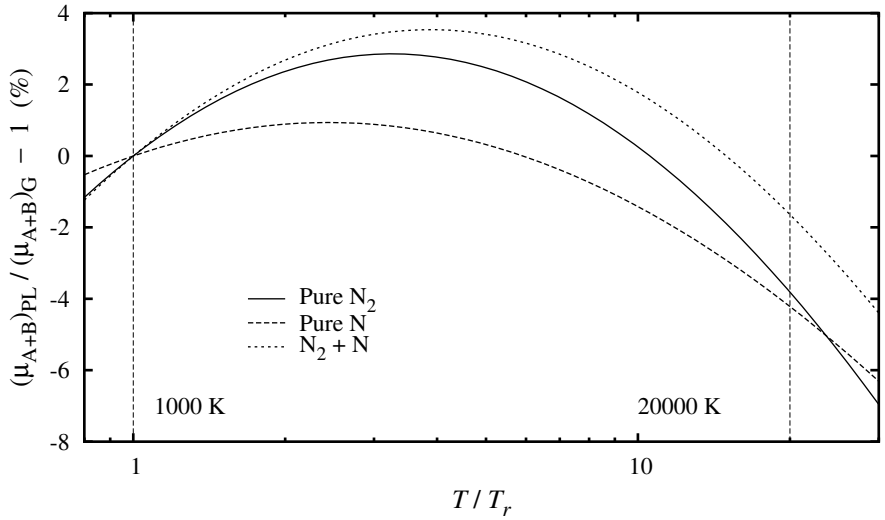

Figure B.4: Comparison of viscosities for the N_2 + N system between 1000 K and 30000 K. Here $(\mu_{A+B})_{PL}$ is the power law approximation and $(\mu_{A+B})_G$ is the viscosity recommended by Gupta *et al.* [70].

For the nitrogen dissociation reaction, the curve fit coefficients G_i^* are given in Table B.2. For a given number density n, the G_i^* values can be approximated by linear interpolation against $\log n$. Fig. B.6 shows that this interpolation method will be quite accurate. A comparison between K_c^* and K_G^* is given in Fig. B.7. This figure shows that differences between K_c^* and K_G^* are large at low n and high T.

B.3 Reaction rates

Some published nitrogen dissociation rates are given in Table B.3. These rates are compared in Figs. B.8 and B.9 for reactions 1 and 2. Using the two-temperature rate model of Park [137], the reduced dissociation rates realised in vibrationally cold condi-

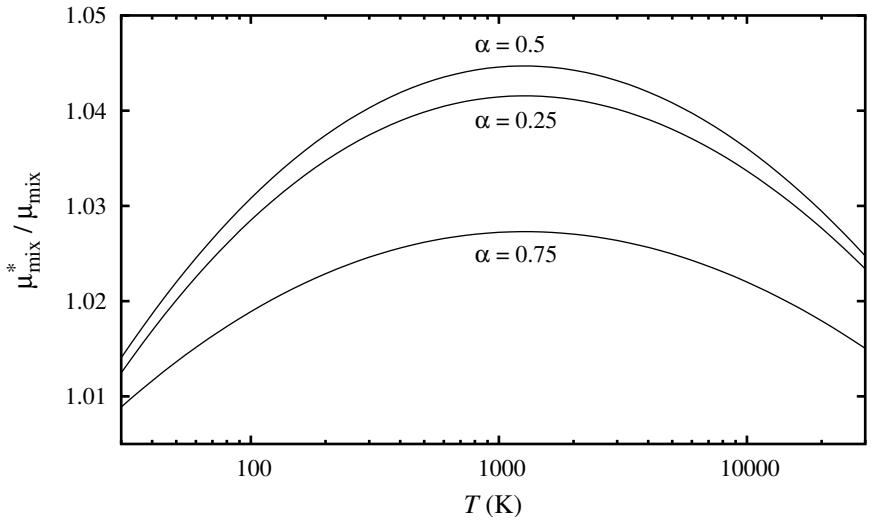

Figure B.5: Comparison of N_2 + N mixture viscosity at various α using accurate and approximate mixture viscosity formulae. The mixture viscosity μ_{mix} was calculated using the accurate formula of Eq. 2.33 and the approximate mixture viscosity μ^*_{mix} using Eq. 2.34. The nitrogen viscosity correlations of Gupta *et al.* [70] were used.

Table B.2: Curve fit coefficients for $K^*_{\text{G}}(T, n)$ for the $N_2 \rightleftharpoons N + N$ dissociation reaction at various number densities, as given by Gupta *et al.* [70]. For this reaction $G^*_5 = 0$. These coefficients are used in Eq. B.3 to provide $K^*_{\text{G}}(T, n)$.

n	G^*_0	G^*_1	G^*_2	G^*_3	G^*_4
$10^{20}/\text{m}^3$	−0.86284	−17.2635	−0.152245	−1.79191	−1.42518
$10^{21}/\text{m}^3$	−1.41108	−15.6315	−0.655486	−2.11364	−1.31460
$10^{22}/\text{m}^3$	−1.79526	−14.0810	−1.23908	−2.40055	−1.20533
$10^{23}/\text{m}^3$	−1.99903	−12.8199	−1.81730	−2.60376	−1.11597
$10^{24}/\text{m}^3$	−2.08088	−11.6894	−2.46330	−2.73172	−1.04068
$10^{25}/\text{m}^3$	−2.06856	−11.0496	−2.93912	−2.74128	−1.00734

tions are shown. Here, the effective temperature T_e was calculated using Eq. 5.8 with $T_{\text{vib}}/T_{\text{tr+rot}} = 0.8$ and 0.5. The rates of Park [138] and $s = 0.7$ was used. Note that $T_{\text{vib}}/T_{\text{tr+rot}} = 1$ refers to thermal equilibrium conditions where $T_{\text{vib}} = T_{\text{tr+rot}} = T$. Where $T_{\text{vib}}/T_{\text{tr+rot}} \neq 1$, the rates in Figs. B.8 and B.9 have been plotted versus $10^4/T_{\text{tr+rot}}$.

It is important to note that most available rate data is limited to moderate temperatures and near-equilibrium conditions. At the high temperature and non-equilibrium conditions of hypersonic flight, reaction rates are poorly known. Through necessity, rates measured at relatively low temperatures are often extrapolated to very high temperatures without experimental confirmation.

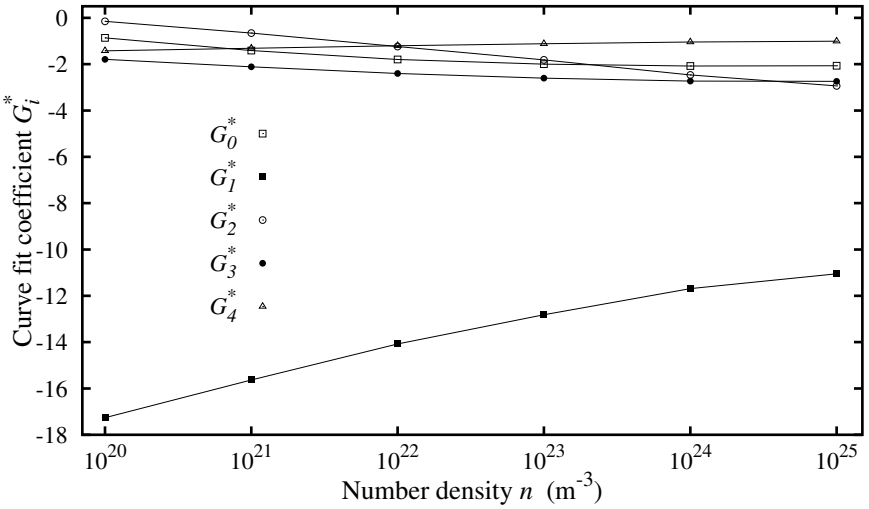

Figure B.6: Curve fit coefficients for $K_{\mathrm{G}}^*(T,n)$ at various number densities, using G_i^* from Table B.2.

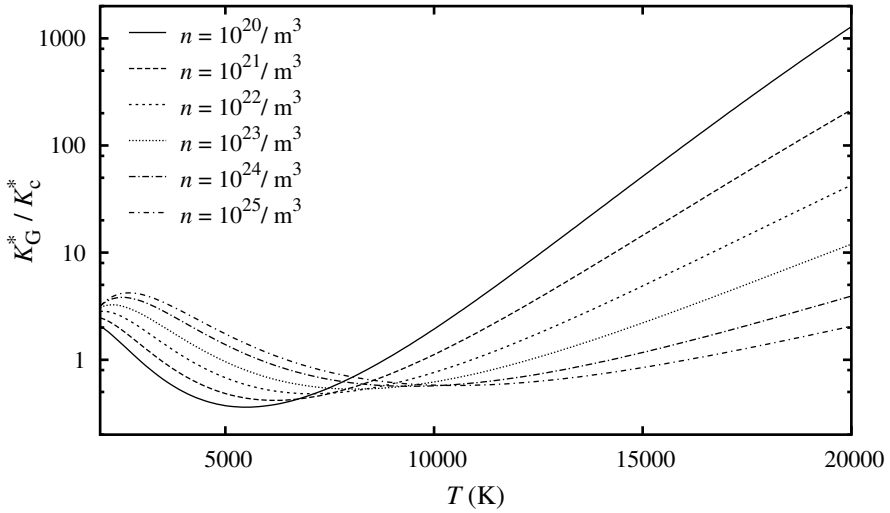

Figure B.7: Ratio of $K_{\mathrm{G}}^*(T,n)$ to $K_c^*(T)$ for dissociating nitrogen.

Table B.3: Some published nitrogen dissociation rates. The parameters C^+ and η^+ refer to the Arrhenius rate equation of Eq. 5.6 where $k^+ = C^+ (T/\Theta_d)^{\eta^+} \exp(-\Theta_d/T)$. For nitrogen, $\Theta_d = 113200K$ [91].

Source	Temperature range	Reaction 1 $N_2 + N \rightleftharpoons N + N + N$		Reaction 2 $N_2 + N_2 \rightleftharpoons N + N + N_2$	
		C^+	η^+	C^+	η^+
	(K)	(m^3/kmol/s)		(m^3/kmol/s)	
Byron [44]	$6000 < T < 9000$	1.129×10^{12}	-1.5	1.427×10^{12}	-0.5
Kewley and Hornung [91]	$6000 < T < 14000$	1.972×10^{10}	-2.5	4.713×10^{8}	-3.5
Park [138]	Not given	2.460×10^{11}	-1.6	5.740×10^{10}	-1.6

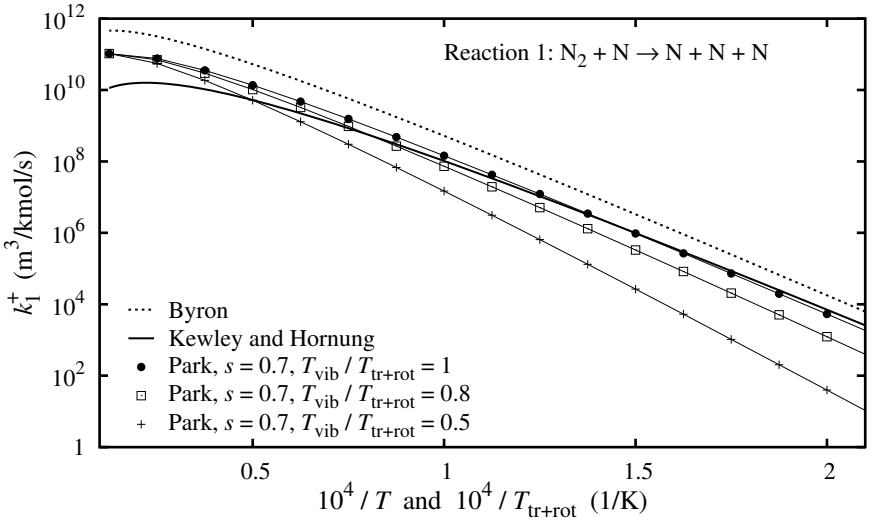

Figure B.8: Comparison of some published rates for the nitrogen dissociation reaction $N_2 + N \rightarrow N + N + N$. The rates of Park [138] are plotted for the two-temperature rate model [137].

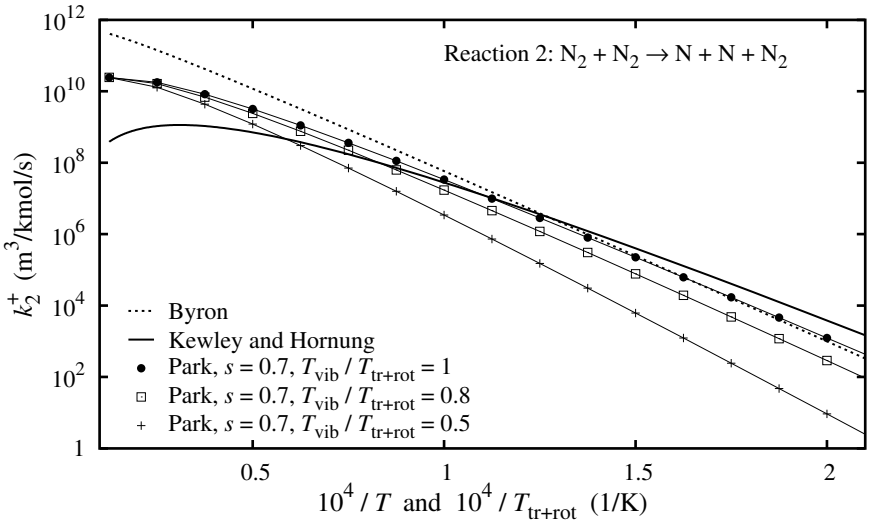

Figure B.9: Comparison of some published rates for the nitrogen dissociation reaction $N_2 + N_2 \rightarrow N + N + N_2$. The rates of Park [138] are plotted for the two-temperature rate model [137].

APPENDIX C

Further DSMC details

This appendix gives some further details of several aspects of the DSMC method that were excluded from Chapters 4 and 6, as listed below.

- Expressions for determining the cell number of a simulator particle are given in §C.1.
- Aspects of particle trajectories in an axisymmetric co-ordinate system are considered in §C.2.
- Further details of the GHS and MGHS collision models are given in §C.3 and §C.4. These include detailed derivations of viscosity and collision rate expressions in a pure gas at equilibrium. The expressions derived here are more general than those given by Macrossan and Lilley [125]. Argon has been used as a test case to compare the models.
- Derivations of the TCE and VFD model parameters are given in §C.5 and §C.6.
- Numerical methods for calculating the macroscopic reaction rates realised by the TLD and EAE dissociation models at thermal equilibrium are given in §C.7 and §C.8.

C.1 Determining the cell number of a particle

In DSMC calculations, efficient algorithms are required to determine the cell in which each simulator particle is located. Consider the one-dimensional grid of N cells as shown in Fig. C.1. For equally sized cells, the cell number n of a particle at x_p is simply

$$n = \lfloor (x_p - x_0) / \Delta x \rfloor,$$

where $\Delta x = (x_N - x_0)/N$ is the cell size.

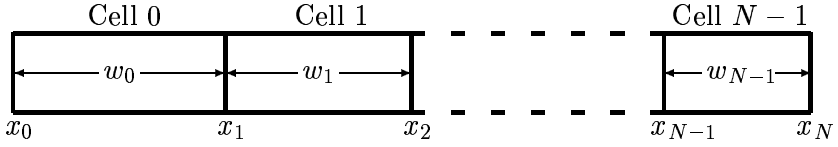

Figure C.1: Schematic representation of a one-dimensional grid.

A more efficient grid uses small cells in high density regions and larger cells in lower density regions. For blunt body flows, it is often convenient to use a geometric progression in cells sizes, with the smallest cells near the body [21]. Referring to Fig. C.1, the widths of adjacent cells i and $i+1$ are related by

$$w_{i+1} = f w_i,$$

where f is the ratio of adjacent cell widths which is constant for a particular grid. The total width $W = x_N - x_0$ of the grid is

$$W = \sum_{i=0}^{N-1} w_i = w_0 + w_1 + w_2 + ... + w_{N-1} = w_0 + f w_0 + f^2 w_0 + ... + f^{N-1} w_0 = w_0 \sum_{i=0}^{N-1} f^i.$$

Using mathematical induction, it can be shown that $\sum_{i=0}^{N-1} f^i = \left(1 - f^N\right)/(1-f)$. The width of the first cell w_0 is therefore

$$w_0 = W(1-f)/\left(1 - f^N\right).$$

This equation is applied to calculate w_0 from given W, N and f. The starting co-ordinate of cell n is given by

$$x_n = x_0 + w_0 + ... + w_{n-1} = x_0 + \sum_{i=0}^{n-1} w_i = x_0 + w_0 \sum_{i=0}^{n-1} f^i = x_0 + w_0 \left(1 - f^n\right) / \left(1 - f\right).$$

For a particle at x_p the position in the grid relative to the cell boundaries is

$$n = \ln \left[1 - \left(\frac{1-f}{w_0} \right) (x_p - x_0) \right] \frac{1}{\ln f}.$$

A particle resides in cell m if $n < m < n+1$. By defining the convenient parameters $\Upsilon_1 \equiv (1-f)/w_0$ and $\Upsilon_2 \equiv 1/\ln f$ which are constant for a particular grid geometry, the cell number of the particle at x_p is given by

$$n = \left\lfloor \Upsilon_2 \ln \left[1 - \Upsilon_1 \left(x_p - x_0 \right) \right] \right\rfloor. \tag{C.1}$$

In a rectangular grid, with a geometric progression in cell sizes in the x and y directions, Eq. C.1 is applied to find the row and column of the cell in which a particle is located. With the base address of the first cell in the region, the cell number can then be calculated. Similar procedures apply in a radial grid with a geometric progression in cell sizes in the radial and angular directions.

C.2 Particle trajectory in axisymmetric co-ordinates

From Eq. 4.3, the axial co-ordinate at the end of the DSMC move step is $z = z_0 + v_z \Delta t$. Therefore

$$\Delta t = (z - z_0)/v_z = \hat{z}/v_z,$$

where $\hat{z} = z - z_0$ is a normalised z co-ordinate. Substituting this into Eq. 4.1 gives

$$\begin{aligned} r^2 &= \left[r_0 + \frac{v_r}{v_z}(z - z_0)\right]^2 + \left[\frac{v_\theta}{v_z}(z - z_0)\right]^2 \\ &= \left(\hat{v}_r^2 + \hat{v}_\theta^2\right) z^2 + \left[2\hat{v}_r \left(r_0 - \hat{v}_r z_0\right) - 2\hat{v}_\theta^2 z_0\right] z + \left(r_0 - \hat{v}_r z_0\right)^2 + \hat{v}_\theta^2 z_0^2 \qquad \text{(C.2)} \\ &= \left(r_0 + \hat{v}_r \hat{z}\right)^2 + \left(\hat{v}_\theta \hat{z}\right)^2, \qquad \text{(C.3)} \end{aligned}$$

which is the trajectory of a particle moving in a straight line projected into the (z, r) plane. Here, $\hat{v}_r = v_r/v_z$ and $\hat{v}_\theta = v_\theta/v_z$ are normalised velocities.

Consider the intersection of this trajectory with the straight line in the (z, r) plane described by $r = m\hat{z} + c = mz + c - mz_0$. Substituting this into Eq. C.3 gives

$$\left(m\hat{z} + c\right)^2 = \left(r_0 + \hat{v}_r \hat{z}\right)^2 + \left(\hat{v}_\theta \hat{z}\right)^2,$$

which may be rearranged to give

$$A\hat{z}^2 + B\hat{z} + C = 0$$

where

$$A = \hat{v}_r^2 + \hat{v}_\theta^2 - m^2, \quad B = 2r_0\hat{v}_r - 2mc \quad \text{and} \quad C = r_0^2 - c^2.$$

The z co-ordinates of the two intersection points are then found by evaluating

$$z = \left[-B \pm \left(B^2 - 4AC\right)\right] / (2A) + z_0.$$

For a line with constant r at r_{const}, the gradient m is zero, and

$$A = \hat{v}_r^2 + \hat{v}_\theta^2, \quad B = 2r_0\hat{v}_r \quad \text{and} \quad C = r_0^2 - r_{\text{const}}^2$$

should be used. For a line with constant $\hat{z}$ at $\hat{z}_{\text{const}} = z_{\text{const}} - z_0$, Eq. C.3 gives the r co-ordinate of the intersection point at

$$r = \left[\left(r_0 + \hat{v}_r \hat{z}_{\text{const}}\right)^2 + \left(\hat{v}_\theta \hat{z}_{\text{const}}\right)^2\right]^{\frac{1}{2}}.$$

Consider a circle centred at the origin with radius R, described by $z^2 + r^2 = R^2$. By letting

$$A = \hat{v}_r^2 + \hat{v}_\theta^2, \quad B = 2\hat{v}_r \left(r_0 - \hat{v}_r z_0\right) - 2\hat{v}_\theta^2 z_0 \quad \text{and} \quad C = \left(r_0 - \hat{v}_r z_0\right)^2 + \hat{v}_\theta^2 z_0^2,$$

the trajectory of Eq. C.2 is simply

$$r^2 = Az^2 + Bz + C.$$

The two intersection points between this trajectory and the circle are found by solving

$$(A+1)z^2 + Bz + C - R^2 = 0,$$

and are

$$z = \frac{-B \pm \left[B^2 - 4(A+1)(C-R^2)\right]^{\frac{1}{2}}}{2\,(A+1)}.$$

C.3 Generalised hard sphere model

The collision cross-section σ of the generalised hard sphere (GHS) model [84] is given as the sum of N VHS terms, such that

$$\sigma = \sum_{i=1}^{N} \sigma_i \left(g_r/g\right)^{2\upsilon_i}.$$

Here σ_i and υ_i are constants and g_r is a reference relative speed defined by $g_r \equiv (4RT_r)^{\frac{1}{2}}$ where T_r is a reference temperature. It is useful to define a normalised relative speed $\hat{g} \equiv g/g_r$. Also, using a reference cross-section σ_r, a normalised cross-section $\hat{\sigma}_i$ can be defined by $\hat{\sigma}_i \equiv \sigma_i/\sigma_r$. The GHS collision cross-section can then be written in the normalised form

$$\hat{\sigma} = \sum_{i=1}^{N} \hat{\sigma}_i/\hat{g}^{2\upsilon_i}. \tag{C.4}$$

Note that the Sutherland-VHS model, described in §4.4.2, is obtained by using $N = 2$, $\upsilon_1 = 0$, $\upsilon_2 = 1$, $\sigma_1 = \sigma_s$ and $\sigma_2 = \sigma_s\,(6kT_s)\,/\,\left(\tilde{m}g_r^2\right)$.

From Eq. 2.28, the Chapman-Enskog viscosity expression can be written

$$\mu = \frac{5m}{8}\frac{(\pi RT)^{\frac{1}{2}}}{\Omega}, \tag{C.5}$$

where Ω is a weighted average viscosity cross-section, given by

$$\Omega = \int_0^\infty \tilde{g}^7 \sigma_\mu \exp\left(-\tilde{g}^2\right) d\tilde{g}. \tag{C.6}$$

Here $\tilde{g}^2 \equiv g^2/(4RT)$ is the reduced relative speed introduced in Eq. 2.11. Using $\sigma_\mu = 2\sigma/3$, this integral is

$$\Omega_{\mathrm{GHS}} = \frac{2}{3}\int_0^\infty \left[\sum_{i=1}^{N} \sigma_i/\hat{g}^{2\upsilon_i}\right] \tilde{g}^7 \exp\left(-\tilde{g}^2\right) d\tilde{g}$$

for the GHS cross-section of Eq. C.4. Note that

$$\hat{g} = \tilde{g}\hat{T}^{\frac{1}{2}}, \tag{C.7}$$

so $\hat{g}^{-2\upsilon_i} = \tilde{g}^{-2\upsilon_i}/\hat{T}^{\upsilon_i}$. Using Eq. A.2,

$$\Omega_{\mathrm{GHS}} = \frac{2}{3}\sum_{i=1}^{N}\frac{\sigma_i}{\hat{T}^{\upsilon_i}}\int_0^\infty \tilde{g}^{7-2\upsilon_i}\exp\left(-\tilde{g}^2\right)d\tilde{g} = \frac{1}{3}\sum_{i=1}^{N}\frac{\sigma_i\Gamma\left(4-\upsilon_i\right)}{\hat{T}^{\upsilon_i}}.$$

This shows that Ω_{GHS} is a function of $\hat{T}$ alone. For $N = 2$,

$$\Omega_{\mathrm{GHS}} = \frac{1}{3}\left[\frac{\sigma_1\Gamma\left(4-\upsilon_1\right)}{\hat{T}^{\upsilon_1}} + \frac{\sigma_2\Gamma\left(4-\upsilon_2\right)}{\hat{T}^{\upsilon_2}}\right]. \tag{C.8}$$

For $N = 2$, Macrossan and Lilley [125] obtained GHS parameters for argon that provided adequate agreement with the viscosity values recommended by Kestin *et al.* [90]. These values were $(\sigma_2/\sigma_1, \upsilon_1, \upsilon_2) = (39/61, 2/13, 14/13)$. By using these values and $\mu_r = 22.83$ μPa·s at $T_r = 300$ K [90] in Eqs. C.8 and C.5, $\sigma_1 = 3.920\times10^{-19}$ m^2 and $\sigma_2 = 2.507\times10^{-19}$ m^2 are obtained. The resulting GHS viscosity behaviour is shown Fig. C.2. This viscosity behaviour is in better agreement with the recommended values than the power law viscosity relation $\mu \propto T^{0.72}$ for $T \lesssim 300$ K.

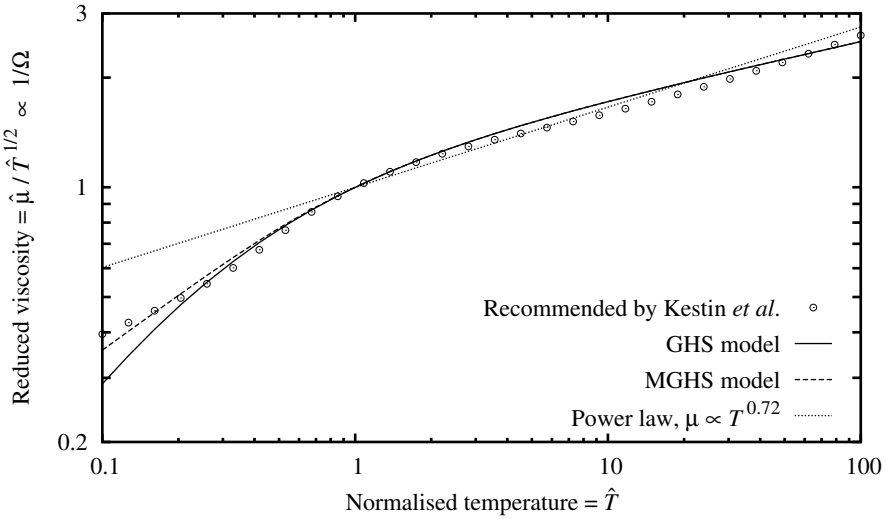

Figure C.2: Reduced viscosity $\hat{\mu}/\hat{T}^{\frac{1}{2}} \equiv (\mu/\mu_r)/(T/T_r)^{1/2} \propto 1/\Omega$ versus normalised temperature $\hat{T} \equiv T/T_r$ for argon using the GHS and MGHS models, compared to that recommended by Kestin *et al.* [90] and the power law viscosity with $\mu \propto T^{0.72}$. Here $\upsilon_1 = 2/13$, $\upsilon_2 = 14/13$, $\sigma_1 = 3.920\times10^{-19}$ m^2, $\sigma_2 = 2.507\times10^{-19}$ m^2 and $\mu_r = 22.83$ μPa·s at $T_r = 300$ K have been used. The MGHS transition point was $(\hat{V}^*, \hat{g}^*) = (\hat{V}_{\min}, \hat{g}_{\min})$.

By defining $V \equiv \sigma g$, $V_r \equiv \sigma_r g_r$ and $\hat{V} \equiv V/V_r$, the mean collision rate ν may be expressed as

$$\nu = n\langle\sigma g\rangle = n\langle V\rangle = n\langle V_r\hat{V}\rangle = nV_r\langle\hat{\sigma}\hat{g}\rangle.$$

From Eq. 2.12, the equilibrium distribution of $\tilde{g}$ is $f(\tilde{g}) = \left(4/\pi^{1/2}\right)\tilde{g}^2 \exp\left(-\tilde{g}^2\right)$, so

$$\nu = \frac{4nV_r}{\pi^{1/2}} \int_0^\infty (\hat{\sigma}\hat{g})\, \tilde{g}^2 \exp\left(-\tilde{g}^2\right) d\tilde{g}. \tag{C.9}$$

For the GHS model,

$$\begin{aligned} \nu_{\mathrm{GHS}} &= \frac{4nV_r}{\pi^{1/2}} \int_0^\infty \sum_{i=1}^{N} \hat{\sigma}_i \hat{g}^{1-2v_i} \tilde{g}^2 \exp\left(-\tilde{g}^2\right) d\tilde{g} \\ &= \frac{4nV_r}{\pi^{1/2}} \sum_{i=1}^{N} \hat{\sigma}_i \hat{T}^{\frac{1}{2}-v_i} \int_0^\infty \tilde{g}^{3-2v_i} \exp\left(-\tilde{g}^2\right) d\tilde{g}. \end{aligned}$$

Using Eq. A.2, this becomes

$$\nu_{\mathrm{GHS}} = 2nV_r \left(\frac{\hat{T}}{\pi}\right)^{\frac{1}{2}} \sum_{i=1}^{N} \frac{\hat{\sigma}_i \Gamma(2-v_i)}{\hat{T}^{v_i}}. \tag{C.10}$$

This shows that ν_{GHS} is a function of n and $\hat{T}$. For $N = 2$,

$$\nu_{\mathrm{GHS}} = 2nV_r \left(\frac{\hat{T}}{\pi}\right)^{\frac{1}{2}} \left[\frac{\hat{\sigma}_1 \Gamma(2-v_1)}{\hat{T}^{v_1}} + \frac{\hat{\sigma}_2 \Gamma(2-v_2)}{\hat{T}^{v_2}}\right].$$

This GHS collision rate, using the argon parameters from above, is shown in Fig. C.3. Here ν_{GHS} has been normalised relative to the nominal collision rate $\nu_{\mathrm{nom}} = (4/\pi)(nkT/\mu)$ from Eq. 2.40, using the argon viscosity $\mu = \mu(T)$ from Kestin *et al.* [90].

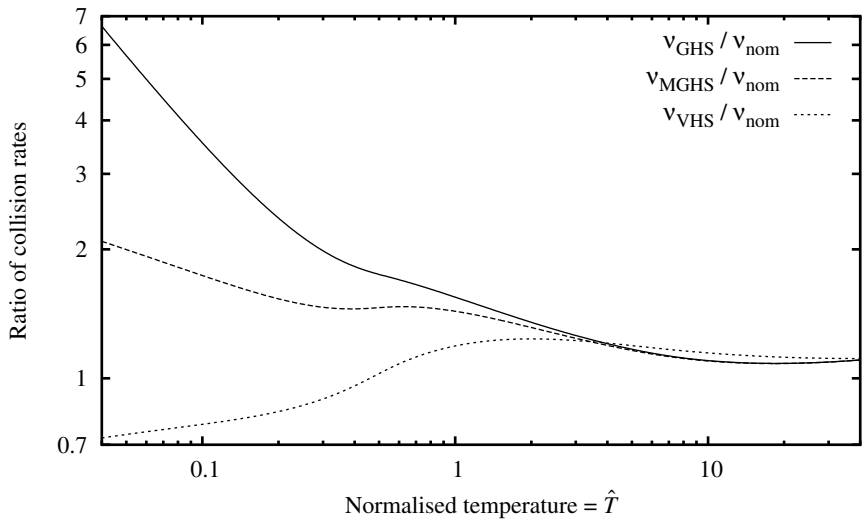

Figure C.3: Relative collision rates for the GHS, MGHS and VHS models. The GHS and MGHS parameters are given in Fig. C.2.

For the GHS model $\hat{V}$ is given by

$$\hat{V} = \sum_{i=1}^{N} \hat{\sigma}_i \hat{g}^{1-2v_i}.$$

For argon, the $\hat{V}$ versus $\hat{g}$ behaviour is shown in Fig. C.4. At low collision speeds, it is apparent that $V \to \infty$. When using the NTC method [20] for selecting collision partners, as described in §4.2.2, the GHS model has poor computational efficiency because N_{pairs} becomes very large as V becomes very large. This results in a very large number of particle pairs being tested for collision, each of which has an extremely small probability of actually participating in a collision.

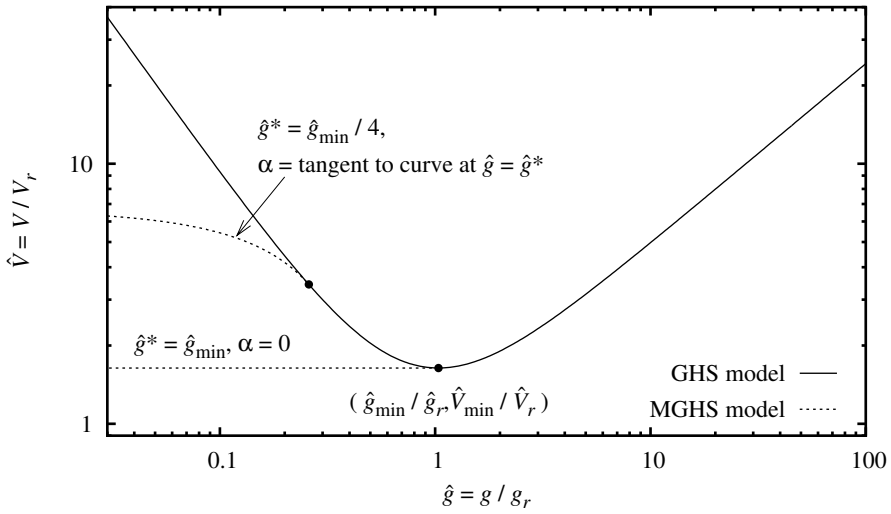

Figure C.4: $\hat{V} \equiv V/V_r = \sigma g/(\sigma_r g_r)$ versus $\hat{g} \equiv g/g_r$ behaviour for the GHS model and two possible versions of the MGHS model. The GHS parameters for argon from Fig. C.2 and $\sigma_r = \sigma_1$ have been used.

For the GHS model, Macrossan and Lilley [125] used an alternative reference cross-section $\sigma_r' = \sigma_1 + \sigma_2$ and defined $\sigma_1 = \phi\sigma_r'$. These give $\sigma_2 = \sigma_r'(1-\phi)$. For $N = 2$,

$$\Omega_{\text{GHS}} = \frac{\sigma_r'}{3}\left[\phi\frac{\Gamma(4-\upsilon_1)}{\hat{T}^{\upsilon_1}} + (1-\phi)\frac{\Gamma(4-\upsilon_2)}{\hat{T}^{\upsilon_2}}\right].$$

Also, $V_r\hat{\sigma}_1 = \phi V_r'$ and $V_r\hat{\sigma}_2 = (1-\phi)V_r'$, so Eq. C.10 reduces to

$$\nu_{\text{GHS}} = 2nV_r'\left(\frac{\hat{T}}{\pi}\right)^{\frac{1}{2}}\left[\phi\frac{\Gamma(2-\upsilon_1)}{\hat{T}^{\upsilon_1}} + (1-\phi)\frac{\Gamma(2-\upsilon_2)}{\hat{T}^{\upsilon_2}}\right].$$

These forms of Ω_{GHS} and ν_{GHS} are identical to those given by Macrossan and Lilley [125].

C.4 Modified generalised hard sphere model

Macrossan and Lilley [125] introduced the modified GHS (MGHS) model to improve the computational efficiency of the GHS model whilst retaining its realistic viscosity behaviour. Essentially, this involved limiting the value of V at low collision speeds, which effectively reduces the number of particle pairs that must be tested for collision when using the NTC method for selecting collision partners. The MGHS model is implemented by first specifying a transition point $(\hat{g}^*, \hat{V}^*)$ in the $\hat{V}$ versus $\hat{g}$ behaviour of the original GHS

model. Then, for $\hat{g} < \hat{g}^*$, the $\hat{V}$ versus $\hat{g}$ behaviour of the GHS model is simply replaced by a straight line. The gradient α of this line may be set to the tangent at the transition point, given by

$$\alpha \equiv \frac{d\hat{V}}{d\hat{g}} = \sum_{i=1}^{N} (1 - 2\upsilon_i)\, \hat{\sigma}_i / \hat{g}^{2\upsilon_i}.$$

Two possible versions of the MGHS model are shown in Fig. C.4. The linear portion of the MGHS model is described by the equation

$$\left(\hat{V}^* - \hat{V}\right) / \left(\hat{g}^* - \hat{g}\right) = \alpha,$$

which provides

$$\hat{V} = \hat{V}^* - \alpha\left(\hat{g}^* - \hat{g}\right) = \alpha\hat{g} + \hat{V}^* - \alpha\hat{g}^*.$$

The normalised collision cross-section of the MGHS model is then given by the conditional equation

$$\hat{\sigma} = \begin{cases} \alpha + \left(\hat{V}^* - \alpha\hat{g}^*\right)/\hat{g} & \text{for} \quad \hat{g} < \hat{g}^* \\ \sum_{i=1}^{N} \hat{\sigma}_i / \hat{g}^{2\upsilon_i} & \text{for} \quad \hat{g} \geq \hat{g}^*. \end{cases} \tag{C.11}$$

The viscosity behaviour of the MGHS model is found by evaluating the viscosity expressions of Eqs. C.5 and C.6 with the MGHS cross-section of Eq. C.11. In this case, Ω is given by

$$\begin{aligned} \Omega_{\text{MGHS}} \;=\; & \frac{2\sigma_r}{3} \int_0^{\hat{g}=\hat{g}^*} \left[\alpha + \left(\hat{V}^* - \alpha\hat{g}^*\right)/\hat{g}\right] \tilde{g}^7 \exp\left(-\tilde{g}^2\right) d\tilde{g} \\ & + \frac{2\sigma_r}{3} \int_{\hat{g}=\hat{g}^*}^{\infty} \left[\sum_{i=1}^{N} \hat{\sigma}_i / \hat{g}^{2\upsilon_i}\right] \tilde{g}^7 \exp\left(-\tilde{g}^2\right) d\tilde{g}. \end{aligned}$$

At the MGHS transition point where $g = g^*$, Eq. C.7 gives $\tilde{g} = \hat{g}^*/\hat{T}^{\frac{1}{2}}$. For convenience, this will be denoted using

$$\omega \equiv \hat{g}^*/\hat{T}^{\frac{1}{2}}.$$

Therefore

$$\begin{aligned} \Omega_{\text{MGHS}} \;=\; & \frac{2\sigma_r}{3} \left[\alpha \int_0^{\omega} \tilde{g}^7 \exp\left(-\tilde{g}^2\right) d\tilde{g} + \frac{\left(\hat{V}^* - \alpha\hat{g}^*\right)}{\hat{T}^{1/2}} \int_0^{\omega} \tilde{g}^6 \exp\left(-\tilde{g}^2\right) d\tilde{g}\right] \\ & + \frac{2\sigma_r}{3} \sum_{i=1}^{N} \frac{\hat{\sigma}_i}{\hat{T}^{\upsilon_i}} \int_{\omega}^{\infty} \tilde{g}^{7-2\upsilon_i} \exp\left(-\tilde{g}^2\right) d\tilde{g}. \end{aligned}$$

Using the integrals in Eqs. A.2, A.5 and A.6, this gives

$$\Omega_{\text{MGHS}} = (2\sigma_r/3)\,(A + B),$$

where

$$A \equiv \alpha I_7'(\omega) + \frac{\hat{V}^* - \alpha\hat{g}^*}{\hat{T}^{1/2}} I_6'(\omega) \quad \text{and} \quad B \equiv \sum_{i=1}^{N} \frac{\hat{\sigma}_i \Gamma\left(4 - v_i, \omega^2\right)}{2\hat{T}^{v_i}}.$$

For a particular version of the MGHS model, Ω_{MGHS} is also a function of $\hat{T}$ alone. The viscosity behaviour of the MGHS model with $\left(\hat{V}^*, \hat{g}^*\right) = \left(\hat{V}_{\min}, \hat{g}_{\min}\right)$ is shown in Fig. C.2. At low temperatures, the viscosity behaviour of the MGHS model is in better agreement with the argon viscosity recommended by Kestin *et al.* [90] than the viscosity behaviour provided by the GHS model.

The MGHS collision rate is derived by evaluating Eq. C.9 with the MGHS expression for $\hat{\sigma}\hat{g}$, which is

$$\hat{\sigma}\hat{g} = \hat{V} = \begin{cases} \alpha\hat{T}^{\frac{1}{2}}\tilde{g} + \left(\hat{V}^* - \alpha\hat{g}^*\right) & \text{for} \quad \hat{g} < \hat{g}^* \\ \hat{T}^{\frac{1}{2}} \sum_{i=1}^{N} \hat{\sigma}_i \tilde{g}^{1-2v_i} / \hat{T}^{v_i} & \text{for} \quad \hat{g} \geq \hat{g}^*. \end{cases}$$

Using Eq. C.9,

$$\begin{aligned} \nu_{\mathrm{MGHS}} &= 4nV_r \left(\frac{\hat{T}}{\pi}\right)^{\frac{1}{2}} \int_0^{\omega} \left[\alpha\tilde{g}^3 + \frac{\hat{V}^* - \alpha\hat{g}^*}{\hat{T}^{1/2}}\tilde{g}^2\right] \exp\left(-\tilde{g}^2\right) d\tilde{g} \\ &\quad + 4nV_r \left(\frac{\hat{T}}{\pi}\right)^{\frac{1}{2}} \sum_{i=1}^{N} \frac{\hat{\sigma}_i}{\hat{T}^{v_i}} \int_{\omega}^{\infty} \tilde{g}^{3-2v_i} \exp\left(-\tilde{g}^2\right) d\tilde{g}. \end{aligned}$$

This can be written

$$\nu_{\mathrm{MGHS}} = 4nV_r \left(\hat{T}/\pi\right)^{\frac{1}{2}} (C + D),$$

where

$$C \equiv \alpha I_3'(\omega) + \frac{\hat{V}^* - \alpha\hat{g}^*}{\hat{T}^{1/2}} I_2'(\omega) \quad \text{and} \quad D \equiv \sum_{i=1}^{N} \hat{\sigma}_i \frac{\Gamma\left(2 - v_i, \omega^2\right)}{2\hat{T}^{v_i}}.$$

It is apparent that ν_{MGHS} depends on $\hat{T}$ and n. The ratio $\nu_{\mathrm{MGHS}}/\nu_{\mathrm{nom}}$ is shown in Fig. C.3 for argon with the MGHS transition point $\left(\hat{V}^*, \hat{g}^*\right) = \left(\hat{V}_{\min}, \hat{g}_{\min}\right)$. At low temperatures, the ν_{MGHS} is much lower than ν_{GHS}.

Using the notation of Macrossan and Lilley [125], it can be shown that the expressions for A and C remain unchanged, and that B and D become

$$B' = \phi \frac{\Gamma\left(4 - v_1, \omega^2\right)}{2\hat{T}^{v_1}} + (1 - \phi) \frac{\Gamma\left(4 - v_2, \omega^2\right)}{2\hat{T}^{v_2}}$$

and

$$D' = \phi \frac{\Gamma\left(2 - v_1, \omega^2\right)}{2\hat{T}^{v_1}} + (1 - \phi) \frac{\Gamma\left(2 - v_2, \omega^2\right)}{2\hat{T}^{v_2}}$$

respectively.

Macrossan and Lilley [125] examined the computational efficiency of the MGHS model relative to the GHS and VHS models. Over a wide range of temperatures, the MGHS model is significantly more efficient than the GHS model. This is due to a combination of

two factors. Firstly, when using the NTC method to select collision partners, the number of collision pairs that must be tested for the MGHS model is greatly reduced relative to that for the GHS model, because $V = \sigma g$ is limited at low collision speeds. Secondly, as shown in Fig. C.3, the MGHS model has a lower collision rate than the GHS model. The MGHS model requires no more than 15% more CPU time than the VHS model.

C.5 Derivation of TCE model parameters

This section gives a method for obtaining expressions for the non-dimensional TCE parameters β_{TCE} and χ_2 that include the Arrhenius rate parameters C^+ and η^+ and the VHS parameters of the collision pair. In deriving these expressions, it is assumed that the total reduced collision energy $\tilde{\epsilon}_c$ is distributed according to the continuous distribution $f(\tilde{\epsilon}_c)$ from Eq. 6.4. Using the TCE reaction probability $\left(P_R^+\right)_{\mathrm{TCE}}$ from Eq. 6.2, the mean TCE reaction probability is

$$\begin{aligned}
\langle P_R^+ \rangle_{\mathrm{TCE}} &= \int_0^\infty \left(P_R^+\right)_{\mathrm{TCE}} (\tilde{\epsilon}_c)\, f(\tilde{\epsilon}_c)\, d\tilde{\epsilon}_c \\
&= \frac{\beta_{\mathrm{TCE}}}{\Gamma(\chi_1+1)\tilde{\epsilon}_a^{\chi_2}} \int_{\tilde{\epsilon}_a}^\infty (\tilde{\epsilon}_c - \tilde{\epsilon}_a)^{\chi_1+\chi_2} \exp(-\tilde{\epsilon}_c)\, d\tilde{\epsilon}_c \\
&= \frac{\beta_{\mathrm{TCE}} \exp(-\tilde{\epsilon}_a)}{\tilde{\epsilon}_a^{\chi_2}} \frac{\Gamma(\chi_1+\chi_2+1)}{\Gamma(\chi_1+1)}.
\end{aligned}$$

Here Eq. A.1 was used to evaluate the definite integral. This mean TCE reaction probability equals the mean VHS reaction probability $\langle P_R^+ \rangle_{\mathrm{VHS}}$ from Eq. 6.1. Therefore

$$k^+ = \beta_{\mathrm{TCE}} \frac{\mathcal{N}\Xi}{f_s} \frac{\exp(-\tilde{\epsilon}_a)}{\tilde{\epsilon}_a^{\chi_2}} \left(\frac{T}{T_r}\right)^{\frac{1}{2}-\upsilon} \frac{\Gamma(\chi_1+\chi_2+1)}{\Gamma(\chi_1+1)}.$$

The TCE model attempts to recover the Arrhenius rate equation at thermal equilibrium, so this expression for k^+ is equated with Eq. 5.6. Therefore

$$C^+ \left(\frac{T}{\Theta_a}\right)^{\eta^+} = \beta_{\mathrm{TCE}} \frac{\mathcal{N}\Xi}{f_s} \left(\frac{T}{\Theta_a}\right)^{\chi_2} \left(\frac{T}{T_r}\right)^{\frac{1}{2}-\upsilon} \frac{\Gamma(\chi_1+\chi_2+1)}{\Gamma(\chi_1+1)}$$

where $\tilde{\epsilon}_a = \Theta_a/T$ has been used. Equating the temperature powers gives

$$\eta^+ = \chi_2 + \frac{1}{2} - \upsilon \quad \text{and} \quad \chi_2 = \eta^+ + \upsilon - \frac{1}{2}.$$

Equating the leading constants gives

$$\beta_{\mathrm{TCE}} = \frac{C^+ f_s}{\mathcal{N}\Xi} \left(\frac{T_r}{\Theta_a}\right)^{\frac{1}{2}-\upsilon} \frac{\Gamma(\chi_1+1)}{\Gamma(\chi_1+\chi_2+1)}.$$

C.6 Derivation of VFD model parameters

This section gives a method for obtaining expressions for the non-dimensional VFD parameters β_{VFD} and ψ that include the Arrhenius rate parameters C^+ and η^+ and the VHS parameters of the collision pair. This derivation applies to the general dissociation reaction AB + M $\rightarrow$ A + B + M. The VFD dissociation probability $\left(P_R^+\right)_{\mathrm{VFD}}$ applies to the dissociation probability of the diatomic particle AB. The vibrational energy of AB, denoted $(\epsilon_{\mathrm{vib}})_{\mathrm{AB}}$, is used directly in calculating $\left(P_R^+\right)_{\mathrm{VFD}}$. The remaining energy ϵ_{rem} is defined as the amount of collision energy remaining in the total collision energy ϵ_c after subtracting ϵ_{vib}. In terms of reduced energies,

$$\tilde{\epsilon}_{\mathrm{rem}} \equiv \tilde{\epsilon}_c - (\tilde{\epsilon}_{\mathrm{vib}})_{\mathrm{AB}} = \tilde{\epsilon}_g + (\tilde{\epsilon}_{\mathrm{rot}})_{\mathrm{AB}} + (\tilde{\epsilon}_{\mathrm{rot}})_{\mathrm{M}} + (\tilde{\epsilon}_{\mathrm{vib}})_{\mathrm{M}}\,.$$

The DOF associated with $\tilde{\epsilon}_{\mathrm{rem}}$ is

$$\zeta_{\mathrm{rem}} \equiv \zeta_g + (\zeta_{\mathrm{rot}})_{\mathrm{AB}} + (\zeta_{\mathrm{rot}})_{\mathrm{M}} + (\zeta_{\mathrm{vib}})_{\mathrm{M}}\,.$$

Here, the effective number of vibrational DOF in the diatomic particle AB being tested for dissociation is denoted ζ_{vib}. The form of $\left(P_R^+\right)_{\mathrm{VFD}}$ in Eq. 6.6 was proposed by Haas and Boyd [73, 74] for harmonic oscillators. However, the derivation of the VFD parameters β_{VFD} and ψ depends on the assumption of continuous equilibrium energy distributions, which have the form of Eq. 2.16. For $\tilde{\epsilon}_{\mathrm{rem}}$ and $\tilde{\epsilon}_{\mathrm{vib}}$, these distributions are

$$f\left(\tilde{\epsilon}_{\mathrm{rem}}\right) = \frac{\tilde{\epsilon}_{\mathrm{rem}}^{\zeta_{\mathrm{rem}}/2-1}\exp\left(-\tilde{\epsilon}_{\mathrm{rem}}\right)}{\Gamma\left(\zeta_{\mathrm{rem}}/2\right)} \quad \text{and} \quad f\left(\tilde{\epsilon}_{\mathrm{vib}}\right) = \frac{\tilde{\epsilon}_{\mathrm{vib}}^{\zeta_{\mathrm{vib}}/2-1}\exp\left(-\tilde{\epsilon}_{\mathrm{vib}}\right)}{\Gamma\left(\zeta_{\mathrm{vib}}/2\right)}.$$

Using Eqs. 4.12, 4.14 and 6.3, it can be shown that

$$\zeta_{\mathrm{rem}}/2 - 1 = 1 - \upsilon + \bar{\zeta}_{\mathrm{int}} - \zeta_{\mathrm{vib}}/2 = \chi_1 - \zeta_{\mathrm{vib}}/2,$$

so

$$f\left(\tilde{\epsilon}_{\mathrm{rem}}\right) = \tilde{\epsilon}_{\mathrm{rem}}^{\chi_1-\zeta_{\mathrm{vib}}/2}\exp\left(-\tilde{\epsilon}_{\mathrm{rem}}\right)/\Gamma\left(\chi_1 - \zeta_{\mathrm{vib}}/2 + 1\right).$$

Assuming that $f(\tilde{\epsilon}_{\mathrm{rem}})$ and $f(\tilde{\epsilon}_{\mathrm{vib}})$ are independently distributed, the joint distribution is

$$f\left(\tilde{\epsilon}_{\mathrm{rem}}, \tilde{\epsilon}_{\mathrm{vib}}\right) = f\left(\tilde{\epsilon}_{\mathrm{rem}}\right) \times f\left(\tilde{\epsilon}_{\mathrm{vib}}\right) = \frac{\tilde{\epsilon}_{\mathrm{rem}}^{\chi_1-\zeta_{\mathrm{vib}}/2}\tilde{\epsilon}_{\mathrm{vib}}^{\zeta_{\mathrm{vib}}/2-1}\exp\left(-\tilde{\epsilon}_c\right)}{\Gamma\left(\chi_1 - \zeta_{\mathrm{vib}}/2 + 1\right)\Gamma\left(\zeta_{\mathrm{vib}}/2\right)}.$$

This joint distribution function may be transformed from $f\left(\tilde{\epsilon}_{\mathrm{rem}}, \tilde{\epsilon}_{\mathrm{vib}}\right)$ to $f\left(\tilde{\epsilon}_c, \tilde{\epsilon}_{\mathrm{vib}}\right)$ using the method in §A.2. For this transformation, $|J| = 1$. Therefore

$$f\left(\tilde{\epsilon}_c, \tilde{\epsilon}_{\mathrm{vib}}\right) = \frac{\left(\tilde{\epsilon}_c - \tilde{\epsilon}_{\mathrm{vib}}\right)^{\chi_1-\zeta_{\mathrm{vib}}/2}\tilde{\epsilon}_{\mathrm{vib}}^{\zeta_{\mathrm{vib}}/2-1}\exp\left(-\tilde{\epsilon}_c\right)}{\Gamma\left(\chi_1 - \zeta_{\mathrm{vib}}/2 + 1\right)\Gamma\left(\zeta_{\mathrm{vib}}/2\right)}$$

The mean VFD dissociation probability $\langle P_R^+ \rangle_{\rm VFD}$ is obtained from

$$\begin{aligned}
\langle P_R^+ \rangle_{\rm VFD} &= \int_0^\infty \int_0^{\tilde{\epsilon}_c} \left(P_R^+\right)_{\rm VFD} f\left(\tilde{\epsilon}_c, \tilde{\epsilon}_{\rm vib}\right) d\tilde{\epsilon}_{\rm vib} d\tilde{\epsilon}_c \\
&= \frac{\beta_{\rm VFD}\ \tilde{\epsilon}_d^{\chi_1 - \psi}}{\Gamma\left(\chi_1 - \zeta_{\rm vib}/2 + 1\right)\Gamma\left(\zeta_{\rm vib}/2\right)} \\
&\quad \times \int_{\tilde{\epsilon}_d}^\infty \frac{\left(\tilde{\epsilon}_c - \tilde{\epsilon}_d\right)^\psi}{\tilde{\epsilon}_c^{\phi + \chi_1}} \exp\left(-\tilde{\epsilon}_c\right) \int_0^{\tilde{\epsilon}_c} \left(\tilde{\epsilon}_c - \tilde{\epsilon}_{\rm vib}\right)^{\chi_1 - \zeta_{\rm vib}/2} \tilde{\epsilon}_{\rm vib}^{\phi + \zeta_{\rm vib}/2 - 1} d\tilde{\epsilon}_{\rm vib}\, d\tilde{\epsilon}_c \\
&= \frac{\beta_{\rm VFD}\ \tilde{\epsilon}_d^{\chi_1 - \psi} \Gamma\left(\phi + \zeta_{\rm vib}/2\right)}{\Gamma\left(\phi + \chi_1 + 1\right)\Gamma\left(\zeta_{\rm vib}/2\right)} \int_{\tilde{\epsilon}_d}^\infty \left(\tilde{\epsilon}_c - \tilde{\epsilon}_d\right)^\psi \exp\left(-\tilde{\epsilon}_c\right) \\
&= \beta_{\rm VFD}\ \tilde{\epsilon}_d^{\chi_1 - \psi} \exp\left(-\tilde{\epsilon}_d\right) \frac{\Gamma\left(\phi + \zeta_{\rm vib}/2\right)\Gamma(\psi + 1)}{\Gamma\left(\phi + \chi_1 + 1\right)\Gamma\left(\zeta_{\rm vib}/2\right)}.
\end{aligned}$$

Eqs. A.8 and A.1 were used here to evaluate the definite integrals. This mean VFD reaction probability $\langle P_R^+ \rangle_{\rm VFD}$ equals the mean VHS reaction probability $\langle P_R^+ \rangle_{\rm VHS}$ from Eq. 6.1. Therefore

$$k^+ = \beta_{\rm VFD} \frac{\mathcal{N}\Xi}{f_s} \left(\frac{T}{T_r}\right)^{\frac{1}{2} - \upsilon} \left(\frac{\Theta_d}{T}\right)^{\chi_1 - \psi} \frac{\Gamma\left(\phi + \zeta_{\rm vib}/2\right)\Gamma(\psi + 1)}{\Gamma\left(\phi + \chi_1 + 1\right)\Gamma\left(\zeta_{\rm vib}/2\right)} \exp\left(-\frac{\Theta_d}{T}\right)$$

where $\tilde{\epsilon}_d = \Theta_d / T$ has been used. The VFD model attempts to recover the Arrhenius rate at thermal equilibrium, so this expression for k^+ is equated with Eq. 5.6. Therefore

$$C^+ \left(\frac{T}{\Theta_d}\right)^{\eta^+} = \beta_{\rm VFD} \frac{\mathcal{N}\Xi}{f_s} \left(\frac{T}{T_r}\right)^{\frac{1}{2} - \upsilon} \left(\frac{\Theta_d}{T}\right)^{\chi_1 - \psi} \frac{\Gamma\left(\phi + \zeta_{\rm vib}/2\right)\Gamma(\psi + 1)}{\Gamma\left(\phi + \chi_1 + 1\right)\Gamma\left(\zeta_{\rm vib}/2\right)}.$$

Equating powers of T gives

$$\eta^+ = \frac{1}{2} - \upsilon - \left(\chi_1 - \psi\right), \quad \text{so} \quad \psi = \eta^+ + \upsilon - \frac{1}{2} + \chi_1 = \chi_1 + \chi_2.$$

Equating leading constants gives

$$\beta_{\rm VFD} = \frac{C^+ f_s}{\mathcal{N}\Xi} \left(\frac{T_r}{\Theta_d}\right)^{\frac{1}{2} - \upsilon} \frac{\Gamma\left(\phi + \chi_1 + 1\right)\Gamma\left(\zeta_{\rm vib}/2\right)}{\Gamma\left(\phi + \zeta_{\rm vib}/2\right)\Gamma\left(\psi + 1\right)}.$$

C.7 Macroscopic dissociation rates for the TLD model

Many published studies use zero-dimensional DSMC heat bath simulations to obtain the macroscopic reaction rates realised by conventional DSMC chemistry models under thermal equilibrium conditions. A heat bath simulation was performed here to calculate the macroscopic nitrogen dissociation rates realised by the TLD model. The calculation used 6×10^5 N_2 particles and 4×10^5 N particles, with the VHS parameters from Table B.1. Colliding particles were selected with probability $\sigma g / (\sigma g)_{\max}$. BL energy exchange was performed using the schemes described in §4.5.2 and §4.5.3. Relaxing particles were selected according to the scheme of Gimelshein *et al.* [65]. TLD reaction probabilities were

calculated using the procedures discussed in §6.4.2. To reduce the number of collisions with $\left(P_R^+\right)_{\text{TLD}} > 1$, $\epsilon_{\text{vib}} = \left(\frac{1}{2} + q\right) k\Theta_{\text{vib}}$ was used in calculating $\left(P_R^+\right)_{\text{TLD}}$ [150]. When $R_f < \left(P_R^+\right)_{\text{TLD}}$ a reaction was counted but not actually performed. For a given temperature a target number of dissociation events, denoted N_R^+, was specified. The simulation was run until this target number of events occurred. Using Eq. 6.1, the dissociation rate at a given temperature was then obtained from

$$k^+(T) = \langle P_R^+ \rangle_{\text{VHS}} \frac{\mathcal{N}\Xi}{f_s} \left(\frac{T}{T_r}\right)^{\frac{1}{2}-\upsilon} = \frac{N_R^+}{N_{\text{colls}}} \frac{\mathcal{N}\Xi}{f_s} \left(\frac{T}{T_r}\right)^{\frac{1}{2}-\upsilon}, \tag{C.12}$$

where N_{colls} is the number of collisions performed to obtain N_R^+ events. The macroscopic TLD rates calculated with this heat bath simulation are compared to some published rates in Fig. C.5.

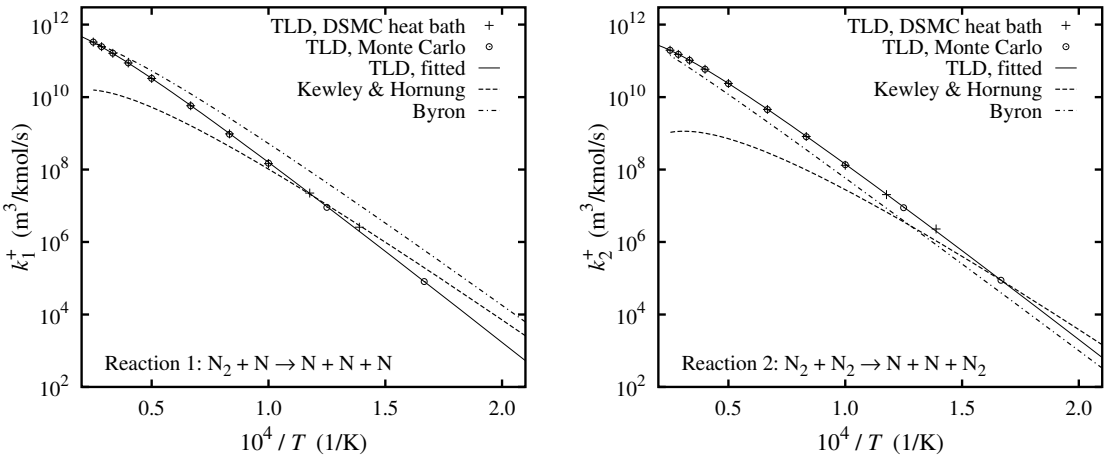

Figure C.5: Calculated macroscopic nitrogen dissociation rates for the TLD model compared to fitted rates and the published rates of Byron [44] and Kewley and Hornung [91].

Essentially, heat bath simulations just sample collision energies, and can therefore be avoided by using a Monte Carlo technique that samples the collision energies from appropriate equilibrium distributions, and then uses these sampled energies to calculate $\left(P_R^+\right)_{\text{TLD}}$. Lilley and Macrossan [106] used such a Monte Carlo sampling technique to calculate the TLD dissociation rates at thermal equilibrium. From Eq. 4.11, the distribution of reduced translational energy in collisions $\tilde{\epsilon}_g$ for VHS molecules is

$$f\left(\tilde{\epsilon}_g\right) = \tilde{\epsilon}_g^{1-\upsilon} \exp\left(-\tilde{\epsilon}_g\right) / \Gamma(2-\upsilon).$$

Here, the Cheng-Feast algorithm [50] was used to sample $\tilde{\epsilon}_g$ from this gamma distribution rather than the much less efficient acceptance-rejection method. ϵ_g was obtained from $\epsilon_g = \tilde{\epsilon}_g kT$. Some details of the Cheng-Feast algorithm are provided in §D.4. For diatoms,

the rotational energy ϵ_{rot} is obtained using

$$\epsilon_{\text{rot}} = -\ln(R_f)\, kT$$

from Eq. 4.22, and the vibrational energy level q for harmonic oscillators using

$$q = \lfloor -\ln(R_f)\, T/\Theta_{\text{vib}} \rfloor$$

from Eq. 4.23. Again, $\epsilon_{\text{vib}} = \left(\frac{1}{2} + q\right) k\Theta_{\text{vib}}$ was used to reduce the number of events with $\left(P_R^+\right)_{\text{TLD}} > 1$ [150]. The sampled collision energies were then used to calculate the dissociation probability $\left(P_R^+\right)_{\text{TLD}}$. A reaction was counted when $R_f < \left(P_R^+\right)_{\text{TLD}}$. Again, a target number of reactions N_R^+ was specified for each temperature examined. The number of samples required to obtain N_R^+ reactions was the number of collisions N_{colls}. The macroscopic dissociation rates were calculated with Eq. C.12, and are shown in Fig. C.5. The Monte Carlo sampling method was much more computationally efficient than the heat bath simulation. For the Monte Carlo results, N_R^+ was generally larger, so these results are subject to less statistical scatter and are regarded as being more reliable.

Accurate fits to the TLD rates calculated with the Monte Carlo sampling method are also included in Fig. C.5. These curve fits were found by trial and error, and are

$$\begin{aligned} k_1^+ &\approx 2.0 \times 10^{12} (T/122000)^{-1.1} \exp(-122000/T) \quad \text{m}^3/\text{kmol/s} \quad \text{and} \\ k_2^+ &\approx 9.5 \times 10^{11} (T/120500)^{-1.3} \exp(-120500/T) \quad \text{m}^3/\text{kmol/s} \end{aligned} \tag{C.13}$$

for reactions 1 and 2 respectively. Note that k_2^+ differs slightly from that used by Lilley and Macrossan [106].

Table C.1 shows the percentage of reaction events with $\left(P_R^+\right)_{\text{TLD}} > 1$. These results show that $\left(P_R^+\right)_{\text{TLD}} > 1$ in a large fraction of reactive collisions.

Table C.1: Percentage of reaction events in Monte Carlo sampling calculation with $\left(P_R^+\right)_{\text{TLD}} > 1$. Reaction 1 is $N_2 + N \rightarrow N + N + N$ and reaction 2 is $N_2 + N_2 \rightarrow N + N + N_2$.

T (K)	Reaction 1	Reaction 2	T (K)	Reaction 1	Reaction 2
6000	35.8%	33.9%	20000	65.0%	73.8%
8000	39.0%	43.5%	25000	72.1%	79.9%
10000	44.4%	50.6%	30000	77.4%	84.2%
12000	49.2%	57.0%	35000	81.5%	87.5%
15000	55.8%	64.9%	40000	84.7%	89.9%

C.8 Macroscopic dissociation rates for the EAE model

This section gives the macroscopic nitrogen dissociation rates realised by the EAE model at thermal equilibrium. The nitrogen VHS parameters from Table B.1 were used. Three different methods were used to obtain these rates, as discussed below. The version of the EAE model examined here applies to VHS harmonic oscillators with the BL vibrational energy exchange scheme of Bergemann and Boyd [9], as described in §4.5.3. The post-exchange vibrational energy level q' was selected as for unbounded harmonic oscillators. Molecules were then dissociated if q' exceeded the dissociation level q_d. A constant vibrational exchange probability $\phi_{\text{vib}} = 0.1$ was used.

The first method was a DSMC heat bath simulation similar to that described in §C.7. In this simulation, the initial vibrational energy levels of the diatoms were sampled from the distribution for bounded harmonic oscillators with $q_{\max} = q_d$. This distribution was used because no diatoms can have $q > q_d$ when the EAE model is used. BL energy exchange was performed according to the schemes described in §4.5.2 and §4.5.3. Relaxing particles were selected according to the scheme of Gimelshein *et al.* [65]. When a diatom had a post-exchange vibrational energy q' greater than the dissociation level $q_d = 33$, a dissociation event was counted, but a reaction was not actually performed. After the event was counted, the vibrational energy level was re-sampled according to the distribution for bounded harmonic oscillators. The simulation was run until a target number of reactions N_R^+ occurred. The macroscopic rates were then calculated with Eq. C.12, and are compared to some published rates in Fig. C.6.

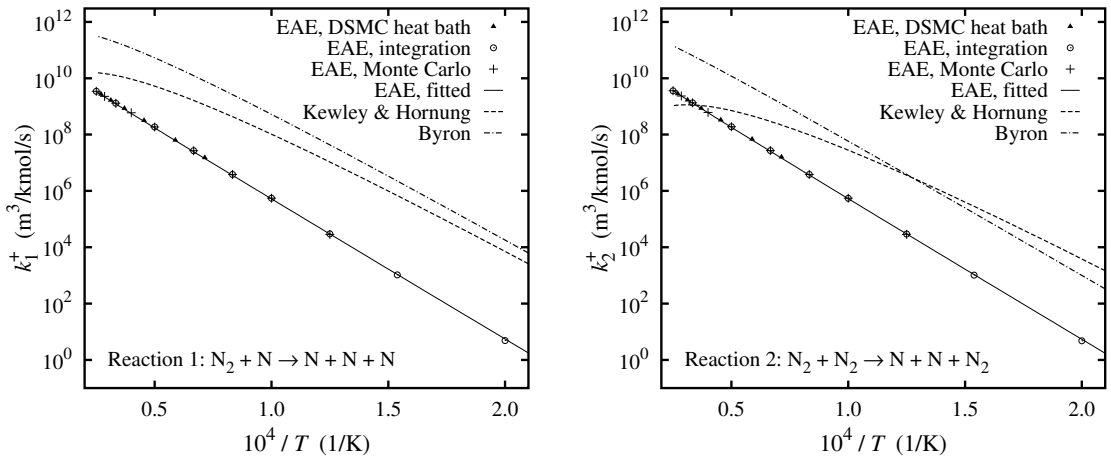

Figure C.6: Calculated macroscopic nitrogen dissociation rates for the EAE model compared to fitted rates and the published rates of Byron [44] and Kewley and Hornung [91]. A constant vibrational energy exchange probability $\phi_{\text{vib}} = 0.1$ was used.

The second method for obtaining the macroscopic EAE rates was a Monte Carlo sampling technique similar to that described in §C.7. Firstly, $\tilde{\epsilon}_g$ was sampled as in §C.7, and ϵ_{vib} was sampled as for bounded harmonic oscillators. These provided $\tilde{\epsilon}_{\text{ex}} = \tilde{\epsilon}_g + \tilde{\epsilon}_{\text{vib}}$. Next,

vibrational energy exchange was performed using the BL method described in §4.5.3. If the post-exchange vibrational energy level q' exceeded the dissociation level q_d, then a dissociation event was counted. The sampling routine was run until a target number of reactions N_R^+ occurred. The number of $\tilde{\epsilon}_{\rm ex}$ samples required for N_R^+ reactions was the number of relaxation events $N_{\rm relax}$. In the particle selection scheme of Gimelshein *et al.* [65], the probability of an exchange event occurring is $\phi_{\rm vib}$ for each diatom. Because both particles are tested for exchange, the probability of a vibrational energy exchange event occurring for a collision pair is $f_s\phi_{\rm vib}$, for constant $\phi_{\rm vib}$. For $N_{\rm colls}$ collisions, $N_{\rm relax} = f_s\phi_{\rm vib}N_{\rm colls}$, which gives $N_{\rm colls} = N_{\rm relax}/\left(f_s\phi_{\rm vib}\right)$. The macroscopic EAE dissociation rates were then calculated with Eq. C.12, and are also shown in Fig. C.6.

The third method for obtaining the macroscopic EAE rates involved deriving an integral expression for the mean EAE reaction probability $\langle P_R^+\rangle_{\rm EAE}$, and evaluating this integral numerically. Consider $N_{\rm colls}$ collisions between diatoms A_2 and species M particles. For a constant BL exchange probability $\phi_{\rm vib}$, the number of these collisions in which A_2 particles are subject to BL vibrational energy exchange is $f_s\phi_{\rm vib}N_{\rm colls}$. The number of these relaxing collisions that have BL exchange energy in class $\tilde{\epsilon}_{\rm ex}$ is then $f_s\phi_{\rm vib}N_{\rm colls}f\left(\tilde{\epsilon}_{\rm ex}\right)d\tilde{\epsilon}_{\rm ex}$. Again, it has been assumed that vibrational energy levels are distributed according to bounded harmonic oscillator model, because all diatoms that have $q' > q_d$ after BL exchange will dissociate. From Eq. A.12, the equilibrium distribution of $\tilde{\epsilon}_{\rm ex}$ for VHS molecules and bounded harmonic oscillators is

$$f\left(\tilde{\epsilon}_{\rm ex}\right) = \frac{\exp\left(-\tilde{\epsilon}_{\rm ex}\right)}{\Gamma(2-\upsilon)Q_{\rm vib}} \times S^{\rm BHO}, \quad \text{where} \quad S^{\rm BHO} = \sum_{q'=0}^{q_{\rm ex}^{\rm BHO}} \left(\tilde{\epsilon}_{\rm ex} - \frac{q'\Theta_{\rm vib}}{T}\right)^{1-\upsilon}.$$

Here,

$$q_{\rm ex}^{\rm BHO} = \min\left(\left\lfloor\frac{\tilde{\epsilon}_{\rm ex}T}{\Theta_{\rm vib}}\right\rfloor, q_d\right)$$

is the maximum possible vibrational energy level for the bounded harmonic oscillator model that corresponds to the reduced exchange energy $\tilde{\epsilon}_{\rm ex}$. Note that $S^{\rm BHO}$ is constant for a given $\tilde{\epsilon}_{\rm ex}$. In this case, the partition function $Q_{\rm vib}$ comes from Eq. 2.22 and is

$$Q_{\rm vib} = \sum_{q'=0}^{q_d} \exp\left(-\frac{q'\Theta_{\rm vib}}{T}\right).$$

For this version of the EAE model, q' was selected as for unbounded harmonic oscillators. From Eq. 4.44, the maximum value of q' is therefore

$$q_{\rm ex}^{\rm UHO} = \lfloor\tilde{\epsilon}_{\rm ex}T/\Theta_{\rm vib}\rfloor.$$

From §4.5.3, possible values of q' are generated according to $R_i\left(0, q_{\rm ex}^{\rm UHO}\right)$ and then accepted

if

$$R_f < \left(1 - \frac{q'\Theta_{\rm vib}}{\tilde{\epsilon}_{\rm ex} T}\right)^{1-v}.$$

If $q_{\rm ex}^{\rm UHO} \leq q_d$, then the dissociation probability is zero, because q' cannot exceed q_d. When $q_{\rm ex}^{\rm UHO} > q_d$, there is a possibility that molecules will dissociate. The mean dissociation probability for class $\tilde{\epsilon}_{\rm ex}$ collisions, denoted $\langle P_R^+ \rangle_{\tilde{\epsilon}_{\rm ex}}$, is obtained from Eq. 4.43 and is

$$\langle P_R^+ \rangle_{\tilde{\epsilon}_{\rm ex}} = \sum_{q'=q_d+1}^{q_{\rm ex}^{\rm UHO}} \Phi\left(q'|\tilde{\epsilon}_{\rm ex}\right) = \frac{1}{S^{\rm UHO}} \sum_{q'=q_d+1}^{q_{\rm ex}^{\rm UHO}} \left(\tilde{\epsilon}_{\rm ex} - \frac{q'\Theta_{\rm vib}}{T}\right)^{1-v},$$

where

$$S^{\rm UHO} = \sum_{q'=0}^{q_{\rm ex}^{\rm UHO}} \left(\tilde{\epsilon}_{\rm ex} - \frac{q'\Theta_{\rm vib}}{T}\right)^{1-v}.$$

Note that $S^{\rm UHO}$ is constant for a given $\tilde{\epsilon}_{\rm ex}$ value.

The number of class $\tilde{\epsilon}_{\rm ex}$ collisions that result in dissociation is

$$\langle P_R^+ \rangle_{\tilde{\epsilon}_{\rm ex}} \times f_s \phi_{\rm vib} N_{\rm colls} f\left(\tilde{\epsilon}_{\rm ex}\right) d\tilde{\epsilon}_{\rm ex},$$

and the total number of dissociation events is given by

$$\begin{aligned} N_R^+ &= \int_{\tilde{\epsilon}_d}^{\infty} f_s \phi_{\rm vib} N_{\rm colls} \langle P_R^+ \rangle_{\tilde{\epsilon}_{\rm ex}} f\left(\tilde{\epsilon}_{\rm ex}\right) d\tilde{\epsilon}_{\rm ex} \\ &= f_s \phi_{\rm vib} N_{\rm colls} \int_{\tilde{\epsilon}_d}^{\infty} \sum_{q'=q_d+1}^{q_{\rm ex}^{\rm UHO}} \left(\tilde{\epsilon}_{\rm ex} - \frac{q'\Theta_{\rm vib}}{T}\right)^{1-v} \frac{\exp\left(-\tilde{\epsilon}_{\rm ex}\right)}{\Gamma(2-v) Q_{\rm vib}} \left(\frac{S^{\rm BHO}}{S^{\rm UHO}}\right) d\tilde{\epsilon}_{\rm ex}. \end{aligned}$$

The mean EAE dissociation probability is given by

$$\langle P_R^+ \rangle_{\rm EAE} = N_R^+ / N_{\rm colls} = f_s \phi_{\rm vib} I$$

where

$$I = \int_{\tilde{\epsilon}_d}^{\infty} \frac{\exp\left(-\tilde{\epsilon}_{\rm ex}\right)}{\Gamma(2-v) Q_{\rm vib}} \left(\frac{S^{\rm BHO}}{S^{\rm UHO}}\right) \sum_{q'=q_d+1}^{q_{\rm ex}^{\rm UHO}} \left(\tilde{\epsilon}_{\rm ex} - \frac{q'\Theta_{\rm vib}}{T}\right)^{1-v} d\tilde{\epsilon}_{\rm ex}. \qquad \text{(C.14)}$$

Using Eq. C.12, the macroscopic dissociation rate is then given by

$$k^+(T) = \phi_{\rm vib} I \mathcal{N} \Xi \left(T/T_r\right)^{\frac{1}{2}-v}, \qquad \text{(C.15)}$$

which is independent of the symmetry factor f_s.

The definite integral I was evaluated numerically at various temperatures to give the macroscopic EAE dissociation rates. Here, I was evaluated using 4×10^5 points in the range $\tilde{\epsilon}_d \leq \tilde{\epsilon}_{\rm ex} \leq 20\tilde{\epsilon}_d$. The resulting k^+ values are shown in Fig. C.6 for reactions 1 and

2 in nitrogen. Good fits to these numerically calculated rates are provided by

$$\begin{aligned} k_1^+ &\approx 7.0 \times 10^{10} \left(T/\Theta_d\right)^{0.2} \exp\left(-\Theta_d/T\right) \quad \mathrm{m}^3/\mathrm{kmol/s} \quad \text{and} \\ k_2^+ &\approx 8.0 \times 10^{10} \left(T/\Theta_d\right)^{0.25} \exp\left(-\Theta_d/T\right) \quad \mathrm{m}^3/\mathrm{kmol/s}, \end{aligned}$$

which are of the Arrhenius form.

There is good agreement between the rates calculated with the three different methods described above. Even with the high vibrational exchange probability $\phi_{\mathrm{vib}} = 0.1$, the dissociation rates are much lower than those recommended by both Byron [44] and Kewley and Hornung [91]. Bird [22] claims that the EAE model provides reaction rates close to published rates, which contrasts with the results obtained here.

APPENDIX **D**

Pseudo-random number generators and sampling

This appendix briefly discusses the pseudo-random number generator used in this study, and gives the results of a basic statistical test to assess its adequacy. Efficient computational algorithms for generating the direction cosines of points uniformly distributed on the surface of a sphere and standard normal variates are also presented. Methods for sampling from continuous Boltzmann energy distributions are also considered.

D.1 Pseudo-random number generator used in this study

This study used the `random()` function, supplied with the LINUX operating system, to generate successive pseudo-random integers in the range $[0, 2^{31} - 1]$. According to the system documentation, `random()` uses a non-linear additive feedback random integer generator and has a large period of approximately $16\left(2^{31} - 1\right)$. A total of 2^{31} integers are available. The function `Rf()` used `random()` to return uniformly distributed double-precision fractions R_f in the range (0,1). The function `Rf()` generated R_f with

$$R_f = \left[0.5 + \texttt{(double)random()}\right]/2^{31}.$$

This formula was used to prevent `Rf()` from returning zero, which causes problems when evaluating $\ln(R_f)$.

Numerous authors, including Knuth [92] and Gentle [62], give the details of several statistical tests that can be used to examine the adequacy of pseudo-random number generators. One simple test, used by Bird [21], considers the two-dimensional distribution of successive pairs of pseudo-random numbers. In this test, the location of each pair within a unit square is given by the point with Cartesian co-ordinates $(R_{f,1}, R_{f,2})$. For 10^8 points, a 100×100 array of equally sized cells is considered within the unit square, and each point is assigned to the cell it occupies. The total number of points within each cell is calculated, and compared to the expected mean number of 10^4 points per cell to determine the deviation of the total from the mean.

For randomly distributed points, the distribution of the number of points in each cell,

denoted N, conforms to the Poisson distribution

$$P(N) = \bar{N}^N \exp\left(-\bar{N}\right)/N!\,.$$

For large N, this is indistinguishable from the normal distribution

$$P(N) = \exp\left[-\left(N-\bar{N}\right)^2/\left(2\bar{N}\right)\right]/\left(2\pi\bar{N}\right)^{\frac{1}{2}}$$

which has a standard deviation $\sigma = \bar{N}^{1/2}$. A perfect random number generator would provide this theoretical distribution of N. For the normal distribution, the theoretical fraction of points within $a\sigma$ of $\bar{N}$ is erf $\left(a/\sqrt{2}\right)$. The adequacy of a pseudo-random number generator can be assessed by comparing the deviation of N from $\bar{N} = 10^4$ for each cell to that for the normal distribution.

This test was performed 40 times on the `Rf()` function, and the mean results are shown in Table D.1. The results are quite close to those for the theoretical normal distribution, and are similar to the results that Bird [21] gives for various other generators. Therefore `Rf()` appears to be adequate.

Table D.1: Mean results for 40 tests performed on the `Rf()` pseudo-random number generator, compared to the normal distribution. $\bar{N} = 10^4$ and $\sigma = 100$.

Range	Number of cells with N in specified range	
	`Rf()` function	Normal distribution
$\leq 1\sigma$	6856.1	6826.9
$> 1\sigma$	3143.9	3173.1
$> 2\sigma$	447.2	455.00
$> 3\sigma$	27.575	26.998
$> 4\sigma$	0.55	0.63342
$> 5\sigma$	0.0	0.005733

D.2 Generating points uniformly distributed on a sphere

Marsaglia [130] provided an efficient algorithm for generating the direction cosines of points uniformly distributed on the surface of a unit sphere. The algorithm is:

1. Generate $u_1 = 2R_f - 1$ and $u_2 = 2R_f - 1$.

2. Let $s = u_1^2 + u_2^2$.

3. If $s > 1$ return to step 1.

4. Let $q = 2(1-s)^{1/2}$.

5. The three direction cosines are then $1-2s$, qu_1 and qu_2.

Approximately 1.273 iterations are required to generate each set of direction cosines. For 10^8 sets, this algorithm requires only about 61% of the CPU time used by the conventional method, where $\cos\phi = 2R_f - 1$ and $\theta = 2\pi R_f$ are generated to give the three direction cosines $\cos\phi$, $\sin\phi\cos\theta$ and $\sin\phi\sin\theta$.

D.3 Generating standard normal variates

The Box-Muller transformation [27] is often used to generate pairs of standard normal variates. In this method $r = (-2\ln R_f)^{1/2}$ and $\theta = 2\pi R_f$ are generated, and then two independent standard normal variates $z_1 = r\cos\theta$ and $z_2 = r\sin\theta$ are calculated. Marsaglia [129] introduced a more efficient polar algorithm for generating standard normal variates. The algorithm is:

1. Generate $u_1 = 2R_f - 1$ and $u_2 = 2R_f - 1$.
2. Let $s = u_1^2 + u_2^2$.
3. If $s \geq 1$ return to step 1.
4. Let $q = (-2\ln s/s)^{1/2}$.
5. Two independent standard normal variates are then calculated by $z_1 = qu_1$ and $z_2 = qu_2$.

Again, approximately 1.273 iterations are required to generate each pair of normal variates. For 10^8 pairs, this polar algorithm requires only about 76% of the CPU time used by the Box-Muller transformation.

D.4 Sampling from a continuous Boltzmann energy distribution

From Eq. 2.16, the continuous Boltzmann energy distribution for ζ DOF is

$$f(\tilde{\epsilon}) = \tilde{\epsilon}^{\,\zeta/2-1}\exp(-\tilde{\epsilon})/\Gamma(\zeta/2),$$

where $\tilde{\epsilon} = \epsilon/(kT)$ is a reduced energy. This distribution is called the gamma distribution. To sample from this distribution using the acceptance-rejection method, the maximum of the distribution $f_{\max}$ is required. From differentiation, $f_{\max}$ occurs at $\tilde{\epsilon} = \zeta/2 - 1$ and is

$$f_{\max} = (\zeta/2-1)^{\zeta/2-1}\exp(-\zeta/2+1)/\Gamma(\zeta/2).$$

For convenience,

$$a \equiv \zeta/2 - 1 \quad \text{and} \quad b \equiv a^a/\exp(a)$$

may be defined, so the acceptance criterion $f/f_{\max}$ becomes

$$f/f_{\max} = \tilde{\epsilon}^{\,a} \exp(-\tilde{\epsilon})/b.$$

When sampling from $f(\tilde{\epsilon})$ with the acceptance-rejection method, uniformly distributed $\tilde{\epsilon}$ values are generated within the range of interest, and are accepted if

$$R_f < f/f_{\max}.$$

When $\zeta = 2$, the gamma distribution reduces to the exponential distribution $f(\tilde{\epsilon}) = \exp(-\tilde{\epsilon})$ and $\tilde{\epsilon}$ is sampled using

$$\tilde{\epsilon} = -\ln(R_f).$$

For this case, $\tilde{\epsilon} \to \infty$ as $R_f \to 0$, so $R_f = 0$ must be avoided.

The Cheng-Feast algorithm [50] can be used to sample from the gamma distribution

$$f(\tilde{\epsilon}) = \tilde{\epsilon}^{\,\alpha-1} \exp(-\tilde{\epsilon})/\Gamma(\alpha)$$

where the shape parameter $\alpha > 1$. Using $a = \alpha - 1$, $b = [\alpha - 1/(6\alpha)]/a$, $c = 2/a$ and $d = c + 2$, the Cheng-Feast algorithm is:

1. Generate $u_1 = R_f$ and $u_2 = R_f$.
2. Let $w = bu_1/u_2$.
3. If $cu_2 - d + w + 1/w \leq 0$ go to step 6.
4. If $c \ln u_2 - \ln w + w < 1$ go to step 6.
5. Return to step 1.
6. Use $\tilde{\epsilon} = aw$.

For the distribution of $\tilde{\epsilon}_g$ in collisions for VHS molecules, given by Eq. 4.11, $\alpha - 1 = 1 - v$ so $\alpha = 2 - v$. For typical $v \approx 0.25$, $\alpha \approx 1.75$ and the Cheng-Feast algorithm can be used for efficient generation of $\tilde{\epsilon}_g$.

For $v = 0.25$, a comparison between the CPU requirements of the Cheng-Feast algorithm and the acceptance-rejection method was performed. 10^8 values of $\tilde{\epsilon}_g$ were generated. The acceptance-rejection method generated $\tilde{\epsilon}_g$ values between 0 and 10. In this test, the Cheng-Feast algorithm required only about 17% of the CPU time required by the acceptance-rejection method. The CPU requirements of the acceptance-rejection method increase quickly as the upper limit of $\tilde{\epsilon}_g$ is increased above 10.